

**THERMODYNAMIC INVESTIGATIONS OF  
PHOSPHATE-BASED CRYSTALLINE CERAMIC  
MATRICES FOR HLW IMMOBILIZATION**

*By*  
**DEEPAK RAWAT**  
**CHEM01201304001**

**BHABHA ATOMIC RESEARCH CENTRE, MUMBAI**

*A thesis submitted to the  
Board of Studies in Chemical Sciences  
In partial fulfillment of requirements  
for the Degree of*

**DOCTOR OF PHILOSOPHY**  
*of*  
**HOMI BHABHA NATIONAL INSTITUTE**



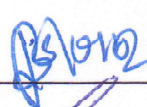
**November, 2019**

# Homi Bhabha National Institute

## Recommendations of the Viva Voce Committee

As members of the Viva Voce Committee, we certify that we have read the dissertation prepared by **Deepak Rawat** entitled "**Thermodynamic Investigations of Phosphate-based Crystalline Ceramic Matrices for HLW Immobilization**" and recommend that it may be accepted as fulfilling the thesis requirement for the award of Degree of Doctor of Philosophy.

Chairman - Prof. B.S.Tomar



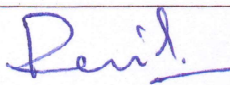
Date: 25/09/2020

Guide / Convener - Dr. Smruti Dash



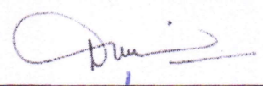
Date: 25/09/2020

Co-guide - Dr. Ratikanta Mishra



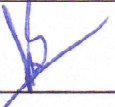
Date: 25/09/2020

Examiner - Prof. Nand Kishore



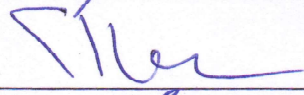
Date: 25-09-2020

Member 1- Dr. S.K. Mukherjee



Date: 25/09/2020

Member 2- Dr. C.P. Kaushik



Date: 25/9/2020

Member 3- Dr. S.C. Parida



Date: 25/09/2020

Final approval and acceptance of this thesis is contingent upon the candidate's submission of the final copies of the thesis to HBNI.

Date: 25-09-2020  
Place: Mumbai

  
(Convener, Viva Voce Board)

## STATEMENT BY AUTHOR

This dissertation has been submitted in partial fulfillment of requirements for an advanced degree at Homi Bhabha National Institute (HBNI) and is deposited in the Library to be made available to borrowers under rules of the HBNI.

Brief quotations from this dissertation are allowable without special permission, provided that accurate acknowledgement of source is made. Requests for permission for extended quotation from or reproduction of this manuscript in whole or in part may be granted by the Competent Authority of HBNI when in his or her judgment the proposed use of the material is in the interests of scholarship. In all other instances, however, permission must be obtained from the author.



(DEEPAK RAWAT)

## DECLARATION

I, hereby declare that the investigation presented in the thesis has been carried out by me. The work is original and has not been submitted earlier as a whole or in part for a degree/diploma at this or any other Institution/University.

A handwritten signature in blue ink that reads "Deepak Rawat". The signature is written in a cursive style with a large initial 'D' and a long horizontal stroke at the end.

(DEEPAK RAWAT)

## List of Publications arising from the thesis

### Journal: Published (04)

1. “Thermodynamic investigation of thorium and strontium substituted monazite solid solution”, **D. Rawat**, S. Phapale, R. Mishra and S. Dash, *Thermochim. Acta.*, **2019**, **674**, 10-20.
2. “Thermodynamic studies on charge-coupled substituted synthetic monazite”, **D. Rawat**, S. Phapale, R. Mishra, S. Dash, *J. Nucl. Mater.*, **2017**, **487**, 406-417.
3. “Thermodynamic studies of thorium phosphate diphosphate and phase investigations of Th-P-O and Th-P-H<sub>2</sub>O systems”, **D. Rawat**, S. Dash, A.R. Joshi, *Thermochim. Acta.*, **2014**, **581**, 1–13.
4. “The standard molar enthalpy of formation of  $LnPO_4$  ( $Ln = La, Nd, Sm$ ) by solution calorimetry”, **D. Rawat**, S. Dash, *J. Therm. Anal. Calorim.*, **2013**, **112**, 147–154.

### Communicated / Under preparation

1. Thermodynamic studies of thorium and barium charge-coupled substituted monazite solid solution. (under preparation)
2. Chemical durability studies of  $La_{1-x}M_{x/2}Th_{x/2}PO_4$  ( $0 \leq x \leq 1$ ) ( $M = Ca, Sr$  and  $Ba$ ) solid solution. (under preparation)

### Conferences (06)

1. Thermochemical study of Barium and Thorium substituted synthetic monazite, **D. Rawat**, P. Samui, R. Mishra, S. Dash, S.K. Rakshit, 14<sup>th</sup> Symposium on Nuclear and Radiochemistry (NUCAR) held at DAE-CC, Anushaktinagar, Mumbai, Jan. 15-19 (2019).
2. Synthesis, characterization and thermodynamic investigation of  $(La_{1-x}Sr_{x/2}Th_{x/2})PO_4$  ( $0 \leq x \leq 1$ ), **D. Rawat**, S. Phapale, R. Mishra, S. Dash, N.K. Shukla, 21<sup>st</sup> Workshop & Symposium of Thermal Analysis (THERMANS) held at Goa University, Goa, Jan. 18-21 (2018)

3. Heat capacity measurement of  $\text{La}_{1-x}\text{Ca}_{x/2}\text{Th}_{x/2}\text{PO}_4$  ( $0 \leq x \leq 1$ ) solid solution using Differential Scanning Calorimeter", **D. Rawat**, S. Phapale, R. Mishra, S. Dash, Proceedings of 13<sup>th</sup> biennial DAE-BRNS Nuclear and Radiochemistry symposium (NUCAR), held at KIIT University, Bhubaneswar, Odisha, Feb. 06-10 (2017).
4. Thermodynamic investigation of  $\text{La}_{1-x}(\text{CaTh})_x\text{PO}_4$  ( $x = 0, 0.25, 0.5, 1$ ) solid solutions", **D. Rawat**, S. Dash, S. Phapale and R. Mishra, Proceedings of 20<sup>th</sup> symposium & workshop on thermal analysis (THERMANS), held at Indian Institute of Technology (Banaras Hindu University) Varanasi, Jan. 18-22 (2016).
5. Studies on Thorium bearing Monazite-Brabantite solid solutions: an actinide storage matrix", **D. Rawat**, M. Sahu, K. Krishnan, S. Dash, Proceedings of International Thorium Energy Conference-2015 (ThEC15), held at NPCIL, Mumbai, Oct. 19-22 (2015).
6. Standard enthalpy of formation of thorium phosphate diphosphate by solution calorimetry; ", **D. Rawat**, S. Dash, S.G. Kulkarni, Proceedings of 11<sup>th</sup> Biennial DAE-BRNS symposium on Nuclear and Radiochemistry (NUCAR), held at Govt. Model Science College, R.D. University, Jabalpur, M.P, Feb 19-23 (2013).



(DEEPAK RAWAT)

*Dedicated to My Family*

## ACKNOWLEDGEMENTS

The realization of this thesis was accomplished with the support and encouragement of numerous people including my well-wishers, friends and colleagues to whom I would like to show my greatest appreciation. Firstly, I would like to express my sincere gratitude to my research guide **Dr. (Smt.) Smruti Dash** and co-guide **Dr. Ratikanta Mishra** for their continuous guidance, support and motivation. Their encouragement, knowledge, and experience helped me a lot during the course of my Ph.D. work. I would like to thank **Prof. B.S. Tomar (Chairman, doctoral committee)** and other members of my doctoral committee; **Dr. C. P. Kaushik, Dr. S. K. Mukherji** and **Dr. S. C. Parida** for their time, encouragement, thoughtful ideas and critical evaluation during the course of my Ph.D.

I am very thankful to **Dr. P.K. Pujari**, Associate Director, Radiochemistry & Isotope (RC&I) group and **Dr. S. C. Parida**, Head, Product Development Section, (RC&I) group for their interest, continuous support and motivation, which helped me a lot during the course of my Ph.D. work.

My sincere thanks to **my lab mates** for all their precious help, valuable discussions, and cooperation. I sincerely thank **Dr. Raman K. Mishra** for his scientific help during the leaching studies. I acknowledge **Dr. K. Krishnan** and **Dr. Bal Govind Vats** for their extended help in diffraction studies and Rietveld refinement of diffraction data. I also acknowledge **Shri Suhas Phapale** for his help during calorimetric studies. I would also like to thank my colleagues **Shri M. Syambabu, Dr. R. Govindan, Dr. S. K. Rakshit, Dr. Ram Avtar Jat, Dr. Pradeep Samui, Dr. D. Chattaraj, Shri. K. B. Modi, Dr. S.M. Bhojane and Dr. N.S. Anand** with **all other members of PDS** for their help, encouragement, and support during the course of my research work.

I wish to express my sincere thanks to all my dear friends for their moral support, encouragement and constant positivity when it was needed. I would also like to thank all **my**

*training school batch mates* for their warm friendship and support. I would like to acknowledge my *teachers* since my childhood; I would not have been here without their guidance, blessings, and support.

I am eternally grateful to *my father (Shri Pradeep Kumar Rawat) and mother (Smt. Pushpa Rawat)* for their unconditional love, support, faith, encouragement and confidence in me. They have been my driving force and inspiration in all pursuits of my life and owe all my accomplishments to them. Heartfelt thank goes to my grandparents for their unconditional love and blessings in my life. I would like to express my warm gratitude towards my wife *Geeta Rawat* for her love and understanding at every step of life, without her support I would not have been able to make it. My heartiest thanks to my *brother (Vijay Rawat) and Sister (Jyoti Rawat)* for their love and confidence in me.

Lastly, I would like to sincerely thank everybody who was important in the realization of this thesis, as well as apologizes that I could not mention everyone personally. Last but most important, I am thankful to God almighty for his kind blessings on me.

# CONTENTS

	<b>Page No.</b>
<b>SYNOPSIS</b>	i
<b>LIST OF ABBREVIATIONS</b>	ix
<b>LIST OF FIGURES</b>	x
<b>LIST OF TABLES</b>	xv
<b>CHAPTER-1</b>	
<b>INTRODUCTION</b>	1
<b>1.1. Nuclear energy</b>	2
<b>1.2. Indian nuclear power programme</b>	3
<b>1.3. Classification of nuclear waste</b>	4
<b>1.3.1. Low-Level Waste (LLW)</b>	5
<b>1.3.2. Intermediate Level Waste (ILW)</b>	5
<b>1.3.3. High-Level Waste (HLW)</b>	6
<b>1.4. Management of HLW</b>	7
<b>1.5. Nuclear waste disposal</b>	8
<b>1.6. Nuclear waste immobilization matrices</b>	10
<b>1.6.1. Properties of immobilization matrices</b>	11
<b>1.6.2. Classification of host matrices</b>	11
<b>1.7. Glass</b>	11
<b>1.7.1. Borosilicate and phosphate glasses</b>	12
<b>1.7.2. Glass composite materials (GCMs)</b>	13
<b>1.7.3. Glass-ceramics</b>	14
<b>1.7.4. Disadvantage of glass waste form</b>	14
<b>1.8. Crystalline ceramics</b>	15

1.8.1. Single phase ceramics	17
1.8.2. Multiphase systems (Synroc)	20
1.9. Suitable matrix for waste disposal	21
1.10. Literature survey on phosphate-based ceramics	21
1.10.1. Monazite	22
1.10.2. Monazite-cheralite solid solution	26
1.10.3. Thorium phosphate diphosphate (TPD)	29
1.11. Scope of the present work	32

## **CHAPTER-2**

### **EXPERIMENTAL TECHNIQUES AND INSTRUMENTATION**

2.1. Introduction	36
2.2. Material Synthesis	36
2.2.1. Solution chemistry method	37
2.2.2. Solid state method	37
2.3. Characterization Techniques	37
2.3.1. Inductively Coupled Plasma-Atomic Emission Spectroscopy (ICP-AES)	38
2.3.2. Powder X-ray Diffraction (XRD)	40
2.3.3. Fourier transform-infrared (FT-IR) spectroscopy	43
2.3.4. Scanning Electron Microscopy (SEM)	45
2.3.5. Thermal analysis	47
2.3.5.1. Thermogravimetric Analysis (TGA)	47
2.3.5.2. Differential Thermal Analysis (DTA)	47
2.4. Thermodynamic measurements techniques	48
2.4.1. Differential Scanning Calorimeter (DSC)	48

2.4.2. Calorimetric techniques	55
2.4.2.1. Isoperibol solution calorimeter	57
2.4.2.2. Calvet oxide melt solution calorimeter	59
2.5. Computational Studies	62
2.5.1. Rietveld refinement of X-ray diffraction data	62
2.5.2. Thermodynamic relations	64
2.5.3. Computation of Phase diagram	65
2.6. Chemical durability studies	68

### CHAPTER-3

#### THERMODYNAMIC INVESTIGATIONS OF RARE EARTH ORTHO-PHOSPHATES, $REPO_4$ (RE = La, Nd, Sm and Gd)

3.1. Introduction	72
3.2. Experimental	72
3.2.1. Material Synthesis	72
3.2.2. Characterization methods	73
3.2.3. Solution calorimeter	74
3.3. Results and Discussions	75
3.3.1. Thermogravimetry analysis (TGA)	75
3.3.2. X-ray diffraction (XRD)	79
3.3.3. Solution calorimeter	80
3.4. Discussions	84
3.5. Conclusions	88

### CHAPTER-4

#### THERMODYNAMIC INVESTIGATIONS OF CHARGE-COUPLED SUBSTITUTED MONAZITE SOLID SOLUTIONS, $(La_{1-x}M_{x/2}Th_{x/2})PO_4$ ( $0 \leq x \leq 1$ ) (M = Ca, Sr and Ba)

4.1. Introduction	91
4.2. Experimental	91
4.2.1. Material Synthesis	91
4.2.2. Characterization methods	92
4.3. Results and Discussions	94
4.3.1. Inductively Coupled Plasma-Atomic Emission Spectroscopy (ICP-AES)	94
4.3.2. X-ray diffraction (XRD)	95
4.3.3. Heat capacity measurements	107
4.3.4. Enthalpy of dissolution ( $\Delta H_{ds}$ ) measurements	111
4.3.5. Standard molar enthalpy of formation ( $\Delta H_{f,m}^0$ ) of $(La_{1-x}M_{x/2}Th_{x/2})PO_4$ ( $0 \leq x \leq 1$ ) ( $M = Ca, Sr$ and $Ba$ )	115
4.3.6. Enthalpy of mixing ( $\Delta H_{mix}$ ) of $(La_{1-x}M_{x/2}Th_{x/2})PO_4$ ( $0 \leq x \leq 1$ ) ( $M = Ca, Sr$ and $Ba$ )	131
4.3.7. Calculation of Thermodynamic Functions	133
4.4. Discussions	145
4.5. Conclusions	152

## CHAPTER-5

### LEACHING STUDIES OF CHARGE COUPLE SUBSTITUTED MONAZITE SOLID SOLUTIONS, $(La_{1-x}M_{x/2}Th_{x/2})PO_4$ ( $0 \leq x \leq 1$ ) ( $M = Ca, Sr$ and $Ba$ )

5.1. Introduction	156
5.2. Experimental	157
5.2.1. Material Synthesis & Characterization	157
5.2.2. Density and surface area measurement	157
5.2.3. Product Consistency Test (PCT)	158
5.2.4. Elemental analysis using ICP-AES technique	158
5.3. Results and Discussions	160

5.4. Conclusions	163
------------------	-----

## **CHAPTER-6**

### **THERMODYNAMIC STUDIES OF THORIUM PHOSPHATE-DIPHOSPHATE (TPD) AND PHASE INVESTIGATIONS OF Th-P-O, Th-P-H<sub>2</sub>O SYSTEMS**

6.1. Introduction	165
6.2. Experimental	165
6.2.1. Material Synthesis	165
6.2.2. Characterization methods	167
6.3. Results and Discussions	169
6.3.1. Thermogravimetric analysis (TGA)	169
6.3.2. X-ray diffraction (XRD)	171
6.3.3. Fourier transform infrared (FT-IR) spectroscopy	172
6.3.4. Enthalpy of dehydration	174
6.3.5. Heat capacity measurements	174
6.3.6. Enthalpy of formation	178
6.3.7. Computational Studies	182
6.3.7.1. Thermodynamic Functions	182
6.3.7.2. Phase diagram of Th-P-O system	182
6.3.7.3. Chemical potential diagram of Th-P-O system	186
6.3.7.4. E <sub>H</sub> -pH diagram for Th-P-H <sub>2</sub> O system	188
6.4. Conclusions	191

## **CHAPTER-7**

<b>SUMMARY, CONCLUSIONS AND FUTURE DIRECTIONS</b>	193
---	-----

<b>REFERENCES</b>	198
-------------------	-----

## SYNOPSIS

The demand for energy has been increasing to meet social and economic development. The fossil fuels used for energy supply have increased greenhouse gas concentrations in the atmosphere and seriously affecting the environment. Thus, a search for an alternative clean and sustainable energy source is required to mitigate the environmental changes. Among others, nuclear power is the most effective non-greenhouse gas emitting energy source that can replace fossil fuels and satisfy global demand. However, nuclear power is associated with production of radioactive wastes during nuclear power plant operations and other nuclear applications. The majority of nuclear radioactive wastes are produced in the front end and in back-end of the nuclear fuel cycle. The front-end nuclear waste is usually alpha-emitting radium and its decay products generated during the extraction of uranium, whereas the back end of the nuclear fuel cycle consists of mostly radioactive fission products such as  $^{90}\text{Sr}$ ,  $^{99}\text{Tc}$ ,  $^{137}\text{Cs}$  and actinides such as  $^{232}\text{Th}$ ,  $^{237}\text{Np}$ ,  $^{234}\text{U}$ ,  $^{238}\text{Pu}$ ,  $^{241}\text{Am}$ ,  $^{244}\text{Cm}$  etc. As radioactive nuclear waste is deleterious to human life as well as to the environment, it is strictly regulated by government agencies for the protection of ecosystem. At present, high level waste (HLW) is disposed by vitrification in sodium borosilicate glass matrix to provide protection against environmental dispersion. In the long term, the vitrified nuclear waste is stored in geological disposal. In geological repository the vitrified waste package will be subjected to harsh environments such as high temperature, radiation, oxygen, water and other aggressive minerals. These factors can cause crystallization of the glass matrix which in turn can lead to release of radioactive waste into the biosphere. These glasses also have low solubility limit for actinides.

Therefore, it is necessary that the immobilization matrix should have prerequisite properties like good mechanical strength, slow crystallization kinetics, low diffusivity of trace elements, chemical durability and thermodynamic stability in hostile environment. For higher loading of minor actinides in future, suitable matrix for waste disposal needs to develop.

Ceramic matrices with mineral structures: monazite, thorite, britholite, pyrochlore, zircon, zirconolite or perovskite are being proposed for the immobilization of long-lived radionuclides [1, 2]. Among these the phosphate-based minerals such as monazite are considered as the most promising waste matrix. They have high melting temperature, high resistance to aqueous corrosion, high radiation resistance and capacity to incorporate large amounts of uranium/thorium along with various elements of different ionic radii/oxidation state.

Phosphate-based ceramic matrix such as rare earth phosphates (monazite), monazite-cheralite solid solutions and thorium phosphate diphosphate are being extensively investigated worldwide for the disposal of long-lived radionuclides. Monazite is a natural light rare earth phosphate ( $REPO_4$ ,  $P2_1/n$ ), where RE-site is occupied by large cations, having nine-fold coordination with trivalent rare earth elements ( $RE^{3+}$ ) and other cations similar in size ( $Ca^{2+}$ ,  $U^{4+}$ ,  $Th^{4+}$ ) while the smaller cation i.e.  $P^{5+}$  has tetrahedral coordination. The monazite structure is highly flexible and can accommodate large number of cations of different ionic sizes. The radiation damage in monazite is very low due to its structural flexibility and low annealing temperature. India has high reserves of monazite i.e. 11.93 million tons in the beach sand along its east and west coastal tracts. The structural, discrete thermodynamic data and leaching studies of synthetic monazite  $REPO_4$  have been reported in the literature [3-5].

In natural systems, monazite can incorporate tetravalent actinide ( $RE^{3+}-Th^{4+}$ ) by two major mechanisms: substitution on tetrahedral sites,  $RE^{3+} + P^{5+} = Th^{4+} + Si^{4+}$  and at large cation position:  $2 RE^{3+} = Th^{4+} + Ca^{2+}$ . Several studies have been made to synthesized monazite-based ceramics incorporating actinides [6, 7]. Of these, the latter (cheralite) type substitution has been extensively studied. The full substitution of di- and tetra-valent actinides leads to the formation of the cheralite end-members, formerly known as brabantite,  $Ca_{0.5}Th_{0.5}PO_4$ . The monazite-cheralite solid solutions viz.  $(La_{1-x}Ca_{x/2}Th_{x/2})PO_4$  ( $0 \leq x \leq 1$ ) is a unique waste form which can accommodate divalent fission products, trivalent rare earths and tetravalent actinides,

simultaneously in a single matrix, which mimics the actual nuclear waste form. The investigations on thermodynamic and leaching properties of monazite-cheralite solid solutions have not been reported in the literature.

Thorium phosphate diphosphate ( $\text{Th}_4(\text{PO}_4)_4\text{P}_2\text{O}_7$ , TPD), is a potential actinide-bearing phase in which  $\text{Th}^{4+}$  is replaced with large amount of smaller tetravalent actinides  $\text{U}^{4+}$ ,  $\text{Np}^{4+}$  and  $\text{Pu}^{4+}$ . The replacement is up to 75 mol. % by  $\text{U}^{4+}$ , up to 52 mol.% by  $\text{Np}^{4+}$  and up to 41 mole % by  $\text{Pu}^{4+}$  leading to the formation of solid solutions of TPD ( $\text{Th}_{1-x}\text{M}_x$ ) $_4(\text{PO}_4)_4\text{P}_2\text{O}_7$  ( $M = \text{U}, \text{Np}, \text{Pu}$ ) as a potential actinide-bearing phase. The resistance of this solid solution to aqueous corrosion has been reported [8, 9]. However, the most fundamental property i.e. Gibbs energy of formation has not been reported. The self-irradiation of  $\text{Th}_4(\text{PO}_4)_4\text{P}_2\text{O}_7$  by  $\alpha$ -decays due to actinides loading could modify its thermodynamic stability, hence, the knowledge of thermodynamic functions of TPD is essential.

There is a requirement for R&D on phosphate-based compounds to bridge the existed gap in the literature. The objective of the thesis is to measure thermodynamic properties and compute important thermodynamic functions for  $\text{REPO}_4$  ( $\text{RE} = \text{La}, \text{Nd}, \text{Sm}$  and  $\text{Gd}$ ),  $(\text{La}_{1-x}\text{M}_{x/2}\text{Th}_{x/2})\text{PO}_4$  ( $0 \leq x \leq 1$ ) ( $M = \text{Ca}, \text{Sr}$  and  $\text{Ba}$ ),  $\text{Th}_4(\text{PO}_4)_4\text{P}_2\text{O}_7$  (TPD) and leaching studies of monazite-cheralite solid solutions.

### **Scope of the study:**

It involves the synthesis, characterization, heat capacity, enthalpy of formation of  $\text{LaPO}_4$ ,  $\text{SmPO}_4$ ,  $\text{NdPO}_4$ ,  $\text{GdPO}_4$ ,  $(\text{La}_{1-x}\text{Ca}_{x/2}\text{Th}_{x/2})\text{PO}_4$  ( $0 \leq x \leq 1$ ),  $(\text{La}_{1-x}\text{Sr}_{x/2}\text{Th}_{x/2})\text{PO}_4$  ( $0 \leq x \leq 1$ ),  $(\text{La}_{1-x}\text{Ba}_{x/2}\text{Th}_{x/2})\text{PO}_4$  ( $0 \leq x \leq 1$ ),  $\text{Th}_4(\text{PO}_4)_4\text{P}_2\text{O}_7$  and leaching studies of monazite-cheralite solid solutions. These phosphate phases were synthesized using different solid state and solutions methods, characterized primarily by XRD and elemental analysis by ICP-AES techniques. The hydrated phases  $\text{Th}_2(\text{PO}_4)_2(\text{HPO}_4) \cdot \text{H}_2\text{O}$  and  $\text{Th}_2(\text{PO}_4)_2(\text{HPO}_4)$  were

characterized using fourier transform infra-red (FT-IR) spectroscopy and thermogravimetry (TG) methods. The heat capacities, which signifies the energy requirement to increase the temperature of a substance, have been determined for  $\text{Th}_2(\text{PO}_4)_2(\text{HPO}_4)\cdot\text{H}_2\text{O}$ ,  $\text{Th}_2(\text{PO}_4)_2(\text{HPO}_4)$ ,  $\alpha\text{-Th}_4(\text{PO}_4)_4\text{P}_2\text{O}_7$ ,  $\beta\text{-Th}_4(\text{PO}_4)_4\text{P}_2\text{O}_7$  and  $(\text{La}_{1-x}\text{M}_{x/2}\text{Th}_{x/2})\text{PO}_4$  ( $0 \leq x \leq 1$ ) ( $\text{M} = \text{Ca}, \text{Sr}$  and  $\text{Ba}$ ) using Differential Scanning Calorimeter (DSC) technique. The enthalpy of formation has been measured for  $\text{LaPO}_4$ ,  $\text{SmPO}_4$ ,  $\text{NdPO}_4$ ,  $\text{GdPO}_4$  and their hydrated rhabdophane forms viz.  $\text{LaPO}_4\cdot 0.8\text{H}_2\text{O}$ ,  $\text{NdPO}_4\cdot 0.75\text{H}_2\text{O}$ ,  $\text{SmPO}_4\cdot 0.65\text{H}_2\text{O}$  and  $\text{GdPO}_4\cdot 0.55\text{H}_2\text{O}$  using a room temperature solution calorimetry. Whereas the enthalpy of formation of monazite-cherallite solid solution  $(\text{La}_{1-x}\text{M}_{x/2}\text{Th}_{x/2})\text{PO}_4$  ( $0 \leq x \leq 1$ ) ( $\text{M} = \text{Ca}, \text{Sr}$  and  $\text{Ba}$ ) and  $\text{Th}_4(\text{PO}_4)_4\text{P}_2\text{O}_7$  have been determined employing a high temperature Calvet oxide melt solution calorimeter. From the measured data the thermodynamic properties of monazite-cherallite solid solutions:  $(\text{La}_{1-x}\text{M}_{x/2}\text{Th}_{x/2})\text{PO}_4$  ( $0 \leq x \leq 1$ ) ( $\text{M} = \text{Ca}, \text{Sr}$  and  $\text{Ba}$ ) and  $\text{Th}_4(\text{PO}_4)_4\text{P}_2\text{O}_7$  have been computed.

The enthalpy of formation with respect to the component oxides i.e.  $0.5\cdot\text{RE}_2\text{O}_3 + 0.5\cdot\text{P}_2\text{O}_5 = \text{REPO}_4$ ; plotted against ionic radii of  $\text{RE}^{3+}$  ( $\text{RE} = \text{La}, \text{Sm}, \text{Nd}$  and  $\text{Gd}$ ) reveals that with decrease in ionic radii of  $\text{RE}^{3+}$ , the values of enthalpy of formation becomes less negative (exothermic). X-ray diffraction analysis of the charge-coupled ( $\text{M}^{2+}, \text{Th}^{4+}$ ) substitution in place of  $\text{La}^{3+}$  showed that  $\text{LaPO}_4$  forms regular solid solutions with ( $\text{M}^{2+}, \text{Th}^{4+}$ ) $\text{PO}_4$  in composition range  $(\text{La}_{1-x}\text{M}_{x/2}\text{Th}_{x/2})\text{PO}_4$  ( $0 \leq x \leq 1$ ) where  $\text{M} = \text{Ca}$  and  $\text{Sr}$ . On the other hand, the solubility limits for  $(\text{La}_{1-x}\text{Ba}_{x/2}\text{Th}_{x/2})\text{PO}_4$  solid solution was found to be  $x = 0.3$ . The enthalpy of formation data for the compounds indicate that there is negative deviation from ideal solid solution behavior with minima at  $x = 0.25$  for  $(\text{La}_{1-x}\text{Ca}_{x/2}\text{Th}_{x/2})\text{PO}_4$  ( $0 \leq x \leq 1$ ),  $x = 0.3$  for  $(\text{La}_{1-x}\text{Sr}_{x/2}\text{Th}_{x/2})\text{PO}_4$  ( $0 \leq x \leq 1$ ) and  $x = 0.2$  for  $(\text{La}_{1-x}\text{Ba}_{x/2}\text{Th}_{x/2})\text{PO}_4$  ( $0 \leq x \leq 1$ ), which suggests that the substitution of charge couple  $\text{M}^{2+}$  and  $\text{Th}^{4+}$  at lattice site of  $\text{La}^{3+}$ , results in formation of thermodynamically stable intermediate phases. Further it was also

observed that the substituted  $(La_{1-x}M_{x/2}Th_{x/2})PO_4$  ( $0 \leq x \leq 1$ ) ( $M = Ca, Sr$  and  $Ba$ ) systems are isentropic in nature and stabilized mainly by enthalpy. The measured heat capacities of  $(La_{1-x}M_{x/2}Th_{x/2})PO_4$  ( $0 \leq x \leq 1$ ) ( $M = Ca, Sr$  and  $Ba$ ) deviated from Neumann-Kopp rule could be attributed to the dissimilarity in co-ordination number of metal cations.

The chemical durability studies of  $(La_{1-x}M_{x/2}Th_{x/2})PO_4$  ( $0 \leq x \leq 1$ ) ( $M = Ca, Sr$  and  $Ba$ ) were performed using ASTM-Product Consistency Test (PCT) method. The elemental analysis of leachate solution was carried out employing ICP-AES technique and normalized leach rate was determined. The observed normalized leach rate for the elements was found to be lower than  $10^{-10} \text{ g}\cdot\text{cm}^{-2}\cdot\text{d}^{-1}$ .

Using thermodynamic data derived from this study, the co-existence of different phases in the Th-P-O system, the stability domain of oxygen and the phosphorous potentials for  $Th_4(PO_4)_4P_2O_7$  have been computed.  $E_H$ -pH diagram for finding the chemical stability of Th-P-H<sub>2</sub>O system has also been determined employing the measured data.

### **Organization of thesis:**

The thesis has been divided into seven chapters.

**Chapter-1:** This chapter gives a brief introduction about the research problem and a short description about the philosophy of radioactive wastes management. The overview of waste form with focus on radiation resistance phosphates-based matrix and criteria for their selections for immobilization of high-level waste have been discussed. The chapter also provides detailed literature survey on the thermophysical and thermochemical properties of phosphate-based compounds. It offers the frame to the thesis and provides motivation for the present dissertation.

**Chapter-2:** The chapter outlines the principles of various experimental techniques and instrumentations. The methods of synthesis of phosphate samples and their solid solutions by solid state and solution route are discussed. Details of the characterization techniques like powder X-ray diffraction technique, thermogravimetry and differential thermal analysis (TG-DTA), Fourier-transform infrared (FT-IR) spectroscopy and inductively coupled plasma-atomic emission spectroscopy (ICP-AES) are discussed. Details of measurements of thermodynamic properties of phosphate-based compounds are described. Principles and operation of calorimetric techniques such as Differential Scanning Calorimeter (DSC), room temperature isoperibol solution calorimeter and high temperature solution calorimeters used to measure heat capacity and enthalpy of formation are given. The relevant relations used for the computations of thermodynamic functions are also mentioned. The methodology and set-up of the chemical durability study are described.

**Chapter-3:** This chapter describes thermodynamic studies of light rare earth orthophosphates,  $REPO_4$  ( $RE = La, Nd, Sm$  and  $Gd$ ) employing room temperature solution calorimetry technique. It delivers the method of synthesis and characterization of these compounds employing different techniques. The measurements of extent of hydration of the rhabdophane compounds and enthalpy of reaction ( $\Delta H_r$ ) corresponds to the precipitation of each rhabdophane compound using solution calorimetry technique are given. The calculation of enthalpy of formation for each compound using appropriate thermochemical cycles are also provided. It also compares the observed enthalpy of formation data for each phase with that of the reported data in the literature.

**Chapter-4:** This chapter is devoted to thermodynamic investigations of charge-coupled substituted monazite solid solutions  $(La_{1-x}M_{x/2}Th_{x/2})PO_4$  ( $0 \leq x \leq 1$ ) ( $M = Ca, Sr$  and  $Ba$ ). The

solid state synthesis, characterization and enthalpy of formation of  $\text{Th}^{4+}$  and  $M^{2+}$  ( $M = \text{Ca}, \text{Sr}$  and  $\text{Ba}$ ) substituted monazite i.e.  $(\text{La}_{1-x}\text{M}_{x/2}\text{Th}_{x/2})\text{PO}_4$  ( $0 \leq x \leq 1$ ) ( $M = \text{Ca}, \text{Sr}$  and  $\text{Ba}$ ) solid solutions are reported. The Rietveld refinement of X-ray diffraction data, heat capacity data of solid solutions and enthalpy of dissolution ( $\Delta H_{\text{ds}}$ ) of each solid solution and their constituents by a high temperature Calvet oxide melt solution calorimeter are incorporated. The standard molar enthalpy of formation of solid solutions from the oxides ( $\Delta H_{\text{f,ox}}^{\circ}$ ) and that from constituting elements ( $\Delta H_{\text{f}}^{\circ}$ ) are also provided and thoroughly discussed.

**Chapter-5:** This chapter provides the results of chemical durability studies carried out on selected compositions of  $(\text{La}_{1-x}\text{M}_{x/2}\text{Th}_{x/2})\text{PO}_4$  ( $0 \leq x \leq 1$ ) ( $M = \text{Ca}, \text{Sr}$  and  $\text{Ba}$ ) solid solutions using ASTM-Product Consistency Test (PCT) method. The analysis of leachate solution was carried out using ICP-AES technique. It also gives the normalized leach rate values determined for different samples. The normalized leach rate results are correlated with the thermodynamic properties of the solid solutions.

**Chapter-6:** The chapter describes detail literature survey on Th-P-O and Th-P-H<sub>2</sub>O systems and characterization of various phases of these systems. It also provides measured heat capacities data employing DSC technique and room temperature enthalpy of precipitation data from isoperibol solution calorimeter. Using these data with formulation of thermo-chemical cycles based on Hess's law, enthalpy of formation of  $\text{Th}_2(\text{PO}_4)_2(\text{HPO}_4) \cdot \text{H}_2\text{O}$ ,  $\text{Th}_2(\text{PO}_4)_2(\text{HPO}_4)$ ,  $\alpha\text{-Th}_4(\text{PO}_4)_4\text{P}_2\text{O}_7$  and  $\beta\text{-Th}_4(\text{PO}_4)_4\text{P}_2\text{O}_7$  ( $\beta\text{-TPD}$ ) were determined and incorporated. The phase diagram, chemical potential diagram of Th-P-O system and  $E_{\text{H}}$ -pH diagram of Th-P-H<sub>2</sub>O to establish the stability of  $\beta\text{-TPD}$  in the ground water are also reported in this chapter.

**Chapter-7:** The summary and conclusions deduced from the present thesis are given in this chapter. It also provides recommendations and directions for the future work.

## REFERENCES:

- [1] W.J. Weber, R.C. Ewing, C.A. Angell, G.W. Arnold, A.N. Cormack, J.M. Delaye, D.L. Griscom, L.W. Hobbs, A. Navrotsky, D.L. Price, A.M. Stoneham, M.C. Weinberg, *J. Mater. Res.*, **12** (1997) 1948-1978.
- [2] D.R. Neuville, L. Cormier, B. Boizot, A. Flank, *J. Non-Cryst. Solids*, **323** (2003) 207-213.
- [3] A.C. Thomas, N. Dacheux, P. Le Coustumer, V. Brandel, M. Genet, *J. Nucl. Mater.*, **281** (2000) 91-105.
- [4] A.C. Thomas, N. Dacheux, P. Le Coustumer, V. Brandel, M. Genet, *J. Nucl. Mater.*, **295** (2001) 249-264.
- [5] N. Clavier, R. Podor, N. Dacheux, *J. Eur. Ceram. Soc.*, **31** (6) (2011) 941-976.
- [6] S.V. Ushakov, K.B. Helean, A. Navrotsky, L.A. Boatner, *J. Mater. Res.*, **16** (2001) 2623–2632.
- [7] O. Terra, N. Clavier, N. Dacheux, R. Podor, *New J. Chem.*, **27** (2003) 957-967.
- [8] J.M. Montel, B. Glorieux, A. M. Seydoux-Guillaume, R. Wirth, *J. Phys. Chem. Solids*, **67** (12) (2006) 2489-2500.
- [9] D. Bregiroux, O. Terra, F. Audubert, N. Dacheux, V. Serin, R. Podor, D. B. Assollant, *Inorg. Chem.*, **46** (24) (2007) 10372-10382.

## LIST OF FIGURES

	<b>Page No.</b>
<b>CHAPTER-1</b>	
<b>Fig. 1.1</b> Production of transuranic in the uranium fueled nuclear reactor.	3
<b>Fig. 1.2</b> Schematic diagram of Indian nuclear power program.	3
<b>Fig. 1.3</b> A schematic diagram of closed nuclear fuel cycle.	5
<b>Fig. 1.4</b> Schematic of a multi-barrier system in a nuclear waste repository.	9
<b>Fig. 1.5</b> Schematic of waste accommodation in glass matrix: (a) incorporation in glass with presence of bubbles and inclusions; (b) encapsulation of waste particles in a glass matrix.	13
<b>Fig. 1.6</b> Schematic of waste immobilisation by crystalline host matrix.	16
<b>Fig. 1.7</b> An illustration of the crystal structure of REPO <sub>4</sub> monazite [30].	23
<b>Fig. 1.8</b> Perspective view of the TPD structure.	30
<b>CHAPTER-2</b>	
<b>Fig. 2.1</b> Schematic of a typical ICP-AES equipment.	39
<b>Fig. 2.2</b> Typical X-ray of Cu target.	41
<b>Fig. 2.3</b> Schematic of powder X-ray diffractometer.	42
<b>Fig. 2.4</b> Schematic of an ATR-FT-IR set up.	44
<b>Fig. 2.5</b> Schematic representation of SEM microscope.	46
<b>Fig. 2.6</b> Interaction of electron beam with the sample.	46
<b>Fig. 2.7</b> Heat flux DSC.	48
<b>Fig. 2.8</b> Power compensation DSC.	49
<b>Fig. 2.9</b> The “classical” three-step method.	54
<b>Fig. 2.10</b> Isoperibol solution calorimeter (TA Instruments Precision Solution Calorimeter) with description of Pyrex-glass reaction vessel	57
<b>Fig. 2.11</b> Schematic of Calvet solution calorimeter.	59
<b>Fig. 2.12</b> Teflon-lined stainless-steel container used in leaching study.	69
<b>CHAPTER-3</b>	
<b>Fig. 3.1</b> Schematic plot of ampoule breaking inside reaction vessel.	75
<b>Fig. 3.2</b> Thermal dehydration of (a) LaCl <sub>3</sub> .7H <sub>2</sub> O(s), (b) NdCl <sub>3</sub> .6H <sub>2</sub> O(s), (c) SmCl <sub>3</sub> .6H <sub>2</sub> O(s) and (d) GdCl <sub>3</sub> .6H <sub>2</sub> O(s).	76

<b>Fig. 3.3</b>	Thermal decomposition of $\text{NH}_4\text{H}_2\text{PO}_4(\text{s})$ .	78
<b>Fig. 3.4</b>	Thermal decomposition of hydrated rhabdophane phases.	78
<b>Fig. 3.5</b>	Rietveld plot for $\text{LaPO}_4$ .	79
<b>Fig. 3.6</b>	Comparison of enthalpy of formation, $\Delta H_{\text{f,ox}}^{\circ}$ of $\text{REPO}_4$ (RE = La, Nd, Sm and Gd) from their constituent oxides.	86

## CHAPTER-4

<b>Fig. 4.1</b>	XRD patterns of $(\text{La}_{1-x}\text{Ca}_{x/2}\text{Th}_{x/2})\text{PO}_4$ ( $x = 0, 0.15, 0.25, 0.40, 0.60, 0.75, 0.85, 1$ ) solid solution.	95
<b>Fig. 4.2</b>	Exaggerated view of the portion of XRD pattern in which solid line has been used to show the shift in peak position with variation in composition.	96
<b>Fig. 4.3</b>	XRD patterns of $(\text{La}_{1-x}\text{Sr}_{x/2}\text{Th}_{x/2})\text{PO}_4$ ( $x = 0, 0.2, 0.4, 0.6, 0.8, 1$ ) solid solution.	96
<b>Fig. 4.4</b>	Exaggerated view of the portion of XRD pattern in which solid line has been used to show the shift in peak position with variation in composition.	96
<b>Fig. 4.5</b>	XRD patterns of $(\text{La}_{1-x}\text{Ba}_{x/2}\text{Th}_{x/2})\text{PO}_4$ ( $x = 0, 0.1, 0.2, 0.3, 0.4, 0.5, 0.6, 0.7, 0.8, 0.9, 1$ ) solid solution.	97
<b>Fig. 4.6</b>	Exaggerated view of the portion of XRD pattern showing phase separation beyond $x = 0.3$ .	97
<b>Fig. 4.7</b>	Variation of unit cell parameters of $(\text{La}_{1-x}\text{Ca}_{x/2}\text{Th}_{x/2})\text{PO}_4$ ( $x = 0, 0.15, 0.25, 0.40, 0.60, 0.75, 0.85, 1$ ) samples; ( $\bullet$ ) present study; ( $\square$ ) Konings et al. [171].	98
<b>Fig. 4.8</b>	Variation of unit cell parameter of $(\text{La}_{1-x}\text{Sr}_{x/2}\text{Th}_{x/2})\text{PO}_4$ ( $x = 0, 0.2, 0.4, 0.6, 0.8, 1$ ) samples.	98
<b>Fig. 4.9</b>	Variation of unit cell parameter of $(\text{La}_{1-x}\text{Ba}_{x/2}\text{Th}_{x/2})\text{PO}_4$ ( $x = 0, 0.1, 0.2, 0.3$ ) samples.	98
<b>Fig. 4.10</b>	Rietveld plot for $\text{LaPO}_4$ .	104
<b>Fig. 4.11</b>	Rietveld plot for $(\text{La}_{0.75}\text{Ca}_{0.125}\text{Th}_{0.125})\text{PO}_4$ .	104
<b>Fig. 4.12</b>	Rietveld plot for $\text{Ca}_{0.5}\text{Th}_{0.5}\text{PO}_4$ .	104
<b>Fig. 4.13</b>	Rietveld plot for $(\text{La}_{0.6}\text{Sr}_{0.2}\text{Th}_{0.2})\text{PO}_4$ .	105
<b>Fig. 4.14</b>	Rietveld plot for $\text{Sr}_{0.5}\text{Th}_{0.5}\text{PO}_4$ .	105

<b>Fig. 4.15</b>	Rietveld plot for $(\text{La}_{0.7}\text{Ba}_{0.15}\text{Th}_{0.15})\text{PO}_4$ .	105
<b>Fig. 4.16</b>	Rietveld plot for $\text{Ba}_{0.5}\text{Th}_{0.5}\text{PO}_4$ .	106
<b>Fig. 4.17</b>	Crystal structure of $(\text{La}_{0.4}\text{Sr}_{0.3}\text{Th}_{0.3})\text{PO}_4$ using VESTA program [186].	106
<b>Fig. 4.18</b>	Comparison of specific heat capacity of $\text{ZrO}_2$ as a function of temperature with literature data [187].	107
<b>Fig. 4.19</b>	Comparison of specific heat capacity of $\text{LaPO}_4$ as a function of temperature.	108
<b>Fig. 4.20</b>	A comparison of specific heat capacity of $\text{Ca}_{0.5}\text{Th}_{0.5}\text{PO}_4$ with that reported by author [179].	108
<b>Fig. 4.21</b>	Variation of specific heat capacity of $(\text{La}_{1-x}\text{Ca}_{x/2}\text{Th}_{x/2})\text{PO}_4$ ( $x = 0, 0.15, 0.25, 0.40, 0.60, 0.75, 0.85, 1$ ) solid solutions as a function of temperature.	109
<b>Fig. 4.22</b>	Variation of specific heat capacity of $(\text{La}_{1-x}\text{Sr}_{x/2}\text{Th}_{x/2})\text{PO}_4$ ( $x = 0, 0.2, 0.4, 0.6, 0.8, 1$ ) solid solutions as a function of temperature.	110
<b>Fig. 4.23</b>	Variation of specific heat capacity of $(\text{La}_{1-x}\text{Ba}_{x/2}\text{Th}_{x/2})\text{PO}_4$ ( $x = 0, 0.1, 0.2, 0.3; x = 1$ ) solid solutions as a function of temperature.	110
<b>Fig. 4.24</b>	Plots of heat flow signals measured for the drop experiments of $\text{La}_{1-x}\text{Ca}_{x/2}\text{Th}_{x/2}\text{PO}_4$ ( $x = 0, 0.15, 0.25, 0.40, 0.60, 0.75, 0.85, 1$ ) samples.	117
<b>Fig. 4.25</b>	Variation of standard molar enthalpy of formation of $(\text{La}_{1-x}\text{Ca}_{x/2}\text{Th}_{x/2})\text{PO}_4$ ( $x = 0, 0.15, 0.25, 0.40, 0.60, 0.75, 0.85, 1$ ) as a function of mole fraction of $\text{Ca}_{0.5}\text{Th}_{0.5}\text{PO}_4$ (with dashed line as a guide to the eye).	119
<b>Fig. 4.26</b>	Trend of molar enthalpy of formation from constituent oxides ( $\Delta H_{f,ox}^0$ ) of $(\text{La}_{1-x}\text{Ca}_{x/2}\text{Th}_{x/2})\text{PO}_4$ ( $x = 0, 0.15, 0.25, 0.40, 0.60, 0.75, 0.85, 1$ ) as a function of mole fraction of $\text{Ca}_{0.5}\text{Th}_{0.5}\text{PO}_4$ (with dashed line as a guide to the eye).	120
<b>Fig. 4.27</b>	Backscattered electron SEM image of the surface of quenched $\text{PbO} + \text{B}_2\text{O}_3$ (2:1 molar ratio) calorimeter solvent with dissolved $(\text{La}_{0.4}\text{Ca}_{0.3}\text{Th}_{0.3})\text{PO}_4$ sample and corresponding elemental maps for La, Ca and Th.	121

<b>Fig. 4.28</b>	Correlation curve between enthalpies of formation of synthetic monazite with the natural composition of monazite present in beach sands.	122
<b>Fig. 4.29</b>	Variation of standard molar enthalpy of formation of $(\text{La}_{1-x}\text{Sr}_{x/2}\text{Th}_{x/2})\text{PO}_4$ ( $x = 0, 0.1, 0.2, 0.3, 0.4, 0.5, 0.6, 0.7, 0.8, 0.9, 1$ ) as a function of mole fraction of $\text{Sr}_{0.5}\text{Th}_{0.5}\text{PO}_4$ (with dashed line as a guide to the eye).	126
<b>Fig. 4.30</b>	Trend of molar enthalpy of formation from constituent oxides ( $\Delta H_{f,\text{ox}}^0$ ) of $(\text{La}_{1-x}\text{Sr}_{x/2}\text{Th}_{x/2})\text{PO}_4$ ( $x = 0, 0.1, 0.2, 0.3, 0.4, 0.5, 0.6, 0.7, 0.8, 0.9, 1$ ) as a function of mole fraction of $\text{Sr}_{0.5}\text{Th}_{0.5}\text{PO}_4$ (with dashed line as a guide to the eye).	126
<b>Fig. 4.31</b>	Variation of standard molar enthalpy of formation, $\Delta H_f^0(298 \text{ K})$ of $(\text{La}_{1-x}\text{Ba}_{x/2}\text{Th}_{x/2})\text{PO}_4$ ( $x = 0, 0.1, 0.2, 0.3; x = 1$ ) as a function of mole fraction of $\text{Ba}_{0.5}\text{Th}_{0.5}\text{PO}_4$ (with dashed line as a guide to the eye).	130
<b>Fig. 4.32</b>	Trend of molar enthalpy of formation from constituent oxides, $\Delta H_{f,\text{ox}}^0(298 \text{ K})$ of $(\text{La}_{1-x}\text{Ba}_{x/2}\text{Th}_{x/2})\text{PO}_4$ ( $x = 0, 0.1, 0.2, 0.3; x = 1$ ) as a function of mole fraction of $\text{Ba}_{0.5}\text{Th}_{0.5}\text{PO}_4$ (with dashed line as a guide to the eye).	130
<b>Fig. 4.33</b>	Variation of enthalpy of mixing, $\Delta H_{\text{mix}}$ of $(\text{La}_{1-x}\text{Ca}_{x/2}\text{Th}_{x/2})\text{PO}_4$ ( $x = 0, 0.15, 0.25, 0.40, 0.60, 0.75, 0.85, 1$ ) as a function of mole fraction of $\text{Ca}_{0.5}\text{Th}_{0.5}\text{PO}_4$ (with dashed line as a guide to the eye).	132
<b>Fig. 4.34</b>	Variation of enthalpy of mixing, $\Delta H_{\text{mix}}$ of $(\text{La}_{1-x}\text{Sr}_{x/2}\text{Th}_{x/2})\text{PO}_4$ ( $x = 0, 0.1, 0.2, 0.3, 0.4, 0.5, 0.6, 0.7, 0.8, 0.9, 1$ ) as a function of mole fraction of $\text{Sr}_{0.5}\text{Th}_{0.5}\text{PO}_4$ (with dashed line as a guide to the eye).	132
<b>Fig. 4.35</b>	Variation of enthalpy of mixing, $\Delta H_{\text{mix}}$ of $(\text{La}_{1-x}\text{Ba}_{x/2}\text{Th}_{x/2})\text{PO}_4$ ( $x = 0, 0.1, 0.2, 0.3; x = 1$ ) as a function of mole fraction of $\text{Ba}_{0.5}\text{Th}_{0.5}\text{PO}_4$ (with dashed line as a guide to the eye).	133
<b>Fig. 4.36</b>	Plots of Gibbs energy of formation of $\text{La}_{1-x}\text{Ca}_{x/2}\text{Th}_{x/2}\text{PO}_4$ ( $x = 0, 0.15, 0.25, 0.40, 0.60, 0.75, 0.85, 1$ ) as a function of temperature.	144
<b>Fig. 4.37</b>	Plots of Gibbs energy of formation of $\text{La}_{1-x}\text{Sr}_{x/2}\text{Th}_{x/2}\text{PO}_4$ ( $x = 0, 0.2, 0.4, 0.6, 0.8, 1$ ) as a function of temperature.	144
<b>Fig. 4.38</b>	Plots of Gibbs energy of formation of $\text{La}_{1-x}\text{Ba}_{x/2}\text{Th}_{x/2}\text{PO}_4$ ( $x = 0, 0.1, 0.2, 0.3; x = 1$ ) as a function of temperature.	144

<b>Fig. 4.39</b>	Heat capacity variations of $\text{LaPO}_4$ and $M_{0.5}\text{Th}_{0.5}\text{PO}_4$ ( $M = \text{Ca, Sr and Ba}$ ).	146
<b>Fig. 4.40</b>	Comparison of the standard molar enthalpies of formation values of $\text{LaPO}_4$ and $M_{0.5}\text{Th}_{0.5}\text{PO}_4$ ( $M = \text{Ca, Sr and Ba}$ ) with that the values reported in the literature.	147
<b>Fig. 4.41</b>	Combined plot of standard molar enthalpy of formation of $(\text{La}_{1-x}\text{M}_{x/2}\text{Th}_{x/2})\text{PO}_4$ ( $0 \leq x \leq 1$ ) ( $M = \text{Ca, Sr and Ba}$ ) from their constituent oxides.	149
<b>Fig. 4.42</b>	Enthalpy of formation from oxides of $\text{LaPO}_4$ and $M_{0.5}\text{Th}_{0.5}\text{PO}_4$ ( $M = \text{Ca, Sr and Ba}$ ) as a function of ionic radii of $\text{La}^{3+}$ substituting ion.	150
<b>Fig. 4.43</b>	Variations of unit cell volume of the solid solutions on substitution.	151
<b>Fig. 4.44</b>	Combined plot of enthalpy of mixing for $(\text{La}_{1-x}\text{M}_{x/2}\text{Th}_{x/2})\text{PO}_4$ ( $0 \leq x \leq 1$ ) ( $M = \text{Ca, Sr and Ba}$ ) as a function of mole fraction of their respective end member.	152

## CHAPTER-6

<b>Fig. 6.1</b>	Thermal decomposition of $\text{Th}(\text{NO}_3)_4 \cdot 5\text{H}_2\text{O}$ .	170
<b>Fig. 6.2</b>	Thermal decomposition of $\text{Th}_2(\text{PO}_4)_2(\text{HPO}_4) \cdot \text{H}_2\text{O}$ .	170
<b>Fig. 6.3</b>	X-ray powder diffraction pattern of $\beta\text{-Th}_4(\text{PO}_4)_4\text{P}_2\text{O}_7$ .	171
<b>Fig. 6.4</b>	Infrared spectra of (a) $\text{Th}_2(\text{PO}_4)_2(\text{HPO}_4) \cdot \text{H}_2\text{O}$ and (b) $\beta\text{-Th}_4(\text{PO}_4)_4\text{P}_2\text{O}_7$ recorded at room temperature.	172
<b>Fig. 6.5</b>	Heat flow curve of $\text{Th}_2(\text{PO}_4)_2(\text{HPO}_4) \cdot \text{H}_2\text{O}$ .	174
<b>Fig. 6.6</b>	A comparison of specific heat capacities of $\alpha\text{-TPD}$ and $\beta\text{-TPD}$ .	178
<b>Fig. 6.7</b>	Schematic diagram depicting stepwise thermal evolution of $\beta\text{-TPD}$ .	180
<b>Fig. 6.8</b>	Thermo-chemical cycle	181
<b>Fig. 6.9</b>	Phase diagram of Th-P-O system.	186
<b>Fig. 6.10</b>	The predominance diagram of Th-P-O system at 1273 K.	186
<b>Fig. 6.11</b>	$E_{\text{H}}$ -pH diagram for Th-P- $\text{H}_2\text{O}$ system.	190

## LIST OF TABLES

	<b>Page No.</b>
<b>CHAPTER-1</b>	
<b>Table 1.1</b> List of fission products and transuranic elements in HLW.	7
<b>CHAPTER-3</b>	
<b>Table 3.1</b> Refined structural parameters of $\text{LaPO}_4(\text{s})$ .	80
<b>Table 3.2</b> Enthalpy of reaction data using solution calorimeter experiment for $\text{LaCl}_3 \cdot 7\text{H}_2\text{O}(\text{s})$ , $\text{NdCl}_3 \cdot 6\text{H}_2\text{O}(\text{s})$ , $\text{SmCl}_3 \cdot 6\text{H}_2\text{O}(\text{s})$ and $\text{GdCl}_3 \cdot 6\text{H}_2\text{O}(\text{s})$ in solution of $\text{NH}_4\text{H}_2\text{PO}_4(\text{aq.})$ at 298 K.	81
<b>Table 3.3</b> Thermo-chemical reaction scheme for standard molar enthalpy of formation of $\text{LaPO}_4 \cdot 0.8\text{H}_2\text{O}_{(\text{s, rhab})}$ at 298 K.	82
<b>Table 3.4</b> Thermo-chemical reaction scheme for standard molar enthalpy of formation of $\text{NdPO}_4 \cdot 0.75\text{H}_2\text{O}_{(\text{s, rhab})}$ at 298 K.	83
<b>Table 3.5</b> Thermo-chemical reaction scheme for standard molar enthalpy of formation of $\text{SmPO}_4 \cdot 0.65\text{H}_2\text{O}_{(\text{s, rhab})}$ at 298 K.	83
<b>Table 3.6</b> Thermo-chemical reaction scheme for standard molar enthalpy of formation of $\text{GdPO}_4 \cdot 0.55\text{H}_2\text{O}_{(\text{s, rhab})}$ at 298.15 K.	84
<b>Table 3.7</b> Comparison of standard molar enthalpy of formation of $\text{LaPO}_4$ , $\text{NdPO}_4$ , $\text{SmPO}_4$ and $\text{GdPO}_4$ with that reported in the literature.	85
<b>CHAPTER-4</b>	
<b>Table 4.1</b> Specifications of chemicals used for the synthesis.	94
<b>Table 4.2</b> Elementary composition of $(\text{La}_{1-x}\text{M}_{x/2}\text{Th}_{x/2})\text{PO}_4$ ( $0 \leq x \leq 1$ ) ( $M = \text{Ca}, \text{Sr}$ and $\text{Ba}$ ) compounds determined using ICP-AES <sup>a</sup> analysis.	94
<b>Table 4.3</b> Refined structural parameters of $(\text{La}_{1-x}\text{Ca}_{x/2}\text{Th}_{x/2})\text{PO}_4$ ( $x = 0, 0.15, 0.25, 0.40, 0.60, 0.75, 0.85, 1$ ) compositions at 298 K and pressure of 101.325 kPa <sup>a</sup> .	100
<b>Table 4.4</b> Refined structural parameters of $(\text{La}_{1-x}\text{Sr}_{x/2}\text{Th}_{x/2})\text{PO}_4$ ( $x = 0, 0.2, 0.4, 0.6, 0.8, 1$ ) ( $0 \leq x \leq 1$ ) composition at 298 K and pressure of 101.325 kPa <sup>a</sup> .	101

<b>Table 4.5</b>	Refined structural parameters of $(\text{La}_{1-x}\text{Ba}_{x/2}\text{Th}_{x/2})\text{PO}_4$ ( $x = 0, 0.1, 0.2, 0.3; x = 1$ ) compositions at 298 K and pressure of 101.325 kPa <sup>a</sup> .	102
<b>Table 4.6</b>	Comparison of lattice parameters viz. a, b, c, unit-cell volume (V) and density ( $\rho$ ) of $\text{LaPO}_4$ and $(\text{M}_{0.5}\text{Th}_{0.5})\text{PO}_4$ ( $M = \text{Ca}, \text{Sr}$ and $\text{Ba}$ ) at 298 K and pressure of 101.325 kPa <sup>a</sup> with that of the reported data in literature.	103
<b>Table 4.7</b>	Experimentally observed data for specific heat capacity of $\text{ZrO}_2$ .	107
<b>Table 4.8</b>	Coefficients of specific heat capacity of $(\text{La}_{1-x}\text{M}_{x/2}\text{Th}_{x/2})\text{PO}_4$ ( $0 \leq x \leq 1$ ) ( $M = \text{Ca}, \text{Sr}$ and $\text{Ba}$ ) samples as a function of temperature (298 $\leq T/\text{K} \leq 800$ ) at a pressure of 101.325 kPa <sup>a</sup> .	111
<b>Table 4.9</b>	Thermo-chemical cycles for calculation of standard molar enthalpy of dissolution <sup>a</sup> ( $\Delta H_{\text{ds}}$ ) of $\text{P}_2\text{O}_5$ from temperature 298K ( $T_r$ ) to temperature of solvent <sup>b</sup> 1089 K ( $T_s$ ) at pressure $P = 101.325$ kPa <sup>c</sup> .	112
<b>Table 4.10</b>	Thermo-chemical cycles for calculation of standard molar enthalpy of dissolution <sup>a</sup> ( $\Delta H_{\text{ds}}$ ) of $\text{MO}$ ( $M = \text{Ca}, \text{Sr}$ and $\text{Ba}$ ) from temperature 298 K ( $T_r$ ) to temperature of solvent <sup>b</sup> 1089 K ( $T_s$ ) at pressure $P = 101.325$ kPa <sup>c</sup> .	113
<b>Table 4.11</b>	Comparison of enthalpy of dissolution ( $\Delta H_{\text{ds}}$ ) values of relevant oxides, carbonates and phosphates with that reported in literature by different authors.	113
<b>Table 4.12</b>	The molar enthalpies of dissolution <sup>a</sup> of $(\text{La}_{1-x}\text{Ca}_{x/2}\text{Th}_{x/2})\text{PO}_4$ ( $x = 0, 0.15, 0.25, 0.40, 0.60, 0.75, 0.85, 1$ ), $\text{La}_2\text{O}_3$ , $\text{CaO}$ , $\text{ThO}_2$ and $\text{Ca}_3(\text{PO}_4)_2$ with mass $m$ , from temperature 298 K ( $T_r$ ) to temperature of solvent <sup>b</sup> 1089 K ( $T_s$ ) at pressure $P = 101.325$ kPa <sup>c</sup> .	115
<b>Table 4.13</b>	Thermo-chemical cycles for derivation of standard molar enthalpies of formation of $(\text{La}_{1-x}\text{Ca}_{x/2}\text{Th}_{x/2})\text{PO}_4$ ( $x = 0, 0.15, 0.25, 0.40, 0.60, 0.75, 0.85, 1$ ) at temperature 298K ( $T_r$ ) using enthalpy of dissolution <sup>a</sup> data at temperature of solvent <sup>b</sup> 1089 K ( $T_s$ ) and pressure $P = 101.325$ kPa <sup>c</sup> .	118
<b>Table 4.14</b>	Measured values of enthalpy of formation from the constituent element and from the constituent oxides for $(\text{La}_{1-x}\text{Ca}_{x/2}\text{Th}_{x/2})\text{PO}_4$ ( $x=0, 0.15, 0.25, 0.40, 0.60, 0.75, 0.85, 1$ ).	120

<b>Table 4.15</b>	The molar enthalpies of dissolution <sup>a</sup> ( $\Delta H_{ds}$ ) of $(La_{1-x}Sr_{x/2}Th_{x/2})PO_4$ ( $x = 0.1, 0.2, 0.3, 0.4, 0.5, 0.6, 0.7, 0.8, 0.9, 1$ ) and $SrCO_3$ with mass $m$ , from temperature 298 K ( $T_r$ ) to temperature of solvent <sup>b</sup> 1089 K ( $T_s$ ) at pressure $P = 101.325$ kPa <sup>c</sup> .	123
<b>Table 4.16</b>	Thermo-chemical cycles for derivation of standard molar enthalpies of formation of $(La_{1-x}Sr_{x/2}Th_{x/2})PO_4$ ( $x = 0, 0.1, 0.2, 0.3, 0.4, 0.5, 0.6, 0.7, 0.8, 0.9, 1$ ) at temperature 298 K ( $T_r$ ) using enthalpy of dissolution <sup>a</sup> data at temperature of solvent <sup>b</sup> 1089 K ( $T_s$ ) and pressure $P = 101.325$ kPa <sup>c</sup> .	125
<b>Table 4.17</b>	Measured values of enthalpy of formation from the constituent elements and from the constituent oxides for $(La_{1-x}Sr_{x/2}Th_{x/2})PO_4$ ( $x = 0, 0.1, 0.2, 0.3, 0.4, 0.5, 0.6, 0.7, 0.8, 0.9, 1$ ).	127
<b>Table 4.18</b>	The molar enthalpies of dissolution <sup>a</sup> ( $\Delta H_{ds}$ ) of $(La_{1-x}Ba_{x/2}Th_{x/2})PO_4$ ( $x = 0.1, 0.2, 0.3; x = 1$ ) and $BaCO_3$ with mass $m$ , from temperature 298K ( $T_r$ ) to temperature of solvent <sup>b</sup> 1089 K ( $T_s$ ) at pressure $P = 101.325$ kPa <sup>c</sup> .	128
<b>Table 4.19</b>	Thermo-chemical cycle for derivation of standard molar enthalpies of formation of $(La_{1-x}Ba_{x/2}Th_{x/2})PO_4$ ( $x = 0, 0.1, 0.2, 0.3; x = 1$ ) at temperature 298 K ( $T_r$ ) using enthalpy of dissolution <sup>a</sup> data at temperature of solvent <sup>b</sup> 1089 K ( $T_s$ ) and pressure $P = 101.325$ kPa <sup>c</sup> .	129
<b>Table 4.20</b>	Measured values of enthalpy of formation from the constituent elements and from the constituent oxides for $(La_{1-x}Ba_{x/2}Th_{x/2})PO_4$ ( $x = 0, 0.1, 0.2, 0.3; x = 1$ ).	131
<b>Table 4.21</b>	Calculated values of enthalpy of mixing, $\Delta H_{mix}$ of $(La_{1-x}M_{x/2}Th_{x/2})PO_4$ ( $0 \leq x \leq 1$ ) ( $M = Ca, Sr$ and $Ba$ ) solid solutions relative to their end members.	131
<b>Table 4.22</b>	Thermodynamic data for $LaPO_4$ , where $T =$ temperature, $C_p^0 =$ standard molar heat capacity, $S_T^0 =$ standard molar entropy, $H_T^0 =$ standard molar enthalpy, $G_T^0 =$ standard Gibbs energy, $-(G_T^0 - H_{298}^0)/T =$ free energy function, $\Delta H_f^0 =$ standard molar enthalpy of formation, $\Delta G_f^0 =$ standard molar free energy of formation as a function of temperature at a pressure of 101.325 kPa <sup>a</sup> .	135

- Table 4.23** Thermodynamic data for  $(\text{La}_{0.85}\text{Ca}_{0.075}\text{Th}_{0.075})\text{PO}_4$ , where  $T =$  135  
temperature,  $C_p^0 =$  standard molar heat capacity,  $S_T^0 =$  standard molar  
entropy,  $H_T^0 =$  standard molar enthalpy,  $G_T^0 =$  standard Gibbs energy,  
 $-(G_T^0 - H_{298}^0)/T =$  free energy function,  $\Delta H_f^0 =$  standard molar  
enthalpy of formation,  $\Delta G_f^0 =$  standard molar free energy of  
formation as a function of temperature at a pressure of 101.325  
kPa<sup>a</sup>.
- Table 4.24** Thermodynamic data for  $(\text{La}_{0.75}\text{Ca}_{0.125}\text{Th}_{0.125})\text{PO}_4$ , where  $T =$  136  
temperature,  $C_p^0 =$  standard molar heat capacity,  $S_T^0 =$  standard molar  
entropy,  $H_T^0 =$  standard molar enthalpy,  $G_T^0 =$  standard Gibbs energy,  
 $-(G_T^0 - H_{298}^0)/T =$  free energy function,  $\Delta H_f^0 =$  standard molar  
enthalpy of formation,  $\Delta G_f^0 =$  standard molar free energy of  
formation as a function of temperature at a pressure of 101.325  
kPa<sup>a</sup>.
- Table 4.25** Thermodynamic data for  $(\text{La}_{0.60}\text{Ca}_{0.20}\text{Th}_{0.20})\text{PO}_4$ , where  $T =$  136  
temperature,  $C_p^0 =$  standard molar heat capacity,  $S_T^0 =$  standard molar  
entropy,  $H_T^0 =$  standard molar enthalpy,  $G_T^0 =$  standard Gibbs energy,  
 $-(G_T^0 - H_{298}^0)/T =$  free energy function,  $\Delta H_f^0 =$  standard molar  
enthalpy of formation,  $\Delta G_f^0 =$  standard molar free energy of  
formation as a function of temperature at a pressure of 101.325  
kPa<sup>a</sup>.
- Table 4.26** Thermodynamic data for  $(\text{La}_{0.40}\text{Ca}_{0.30}\text{Th}_{0.30})\text{PO}_4$ , where  $T =$  137  
temperature,  $C_p^0 =$  standard molar heat capacity,  $S_T^0 =$  standard molar  
entropy,  $H_T^0 =$  standard molar enthalpy,  $G_T^0 =$  standard Gibbs energy,  
 $-(G_T^0 - H_{298}^0)/T =$  free energy function,  $\Delta H_f^0 =$  standard molar  
enthalpy of formation,  $\Delta G_f^0 =$  standard molar free energy of  
formation as a function of temperature at a pressure of 101.325  
kPa<sup>a</sup>.
- Table 4.27** Thermodynamic data for  $(\text{La}_{0.25}\text{Ca}_{0.375}\text{Th}_{0.375})\text{PO}_4$ , where  $T =$  137  
temperature,  $C_p^0 =$  standard molar heat capacity,  $S_T^0 =$  standard molar  
entropy,  $H_T^0 =$  standard molar enthalpy,  $G_T^0 =$  standard Gibbs energy,  
 $-(G_T^0 - H_{298}^0)/T =$  free energy function,  $\Delta H_f^0 =$  standard molar

	enthalpy of formation, $\Delta G_f^0$ = standard molar free energy of formation as a function of temperature at a pressure of 101.325 kPa <sup>a</sup> .	
<b>Table 4.28</b>	Thermodynamic data for $(La_{0.15}Ca_{0.425}Th_{0.425})PO_4$ , where $T$ = temperature, $C_p^0$ = standard molar heat capacity, $S_T^0$ = standard molar entropy, $H_T^0$ = standard molar enthalpy, $G_T^0$ = standard Gibbs energy, $-(G_T^0 - H_{298}^0)/T$ = free energy function, $\Delta H_f^0$ = standard molar enthalpy of formation, $\Delta G_f^0$ = standard molar free energy of formation as a function of temperature at a pressure of 101.325 kPa <sup>a</sup> .	138
<b>Table 4.29</b>	Thermodynamic data for $Ca_{0.5}Th_{0.5}PO_4$ , where $T$ = temperature, $C_p^0$ = standard molar heat capacity, $S_T^0$ = standard molar entropy, $H_T^0$ = standard molar enthalpy, $G_T^0$ = standard Gibbs energy, $-(G_T^0 - H_{298}^0)/T$ = free energy function, $\Delta H_f^0$ = standard molar enthalpy of formation, $\Delta G_f^0$ = standard molar free energy of formation as a function of temperature at a pressure of 101.325 kPa <sup>a</sup> .	138
<b>Table 4.30</b>	Thermodynamic data for $(La_{0.8}Sr_{0.1}Th_{0.1})PO_4$ , where $T$ = temperature, $C_p^0$ = standard molar heat capacity, $S_T^0$ = standard molar entropy, $H_T^0$ = standard molar enthalpy, $G_T^0$ = standard Gibbs energy, $-(G_T^0 - H_{298}^0)/T$ = free energy function, $\Delta H_f^0$ = standard molar enthalpy of formation, $\Delta G_f^0$ = standard molar free energy of formation as a function of temperature at a pressure of 101.325 kPa <sup>a</sup> .	139
<b>Table 4.31</b>	Thermodynamic data for $(La_{0.6}Sr_{0.2}Th_{0.2})PO_4$ , where $T$ = temperature, $C_p^0$ = standard molar heat capacity, $S_T^0$ = standard molar entropy, $H_T^0$ = standard molar enthalpy, $G_T^0$ = standard Gibbs energy, $-(G_T^0 - H_{298}^0)/T$ = free energy function, $\Delta H_f^0$ = standard molar enthalpy of formation, $\Delta G_f^0$ = standard molar free energy of formation as a function of temperature at a pressure of 101.325 kPa <sup>a</sup> .	139
<b>Table 4.32</b>	Thermodynamic data for $(La_{0.4}Sr_{0.3}Th_{0.3})PO_4$ , where $T$ = temperature, $C_p^0$ = standard molar heat capacity, $S_T^0$ = standard molar	140

entropy,  $H_T^0$  = standard molar enthalpy,  $G_T^0$  = standard Gibbs energy,  $-(G_T^0 - H_{298}^0)/T$  = free energy function,  $\Delta H_f^0$  = standard molar enthalpy of formation,  $\Delta G_f^0$  = standard molar free energy of formation as a function of temperature at a pressure of 101.325 kPa<sup>a</sup>.

- Table 4.33** Thermodynamic data for  $(La_{0.2}Sr_{0.4}Th_{0.4})PO_4$ , where  $T$  = 140  
 temperature,  $C_p^0$  = standard molar heat capacity,  $S_T^0$  = standard molar  
 entropy,  $H_T^0$  = standard molar enthalpy,  $G_T^0$  = standard Gibbs energy,  
 $-(G_T^0 - H_{298}^0)/T$  = free energy function,  $\Delta H_f^0$  = standard molar  
 enthalpy of formation,  $\Delta G_f^0$  = standard molar free energy of  
 formation as a function of temperature at a pressure of 101.325  
 kPa<sup>a</sup>.
- Table 4.34** Thermodynamic data for  $Sr_{0.5}Th_{0.5}PO_4$ , where  $T$  = temperature, 141  
 $C_p^0$  = standard molar heat capacity,  $S_T^0$  = standard molar entropy,  
 $H_T^0$  = standard molar enthalpy,  $G_T^0$  = standard Gibbs energy,  $-(G_T^0 -$   
 $H_{298}^0)/T$  = free energy function,  $\Delta H_f^0$  = standard molar enthalpy of  
 formation,  $\Delta G_f^0$  = standard molar free energy of formation as a  
 function of temperature at a pressure of 101.325 kPa<sup>a</sup>.
- Table 4.35** Thermodynamic data for  $(La_{0.9}Ba_{0.05}Th_{0.05})PO_4$ , where  $T$  = 141  
 temperature,  $C_p^0$  = standard molar heat capacity,  $S_T^0$  = standard molar  
 entropy,  $H_T^0$  = standard molar enthalpy,  $G_T^0$  = standard Gibbs  
 energy,  $-(G_T^0 - H_{298}^0)/T$  = free energy function,  $\Delta H_f^0$  = standard molar  
 enthalpy of formation,  $\Delta G_f^0$  = standard molar free energy of  
 formation as a function of temperature at a pressure of 101.325  
 kPa<sup>a</sup>.
- Table 4.36** Thermodynamic data for  $(La_{0.8}Ba_{0.1}Th_{0.1})PO_4$ , where  $T$  = 142  
 temperature,  $C_p^0$  = standard molar heat capacity,  $S_T^0$  = standard molar  
 entropy,  $H_T^0$  = standard molar enthalpy,  $G_T^0$  = standard Gibbs  
 energy,  $-(G_T^0 - H_{298}^0)/T$  = free energy function,  $\Delta H_f^0$  = standard molar  
 enthalpy of formation,  $\Delta G_f^0$  = standard molar free energy of  
 formation as a function of temperature at a pressure of 101.325  
 kPa<sup>a</sup>.

<b>Table 4.37</b>	Thermodynamic data for $(\text{La}_{0.7}\text{Ba}_{0.15}\text{Th}_{0.15})\text{PO}_4$ , where $T$ = temperature, $C_p^0$ = standard molar heat capacity, $S_T^0$ = standard molar entropy, $H_T^0$ = standard molar enthalpy, $G_T^0$ = standard Gibbs energy, $-(G_T^0 - H_{298}^0)/T$ = free energy function, $\Delta H_f^0$ = standard molar enthalpy of formation, $\Delta G_f^0$ = standard molar free energy of formation as a function of temperature at a pressure of 101.325 kPa <sup>a</sup> .	142
<b>Table 4.38</b>	Thermodynamic data for $\text{Ba}_{0.5}\text{Th}_{0.5}\text{PO}_4$ , where $T$ = temperature, $C_p^0$ = standard molar heat capacity, $S_T^0$ = standard molar entropy, $H_T^0$ = standard molar enthalpy, $G_T^0$ = standard Gibbs energy, $-(G_T^0 - H_{298}^0)/T$ = free energy function, $\Delta H_f^0$ = standard molar enthalpy of formation, $\Delta G_f^0$ = standard molar free energy of formation as a function of temperature at a pressure of 101.325 kPa <sup>a</sup> .	143
<b>Table 4.39</b>	The coefficients of Gibbs energy of formation of $\text{La}_{1-x}\text{M}_{x/2}\text{Th}_{x/2}\text{PO}_4$ ( $0 \leq x \leq 1$ ) ( $M = \text{Ca}, \text{Sr}$ and $\text{Ba}$ ) as a function of temperature at $P = 101.325$ kPa <sup>a</sup> .	145
<b>Table 4.40</b>	Comparison of the standard molar enthalpies of formation values of $\text{LaPO}_4$ and $\text{Ca}_{0.5}\text{Th}_{0.5}\text{PO}_4$ with that reported in the literature.	147
<b>Table 4.41</b>	List of possible combinations of tetravalent/divalent and trivalent/trivalent charge coupled ions for synthetic monazite.	153
<b>Table 4.42</b>	List of surrogate elements for trivalent and tetravalent actinides [204-208].	154

## CHAPTER-5

<b>Table 5.1</b>	ICP-AES instrumental parameters and operational conditions.	159
<b>Table 5.2</b>	Analytical line of elements obtained using ICP-AES technique.	160
<b>Table 5.3</b>	Normalized leaching rates of monazite-cheralite solid solutions leached in aqueous medium under static conditions at 363 K for 7 days.	162

## CHAPTER-6

<b>Table 6.1</b>	X-ray powder diffraction data for $\beta$ - $\text{Th}_4(\text{PO}_4)_4\text{P}_2\text{O}_7$ .	171
------------------	--	-----

<b>Table 6.2</b>	Assignments of the vibrational frequencies of $\text{Th}_2(\text{PO}_4)_2(\text{HPO}_4)\cdot\text{H}_2\text{O}$ and $\beta\text{-Th}_4(\text{PO}_4)_4\text{P}_2\text{O}_7$ at room temperature.	173
<b>Table 6.3</b>	Heat capacity data of $\text{Th}_2(\text{PO}_4)_2(\text{HPO}_4)\cdot\text{H}_2\text{O}$ and $\text{Th}_2(\text{PO}_4)_2(\text{HPO}_4)$ .	175
<b>Table 6.4</b>	Heat capacity data of $\alpha\text{-Th}_4(\text{PO}_4)_4\text{P}_2\text{O}_7$ ( $\alpha\text{-TPD}$ ).	175
<b>Table 6.5</b>	Heat capacity data of $\beta\text{-Th}_4(\text{PO}_4)_4\text{P}_2\text{O}_7$ ( $\beta\text{-TPD}$ ).	177
<b>Table 6.6</b>	Enthalpy of reaction data using solution calorimeter experiment for $\text{Th}(\text{NO}_3)_4\cdot 5\text{H}_2\text{O}(\text{s})$ in solution of $\text{NH}_4\text{H}_2\text{PO}_4(\text{aq.})$ at 298 K.	178
<b>Table 6.7</b>	Thermochemical-cycle for calculation of standard molar enthalpy of formation, $\Delta H_{\text{f,m}}^\circ$ of $\text{Th}_2(\text{PO}_4)_2(\text{HPO}_4)\cdot\text{H}_2\text{O}$ (TPHPH) at 298 K.	179
<b>Table 6.8</b>	Standard enthalpy of formation of $\beta\text{-TPD}$ at 298 K.	181
<b>Table 6.9</b>	Standard enthalpy of formation of TPHP at 298 K.	181
<b>Table 6.10</b>	Standard enthalpy of formation of $\alpha\text{-TPD}$ at 298 K.	181
<b>Table 6.11</b>	Thermodynamic functions for $\beta\text{-Th}_4(\text{PO}_4)_4\text{P}_2\text{O}_7$ (TPD).	182
<b>Table 6.12</b>	Constants of the fitted equations for enthalpy increment and heat capacity data of compounds in binary Th-P system, ternary Th-P-O system and quaternary Th-P-O-H system. The enthalpy of formation and entropy at 298 K are also included.	185
<b>Table 6.13</b>	The chemical potentials of phosphorus and oxygen at invariant points.	188

## Thesis Highlight

**Name of the Student:** DEEPAK RAWAT  
**Name of the CI/OCC:** Bhabha Atomic Research Centre  
**Enrolment No.:** CHEM01201304001  
**Thesis Title:** “Thermodynamic Investigations of Phosphate-based Crystalline Ceramic Matrices for HLW Immobilization”  
**Discipline:** Chemical Sciences  
**Sub-Area of Discipline:** Thermodynamics of crystalline materials  
**Date of viva voce:** 25<sup>th</sup> September, 2020

The disposal of radioactive waste is a serious environmental problem for which complete satisfactory solution is not available. A vast variety of studies have been reported for search of alternate suitable host matrices to present borosilicate glass matrix. Among them, phosphate-based crystalline ceramic materials are proposed as potential host matrices for the immobilization of trivalent and tetravalent actinides. Monazite has a number of advantages such as ability to incorporate high amounts of U, Th and other actinides, high chemical durability and high radiation resistant property.

This dissertation focuses on the understanding of the thermodynamic stability and energetics of the phosphate-based materials such as rare-earth orthophosphates (synthetic monazite)  $REPO_4$  ( $RE = La, Nd, Sm$  and  $Gd$ ), monazite-cheralite solid solutions  $(La_{1-x}M_xTh_{x/2})PO_4$  ( $0 \leq x \leq 1$ ;  $M = Ca, Sr$  and  $Ba$ ) and thorium phosphate-diphosphate, TPD,  $(Th_4(PO_4)_4P_2O_7)$ . In this Thesis, thermodynamic parameters such as heat capacities, enthalpies of dissolution and standard molar enthalpies of formation of these phosphate-based materials were determined using Differential Scanning Calorimeter, oxide melt Calvet solution calorimeter and isoperibol solution calorimeter.

The standard molar enthalpy of formation,  $\Delta H_f^0$ , of  $LaPO_4$  was found to be most negative. Thereby showing most thermodynamic stability amongst other rare-earth phosphate, Fig. 1 (a) and could be considered as a stable host matrix for safe immobilization of tri- and tetra-valent actinides. However, the phase  $(La_{0.7}Sr_{0.15}Th_{0.15})PO_4$  has been identified to be thermodynamically most

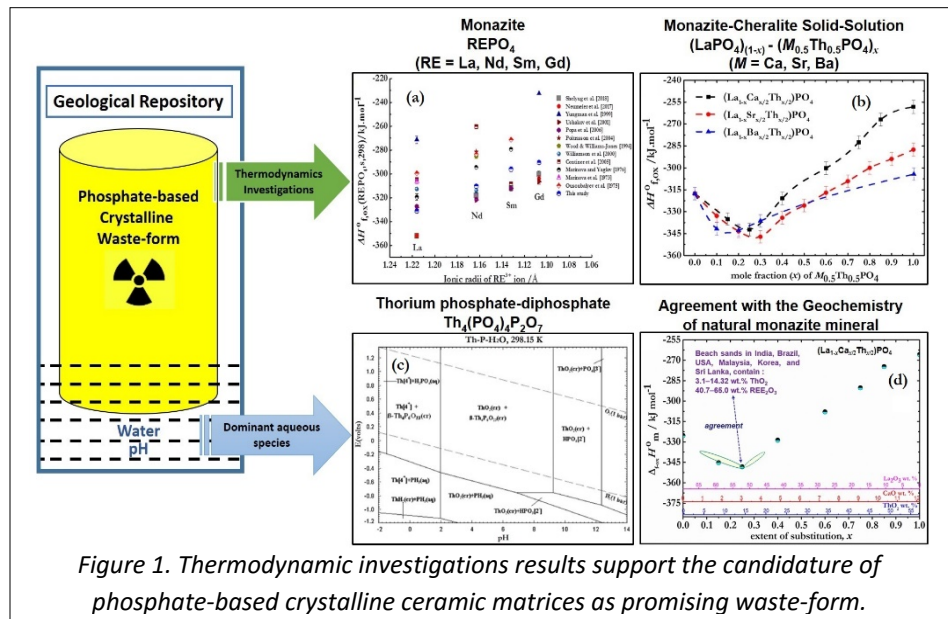


Figure 1. Thermodynamic investigations results support the candidature of phosphate-based crystalline ceramic matrices as promising waste-form.

stable phase in monazite-cheralite solid solutions, Fig. 1 (b). The leaching studies showed the chemical durability of  $(La_{1-x}M_xTh_{x/2})PO_4$  ( $0 \leq x \leq 1$ ;  $M = Ca, Sr, Ba$ ) solid solutions under off-normal conditions. The normalized leach rate values for the substituted elements (La and Th) were below  $10^{-10} \text{ g}\cdot\text{cm}^{-2}\cdot\text{d}^{-1}$ , which is lower compared to leaching rate ( $10^{-4} \text{ g}\cdot\text{cm}^{-2}\cdot\text{d}^{-1}$ ) of elements present in borosilicate glass and corroborates the results of thermodynamic stability of substituted monazite-cheralite solid solutions.

The ternary phase diagram and chemical potential diagram of Th-P-O system have been investigated.  $E_H$ -pH diagram for Th-P-H<sub>2</sub>O system showed the stability of  $Th_4(PO_4)_4P_2O_7$  in ground water in the pH range 2-9, Fig. 1 (c) and suitable for incorporation of tetravalent actinide ions or ions having similar radius  $\sim 1.09 \text{ \AA}$ .

This thesis purposes  $(La_{0.7}Sr_{0.15}Th_{0.15})PO_4$  as the most suitable composition for immobilization of divalent fission product ( $Sr^{2+}$ ), trivalent actinides ( $Am^{3+}$ ,  $Cm^{3+}$ ) and tetravalent actinides ( $Pu^{4+}$ ,  $Np^{4+}$ ). The synthetic monazite composition arrived from present thermodynamic study matched qualitatively with the natural composition of monazite present in beach sands of India, Brazil, USA etc., Fig. 1 (d).

# ***CHAPTER-1***

---

## ***INTRODUCTION***

The global warming due to burning of the fossil fuels can be minimized with alternate non-polluting power production methods utilizing hydro, nuclear, solar and wind energy. The production of nuclear power is considered as one of the best technologies since it does not emit greenhouse gases and could be considered as a solution for mitigating climate change. Nuclear waste arises during nuclear fuel cycle (NFC) involved mining, processing, enrichment, fabrication of fuel, transportation, installation of fuel in nuclear reactors, production of electrical energy by controlled nuclear fission and reprocessing of spent nuclear fuel. Though, nuclear waste is generated at various steps of NFC, the highly radioactive waste called High-Level Waste (HLW) is produced from the reprocessing of spent nuclear fuel. The highly radioactive HLW contains long-lived radionuclides and thus requires great attention for their safe immobilization. The safe disposal of nuclear waste is considered as a serious challenge in nuclear energy production [1]. Proper principles and techniques need to be followed during disposal of nuclear waste. The main goal of nuclear waste immobilization includes protection of human health, environment and the future generations [2].

## **1.1. Nuclear energy**

Global electricity demand is expanding nearly twice as fast as the overall requirement for energy and this demand will continue to grow in the future [3]. To meet this ever-growing global demand for sustainable energy, the nuclear power must provide at least 25% of electricity by 2050, at present nuclear energy provides about 11% of the world's electricity from about 450 power reactors [4]. Nuclear power technology is the world's second largest source of low-carbon power after hydropower. Since its commercialization in 1970s, more than 60 Gt of CO<sub>2</sub> emissions have been avoided globally, equivalent to five years' worth of CO<sub>2</sub> emissions from the electricity sector [5]. Hence, to meet global demand for sustainable energy and saving our planet from climate change, nuclear power is inevitable.

Nuclear energy is produced by neutron-induced fission of fissile atoms viz.  $^{235}\text{U}$ ,  $^{233}\text{U}$  and  $^{239}\text{Pu}$  to sustain the nuclear chain reaction [6]. Large amount of energy is released during nuclear fission reaction. For instance, one fission event results in the release of about 200 MeV of energy. The nuclear energy comes with simultaneous generation of radioactive waste consisting of different fission products and transuranic elements. Long-lived transuranic elements such as  $^{237}\text{Np}$ ,  $^{241}\text{Am}$ ,  $^{243}\text{Am}$  and  $^{245}\text{Cm}$  are formed in significant quantities as activation products in the uranium fueled nuclear reactor by  $(n, \gamma)$  reaction followed by  $\beta$ -decay as given in **Fig. 1.1**.

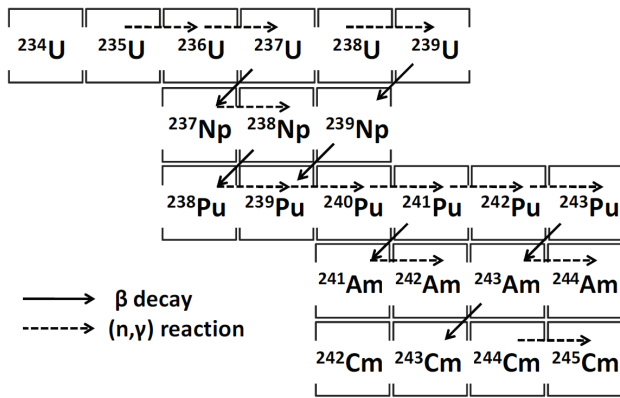


**Fig.1.1:** Production of transuranic radionuclides in the uranium fueled nuclear reactor.

## 1.2. Indian nuclear power programme

Nuclear power is the fifth-largest source of electricity in India. At present, India has 22 nuclear reactors in operation in 7 nuclear power plants with total installed capacity of 6,780 MW [7]. India follows a three-stage nuclear power programme which is represented in **Fig. 1.2**.

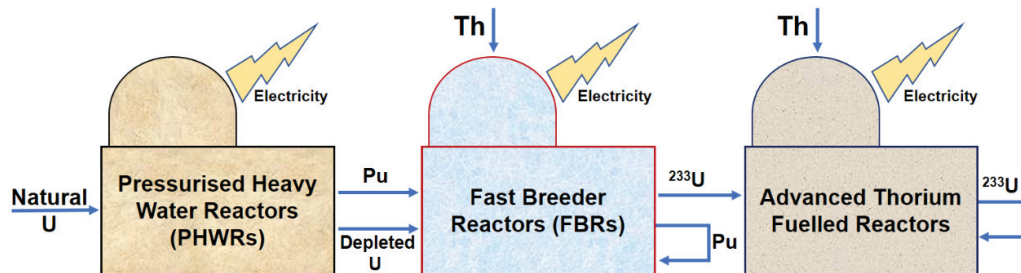


**Fig. 1.2:** Schematic diagram of Indian nuclear power program.

First stage reactors, Pressurized Heavy Water Reactors (PHWRs) use natural uranium as fuel and produce electricity while generating  $^{239}\text{Pu}$  which is recovered as mixed oxide of  $^{238}\text{U}$  and  $^{239}\text{Pu}$  fuel for the second stage- Fast Breeder Reactors (FBRs). Thorium is used as a blanket material around the fuel in FBRs in the second stage to produce fissile element  $^{233}\text{U}$  which will be the fuel for the next stage. In the third stage,  $^{233}\text{U}$  will be used in thermal or fast breeder reactors to produce electricity as well as for further breeding of  $^{233}\text{U}$  from naturally occurring thorium [8].

The radioactive waste is a byproduct of operating nuclear reactor for the power generation. When the irradiated nuclear fuel is no longer useful in sustaining a nuclear chain reaction [9, 10], it is discharged from the reactors, which is highly radioactive and consists of fission products, fissile elements and transuranic elements, formed by the absorption of neutrons along with un-burnt fuel. Based on the management of this spent fuel, the nuclear fuel cycle can be classified into two types viz. *open and closed fuel cycles*. The open nuclear fuel cycle involves the disposal of highly radioactive waste without any reprocessing and the closed fuel cycle allows the recovery of valuables such as plutonium, useful fission products, and depleted uranium from the high-level radioactive waste using aqueous reprocessing (PUREX). India has chosen to follow a closed fuel cycle strategy to ensure long term energy security. A schematic plan of closed nuclear fuel cycle is showed in **Fig. 1.3**. Irrespective of open and closed fuel cycle, both policies demand for an efficient and safe waste management strategies.

### 1.3. Classification of nuclear waste

Based on the amount and type of radioactivity, nuclear waste can be classified under three categories viz. Low-Level Waste (LLW), Intermediate-Level Waste (ILW) and High-Level Waste (HLW).



< 4 % radioactivity comes under ILW which can be solidified in concrete matrices before final disposal. ILW comprises used resins, chemical sludge, nuclear reactor components, reprocessing equipment as well as contaminated equipment of weapon decommissioning.

### 1.3.3. High-Level Waste (HLW)

The nuclear waste containing radioactivity above  $3.7 \times 10^{11} \text{ Bq}\cdot\text{L}^{-1}$  is called High Level Waste (HLW). Relative to the total volume of waste generated in nuclear power production, HLW constitutes only a small fraction ( $\sim 3 \%$ ) by volume but the majority of the radioactivity ( $> 95 \%$ ) resides in HLW. The aqueous waste stream of HLW produced during spent fuel reprocessing, contains radionuclides such as U, Pu, alpha emitting minor actinides (Np, Am, Cm) and fission products (Cs, Sr etc.). The major components of the HLW are given below:

- Unrecovered U and Pu
- Fission products, such as,  $^{90}\text{Sr}$ ,  $^{99}\text{Tc}$ ,  $^{106}\text{Ru}$ ,  $^{129}\text{I}$ ,  $^{135}\text{Cs}$ ,  $^{137}\text{Cs}$ ,  $^{144}\text{Ce}$ ,  $^{147}\text{Pm}$  etc.
- Minor actinides such as  $^{237}\text{Np}$ ,  $^{241}\text{Am}$ ,  $^{243}\text{Am}$ ,  $^{242}\text{Cm}$ ,  $^{244}\text{Cm}$ ,  $^{245}\text{Cm}$
- Corrosion products of stainless steel & other structural material (Fe, Ni, Cr, Mn etc.),
- Alloying elements such as Fe, Al, Si, Mo etc. in the case of metallic fuel,
- Chemicals introduced in the reprocessing plant like nitric acid, sulphates, sodium nitrate, aluminium nitrate, chlorides, fluorides, traces of TBP and its degradation products,
- Soluble neutron poisons such as Gd, B and Cd.

Radionuclides present in HLW along with their respective half-lives and decay mode are listed in **Table 1.1**. The presence of long-lived minor actinides having high radioactivity cause major challenges in its final disposal. Global efforts are being made for the development of appropriate methods to separate the long-lived minor actinides for their safe long-term disposal.

## 1.4. Management of HLW

The HLW should be immobilized in a suitable matrix owing to the high level of radioactivity. It should be isolated from the biosphere for a very long period  $\sim 10^6$  years with control and surveillance in order to render the waste harmless [11].

The spent nuclear fuel of Fast Reactors (FRs) in the second stage of the Indian nuclear power programme will demand major tasks for its reprocessing and subsequently the management of the generated HLW. The concentration of fission products, corrosion products (such as Fe, Ni, and Cr) and minor actinides will be high owing to high burn up and short cooling time. Due to their alpha activity and very long half-lives, actinides present in such HLW require isolation for longer time span compared to the fission and activation products of irradiated fuels.

**Table 1.1:** List of fission products and transuranic elements in HLW.

Radionuclide	Half-life	Decay mode	Radionuclide	Half-life	Decay mode
<b>Fission products</b>			<b>Fission products</b>		
$^{99}\text{Tc}$	$2.1 \times 10^5 \text{ y}$	$\beta$	$^{152}\text{Eu}$	13.33 y	$\gamma$
$^{90}\text{Sr}$ - $^{90}\text{Y}$	28.5 y	$\beta$	$^{154}\text{Eu}$	8.8 y	$\gamma$
$^{93}\text{Zr}$	$1.5 \times 10^6 \text{ y}$	$\beta$	$^{155}\text{Eu}$	4.96 y	$\beta, \gamma$
$^{106}\text{Ru}$ - $^{106}\text{Rh}$	368 d	$\gamma$	<b>Transuranics</b>		
$^{107}\text{Pb}$	$6.5 \times 10^6 \text{ y}$	$\beta$	$^{237}\text{Np}$	$2.14 \times 10^6 \text{ y}$	$\alpha$
$^{125}\text{Sb}$	2.77 y	$\gamma$	$^{238}\text{Pu}$	87.74 y	$\alpha$
$^{129}\text{I}$	$1.57 \times 10^7 \text{ y}$	$\beta, \gamma$	$^{239}\text{Pu}$	$2.41 \times 10^4 \text{ y}$	$\alpha$
$^{134}\text{Cs}$	2.06 y	$\beta, \gamma$	$^{240}\text{Pu}$	$6.5 \times 10^3 \text{ y}$	$\alpha$
$^{135}\text{Cs}$	$2 \times 10^6 \text{ y}$	$\beta$	$^{241}\text{Pu}$	14.4 y	$\beta$
$^{137}\text{Cs}$	30.17 y	$\beta, \gamma$	$^{241}\text{Am}$	$4.32 \times 10^2 \text{ y}$	$\alpha$
$^{144}\text{Ce}$ - $^{144}\text{Pr}$	284 d	$\beta, \gamma$	$^{243}\text{Am}$	$7.3 \times 10^3 \text{ y}$	$\alpha$
$^{147}\text{Pm}$	2.62 y	$\beta$	$^{244}\text{Cm}$	18.11 y	$\alpha$
$^{151}\text{Sm}$	93 y	$\beta$	$^{245}\text{Cm}$	$8.5 \times 10^3 \text{ y}$	$\alpha$

(Here, d=day, y= year)

The policy of ‘concentrate and contain’ is used for the management of HLW in which the liquid waste is converted into a suitable solid waste form having thermal, mechanical and chemical stability over the time scale of major long-lived radionuclides. The solid waste form offers enhanced safety during handling and transportation. It also restricts the release of radionuclides to the ground water in accidental conditions. The solid waste form of HLW is normally kept in an interim storage facility to allow the decay of short-lived radioisotopes viz.  $^{90}\text{Sr}$ ,  $^{106}\text{Ru}$ ,  $^{137}\text{Cs}$ ,  $^{144}\text{Ce}$ ,  $^{147}\text{Pm}$  and  $^{244}\text{Cm}$  followed by ultimate disposal of the waste form in deep geological repository.

### 1.5. Nuclear waste disposal

It is an ultimate step in the radioactive waste management that involves confinement and isolation of the nuclear waste from the biosphere. The repository for disposal could be either ‘Near Surface’ or ‘Deep Geological’ on the basis of half-lives and activity of radionuclides. Near surface disposal facilities (NSDFs) help to keep the radiation levels and radionuclides contamination in soil, water and air, in and around the disposal facilities within the safe limits of regulatory body [12].

Globally, the nuclear waste immobilization using a glass matrix which is encased inside the steel canister (about 10 feet long by 1 foot in diameter) for long-term storage is practiced. After an interim storage for a sufficient period, the glass waste form is buried inside an underground deep geological repository (typically below 300 m) with horizontal spacing of about 10 m between canisters [13]. For the first 400 years the decay heat is mainly due to  $^{137}\text{Cs}$ ,  $^{90}\text{Sr}$  and their daughter products. After this period, the main contributors to the decay heat are the transuranics [13]. In order to reduce the radiotoxicity and the heat generated by the decay of the fission products, waste forms are temporarily stored in a well-designed solid storage and surveillance facility. For long-term strategy, the nuclear waste is permanently disposed in a

deep geological repository employing a multi-barrier approach. It is used in a geological repository for the isolation the nuclear waste from the biosphere [14]. The salt, clay and granite deposits sites are largely used for the construction of a geological repository.

This multi-barrier system includes the natural geological barrier provided by the host rock and an engineered barrier system (EBS) shown in **Fig. 1.4**. The EBS involves a number of sub-barriers such as the nuclear waste matrix, container or over-pack, buffer or backfill, repository walls and wall linings.

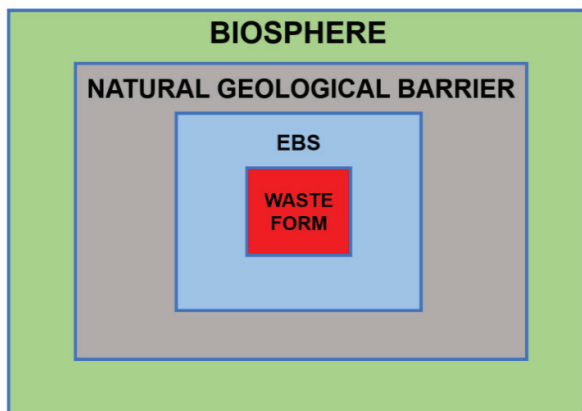


**Fig. 1.4:** Schematic of a multi-barrier system in a nuclear waste repository.

The various barriers work together to hold the radionuclides and then to limit their release to the biosphere. The key purposes of a deep geological repository are as follow:

- *Exclude waste from near-surface processes and human activities,*
- *Biosphere protection,*
- *Restrict the release of waste from the gradually degrading EBS,*
- *Distribute and dilute the flux of long-lived radionuclides.*

The immobilized waste form provides the prime barrier to the radionuclides in the deep geological repository. The container or over-pack material would consist of a corrosion

resistant metal, such as titanium or iron alloy that would corrode at a slow and predictable rate. The backfill or the host rock should have high sorption capacity which restrict the release of radioactive materials to the environment. The design of EBS is based on the disposal option selected and the radioactive waste forms viz. glass, ceramic, glass-ceramic, involved. Although the release of the radionuclides from the repository to biosphere is expected to be prevented by multi barrier system, radionuclides may diffuse out of the waste matrix due to their decay heat, environmental factors like groundwater movement, structure of rock, erosion, flood, natural calamities such as earth quakes, volcanic eruptions and subsequent dispersion and dissolution, which can ultimately lead to their release into the biosphere. Therefore, it is imperative to have detailed knowledge about the stability of waste loaded matrix under off-normal conditions. So far nuclear waste has not been stored in the final disposal site. Further studies on nuclear waste storage sites are continuing in the world.

## **1.6. Nuclear waste immobilization matrices**

The goal of immobilization of nuclear waste is to fix the radionuclides in a suitable solid matrix that will not allow them to enter the biosphere over the time scale of millions of years. Thus, the safety of nuclear-waste management relies mainly on the radioactive constituents to be immobilized, materials of the host matrix and long-term isolation of these materials from the biosphere. As materials issues gain importance, thus ultimate goal in nuclear-waste management is to develop a highly durable waste package (waste form and the surrounding container barriers) that ensures the long-term stability as well as isolation of radioactivity. The waste form also represents the first and foremost barrier to retard radionuclides leaching from the nuclear waste disposal site.

### 1.6.1. Properties of immobilization matrices

The desirable properties of the matrices to immobilize HLW are as follows:

- i.* High waste loading and high density to minimize the waste volume,
- ii.* High chemical durability (low leachability) to minimize the release of radioactive elements to the biosphere,
- iii.* High thermal conductivity and specific heat capacity, so that the heat generated due to decay of radioactive isotopes will well dissipated,
- iv.* Low thermal expansion, so that it has thermal shock resistance and avoid formation of cracks by thermal stresses,
- v.* High thermal and radiation stability over extended periods of time to retain its original structure,
- vi.* High mechanical strength and shock resistance so that transportation to storage or disposal site is safe,
- vii.* Compatibility with storage container and geological repositories,
- viii.* Economic and technical aspects (raw materials, process parameters).

### 1.6.2. Classification of host matrices

The host matrices available for the immobilization of HLW can be classified broadly under two major categories:

1. *Glass*
2. *Crystalline ceramic*

## 1.7. Glass

Glass is one of the most ancient of all materials known to mankind and has been used by nuclear countries worldwide for vitrification of nuclear waste for more than 40 years. The main adva-

Advantages of the glass waste form are as follows:

- Glass is an amorphous system that can accommodate the large variety of elements of HLW,
- Favourable long-term behaviour, chemical durability and radiation resistant property,
- Simplicity of vitrification process i.e., melting of waste with glass frit,
- Knowledge and know-how of vitrification process is well documented for the past 30 years,
- Commercially accepted and production under remote operation.

The most widely studied and used glassy waste form are:

- a. Borosilicates and phosphates glass*
- b. Glass composite materials (GCMs)*
- c. Glass-ceramics*

### **1.7.1. Borosilicate and phosphate glasses**

Borosilicate and phosphate glasses are the most common glasses used in vitrification of nuclear waste by virtue of their low processing temperature and durable product formation. In borosilicate glasses,  $B_2O_3$  and  $SiO_2$  are the basic glass forming oxides while  $Na_2O$ ,  $Cs_2O$ ,  $SrO$ ,  $BaO$  etc. are glass modifiers. Development of glass matrix for HLW is governed by its composition, glass additives and the processing temperatures. Loading of radionuclides into glass matrix is restricted by solubility of the waste components and the decay heat. The processing temperature of the glass depends upon compatibility of the melter material under corrosive environment of molten glass and volatility of the radionuclide [15].

Nuclear waste constituents are immobilised either by direct incorporation into the glass structure or by encapsulation. In direct incorporation, waste constituents are dissolved in the

glass melt, some being included into the glass network on cooling while others are confined as modifiers. Nuclear waste glasses are not completely homogeneous vitreous materials as a result contain large amounts of bubbles, foreign inclusions (**Fig. 1.5 (a)**) such as refractory oxides and other immiscible constituents. Encapsulation approach is used for the elements and compounds with low solubility which cannot fit into the glass network. Low miscibility waste includes sulphates, chlorides and molybdates as well as noble metals such as Rh and Pd, refractory oxides with high liquidus temperatures such as  $\text{PuO}_2$ , noble metal oxides and spinels [6]. Thus, they are immobilised in the glass matrix by encapsulation and are dispersed in its microstructure as represented in **Fig. 1.5 (b)**.

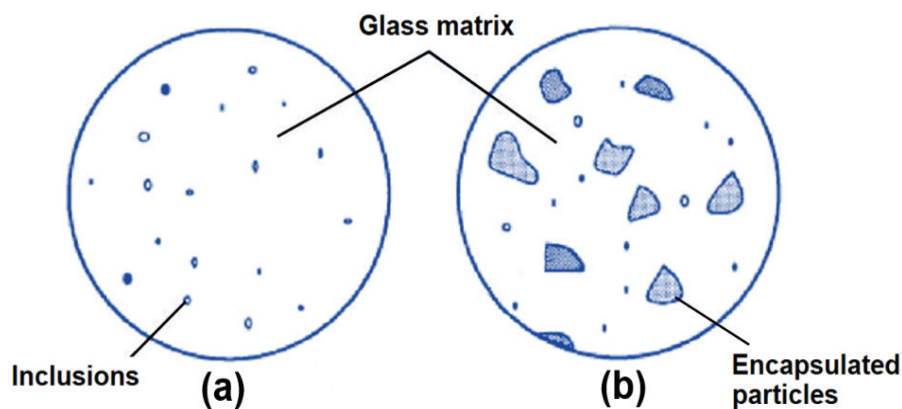


**Fig. 1.5:** Schematic of waste accommodation in glass matrix: (a) incorporation in glass with presence of bubbles and inclusions; (b) encapsulation of waste particles in a glass matrix.

### 1.7.2. Glass composite materials (GCMs)

Glass composite materials (GCMs) are classified as systems intermediate between completely glass vitreous waste form and completely crystalline ceramic waste form. GCMs can immobilize waste components viz. sulphates, chlorides, molybdates and refractory materials which are glass immiscible and need high melting temperatures. GCMs may be used to arrest long-lived actinide species by incorporating them into the more durable crystalline phases.

GCMs formed when a fully melted system is crystallised during cooling or in a separate heat treatment operation or by dispersion of solid particles into a liquid phase which later freezes to a glassy waste form. Crystalline phase can form the major component of GCMs with vitreous phase acting as a bonding agent. Alternatively, the major component can be a vitreous phase, with crystalline phase particles dispersed in the glass matrix for example Synroc-glass, which is a GCM with Synroc crystalline phases in a vitreous matrix.

### **1.7.3. Glass-ceramics**

Glass-ceramics are polycrystalline materials formed by controlled crystallization of amorphous glasses. The glass-ceramics are mechanically durable and can be tailored to use for a specific application. The crystallization of  $\text{SiO}_2\text{-Al}_2\text{O}_3\text{-CaO-TiO}_2\text{-ZrO}_2\text{-Nd}_2\text{O}_3$  (Nd is surrogate for minor actinides) in a controlled way results in the formation of zirconolite-type glass ceramic, which is found to be highly durable and can accommodate minor actinides. Due to the poor chemical durability of barium aluminosilicate glass ceramic and barium titanium silicate glass ceramic, they are not the favourable choices as glass ceramic waste forms, though they possess good mechanical durability compared to glass.

### **1.7.4. Disadvantage of glass waste form**

The major disadvantage of glass waste form is that glass is a thermodynamically metastable phase. Crystallization of the nuclear waste loaded glass mainly due to the decay heat from the radioactive elements in HLW during storage. The crystallization (devitrification), which leads to decrease in volume, develops crack in the waste form and result in increased surface area and increased leaching. Hence, the chemical, thermal and radiation stability of the glass waste form need to be ascertained before the vitrification process. Though, borosilicate glass is a commercially acceptable waste form, nuclear wastes containing phosphates, sulphates, iron

oxides and heavy metal oxides along with sodium, molybdenum and chromium rich wastes could not be loaded into borosilicate glass [16]. These facts necessitate the search for alternate host matrices for nuclear waste immobilization specially in the context of fast breeder reactors (FBR), where the concentration of fission products, corrosion products and minor actinides will be high. The Immobilization of HLW containing high concentrations of radionuclides could be achieved by directly incorporating them into a crystalline ceramic waste form without vitrification [17], however, there are currently no commercial plants in operation for the immobilization of HLW employing crystalline ceramic materials.

## 1.8. Crystalline ceramics

The natural crystalline ceramic materials are thermodynamically stable and found with high radionuclides content which are retained for millions of years without undergoing any metamictization. Thus, crystalline ceramic materials could be promising materials for immobilization of long-lived radionuclides present in HLW of spent nuclear fuel. In the last decades, the focus of the research was directed at the study of the ceramic waste forms. The main advantages of the crystalline ceramic waste forms are as follows:

- *Higher density and chemical durability compared to borosilicate glass,*
- *Higher thermal stability and thermal conductivity compared to glass,*
- *Ability to incorporate large volumes of waste types (i.e., high waste loading),*
- *Ability to accommodate minor actinides and Pu (limited solubility in glass),*
- *Superior mechanical properties,*
- *Proven long-term resistance to radiation damage (natural mineral analogues).*

The objective is to use these durable crystalline minerals as immobilising waste form which have been preserved in natural conditions for geological times, called “natural analogues”. Two

promising mechanisms for immobilization of radionuclides in crystalline matrices are: by *incorporation* into the crystalline structure of mineral phases and by *encapsulation* within non-radioactive phases as represented in **Fig. 1.6 (a)** and **(b)**, respectively.

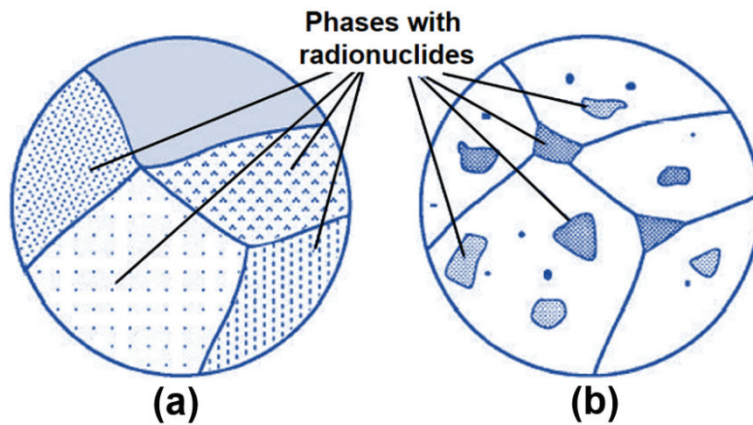


**Fig. 1.6:** Schematic of waste immobilisation by crystalline host matrix.

Although radionuclides accommodation varies with species and crystal type, there are some predominant mechanisms through which immobilization of radionuclides in crystalline ceramic takes place. They are given as follows:

- Direct substitution of iso-valent species on particular lattice sites,
- Alter-valent substitution facilitated by charge compensation on a nearby site,
- Insertion into open channels within the crystal structure,
- Incorporation by generation of planar defects such as twins and crystallographic shear planes.

A limitation of crystalline ceramics waste form compared to vitrified glasses is that crystalline ceramics are capable to immobilize only a limited number of radionuclides on specific sites in their crystal structures. Based on aforementioned conditions, crystalline ceramics can be categorised into two classes:

- i. Single phase ceramics*
- ii. Multiphase systems (Synroc)*

Single phase ceramics can deal with pure single-phase wastes for instance weapons grade plutonium oxides, whereas multiphase systems like Synroc, is being developed for more complex waste streams.

### 1.8.1. Single phase ceramics

**1.8.1.1 Apatites** has a generic formula  $M_{10}(XO_4)_6Y_2$ , where M is a divalent cation (Ca, Pb, Ba),  $XO_4$  is a trivalent anion ( $PO_4$ ,  $VO_4$ ,  $SiO_4$ ) and Y is a monovalent anion (F, Cl, OH, Br). Apatites crystallise in the hexagonal structure. Calcium phosphate apatites,  $Ca_{10}(PO_4)_6(F,OH,Cl)_2$ , including fluorapatite, hydroxyapatite and chlorapatite are jointly the tenth most abundant mineral. It has high thermal, chemical and radiation stability.  $Cs^+$  shows a high affinity for  $Ca_8NdCs(PO_4)_6F_2$  and much less affinity for britholites (silicate apatite) with a nominal formula of  $Ca_7Nd_2Cs(PO_4)_5(SiO_4)F_2$ .

**1.8.1.2. NZP and Kosnarite** are single phase sodium and potassium analogue of zirconium phosphate with the composition,  $NaZr_2(PO_4)_3$  and  $KZr_2(PO_4)_3$ , respectively. Sodium zirconium phosphate (NZP), not only allow substitution of actinides for Zr, but also many other radionuclides present in HLW. There are three types of crystallographic sites present in the structure of NZP and thereby have good compositional flexibility. 20 % waste loading of NZP resulted in a two-phase material, with monazite as the second phase. These ceramics can be synthesised at low temperature (900–1000°C) but fabrication of dense NZP ceramics by sintering in air is difficult. The mechanical durability of kosnarite-type ceramic is low as compared to borosilicate glass.

**1.8.1.3. Zircon** is a silicate mineral ( $ZrSiO_4$ ). Zircon is a well-known accessory mineral which occurs in different rock types, including lunar rock, placers, pegmatites and meteorites. It is the main source of zirconium and found as an accessory mineral in acid igneous rocks. Zircon contains upto 20 wt. % of U and Th oxides. Several synthesis methods have been

demonstrated on a laboratory scale for the preparation of zircon and Pu-substituted zircon powders. Since it is generally used in the dating of mineral samples (from the U/Pb ratio present), its mineralogy has been studied thoroughly.

**1.8.1.4. Zirconolite** has the generic formulation  $\text{CaZr}_x\text{Ti}_{(3-x)}\text{O}_7$  ( $0.8 < x < 1.35$ ). Natural zirconolite contains up to 20 and 14 wt. % of  $\text{ThO}_2$  and  $\text{UO}_2$ , respectively. In zirconolite, Ca and Zr sites can be substituted with Hf, lanthanides, trivalent and tetravalent actinides. In doing that required charge compensation achieved by substitution of trivalent cations ( $\text{Al}^{3+}$ ,  $\text{Ti}^{3+}$ ) at the  $\text{Ti}^{4+}$  site. One method of zirconolite preparation is ceramication process in which powders are synthesised by the alkoxide route and later the powder is sintered in air at  $1400^\circ\text{C}$ . Second method involves an oxide melting process using high temperature in the range of  $1700\text{--}1800^\circ\text{C}$  using a cold crucible.

**1.8.1.5. Hollandite** has the general formula  $\text{A}_2\text{B}_8\text{O}_{16}$ , where A is a monovalent or divalent atom and B has a valence between 2 and 5. A range of natural minerals crystallise in this structure with difference in the chemical elements substituting for Ti on the B-site. For example, hollandite (Mn totally substituted for Ti), ankangite (Cr, V), henrymeyerite ( $\text{Fe}^{2+}$ ), priderite ( $\text{Fe}^{3+}$ ) and redledgeite (Cr). Hollandite powder is prepared using an alkoxide process and pressure-assisted sintering at  $1200^\circ\text{C}$  is carried out for the densification of the ceramic.

**1.8.1.6. Britholite** minerals are the natural analogues rare earth silicates and actinides with the apatite-type structure. For example, Britholite-monosilicate,  $\text{Ca}_9\text{Nd}(\text{PO}_4)_5(\text{SiO}_4)\text{F}_2$ , where  $\text{Nd}^{3+}$  can be substituted with minor actinides viz.  $\text{Am}^{3+}$  and  $\text{Cm}^{3+}$ . It is synthesised by solid state reaction route with their precursors, followed by final sintering at  $1400^\circ\text{C}$  in oxidative atmosphere. Britholite has been found in the vicinity of natural fission reactors, dating back more than one thousand million years.

**1.8.1.7. Pyrochlores** have the structural formula,  $^{\text{VIII}}\text{A}_2^{\text{VI}}\text{B}_2^{\text{IV}}\text{X}_6^{\text{IV}}\text{Y}$ , where the A and B-sites contain metal cations; X ( $=\text{O}^{2-}$ ) and Y ( $=\text{O}^{2-}$ ,  $\text{OH}^-$ ,  $\text{F}^-$ ) are anions. It is plentiful in nature

and over 500 synthetic compositions have been prepared, including zirconates, titanates and niobates. Pyrochlores present in Synroc and can be synthesized by coprecipitation of oxides from solution, e.g., the sol-gel process. Ti-based Pyrochlore,  $Gd_2Ti_2O_7$ , suffers a radiation induced transformation from crystalline to amorphous state. Zr-based radiation resistant compositions e.g.  $Gd_2Zr_2O_7$  and  $Er_2Zr_2O_7$ , have recently been discovered.

**1.8.1.8. Monazite** is a natural phosphate mineral discovered by Johann August Friedrich Breithaupt in 1829 for the first time. The term “monazite” has its etymological origins from the Greek meaning “*to be alone*”, because of its crystals standing alone in the rock [18]. It is a mixed rare earth orthophosphate natural mineral  $[(Ce, La, Nd, Th)PO_4]$  and known to contain the radioactive elements Th and U for billions of years. This material is also considered as an alternate ceramic waste form for the immobilization of HLW. It is the source of rare earths, thorium and uranium. Monazite contains up to 27 wt. % of U and Th oxides. Synthetic lanthanide phosphates exist in several crystalline forms viz. hexagonal, monoclinic and tetragonal. A low temperature hexagonal phase forms for compositions in the first half of the lanthanide series (La-Dy). The hexagonal phase is metastable and will not form once the structure is transformed into the monoclinic (monazite) structure. The heavier lanthanides (Er-Y) have a high temperature tetragonal structure isostructural with zircon ( $ZrSiO_4$ ). The monazite waste forms for the point of view of nuclear waste immobilization is discussed in detail in a separate section below (Section 1.5).

In view of a potential waste form, important properties of monazite are listed as follows:

- i.* Monazite has excellent chemical and radiation stability [19]. In spite of the high  $\alpha$ -decay doses ( $>1$  dpa) induced by high content of natural thorium and uranium, monazite found to undergo no metamictization,
- ii.* Monazite has good thermal stability. The melting point of  $LaPO_4$  is very high  $2072^\circ C$  and it does not decompose till it melts,

- iii.* Monazites has the unique property of negative temperature coefficients of solubility in water [20, 21] compared to other candidate nuclear waste forms, including borosilicate glass and synroc. As a result, solubility in aqueous environments decreases with increasing temperature,
- iv.* Monazites have survived many of the conditions such as earthquakes, meteorite impact and intrusion of igneous melts, that might be imposed on the repository by unpredicted geological disruptions.

**1.8.1.9. Thorium phosphate diphosphate (TPD)** with the general formula  $\text{Th}_4(\text{PO}_4)_4\text{P}_2\text{O}_7$ , were developed for the immobilisation of weapons grade plutonium and other actinides. TPD can accommodate actinides in thorium sites 47.6 wt. % for U; 33.2 wt. % for Np; 26.1 wt. % for Pu. Single-phase TPD solid solution  $(\text{Th,Pu})_4(\text{PO}_4)_4\text{P}_2\text{O}_7$  and  $(\text{Th,Np})_4(\text{PO}_4)_4\text{P}_2\text{O}_7$  have been successfully synthesised. Advantage of TPD lies in the simplicity of precursor preparation by mixing concentrated Th-nitrate and phosphoric acid followed by sintering in air at 1100-1350°C. The mechanical durability is similar to that of other phosphate ceramics [14].

## **1.8.2. Multiphase systems (Synroc)**

Synroc or “*Synthetic rock*” is the titanite polyphase ceramic. It is a tailored made ceramic with phases: zirconolite ( $\text{CaZrTi}_2\text{O}_7$ ), perovskite ( $\text{CaTiO}_3$ ), hollandite ( $\text{BaAl}_2\text{Ti}_6\text{O}_{16}$ ) and rutile ( $\text{TiO}_2$ ). The approach for preparing a tailored ceramic is to change the waste stream composition by external additives so as to form stable, crystalline phase assemblages upon processing by high temperature-high pressure methods. A range of phases viz. silicates, oxides and phosphates are taken for specific radionuclide immobilization.

## 1.9. Suitable matrix for waste disposal

There have been a number of studies to assess the suitability of alternative ceramics to SYNROC for the immobilization of HLW. Immobilization of radioactive wastes in relatively inert solid matrices before storage is advantageous for safety and economic reasons. One of the ways to assess the radiation stability of compounds is the study of their natural analogues that contain radioactive elements. The naturally occurring phosphate-based mineral structure can host actinides for high-level wastes (HLW). Different ceramic waste forms have been discussed which offers a broad spectrum to immobilize the different radionuclides into their crystal structure.

Current information in the literature suggests that phosphate-based compounds is potentially a good host-phase for radionuclides immobilization. The main emphasis of the present research is on following three important phosphate-based crystalline ceramic waste forms:

- *Monazite,  $REPO_4$  ( $RE = La, Nd, Sm$  and  $Gd$ )*
- *Monazite-cheralite solid solutions,  $(La_{1-x}M_{x/2}Th_{x/2})PO_4$  ( $0 \leq x \leq 1$ ) ( $M = Ca, Sr$  and  $Ba$ )*
- *Thorium phosphate-diphosphate,  $Th_4(PO_4)_4P_2O_7$*

In order to conduct focus studies of the thesis, the thorough literature survey of these systems is imperative.

## 1.10. Literature survey on phosphate-based ceramics

The reported studies on the synthesis, structure, thermodynamic properties and leaching studies of monazite, monazite-cheralite solid solutions and thorium phosphate-diphosphate [22-111] have been searched and given in sequence below from which the scope of the thesis has been determined.

### 1.10.1. Monazite

Monazite is a naturally occurring mixed light Rare earth orthophosphate ( $\text{REPO}_4$ ) mineral that generally contains large amounts of uranium and thorium [22-26]. It is found in placer deposits in India for which India holds an important place on the rare earths map of the world. The best-known monazite deposits of commercial importance are found in the beach sands of the coastal tracts of Kerala. It is found along with other minerals viz., ilmenite, garnet, rutile, zircon and sillimanite. It is the most important industrial raw materials having great scientific potential for green energy technologies as well as high-tech applications in defence systems. As monazite contains thorium/uranium, it is unacceptable as a commercial ore. In India, this mineral is a prescribed substance as per the notification under the Atomic Energy Act, 1962 and its resource estimate is 11.93 million tonnes in 2014. During the extraction of Th/U from monazite, rare earths are by-products; whose one of the important uses could be as waste immobilization matrix. It contains significant amounts of thorium and uranium for billions of years [27]. This provides a scientific basis [28, 29] for using analogue of monazite minerals as an ideal host for the immobilization of HLW.

#### 1.10.1.1. Structure

The monazite-type compounds crystallize in a monoclinic structure with space group  $P2_1/n$  ( $Z = 4$ ). The metal ion in monazite has a nine-fold coordination  $\text{REO}_9$  and is usually described as an equatorial pentagon (formed by 5 oxygen atoms belonging to monodentate anionic tetrahedrons) interpenetrated by a tetrahedron (formed by 4 oxygen atoms belonging to two bidentate tetrahedrons) shown in **Fig. 1.7**. The tetrahedrons located out of the equatorial plane could then be defined as a link between the  $\text{REO}_9$  polyhedra, resulting in the formation of infinite chains along the c-axis ( $[0\ 0\ 1]$  direction). A complete explanation of the structure and

coordination polyhedra of the rare earth element was reported by Beall et al. [31] and Mullica et al. [32, 33].

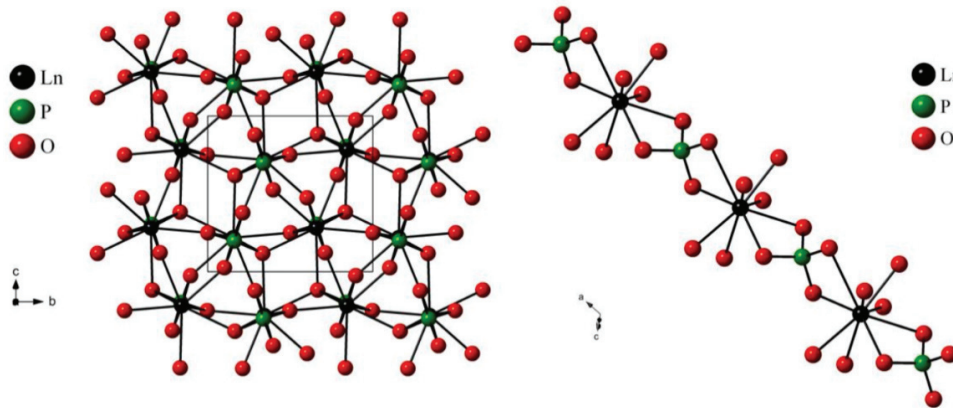


**Fig. 1.7:** An illustration of the crystal structure of REPO<sub>4</sub> monazite [30].

The REPO<sub>4</sub> monazite structure accommodates a wide range of radionuclides, which makes it a material of interest in the field of nuclear waste immobilization. The surprising structural flexibility is correlated to the low symmetry of the REO<sub>9</sub> polyhedron, which does not induce severe charge or size constraints on the accommodating cations [34]. In monazite structure, two distinct RE-P distances exist along the chains which induce a distortion of the REO<sub>9</sub> polyhedron, and a set of nine distinct bond distances between lanthanide and oxygen atoms as a result incorporation of large variety of cations is possible.

Monazite, a single-phase ceramic host matrix can accommodate nearly all the elements of the HLW by formation of solid solution. The formation of solid solutions follows two different mechanisms, either by *direct substitution* of iso-valent species on particular lattice sites or by *alter-valent substitution* coupled by charge compensation on a nearby site in monazite crystal lattice. It is suitable for the immobilization of rare earths and actinide wastes which form a major portion of the HLW after the spent fuel reprocessing.

### 1.10.1.2. Synthesis

Monazites can be synthesized following various methods described by Byrappa et.al [35]. Several chemical processes have been used to synthesize rare earth orthophosphate. Bregiroux et al. [36] employed a high temperature solid-state route for  $\text{LnPO}_4$  ( $\text{Ln} = \text{La-Gd}$ ) preparation. The wet-chemical methods have been successfully used by Terra et al. [37], Boakye & Mogilevsky [38] and Lucas et al. [39]. Meyssamy et al. [40] have used hydrothermal route for the synthesis of phosphate materials.

Single crystals of  $\text{PrPO}_4$  and  $\text{NdPO}_4$  were prepared by Mullica et al. [41]. The same group also synthesized  $\text{SmPO}_4$ ,  $\text{EuPO}_4$  and  $\text{GdPO}_4$  using high-temperature flux technique. Thiriet et al. [42] prepared  $\text{LaPO}_4$  and  $\text{GdPO}_4$  using precipitation reaction of lanthanide nitrate with diammonium hydrogen phosphate at room temperature. Horchani-Naifer and Férid [43] synthesized single crystals of  $\text{PrPO}_4$  by high temperature solution reaction, using analytical reagents  $\text{Pr}_5\text{O}_{11}$  and  $\text{NH}_4\text{H}_2\text{PO}_4$  at the molar ratio of  $\text{Pr/P} = 1:20$ . Jardin et al. [44] prepared  $\text{PuPO}_4$  by sol-gel reaction starting from  $\text{Pu(IV)}$  solution.  $\text{PuPO}_4$  observed to decompose above 1473 K whereas  $\text{CePO}_4$  and  $\text{NdPO}_4$  were stable.

### 1.10.1.3. Thermodynamic properties

Popa and Konings [45] have determined the high-temperature heat capacities of  $\text{EuPO}_4$  and  $\text{SmPO}_4$  synthetic monazites by drop calorimetry. Ushakov et al. [46] have performed systematic thermochemistry of rare earth orthophosphates series using oxide-melt solution calorimetry. Popa et al. [47, 48] determined high-temperature heat capacity of  $\text{LnPO}_4$  ( $\text{Ln} = \text{La, Ce, Nd and Gd}$ ) using drop calorimetry. Low-temperature heat capacity and thermodynamic properties of  $\text{PrPO}_4$  was measured by Gavrichev et al. [49]. A linear trend was observed for enthalpies of formation of  $\text{LnPO}_4$  as a function of lanthanides contraction which was corroborated by ab initio calculations from Blanca-Romero et al. [50] and Rustad [51]. Popa et

al. prepared monazite-type solid solutions  $(\text{La}_{1-x}\text{Ln}_x)\text{PO}_4$  ( $\text{Ln} = \text{Nd}, \text{Eu}$  and  $\text{Gd}$ ) using sol-gel reaction and carried out detailed high-temperature calorimetry of the solid solutions using drop-calorimetry at 1000 K [52]. Konings et al. [53] determined the excess thermodynamic properties of  $\text{LaPO}_4\text{-Ca}_{0.5}\text{Th}_{0.5}\text{PO}_4$  and  $\text{CePO}_4\text{-Ca}_{0.5}\text{Th}_{0.5}\text{PO}_4$  solid solutions using drop calorimetry measurements at 1005 K. Recently, Neumeier et al. [54] measured the enthalpy of formation of single-phase orthophosphate solid solutions  $\text{La}_{1-x}\text{Ln}_x\text{PO}_4$  ( $\text{Ln} = \text{Eu}$  and  $\text{Gd}$ ) using high temperature oxide melt solution calorimeter. Thust et al. [55] measured the physical properties and microstructures of  $\text{La}_{1-x}\text{Pr}_x\text{PO}_4$  monazite solid solution.

#### 1.10.1.4. Other Properties

Nasdala et al. [56] and Picot et al. [57] studied the performance of  $\text{CePO}_4$  under 1-7 MeV Au ion irradiation at total fluences of  $0.6 \times 10^{13}$ – $5.1 \times 10^{13}$  ions $\cdot\text{cm}^{-2}$  resulting an amorphization at highest dose. The consequence of matrix elements and dose rate on monazite amorphization was studied by Burakov et al. [58] and Bregiroux et al. [59], respectively, using the direct incorporation of relatively short-lived  $^{238}\text{Pu}$  ( $T_{1/2} = 87.74$  y) and  $^{241}\text{Am}$  ( $T_{1/2} = 432.6$  y) radionuclides. Burakov et al. observed that  $^{238}\text{Pu}$  doped  $\text{LaPO}_4$  monazite remained crystalline at a dose of  $1.19 \times 10^{25}$   $\alpha\cdot\text{m}^{-3}$ . Petek et al. [60] prepared  $\text{LaPO}_4$  with  $\sim 20$  wt. % simulated HLW and the leach rate  $\sim 100$  times lower than that of glass waste form was reported. He et al. [61] have reported the preparation and characterization of simulated HLW loaded monazite glass ceramics by mixing lanthanum metaphosphate glass and HLW oxides and heating at  $1200^\circ\text{C}$  in pellet form. The amorphization dose for different rare earths is observed in the range of  $10^{14}$  to  $10^{16}$  ions $\cdot\text{cm}^{-2}$ , depending on the temperature.

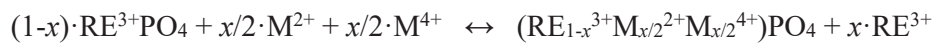
#### 1.10.1.5. Leaching studies

The dissolution behavior of  $\text{LnPO}_4$  monazite ( $\text{Ln} = \text{La}, \text{Ce}, \text{Nd}, \text{Eu}$  and  $\text{Gd}$ ) in static conditions

was investigated by du Fou de Kerdaniel [62] using 0.1 M HNO<sub>3</sub> at 363 K, obtaining similar normalized dissolution rate ( $1 \times 10^{-7} \text{ g}\cdot\text{cm}^{-2}\cdot\text{day}^{-1}$  to  $1.8 \times 10^{-7} \text{ g}\cdot\text{cm}^{-2}\cdot\text{day}^{-1}$ ) for all lanthanides consistent to the results of Oelkers and Poitrasson [63]. Ishida et al. [64] and Sales et al. [65] observed that the dissolution rate of synthetic monazite is three orders of magnitude lower than that of borosilicate glass. Terra et al. [37] investigated the dissolution rate of La<sub>1-x</sub>Gd<sub>x</sub>PO<sub>4</sub> and found to decrease from pH 1<sub>HCl</sub> ( $3.8 \times 10^{-8} \text{ g}\cdot\text{cm}^{-2}\cdot\text{day}^{-1}$ ) to pH 4<sub>HCl</sub> ( $4.8 \times 10^{-10} \text{ g}\cdot\text{cm}^{-2}\cdot\text{day}^{-1}$ ) at 363 K in static dissolution experiments. Ma et al. [66] observed the similar behavior for Ce<sub>0.5</sub>Pr<sub>0.5</sub>PO<sub>4</sub>. The dissolution rate varied from  $\sim 10^{-7} \text{ g}\cdot\text{cm}^{-2}\cdot\text{day}^{-1}$  at pH 3 to  $\sim 10^{-11} \text{ g}\cdot\text{cm}^{-2}\cdot\text{day}^{-1}$  at pH 7. In their study [67], no variation due to temperature increment from 363 K to 200°C and from fabrication method was observed. Brandt et al. [68] investigated the dissolution behavior of La<sub>1-x</sub>Eu<sub>x</sub>PO<sub>4</sub> solid solutions in dynamic dissolution experiments at pH 2 and 363 K. They reported a normalized dissolution rate between  $5 \times 10^{-5} \text{ g}\cdot\text{m}^{-2}\cdot\text{day}^{-1}$  and  $1.7 \times 10^{-3} \text{ g}\cdot\text{m}^{-2}\cdot\text{day}^{-1}$  and showed a dependence of Eu content on the dissolution rate.

### 1.10.2. Monazite-cheralite solid solution

The main mechanism for the substitution of trivalent lanthanides with divalent and tetravalent radionuclides is a charge-coupled substitution mechanism, namely, “*cheralite-type*” substitution. This mechanism seems to avoid the formation of vacancies in the structure as:



The full substitution of divalent and tetravalent actinides leads to the formation of the cheralite end-members, formerly known as brabantite, Ca<sub>0.5</sub>Th<sub>0.5</sub>PO<sub>4</sub>. The monazite-cheralite solid solutions viz. (La<sub>1-x</sub>M<sub>x/2</sub>Th<sub>x/2</sub>)PO<sub>4</sub> ( $0 \leq x \leq 1$ ) ( $M = \text{Ca}, \text{Sr}$  and  $\text{Ba}$ ) is a unique waste form which can accommodate divalent fission products, trivalent rare earths and tetravalent actinides, simultaneously in a single matrix, which mimics the actual nuclear waste form. The

investigation of monazite-cheralite solid solutions has to be ascertained thoroughly prior to its actual use for a waste immobilization waste matrix.

### 1.10.2.1. Structure

The complete substitution results in the formation of the cheralite family [69] having general formulae  $A_{0.5}B_{0.5}PO_4$  (formerly called brabantite). These solid solutions crystallize in monazite structure in which  $La^{3+}$  ions are randomly substituted by  $M^{2+}$  ( $Ca^{2+}$ ,  $Sr^{2+}$  and  $Ba^{2+}$ ) and  $M^{4+}$  ( $Th^{4+}$ ) ions resulting charge coupled substituted  $(La_{1-x}M_{x/2}Th_{x/2})PO_4$  ( $0 \leq x \leq 1$ ) ( $M = Ca, Sr$  and  $Ba$ ) solid solutions. The solid solutions with monoclinic crystal structure and space group  $P2_1/n$  consist of long chain of interconnected  $(M^{2+}, M^{4+})O_9$  polyhedra and  $PO_4$  tetrahedra.

### 1.10.2.2. Synthesis

Raison et al. [70] prepared  $CaAn(PO_4)_2$  ( $An = Th$  and  $Np$ ) by solid-state reactions using high purity polycrystalline  $AnO_2$ ,  $CaCO_3$  and  $(NH_4)_2HPO_4$  as starting materials. Popa et al. [71] also prepared  $CaTh(PO_4)_2$  using solid-state reaction whereas Podor et al. [72] used Hydrothermal synthesis. Dusausooy et al. [73] prepared  $CaU(PO_4)_2$  using Hydrothermal precipitation at 773 K and 200 MPa whereas Podor et al. [74] prepared the same at 1053 K and 200 MPa. Keskar et al. [75] prepared  $SrTh(PO_4)_2$  through solid-state reactions. The same author has prepared  $SrU(PO_4)_2$  and  $BaU(PO_4)_2$  by solid state route in Ar atmosphere [76]. Popa et al. [77] prepared  $SrNp(PO_4)_2$  using solid state route Wallez et al. [78] prepared  $BaTh(PO_4)_2$  by a wet chemistry route and  $BaNp(PO_4)_2$  by solid-state reaction. Montel et al. [79] synthesized compounds with stoichiometry of  $MTh(PO_4)_2$  with  $M = Ca, Cd, Sr, Pb, Ba$  at 1 bar, 1200°C and 2.5 kbar, 700°C.

Montel et al. [79] also prepared the solid solution  $LaPO_4-MTh(PO_4)_2$ , at 1200°C at 1 bar. Terra et al. [80] reported the synthesis of  $CaTh_{1-x}U_x(PO_4)_2$  compounds whereas Tabuteau et al. [81] prepared  $CaNp_{1-x}Pu_x(PO_4)_2$  through solid-state route.

### 1.10.2.3. Thermodynamic properties

Qin et al. [82] reported the incorporation of thorium in rhabdophane structure as  $\text{Pr}_{1-2x}\text{Ca}_x\text{Th}_x\text{PO}_4 \cdot n\text{H}_2\text{O}$  solid solutions. Thust et al. [83] have prepared  $\text{La}_{1-x}\text{Eu}_x\text{PO}_4$  monazite-type ceramics and characterized by ultrasound techniques, dilatometry and micro-calorimetry. Huittinen et al. [84] investigated the homogeneity of  $\text{Eu}^{3+}$ -doped  $\text{La}_{1-x}\text{Gd}_x\text{PO}_4$  solid solutions by combining spectroscopic and computational studies. Kowalski et al. [85] performed ab-initio calculations of different parameters of  $\text{La}_{1-x}\text{Eu}_x\text{PO}_4$  solid solution. Li et al. [86] used ab-initio calculation for the measurement of excess properties of  $\text{La}_{1-x}(\text{Ln},\text{An})_x\text{PO}_4$  solid solutions. Kowalski and Li [87] establish a relationship between the thermodynamic excess properties of mixing and the elastic moduli in the monazite-type ceramics using ab initio calculation.

The majority of thermochemical investigations were made on pure  $\text{LnPO}_4$  end-members [45-49, 88], monazite-type solid solutions [52, 54, 89] and to a lesser extent on monazite-cheralite-type solid solutions [53,90].

### 1.10.2.4. Other Properties

Qin et al. [91] have carried out sintering studies of  $\text{Nd}_{1-2x}\text{Ca}_x\text{Th}_x\text{PO}_4 \cdot n\text{H}_2\text{O}$  rhabdophanes ( $x=0-0.1$ ) resulting in homogeneous high-density monazite-cheralite solid solution. They reported the activation energy to convert rhabdophane to monazite-cheralite, depending on the thorium incorporation lies in the range of  $361 \pm 90$  and  $530 \pm 90$   $\text{kJ}\cdot\text{mol}^{-1}$ . They have also determined the micro hardness of  $\text{Nd}_{1-2x}\text{Ca}_x\text{Th}_x\text{PO}_4$ , which was about  $4.9 \pm 0.8$  GPa, which is in the typical range of the values determined for phosphate-based waste forms designed for actinides conditioning.

### 1.10.2.5. Leaching studies

Literature data for the chemical durability of monazite-cheralite solid solutions is very scarce.

Sales et al. [92] and Oelkers and Poitrasson [63] reported the dissolution rates for natural samples of monazite-cheralite solid solutions. The results on the dissolution of homogeneous and single phase  $\text{CaTh}_{0.5-x}\text{U}_x(\text{PO}_4)$  at 363 K in  $10^{-1}$  and  $10^{-4}$  M  $\text{HNO}_3$  was reported by Terra et al. [37] and Veilly et al. [93]. Du Fou de Kerdaniel [94] investigated the dissolution kinetics of various  $\text{La}_{0.4}\text{Eu}_{0.1}\text{Ca}_{0.25}\text{An}_{0.25}\text{PO}_4$  ( $\text{An} = \text{Th}, \text{U}$ ) solid solutions at pH 1 and 363 K. In contrast to the several leaching studies on monazite based matrix, very few results are available on aqueous durability of cheralite-type ( $\text{Ca}_{0.5}(\text{U},\text{Th})_{0.5}\text{PO}_4$ ) compound and monazite-cheralite ( $\text{Ln}_{1-2x}\text{Ca}_x(\text{U},\text{Th})_x\text{PO}_4$ ) solid solutions.

### 1.10.3. Thorium phosphate diphosphate (TPD)

Ceramic host matrix based on thorium phosphate diphosphate (TPD) with the general formula  $\text{Th}_{4-x}\text{M}_x(\text{PO}_4)_4\text{P}_2\text{O}_7$  ( $\text{M} = \text{U}, \text{Pu}, \text{Np}$ ) were studied by French scientists for the immobilization of weapons plutonium and other actinides. Different TPD samples based on single-phase solid solutions  $(\text{Th},\text{Pu})_4(\text{PO}_4)_4\text{P}_2\text{O}_7$  and  $(\text{Th},\text{Np})_4(\text{PO}_4)_4\text{P}_2\text{O}_7$  have been synthesized by Dacheux *et al.* [95, 96]. They determined the maximum loading to be about 47.6 wt. % for uranium, 33.2 wt. % for neptunium and 26.1 wt. % for plutonium [97]. Precursor preparation is easy and prepared by mixing concentrated thorium nitrate and phosphoric acid. The product is then obtained by sintering the mixture in air at 1100-1350°C. Mechanical durability of TPD is analogous to other phosphate ceramics and comparable or less than that of borosilicate glasses [14]. The property to resist the aqueous corrosion enables TPD to be used as a potential nuclear waste storage matrix.

#### 1.10.3.1. Structure

It crystallizes in an orthorhombic crystal system, *Pcam* ( $Z=2$ ).  $\text{Th}^{4+}$  is the largest tetravalent cation with ionic radii in eight-fold coordination ( $^{\text{VIII}}r_{\text{cat.}}$ ) is 1.05 Å and can be substituted by

other smaller tetravalent actinides viz.  $U^{4+}$  (1.00 Å),  $Np^{4+}$  (0.98 Å) and  $Pu^{4+}$  (0.96 Å) in TPD crystal lattice [18]. Such substitution brings about a deformation of the crystal cell and limits the extent of substitution in TPD which follows the similar trend of their tetravalent ionic radius viz.  $^{VIII}r_U > ^{VIII}r_{Np} > ^{VIII}r_{Pu}$ . The structure comprises of layer parallel to (010) containing both  $PO_4$  tetrahedra and  $P_2O_7$  groups. These layers alternate with planes of thorium atoms. A perspective view of the TPD structure along the (100) direction is given in **Fig.1.8**.

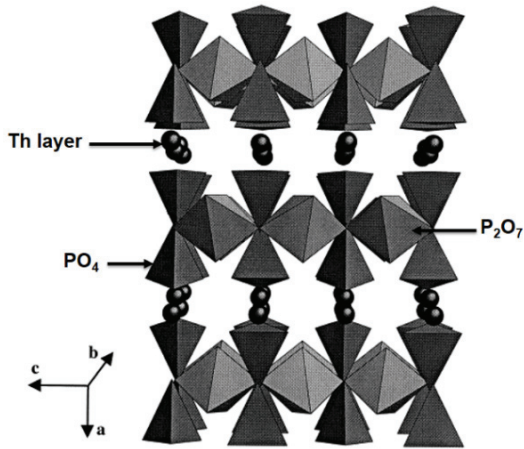


**Fig. 1.8:** Perspective view of the TPD structure.

### 1.10.3.2. Synthesis

Brandel et al. [98, 99] synthesized  $Th_4(PO_4)_4P_2O_7$  (TPD) and its actinide substituted solid solutions following several ways including either wet or dry chemistry routes. Sintered pellets were prepared using a two-step procedure which involves a uniaxial pressing at room temperature followed by a heat treatment at 1250°C. Thorium phosphate hydrogen phosphate hydrate ( $Th_2(PO_4)_2(HPO_4) \cdot H_2O$  (TPHPH)) has been prepared using low temperature wet chemical synthesis method which is analogous to the monazite-type phosphates [100, 101]. TPHPH converts to  $\beta$ -TPD under heat treatment at 900°C to 1000°C in air [102, 103].

### 1.10.3.3. Thermodynamic studies

Dacheux et al. [104] measured the specific heat and thermal conductivity of TPD sample. The experimental values of specific heat ranged from  $0.380 \text{ J}\cdot\text{g}^{-1}\cdot\text{K}^{-1}$  at  $28^\circ\text{C}$  to  $0.528 \text{ J}\cdot\text{g}^{-1}\cdot\text{K}^{-1}$  at  $789^\circ\text{C}$  whereas the thermal conductivity ranged from  $0.98$  to  $0.85 \text{ W}\cdot\text{m}^{-1}\cdot\text{K}^{-1}$  respectively for  $29$  and  $1000^\circ\text{C}$ . Launay et al. [105] determined the thermal expansion of TPD from  $20$  to  $800^\circ\text{C}$  by dilatometry and high-temperature X-ray diffraction techniques. They found an ultralow thermal expansion coefficient value: about  $1.9 \times 10^{-6} \text{ }^\circ\text{C}^{-1}$  in the temperature range studied.

### 1.10.3.4. Other Properties

Dacheux et al. [104] reported the Vickers hardness of the sintered TPD samples between  $350$  and  $500 \text{ HV}$ . The same authors also reported the thermal diffusivity value for TPD from  $5.2 \times 10^{-7} \text{ m}^2\cdot\text{s}^{-1}$  at  $29^\circ\text{C}$  to  $3.32 \times 10^{-7} \text{ m}^2\cdot\text{s}^{-1}$  at  $1000^\circ\text{C}$ . The amorphization of  $\beta$ -TPD and  $\beta$ -TUPD was studied using  $840 \text{ MeV Kr}$ -irradiation at a fluence of  $10^{13} \text{ ions}\cdot\text{cm}^{-2}$  and significantly depends on the electronic stopping power [106-108]. In the nuclear stopping regime, a complete amorphization occurs at a critical dose of  $0.2 \text{ dpa}$ . Thomas et al. [109] reported that TPD sample with high  $^{239}\text{Pu}$  loading ( $\sim 16.1 \text{ wt. } \%$ ) continued to be crystalline in spite of receiving high dose.

### 1.10.3.5. Leaching studies

Thomas et al. [110] systematically studied the dissolution of the thorium phosphate diphosphate (TPD) as a function of several parameters such as surface, leaching flow, temperature, acidity/basicity of the leachate and phosphate concentration and obtained activation energy equal to about  $42 \pm 3 \text{ kJ}\cdot\text{mol}^{-1}$  for the normalized leaching rate with the temperature. Robisson et al. [111] have also studied several leaching tests on  $\text{Th}_{4-x}\text{M}_x(\text{PO}_4)_4\text{P}_2\text{O}_7$  ( $\text{M} = \text{U}, \text{Pu}$ ) solid solutions and found normalized leaching rates to be low.

For  $\beta$ -TPD and  $\beta$ -TAnPD solid solutions at room temperature, dissolution rates varied from  $1.2 \times 10^{-9} \text{ g}\cdot\text{cm}^{-2}\cdot\text{day}^{-1}$  at pH 1 to  $4.8 \times 10^{-12} \text{ g}\cdot\text{cm}^{-2}\cdot\text{day}^{-1}$  at pH 4. The  $^{239}\text{Pu}$  doped  $\beta$ -TPD dissolved with the same rate compared to the other samples which validates the high resistance of these materials to radiation damages.

### 1.11. Scope of the present work

The reported literature studies revealed the structural stability, high chemical durability during leaching and radiation resistance properties of phosphate-based crystalline ceramics. Nevertheless, the selection of matrix for incorporation of HLW requires a refined understanding of the long-term behavior of waste form under repository relevant conditions which includes insight into the structural energetic of the matrix and prediction of stability of the waste form over very long-time scales on the basis of reliable thermodynamic and kinetic database of the waste matrix. Despite of broad interest in the phosphate-based ceramic materials, there is very little information exists about their thermodynamic stabilities. Especially, systematic studies on the structure, thermodynamic properties and leaching studies have not been reported for the phosphate-based crystalline matrices relevant for the HLW immobilization. Thus, the aim of this study is to determine these properties and make a comprehensive thermodynamic database of synthetic monazites,  $\text{REPO}_4$  ( $\text{RE} = \text{La}, \text{Nd}, \text{Sm}$  and  $\text{Gd}$ ), monazite-cheralite solid solutions,  $(\text{La}_{1-x}\text{M}_{x/2}\text{Th}_{x/2})\text{PO}_4$  ( $0 \leq x \leq 1$ ) ( $M = \text{Ca}, \text{Sr}$  and  $\text{Ba}$ ) and thorium phosphate-diphosphate (TPD),  $\text{Th}_4(\text{PO}_4)_4\text{P}_2\text{O}_7$ .

The standard molar enthalpy of formation of rhabdophane phases viz.  $\text{LaPO}_4\cdot 0.8\text{H}_2\text{O}$ ,  $\text{NdPO}_4\cdot 0.75\text{H}_2\text{O}$ ,  $\text{SmPO}_4\cdot 0.65\text{H}_2\text{O}$ ,  $\text{GdPO}_4\cdot 0.55\text{H}_2\text{O}$  and synthetic monazite phases viz.  $\text{LaPO}_4$ ,  $\text{SmPO}_4$ ,  $\text{NdPO}_4$ ,  $\text{GdPO}_4$  revealed the energetic trends in rhabdophane and monazite phases. The molar enthalpy of formation with respect to the constituent oxides according to the reaction:  $0.5\cdot\text{RE}_2\text{O}_3 + 0.5\cdot\text{P}_2\text{O}_5 = \text{REPO}_4$ , have been plotted against ionic radii of nine

coordinated  $RE^{3+}$  ( $RE = La, Sm, Nd$  and  $Gd$ ) ions. The plot was compared and the results showed that with increase in ionic radii of  $RE^{3+}$  ion from  $Gd^{3+}$  to  $La^{3+}$  ion, the values of enthalpy of formation becomes more negative i.e.  $LaPO_4$  is the most thermodynamically stable orthophosphate compound and it can be used a suitable host matrix for the immobilization of long-lived radionuclides.

Based on the results of thermodynamic stability of rare earth orthophosphates, synthetic monazite i.e.  $LaPO_4$  was selected as the host matrix for the immobilization of actinides. Immobilization of tetravalent actinide i.e. Th, was coupled with divalent cations i.e.  $Ca^{2+}$ ,  $Sr^{2+}$  and  $Ba^{2+}$  to maintain the charge neutrality. Various compositions of charge-coupled substituted monazite-cheralite solid solutions viz.  $(La_{1-x}Ca_{x/2}Th_{x/2})PO_4$  ( $0 \leq x \leq 1$ ),  $(La_{1-x}Sr_{x/2}Th_{x/2})PO_4$  ( $0 \leq x \leq 1$ ),  $(La_{1-x}Ba_{x/2}Th_{x/2})PO_4$  ( $0 \leq x \leq 1$ ) were prepared and characterized using different techniques. The results revealed that charge-coupled monazite-cheralite system forms regular solid solutions in the entire composition range for  $(La_{1-x}Ca_{x/2}Th_{x/2})PO_4$  ( $0 \leq x \leq 1$ ) and  $(La_{1-x}Sr_{x/2}Th_{x/2})PO_4$  ( $0 \leq x \leq 1$ ) solid solutions. On the other hand the solubility limit for  $(La_{1-x}Ba_{x/2}Th_{x/2})PO_4$  ( $0 \leq x \leq 1$ ) solid solution is found to be up to  $x = 0.3$ , beyond this a thorium rich phase separates out. The standard molar enthalpy of formation data for these samples indicate that there is negative deviation from ideal solid solution behavior with a minima at  $x = 0.25$  for  $(La_{1-x}Ca_{x/2}Th_{x/2})PO_4$  ( $0 \leq x \leq 1$ ),  $x = 0.3$  for  $(La_{1-x}Sr_{x/2}Th_{x/2})PO_4$  ( $0 \leq x \leq 1$ ) and  $x = 0.2$  for  $(La_{1-x}Ba_{x/2}Th_{x/2})PO_4$  ( $0 \leq x \leq 1$ ). The results suggest that the substitution of charge couple  $M^{2+}$  ( $M = Ca, Sr$  and  $Ba$ ) and  $Th^{4+}$  at lattice site of  $La^{3+}$ , results in formation of thermodynamically stable intermediate phases. Further it is also observed that the substituted  $(La_{1-x}M_{x/2}Th_{x/2})PO_4$  ( $0 \leq x \leq 1$ ) ( $M = Ca, Sr$  and  $Ba$ ) systems are isentropic in nature and stabilized mainly by enthalpy. The present work contributes towards the understanding of the thermodynamic stability of systematically substituted synthetic monazite  $LaPO_4$  which results in charge-coupled substituted monazite-cheralite solid solutions.

The present work also contributes towards the chemical durability studies of selected compositions of charge-coupled substituted monazite-cheralite solid solutions  $(\text{La}_{1-x}\text{M}_{x/2}\text{Th}_{x/2})\text{PO}_4$  ( $0 \leq x \leq 1$ ) ( $M = \text{Ca}, \text{Sr}$  and  $\text{Ba}$ ), employing standard Product Consistency Test (PCT) approved by the American Society of Testing Materials (ASTM). The normalized leach rate values were determined using ICP-AES technique for the leached ions and the results revealed the behavior of these ions in the off normal conditions. The chemical durability data was in agreement with the experimentally measured thermodynamic data in the present work.

The present study provided important thermodynamic database for thorium phosphate-diphosphate (TPD) compound relevant for the immobilization of tetravalent actinides. The enthalpy of formation for all the important phases viz. thorium phosphate-hydrogenphosphate hydrate,  $\text{Th}_2(\text{PO}_4)_2(\text{HPO}_4) \cdot \text{H}_2\text{O}$  (TPHPH), thorium phosphate-hydrogen phosphate,  $\text{Th}_2(\text{PO}_4)_2(\text{HPO}_4)$  (TPHP);  $\alpha$ -thorium phosphate-diphosphate,  $\alpha\text{-Th}_4(\text{PO}_4)_4\text{P}_2\text{O}_7$  ( $\alpha$ -TPD) and  $\beta$ -thorium phosphate-diphosphate,  $\beta\text{-Th}_4(\text{PO}_4)_4\text{P}_2\text{O}_7$  ( $\beta$ -TPD) have been measured. Further, Gibbs phase diagram and predominant area diagrams for Th-P-O system have been computed using the thermodynamic properties of the various phases present in Th-P, P-O and  $\text{ThO}_2\text{-P}_2\text{O}_5$  systems.  $E_{\text{H}}\text{-pH}$  diagram of Th-P- $\text{H}_2\text{O}$  system has been computed to determine the stability region of TPD phase in groundwater.

The objectives of the study identified above are addressed in separate sections within this thesis. Each section contains a separate introduction relating to the specific objective is provided and appropriate conclusions are drawn at its end. The overall conclusions are then brought together at the end of the thesis under conclusion and future directions.

Finally, the main conclusions arising from this work as well as research prospective are discussed and future direction of study evolved from this work has been suggested.

# ***CHAPTER-2***

---

## ***EXPERIMENTAL TECHNIQUES AND INSTRUMENTATION***

## 2.1. INTRODUCTION

Present chapter elaborates details of different experimental techniques used in the thesis. It includes synthesis of compounds and solid solutions by solution and solid-state methods, their characterization by Chemical analysis, thermal techniques, X-ray diffraction (XRD) and spectroscopic technique. Inductively coupled plasma atomic emission spectrometer (ICP-AES) was employed for determination of stoichiometry as well as impurity analysis of samples. Thermogravimetry analysis (TGA) and Differential thermal analysis (DTA) was employed for the determination of water of crystallization of the hydrated precursors, thermal stability and crystallographic phase transition of the compounds. Structural characterization was carried out using X-ray diffraction and FT-IR spectroscopy. Heat capacity of samples was measured using Differential Scanning Calorimeter (DSC). Standard enthalpy of formation of the samples was measured using room temperature isoperibol solution calorimeter and high temperature oxide melt solution calorimetry. The thermodynamic functions for the samples were calculated using the measured heat capacity and standard molar enthalpy of formation data. Leaching studies in aqueous medium at elevated temperature were carried out to determine the chemical stability of the samples. A brief description of the working principle and experimental details of each technique is described in this chapter.

## 2.2. MATERIAL SYNTHESIS

Both solution and solid-state synthesis routes were used to prepare phosphate-based compounds and their solid solutions. Synthetic monazite,  $\text{REPO}_4$  (RE = La, Nd, Sm and Gd) and thorium phosphate diphosphate (TPD),  $\text{Th}_4(\text{PO}_4)_4\text{P}_2\text{O}_7$  were precipitated from their respective metal solutions by adding ammonium dihydrogen phosphate as a phosphating agent at room temperature. Charge coupled substituted monazite solid solutions,  $(\text{La}_{1-x}\text{M}_{x/2}\text{Th}_{x/2})\text{PO}_4$

( $0 \leq x \leq 1$ ) ( $M = \text{Ca, Sr and Ba}$ ) were prepared using solid-state synthesis method. Details of each synthesis procedure are described below.

### **2.2.1. Solution chemistry method**

In this method, aqueous metal nitrate solutions of required concentration were mixed with appropriate amounts of phosphating agent [112] at room temperature at pH = 5.4. This resulted in a quantitative precipitation of metal phosphates/diphosphates, which were then filtered and washed in distilled water to remove occluded nitrate, phosphate and metal ions. The precipitates were dried under Infra-red (IR) lamp, ground and vacuum heated to remove adsorbed water.

### **2.2.2. Solid state method**

In this method, metal carbonates/metal oxides, thorium oxides and ammonium dihydrogen phosphates were thoroughly mixed by mortar and pestle to form homogeneous mixture [112]. The homogeneous mixtures were compacted, pelletized and heated in a controlled manner at different temperature in static air atmosphere for long period. Substituted monazite solid solutions were successfully prepared following the aforesaid procedure. Details of the synthesis procedure for various phosphates/diphosphates and phosphate-based solid solutions are described in their respective chapters.

## **2.3. CHARACTERIZATION TECHNIQUES**

Synthetic monazite  $\text{REPO}_4$  ( $\text{RE} = \text{La, Nd, Sm and Gd}$ ), monazite-cheralite solid solutions ( $\text{La}_{1-x}\text{M}_{x/2}\text{Th}_{x/2}\text{PO}_4$  ( $0 \leq x \leq 1$ ) ( $M = \text{Ca, Sr and Ba}$ ) and thorium phosphate-diphosphates  $\text{Th}_4(\text{PO}_4)_4\text{P}_2\text{O}_7$  samples prepared using co-precipitation and solid-state routes were

characterized by Inductively Coupled Plasma-Atomic Emission Spectroscopy (ICP-AES), Thermogravimetric analysis (TGA), Powder X-ray Diffraction (XRD) and Fourier transform infrared (FT-IR) spectroscopic techniques. The heat capacity of the characterized samples was measured employing a Differential Scanning Calorimeter (DSC) as a function of temperature. The standard molar enthalpy of formation of the samples was determined employing a room temperature isoperibol solution calorimeter and a high temperature oxide melt solution calorimeter. The leaching studies of the samples were performed using an ASTM-Product Consistency Test (PCT) method. The working principle of different techniques used in the present work are described and discussed below.

### **2.3.1. Inductively coupled plasma-atomic emission spectroscopy (ICP-AES)**

ICP-AES technique is used for elemental analysis of the phosphate/diphosphate sample(s) prepared in the present work. This technique has multi-element capability, high specificity and good detection limit. A plasma torch is used to dissociate the sample into its constituent atoms or ions and excite them to a higher energy level. While returning to their ground state the excited atoms or ions emit photons of a characteristic wavelength of the element present and recorded by an optical spectrometer. Using the calibration standards, a quantitative chemical analysis of the sample of interest can be achieved.

The main components of ICP-AES are:

- (i) sample introduction,
- (ii) plasma, and
- (iii) spectrometer and detector.

**Sample introduction:** A solid sample is first dissolved by acid digestion with HF/HNO<sub>3</sub>/HCl in a PTFE closed vessel and subsequent treatment with HClO<sub>4</sub>. The solution is converted into an aerosol by a nebulizer. The smallest droplets (1-10 μm) are separated and transferred into

the argon plasma inside a spray chamber whereas the bigger droplets (> 90%) are pumped to waste.

**Plasma:** Strong atomic emission from all chemical elements is produced by achieving high temperature. Temperature in the range of 7,000 – 10,000 K is obtained employing an inert-gas plasma. When the aerosol droplets enter into the plasma region, the droplets are transformed into salt particles by desolvation. These salt particles are divided into separate molecules and subsequently to atoms and ions which then excited to higher energy levels. When these excited atoms and ions come back to their ground energy state they will produce electromagnetic radiation in the ultra-violet/visible range of the spectrum.

**Spectrometer and Detector:** A spectrometer consists of a multi-component part containing mirrors and prisms. It is used to separate the specific wavelengths of interest. Since the emission lines from the excited atoms and ions are very narrow lines, a high-resolution detector is essential. A CCD detector is commonly used for detection, which provides high resolution and simultaneous detection of the elements. In the present work, ICP-AES analyses were carried out using high Ultima 2, Horiba Jobin-Yvon, France. A schematic of ICP-AES equipment is given in **Fig. 2.1**.

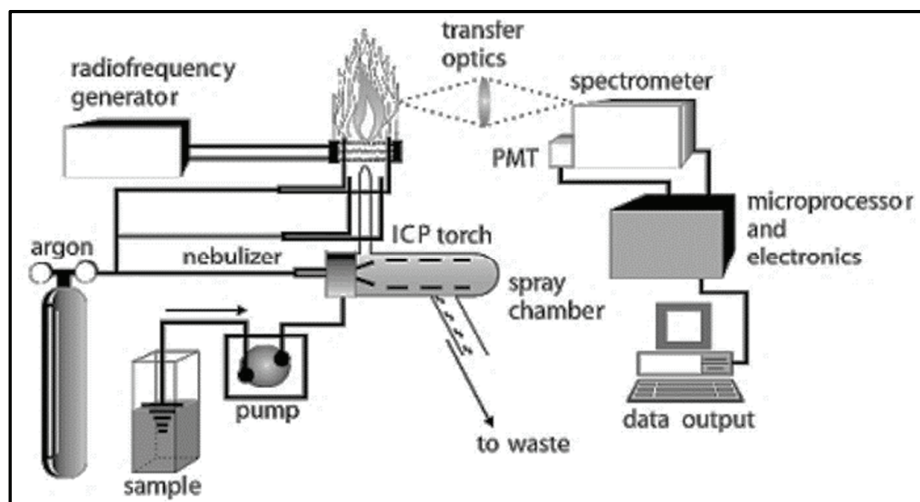


**Fig. 2.1:** Schematic of a typical ICP-AES equipment.

### 2.3.2. Powder X-ray Diffraction (XRD)

X-ray diffraction (XRD) is the most comprehensively used technique to characterize the crystalline phases and to determine the crystal structure of materials. This technique is mostly used for fingerprint characterization of crystalline samples, in addition determination of their unit cell parameters, phase and crystal structure.

According to German physicist Max von Laue, the wavelength of X-ray is comparable to the spacing between adjacent atoms in crystal lattice of the material and suggested that a crystal could be used as a diffraction grating in three dimensions. X-rays are electromagnetic radiation with energies in the range of 100 eV-100 keV. For diffraction, short wavelength X-rays (i.e. hard X- rays) in the range of a few angstroms to 0.1 angstrom (i.e. 1 keV - 120 keV) are used. The energetic X-rays penetrate into the material and produce information about their bulk structure, structural arrangement of atoms and molecules in a wide range of materials.

The theory of diffraction is based on Bragg's law. It describes how an electromagnetic wave of wavelength ( $\lambda$ ) interfere with a regular crystal lattice. At a certain angle of incidence ' $\theta$ ' (known as Bragg's angle) with respect to set of parallel crystal planes, constructive interference takes place according to the relation:

$$n\lambda = 2d_{hkl} \cdot \sin\theta \quad (2.1)$$

where,  $n$  is a positive integer,  $d_{hkl}$  is the inter planer spacing between the parallel crystal planes causing constructive interference and  $\lambda$  is the wavelength of the incident X-ray beam.

#### 2.3.2.1 Generation of X-rays and experimental method

In XRD technique, X-rays are generated using a cathode ray tube by heating a filament to emit electrons, accelerating the emitted electrons by applying a voltage and bombarding the accelerated electrons upon a target material viz. Cu, Mo, Cr, Fe. The energetic electrons with

sufficient energy to knock out inner shell electrons of the target material, produce the characteristic X-ray spectra. The typical X-ray spectrum of Cu element is given in **Fig. 2.2**.

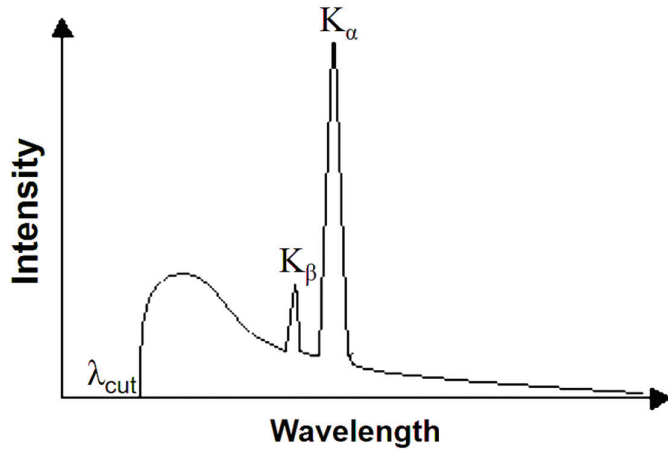


**Fig. 2.2:** Typical X-ray of Cu target.

Though the X-rays are produced in all the directions, it is allowed to escape only through a beryllium window. X-rays beam is then passed through the divergence slits and allowed to fall on the sample material. When conditions of Bragg's law satisfy, the interaction of the incident rays and the sample produces constructive interference and diffracted X-rays. The diffracted X-rays are scanned by sweeping the detector (gas filled tube or scintillation counter) from one angle to another. All the possible diffraction directions of the lattice can be achieved by scanning the sample through a range of  $2\theta$  angles due to the random orientation of the powdered sample.

The conversion of the diffraction peaks into d-spacing permits identification of the sample material by comparison of d-spacing with the standard reference patterns as each material has a unique set of d-spacing. The schematic of a powder X-ray diffractometer is shown in **Fig. 2.3**. The peaks (also called as reflections) in a typical X-ray diffraction plot correspond to a set of parallel planes having inter-planar spacing  $d_{hkl}$  which is calculated from the position of the peaks.

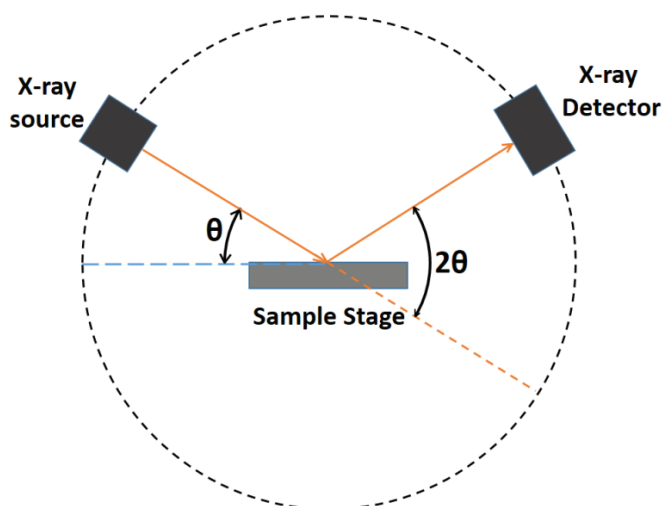


**Fig. 2.3:** Schematic of powder X-ray diffractometer.

Thus, for a particular sample a set of  $d$ -values giving constructive interference is observed. The peak positions ( $d$  values) are related with the unit cell parameters of the lattice. Thus, can provide a vital tool to identify the materials and they commonly act as the finger print for the crystalline materials.

In general, a short time scan in the two-theta ( $2\theta$ ) range of  $10$  to  $80^\circ$  is sufficient for the identification of a crystalline inorganic material. Whereas samples with low symmetry and having weak X-ray scattering power need a slow scan. After the diffraction experiment, observed  $d$ -values were fitted to standard patterns and the unit cell parameters were refined with respect to the standard data. By comparing the observed diffraction pattern with JCPDS (Joint Committee on Powder Diffraction Standards) files available for reported crystalline samples, fingerprinting of sample materials is normally done. The unit cell parameters are made free to adjusting the best way to fit the observed experimental data.

In the present work, the synthesized compounds are characterized using a Stoe theta–theta X-ray diffractometer using monochromatic  $\text{Cu K}\alpha$  radiation ( $\lambda = 1.5418 \text{ \AA}$ ) and graphite monochromator with  $\text{NaI(Tl)}$  detector. The powder sample was ground using mortar and pestle with 1-2 drops of 10 % collodin-amyl acetate mixture and spread on a glass slide for room

temperature identification of phase. The sample were scanned in the range  $10^{\circ}$  to  $80^{\circ}$  with an interval of  $0.02^{\circ}$  and counting time of 2s. The recorded 'd' values are used for indexing.

### **2.3.3. Fourier transform-infrared (FT-IR) spectroscopy**

FT-IR method is based on Michelson interferometer consisting of a movable mirror, fixed mirror and a beam splitter [113]. The interferometer shifts the phase of one of the beams with respect to other by moving one of the mirrors and keeping the other mirror at fixed position. Due to overlapping of two beams, constructive and destructive interference takes place. The intensity of the interference pattern will rise and fall periodically if the light source is monochromatic and the detector will measure a sinusoidal signal as a function of the optical path difference. Radiation emitted from a Globar IR source contains many frequencies, the intensity measured,  $I(x)$ , as function of optical path difference,  $(x)$  is called as the interferogram. Fourier transformation of such interferogram results in the frequency spectrum,  $I(\nu)$ . The optical path difference  $(x)$ , can be accurately obtained from the interference patterns generated from the interferometer using a laser source, whose frequency is accurately known.

In the present study, experiments were carried out from  $500$  to  $4000\text{ cm}^{-1}$  using a diamond ATR, employing IR Affinity-1 FT-IR spectrophotometer, Shimadzu. IR radiation was generated from a Globar source (bonded silicon carbide rod). The instrument uses CsI single-crystal, as beam splitter and deuterated triglycine sulphate (DTGS) as the detector. A He-Ne laser having a wavelength of  $632.9\text{ nm}$  (max. power of  $25\mu\text{W}$ ) has been used for the calibration purpose. Prior to spectroscopic experiment, all samples were ground thoroughly using dry KBr powder and a thin pellet of made in the form of and introduced into the sample chamber for recording the IR spectra.

### **Attenuated Total Reflection (ATR)**

In attenuated total reflection, the changes that occur in a totally internally reflected IR beam

when the beam comes in contact with a sample is measured. An IR beam is focused onto an optically dense crystal which have a high refractive index at a certain angle. The sample under investigation is kept in good contact with the crystal surface. The internal reflectance produces an evanescent wave as shown in the **Fig. 2.4**.

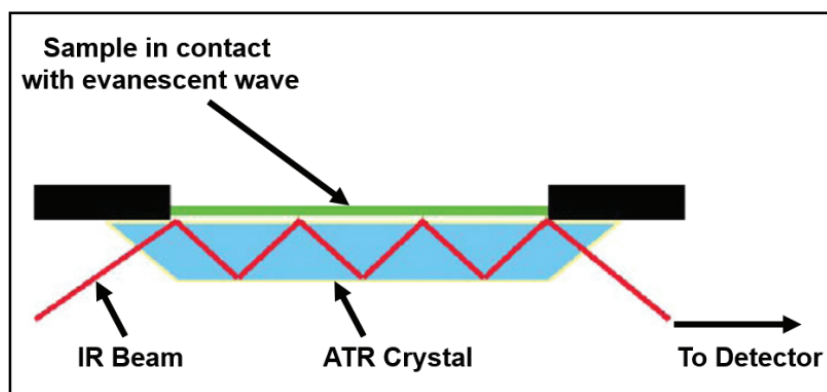


**Fig. 2.4:** Schematic of an ATR-FT-IR set up.

The evanescent wave can be assumed as a bubble of IR that is placed on the surface of the crystal and the wave extends only a few microns ( $0.5\text{-}5\ \mu$ ) beyond the surface of crystal and into the sample. Thus, it can probe the surface and few microns into the sample. The evanescent wave will be attenuated or altered where the sample absorbs energy in regions of the IR spectrum. The attenuated energy is then passed back to the IR beam which then come out from the opposite end of the crystal and passed to the IR detector which in turn records the IR spectrum.

Following two requirements should be satisfied for this technique to be successful:

- 1) Sample must be in direct contact with ATR crystal
- 2) Refractive index of ATR crystal must be considerably greater than that of the sample otherwise internal reflection will not occur. The transmission of light occurs instead of internal reflection. The refractive index of an ATR crystal has a typically value between 2.38 and 4.01 at  $2000\ \text{cm}^{-1}$ .

The excellent mechanical properties of 'diamond' make it an ideal material for ATR, particularly when studying very hard solids, but its higher cost limits its use. Germanium, KRS-5 and zinc selenide are some typical materials for ATR crystals. The shape of the crystal is determined by the nature of the sample and the type of spectrometer. With dispersive spectrometers, the crystal is a rectangular slab with chamfered edges. Other geometries use prisms, half-spheres, or thin sheets.

#### **2.3.4. Scanning Electron Microscopy (SEM)**

Scanning electron microscope consists of five main components, viz. turbo molecular high vacuum system, electron gun, beam shaping column, scanning system and detector. A schematic of SEM microscope is given in **Fig. 2.5**. A tungsten filament is used to produce the electrons. The electrons are accelerated towards the specimen employing high negative potential to the filament. The electrons are then collimated by passing through a magnetic field using electromagnetic lenses. Finally, the well-focused incident electron beam is used to scan the sample. The possible interactions of energetic electron beam with the sample are shown in **Fig. 2.6**.

#### **Backscattered-electron (BSE) imaging**

Backscattered electrons are originated from the elastic collisions of electrons with atoms, which results in a change in the electrons' trajectory. The number of the backscattered electrons reaching the detector is proportional to the atomic number ( $Z$ ). This dependence of the number of BSE on the atomic number helps us differentiate between different phases, providing images that hold information about the composition of sample. Moreover, BSE images can also provide valuable information on crystallography, topography and the magnetic field of the sample.

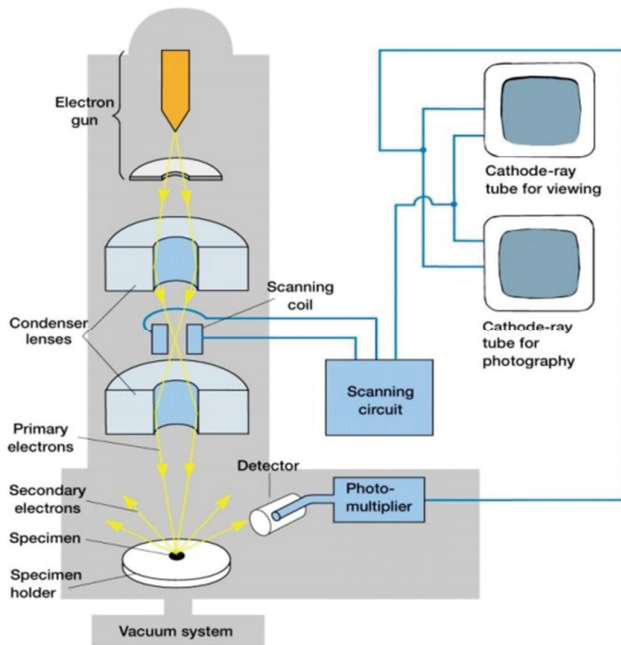


Fig. 2.5: Schematic representation of SEM microscope.

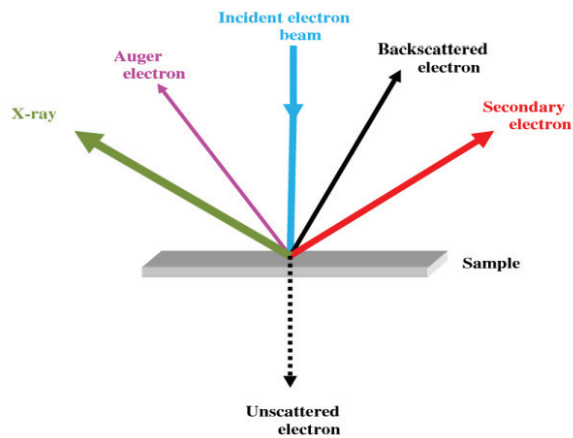


Fig. 2.6: Interaction of electron beam with the sample.

Solid state detectors are the common BSE detectors which typically contain p-n junctions. The working principle is based on the production of electron-hole pairs by the backscattered electrons which escape the sample and absorbed by the detector. The number of these pairs produced depends on the energy of the backscattered electrons. Backscattered electron detectors are located above the sample in a "doughnut" type arrangement, concentric with the

electron beam in order to maximize the solid angle of collection and consist of symmetrically divided parts [114]. Topographical information of the sample can be obtained by enabling only specific quadrant of the detector. Alternatively, when all parts are enabled, the contrast of the image represents the atomic number ( $Z$ ) of the element.

### **2.3.5. Thermal analysis**

Thermal analysis methods are essential for understanding the compositional and enthalpy (heat) changes involved during a reaction. The methods are useful for investigating phase changes, decomposition, and loss of water or oxygen and for constructing phase diagrams.

#### **2.3.5.1. Thermogravimetric Analysis (TGA)**

In TGA, the weight of a sample is measured as a function of time as the temperature is increased at a controlled uniform rate [115]. In this technique the heating can be done under air (oxidative) or nitrogen/argon (inert) atmosphere. Loss of water of crystallization or volatile substances (such as  $O_2$ ,  $CO_2$ ,  $NH_3$  etc.) is revealed by a weight loss in a thermogram. Whereas oxidation or adsorption of a gas shows up as a weight gain of the sample.

#### **2.3.5.2. Differential Thermal Analysis (DTA)**

In DTA technique, a sample and an inert reference material ( $\alpha-Al_2O_3$ ) are kept in two different crucibles and heated simultaneously at a controlled uniform rate inside a furnace. The temperature difference ( $\Delta T$ ) between sample and reference material is recorded as a function of time or temperature ( $T$ ). A phase change phenomenon is generally associated with either absorption or evolution of heat. Any reaction involving heat change in the sample material will be characterized as a peak in the plot of  $\Delta T$  vs  $T$ . An increase in temperature indicates an exothermic reaction whereas a decrease in temperature shows an endothermic reaction and their corresponding peak appear in opposite directions.

## 2.4. THERMODYNAMIC MEASUREMENTS TECHNIQUES

### 2.4.1. Differential Scanning Calorimeter (DSC)

It is a heat flow calorimeter and a widely used calorimeter for determination of heat capacity of materials [116-119]. In this technique the heat flow rate to the sample is measured against time or temperature. Sample and reference materials are maintained at nearly the same temperature throughout the measurements and the change in the amount of heat required to raise the temperature of the sample and reference are measured. DSC can be used to measure various properties viz. heat capacity, melting temperature, glass transition temperature, crystallization, phase transition, magnetic transition. DSC can be categorized into two types viz. heat flux DSC and power compensation DSC.

#### 2.4.1.1. Heat flux DSC

In heat flux DSC, the temperature difference between the sample and the reference which is proportional to heat flow rate is measured. A typical design of a heat flux DSC with disc type measuring system is shown in **Fig. 2.7**.

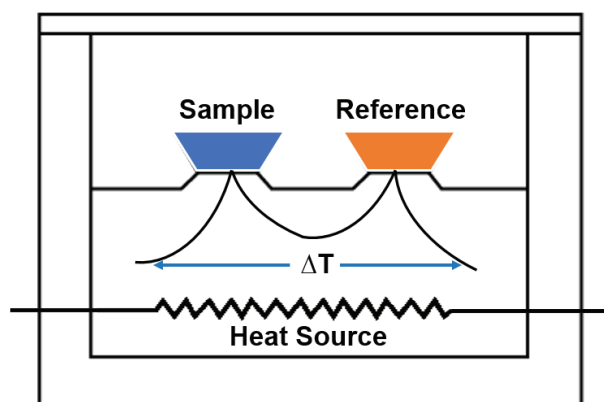


**Fig. 2.7:** Heat flux DSC.

The sample and reference pans are similar with respect to their weight and material. The sample and reference crucibles are situated symmetrically to the center of the calorimeter and the heat

flow rate from the furnace to the sample and reference would be equal and the differential signal,  $\Delta T$  would be zero. Thermal events in the sample of interest result in a differential signal, proportional to the difference between the heat flow rates to the sample and the reference.

### 2.4.1.2. Power compensation DSC

In power compensation DSC, the temperature difference between the sample and reference is maintained to zero by increasing or decreasing the compensating electric energy using micro heaters [116, 120]. The compensating electrical energy supplied to the sample or reference is the measuring signal. A typical power compensation DSC is given in **Fig. 2.8**.

It consists of two identical micro furnaces with a Pt-resistance temperature sensor and a heating resistor. Both micro furnaces are thermally decoupled from each other and are placed in a silver block of constant temperature. The same heating power is supplied to both micro furnaces with a preset heating programme.

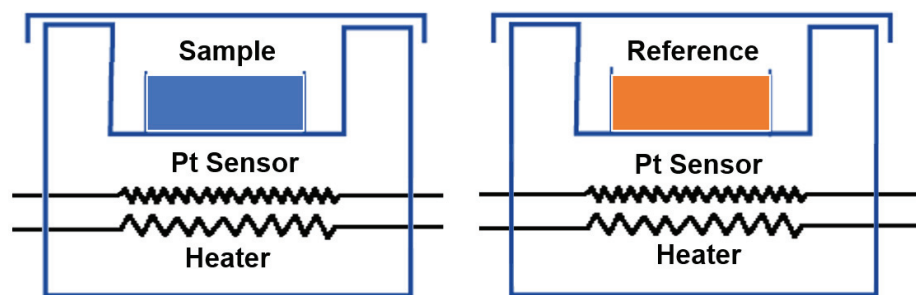


**Fig. 2.8:** Power compensation DSC.

A temperature difference between the micro furnaces arises during a thermal event which is the measurement signal as well as the input signal to a feedback circuit. The feedback circuit compensates the reaction heat flow rate by proportional control through increasing or decreasing the additional heating power. The compensating heating power is proportional to the  $\Delta T$ . The time integral over the compensating heating power is proportional to the heat released or consumed in the sample.

### 2.4.1.3. Calibration of DSC

As DSC is not an absolute heat and temperature measuring device, the relative data obtained must be correlated to absolute values by calibration [121, 122]. In DSC measurements, mostly, two types of calibrations are important:

1. *Temperature calibration*
2. *Caloric calibration or heat flow calibration*

#### 2.4.1.3.1. Temperature Calibration

DSC does not record the true temperature due to the thermal resistance of the DSC disc, crucibles and the gas atmosphere. Hence, temperature calibration is necessary prior to the actual experiment. Temperature calibration stands for unambiguous assignment of the temperature indicated by the DSC instrument to the true temperature.

Temperature calibration is done by determining melting points of high purity metals [123]. DSC measurements are dynamic whereas thermodynamically defined transition temperature is always the equilibrium temperature. Thus, calibration results must be extrapolated to equilibrium conditions to ensure a temperature calibration, which is independent of the heating rate used. This is achieved by measuring the melting point of reference materials as a function of heating rate and extrapolated to zero heating rate.

#### **Characteristic of material used for temperature calibration [119]:**

- Should represent fixed points of International Temperature Scale 1990 (ITS-90),
- Should have a transition point explicitly defined from the point of view of thermodynamics,
- Should not have quantifiable influence of the grain size on the transition temperature,
- Should not be hygroscopic,

- Should have a high rate of transition,
- Should be available in suitably high purity,
- Should not react with the crucible material or purge gas,
- Should be stable over a long period of time,
- Should display no measurable overheating,
- Should not undergo secondary reaction with gas and crucible.

For temperature calibration, the following procedure was followed:

Selection of minimum three calibration materials covering the desired temperature range as uniformly as possible. Three calibration substances are required to detect possible non-linear temperature dependence. The transition is to be measured with each calibration material at least for three different heating rates in the range of interest.

The extrapolated peak onset temperature ( $T_e$ ) for melting or transition peak is determined. If there is no significant difference between  $T_e$  obtained at identical heating rate, then extrapolation of  $T_e$  to zero heating rate is determined  $T_e(\beta = 0)$ .

The difference  $\Delta T_{corr} = T_e(\beta = 0) - T_{fix}$  (or  $T_{lit}$ ) is calculated for each sample with all different heating rates.

The calculated temperature correction terms  $\Delta T_{corr}$  are finally plotted as a function of  $T_e(\beta = 0)$

The true temperature is given as:  $T_{true} = T_e(\beta = 0) + \Delta T_{corr}$

The correct temperature is determined as:  $T_{true} = T_e(\beta \rightarrow 0) + \Delta T_{corr}(\beta = 0)$ .

#### 2.4.1.3.2. Caloric Calibration

The measurement signal equivalent to temperature difference,  $\Delta T$ , is obtained as electrical voltage signal. A calibration factor ( $K$ ) is assigned to the measured heat flow rate,  $\Phi_m$  [124].

The calibration factor,  $K$ , is determined by measuring the steady-state heat flow rate into a sample of well-known heat capacity  $C$  with a constant heating rate  $\beta = dT/dt$ .

$$C \cdot \beta = \phi_{\text{true}} = K \cdot \phi_m \quad (2.2)$$

A known heat  $Q_{\text{true}}$  dissipated or consumed during phase transformation route is compared with the area of the resulting peak. Then the calibration factor is found out from the following relation:

$$Q_{\text{true}} = K \cdot \int_{t_1}^{t_2} [\phi_m - \phi_{bl}] dt \quad (2.3)$$

Where,  $\phi_{bl}$  signifies the heat flow rate corresponding to the baseline. The calibration factor  $K$  depends on temperature, uncertainties arising due to shape of the baseline and systematic uncertainties due to shape of the DSC curve.

Hence the following procedures are generally followed to escape such problems.

- 1) Selection of calibration substance which covers the preferred temperature range and whose thermophysical properties are similar to those of the sample
- 2) Heat effect of calibration standard and sample should match by taking required amount of standard.
- 3) Determining calibration constants at different heating rates and measurement of the repeatability of the errors of calibration factor

For accurate calibration five standards are chosen. Let  $m_i$  be the mass of a standard 'i' and  $Q_i$  (J/g) be the heat involved during a transition of this standard sample. If  $A_i$  be the area of the transition peak (in  $\mu\text{V}\cdot\text{s}$ ), then the calibration factor  $K_i$  is given by:

$$K_i (\mu\text{V}/\text{W}) = \frac{A_i}{Q_i} \cdot \frac{1}{m_i} \quad (2.4)$$

The unit of  $K_i$  is  $\mu\text{V}/\text{mW}$  and a functional relationship is determined by following polynomial expression:

$$K = a_0 + a_1T + a_2T^2 + a_3T^3 + \dots \quad (2.5)$$

This calibration factor is used to convert the DSC signal into heat flow rates.

#### 2.4.1.4. Heat capacity measurement using DSC

The “Classical” three step method is used to measure the heat capacity of the samples as a function of temperature by DSC.

##### *The “Classical” Three-Step Method*

The method involves following three different steps:

(1) *blank run*, (2) *calibration run* and (3) *sample run*.

**Blank run:** In this step, the heat flow rate of the zero-line ( $\Phi_0$ ) is measured. This is done by measuring the heat flow rate as a function of temperature by means of two identical empty crucibles with equal weight and similar material in the sample and reference sides.

**Calibration run:** A calibration substance or reference material of well-known heat capacity ( $C_{p,\text{ref}}$ ) is loaded into the sample crucible, whereas the reference side crucible is empty. Using the identical experimental conditions as for the blank run, the heat flow rate is measured. The heat capacity of the reference material is calculated using the following expression:

$$C_{p,\text{ref}} \cdot m_{\text{ref}} \cdot \beta = K \cdot \Phi(T) \cdot (\Phi_{\text{ref}} - \Phi_0) \quad (2.6)$$

**Sample run:** The sample of interest is placed in sample crucible. Under the identical conditions as in other runs, the heat flow rate of the sample material is calculated using the following expression:

$$C_{\text{sample}} \cdot m_{\text{sample}} \cdot \beta = K \cdot \Phi(T) \cdot \{\Phi_{\text{sample}} - \Phi_0\} \quad (2.7)$$

Now, using a simple comparison of the heat flow rates into the sample and into the calibration substance, the specific heat capacity of the sample is calculated as shown in **Fig. 2.9**. The following equation is used for the calculation of specific heat capacity of the sample. Here, calibration factor  $K \cdot \Phi(T)$ , need not be known:

$$\frac{C_{p,\text{sample}}}{C_{p,\text{ref.}}} = \frac{\{\Phi_{\text{sample}} - \Phi_0\}}{\{\Phi_{\text{ref.}} - \Phi_0\}} \cdot \frac{m_{\text{ref.}}}{m_{\text{sample}}} \quad (2.8)$$

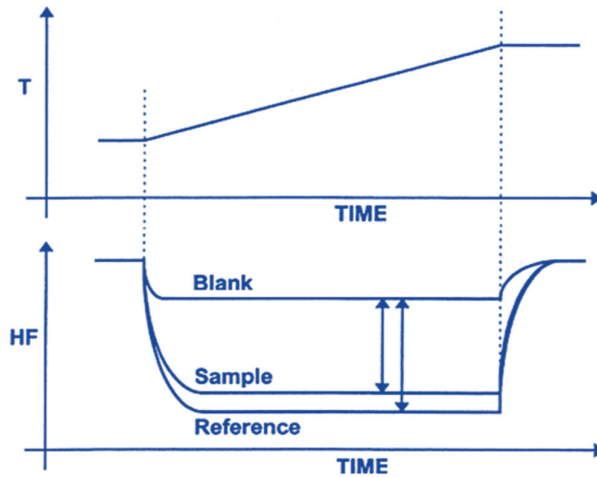


**Fig. 2.9:** The “classical” three-step method.

A typical three segment heating programme is used in each run. The first segment is an isothermal segment at the initial temperature; the second segment is a dynamic segment with a predefined heating rate and the final segment is another isothermal segment at the final temperature of interest. At isothermal segments, heat flow rate from furnace to the sample is zero whereas the moment dynamic heating segment starts, an exponential endothermic effect is noticed owing to the flow of heat from the furnace to the sample and is proportional to the heat capacity of the sample taken. During the dynamic segment, slope of the line signifies the

variation of the heat capacity of the sample with temperature. Commonly, aluminium sample pans are used for the sample and reference and are hermetically sealed with a pin hole on the lid to ensure that the measurements are carried out under constant pressure condition.

For heat capacity measurements, the samples are generally taken in the form of a flat disc similar to the standard material due to the following reasons:

- a) To simulate the geometry of the calibration material and
- b) To get a good thermal contact between the pan and the sample
- c) To eliminate any possible errors due to temperature gradient within the sample

A heat flux type differential scanning calorimeter, of M/s. Mettler Toledo GmbH (model number DSC821e/700), Switzerland was used in the present study. The heat capacities of all the samples in the present study in the temperature range 298-800 K were measured using this instrument. Temperature calibration of the calorimeter was carried out prior to the sample experiment using the phase transition temperature of NIST reference materials (Indium:  $T_{\text{fus}} = 429.748$  K; Tin:  $T_{\text{fus}} = 505.09$  K; Lead:  $T_{\text{fus}} = 600.62$  K; Zinc:  $T_{\text{fus}} = 692.71$  K; Gold:  $T_{\text{fus}} = 1337.33$  K). Heat calibration of the calorimeter was carried out by using the transition heats of the above reference materials. For the determination of heat capacity, NIST synthetic sapphire (SRM 720) in the powdered form was used as the reference sample material. Heat capacities of all the samples were measured by the Classical three-step method in the continuous heating mode.

### **2.4.2. Calorimetric techniques**

Calorimetry is the method used to measure the heat or enthalpy changes associated with a physical process or a chemical reaction. This heat change can be used to determine the thermochemical properties of compounds. Calorimetry can be classified into two groups viz.

(i) reaction calorimetry and (ii) non-reaction calorimetry. In reaction calorimetry, heat change as a result of chemical reaction is measured whereas in non-reaction calorimetry, heat change owing to a physical change is measured. Calorimetric measurements can be carried out under constant pressure and constant volume conditions. While the heat measured under constant pressure gives the change in the enthalpy of the system, heat measured under constant volume gives the change in the internal energy of the system.

Calorimeter has three main variables viz. the temperature of the calorimeter ( $T_c$ ), the temperature of its surroundings ( $T_s$ ), and the heat change ( $Q$ ). Based on these variables, there are four different types of calorimeters, which are described below:

**(a) Isothermal calorimeter** in which  $T_c = T_s = \text{constant}$ . The heat change,  $Q$ , is measured by measuring change in the physical property of some other material acting as surrounding to the system being investigated e.g. ice calorimeter and diphenyl ether calorimeter [125].

**(b) Adiabatic calorimeter** in which  $T_c = T_s$ , but  $T_c$  and  $T_s$  vary. Physical or chemical changes of the system change the temperature of calorimeter. In order to maintain  $T_c = T_s$ , a measured quantity of heat is supplied either to the system or to the calorimetric block around the system acting as surrounding. The compensated heat is the measure of heat change of the system under investigation.

**(c) Heat flow calorimeter** in which instead of measuring  $T_c$ , the heat flow between the system and the surrounding due to temperature difference between them is measured. Initially  $T_c$  and  $T_s$  same.  $T_s$  is kept constant but  $T_c$  varies because of the heat change in the calorimeter. In this calorimeter there is a deliberate heat exchange between the system and the surrounding, which is channelized through a thermopile. Thermopile develops a voltage difference due to

this heat flow and the electrical signal due to this voltage difference is a measure of the heat changes occurring in the system. A specific example of the heat flow calorimeter is the Calvet calorimeter used in this study [126].

**(d) Isoperibol calorimeter** in which the surrounding is maintained at a constant temperature, and the change in temperature of the system is monitored [127]. Heat exchange between the system and the surrounding is prevented by thermally insulating the system. The temperature variation of the system reflects the heat changes taking place in the system.

In the present work, an isoperibol and a heat flow calorimeter were used to measure the heat of reaction and deduce their standard enthalpies of formation.

#### 2.4.2.1. Isoperibol solution calorimeter

The enthalpy of reaction was measured using a TA Instruments Precision Solution Calorimeter Model-2225 (isoperibol calorimeter) and TAM III thermostat (**Fig. 2.10**).

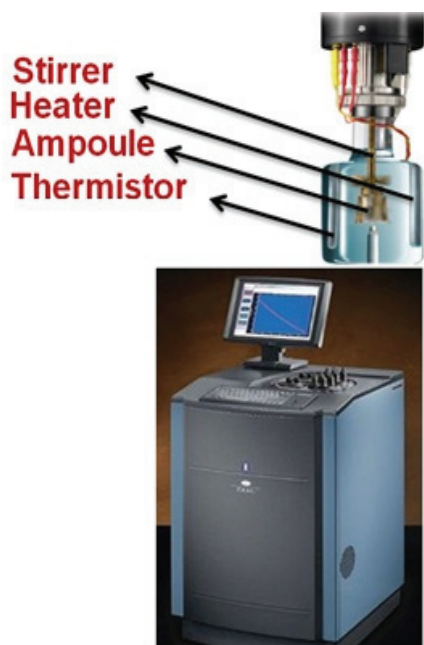


**Fig. 2.10:** Isoperibol solution calorimeter (TA Instruments Precision Solution Calorimeter) with description of Pyrex-glass reaction vessel.

The outer part of the calorimeter was a stainless-steel cylinder mounted in a TAM-III bath, which consists of an oil bath with high temperature stability of  $\pm 1 \mu\text{K}$ . The actual calorimeter involved a thin-walled 25 ml Pyrex-glass reaction vessel containing the solvent, fitted with a thermister for measuring temperature and a heater for calibration and equilibration. The resistance of thermister was measured using a Wheatstone bridge assembly, located in the cylindrical backbone. The calorimetric reaction vessel was attached to the cylindrical backbone which also contained motor for stirrer, which could hold the ampoule containing the sample (solute). The smallest heat exchange with the environment during the reaction and the heat arising from stirring were mathematically adjusted using the information obtained from the baseline temperature changes before and after the chemical reaction. The calorimeter was provided with a SolCal software program for experimental data acquisition, graphical data presentation and data analysis. The temperature offset from the calorimetric bath was measured as a function of time by SolCal program.

### ***Electrical calibration:***

The heat energy for electrical calibration during the experiment was supplied to the reaction vessel with the help of heater. A known precision resistance ( $20 \Omega$ ) was mounted in series with the heater. By measuring the voltage across this precision resistance, the actual value of current passing through the heater could be determined. The actual current and the voltage were multiplied to give the electrical power that was dissipated as heat inside the calorimetric vessel.

### ***Chemical calibration:***

The solution calorimeter was chemically calibrated by measuring the enthalpy of dilution of  $\text{KCl(s)}$ . For each experiment the water equivalent of the calorimeter was determined. The water equivalent of the calorimeter was obtained by dividing the heat input to the calorimeter by the corrected temperature change ( $C = Q/\Delta T$ ). The quantity of heat was determined by passing

known amount of current for a fixed period through the electrical heater submerged in the solution. The temperature rise of the calorimeter was measured by the thermister and system was calibrated electrically before and after each reaction. The average value of the water equivalent was used for the calculations of enthalpy of reaction.

### 2.4.2.2. Calvet oxide melt solution calorimeter

Calvet calorimeter (SETARAM, Model HT-1000) based on the heat flow principle is used to measure the enthalpy of dissolution. The Calvet calorimeter is an isothermal calorimeter with massive blocks of alumina to maintain constant temperature. A schematic layout of the Calvet calorimeter is shown in **Fig. 2.11**.

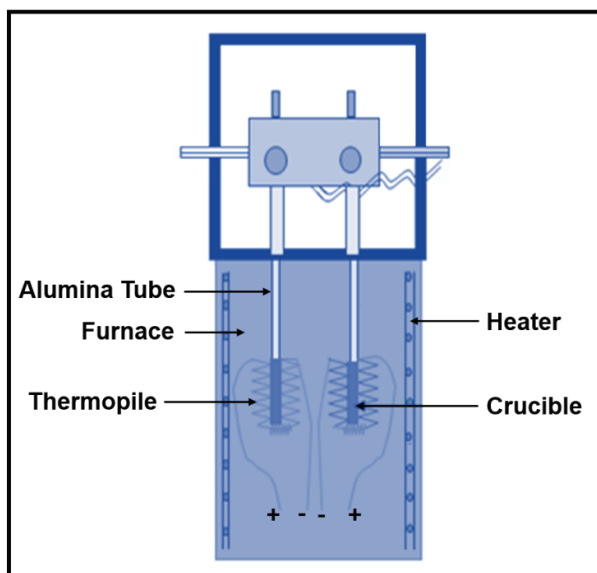


**Fig. 2.11:** Schematic of Calvet solution calorimeter.

It consists of two identical cylindrical holes enclosed by identical Pt/Pt–Rh thermopiles capable of detecting heat change. Two identical alumina tubes with one-end-close are placed in these holes. The top ends of these alumina cells are connected to thermostatic dropping mechanism where the samples are maintained at 298 K, using a water bath. The Pt/(Pt + 10% Rh) thermopiles are connected in opposition to give a null signal when both cells are at the same

temperature. However, as soon as heat is absorbed or released in one of the calorimetric cells by dropping a sample, a net emf will generate. If the heat effect is of short duration, this emf will rise quite fast and then decay exponentially to a near zero value in a period ranging from 20 to 40 minutes depending on the temperature and heat changes involved in the system.

The total area between the emf–time curve and the zero baselines are proportional to the total heat effect associated with the process in the calorimeter. The electrical signal in nanovolt range is amplified by a nanovolt amplifier, to read it on micro or millivoltmeter. Since these amplified signals represent the instantaneous amount of thermal energy absorbed or evolved due to reaction in one of the cells, the total energy over a given period of time can be determined by integrating the signals over that time period.

The precision and accuracy of the temperature measurement of the calorimeter was tested by determining the phase transition temperatures of NIST reference materials [128, 129] (Indium:  $T_{\text{fus}} = 429.748$  K; Tin:  $T_{\text{fus}} = 505.09$  K; Lead:  $T_{\text{fus}} = 600.62$  K; Aluminium:  $T_{\text{fus}} = 660.1$  K). The accuracy of calorimeter obtained by using enthalpy increment values of high purity molybdenum (99.997 wt.%) and NBS standard synthetic sapphire (SRM-720) was better than  $\pm 2\%$ . The sensitivity factor of calorimeter can be determined by carrying out the caloric calibration. Synthetic sapphire (SRM 720) was used as a standard reference material. In order to calibrate the calorimeter, drop experiments using the single crystal rod of alpha alumina were carried out at all individual experimental temperatures at which samples were investigated. Alumina was dropped from the reference temperature (298 K) to the isothermal zone of the calorimeter.

#### **2.4.2.2.1. Preparation of molten PbO + B<sub>2</sub>O<sub>3</sub> (2:1 molar ratio) solvent**

The solvent was prepared by heating 2:1 molar mixture of perfectly dried Pb(NO<sub>3</sub>)<sub>2</sub> (BDH, reagent grade) and boric acid (BDH, reagent grade) in an ALLOY-690 container at 933 K.

$\text{Pb}(\text{NO}_3)_2$  and boric acid decomposed to produce  $\text{PbO}$  and  $\text{B}_2\text{O}_3$ , forming a eutectic mixture. The melt was kept at 933 K for 3 h for homogenization. The entire mass was removed from the ALLOY-690 container and grinded again to make uniform powder. The solvent powder was characterized by chemical analysis and XRD techniques. The atom percent of Pb, B and O obtained from the chemical analysis of the solvent were found to be  $22.21 \pm 0.04$ ,  $22.23 \pm 0.05$  and  $55.54 \pm 0.08$ , respectively. No other chemical impurity was observed from elemental analysis of the solvent mixture. Powder ( $\text{PbO} + \text{B}_2\text{O}_3$ , 2:1 molar ratio) from the same lot was used as solvent in all reaction enthalpy measurements.

#### **2.4.2.2.2. Enthalpy of dissolution measurements**

10 g of  $\text{PbO} + \text{B}_2\text{O}_3$  solvent was taken in each of the two identical platinum tubes which act as a protective lining and having outer diameter matching exactly with the alumina reaction tube for proper thermal contact. The reaction cell assembly was slowly lowered into the calorimeter and it was programmed up to 1089 K at a heating rate of  $0.5 \text{ K}\cdot\text{min}^{-1}$  and maintained at  $1089 \pm 0.05 \text{ K}$  during each drop experiment. The reaction tubes were equilibrated inside the chamber for 12 h to attain a steady base line for heat flux signal. The slope of the base line of the differential heat flow signal was nearly zero since the heat effects due to any small loss of the volatile components are same in the sample and reference cells and thus, they were nullified. Small pellets containing few milligrams of the reactants were dropped from room temperature to the reaction cell containing liquid solvent maintained at 1089 K and the corresponding enthalpy change was determined by integrating the heat flow signal with respect to time. The time required for the completion of the reaction was determined by recording the heat flow signal ( $\text{J}\cdot\text{g}^{-1}$ ) for different time interval. The reaction time was concluded when a steady base line was achieved and the reaction enthalpy obtained as a function of time converged into a constant value. For each dissolution experiment the reaction time was determined and the heat

flow signals recorded for the same time period for all experiments. Similarly, for each experiment fresh solvent was used so that the similar dilution condition was maintained. The amount of the reactant dropped into solvent was chosen in such a manner that the concentration of La,  $M$  ( $M = \text{Ca, Sr and Ba}$ ) and Th remained well below 1 atom percent. The infinite dilution condition prevailing during the dissolution process was established by repeating the dissolution experiments on a same lot of the solvent. The consistency in the values of the heat of reaction per unit mass of the reactants was indicated the maintenance of infinite dilution condition during the experimental measurements.

## 2.5. Computational Studies

### 2.5.1. Rietveld refinement of X-ray diffraction data

Rietveld refinement is a method used to refine the crystal structure which is a powerful method for extracting comprehensive crystal structural information from X-ray. Rietveld method is now extensively used in all branches of science that deal with materials at the atomic level. For various compounds, it is not possible to grow single crystals that are sufficiently good for their structure determination. In such cases, it is possible to refine the structure using powder data, provided a sufficiently good starting structural model can be devised.

In a powder pattern, the information contained in the spatial distribution of the reflections is missing. Only the single dimension of scattering angle remains and thereby makes it difficult or sometimes even impossible to index the data. The Rietveld refinement is a sophisticated solution to this problem since the refinement is made against the entire profile. It is thus necessary to measure the entire profile accurately. The profile must be taken in small steps of the scattering angle and considering all reflections which contribute to each step.

In late 1960s, Rietveld proposed a least-square method to analyze more complex diffraction patterns, obtained from low-symmetry materials using a curve-fitting procedure.

The least-squares refinement minimizes the difference between the observed and calculated profiles, rather than individual reflections. In the first instance, this procedure was carried out with constant wavelength neutrons, rather than X-rays, with a simpler shape of the Bragg reflection profiles. The problem of the more complex peak shape was fixed by employing alternative peak-shape functions, such as Lorentzian and pseudo-Voigt. The quality of a Rietveld refinement is assessed by the calculation of an “R-factor”.

Some often-used numerical criteria of fit for Rietveld refinement are given by Young [130] which are as follows:

$$R_F = \frac{\sum |I_K^{1/2}(i(o)) - I_K^{1/2}(i(c))|}{\sum I_K^{1/2}(i(o))} \quad (\text{R-structure factor}) \quad (2.9)$$

$$R_B = \frac{\sum |I_K(i(o)) - I_K(i(c))|}{\sum I_K(i(o))} \quad (\text{R-Bragg factor}) \quad (2.10)$$

$$R_P = \frac{\sum |y_{i(o)} - y_{i(c)}|}{\sum y_{i(o)}} \quad (\text{R-pattern}) \quad (2.11)$$

$$R_{wp} = \sqrt{\frac{\sum w_i |y_{i(o)} - y_{i(c)}|^2}{\sum w_i |y_{i(o)}|^2}} \quad (\text{R-weighted pattern}) \quad (2.12)$$

The ‘goodness of fit’ indicator is given as:

$$\chi = R_{wp}/R_e = R_{wp}/\left[(N-P)/\sum w_i y_{i(o)}\right]^{1/2} \quad (2.13)$$

where, the weight,  $w_i$ , is  $1/\sigma^2[y_{i(o)}]$ ;  $N$  is the number of parameters being refined;  $P$  is

the number of observations.

The quantity minimized is the sum of the squares of weighted differences between the measured and calculated values for each measured point on the profile that is used for least-squares refinement. In this thesis, the observed X-ray powder diffraction patterns were refined

using Rietveld method with the help of Fullprof-2k software program [131].

### 2.5.2. Thermodynamic relations

A knowledge of the heat capacity of a material as a function of temperature is the basis for determination of thermodynamic quantities like enthalpy increment  $\{H_m^o(T) - H_m^o(298 \text{ K})\}$ ,

entropy  $\{S_m^o(T) - S_m^o(0 \text{ K})\}$ , Gibbs energy functions  $-\left\{\frac{G_m^o(T) - H_m^o(298.15 \text{ K})}{T}\right\}$ . These quantities

help in construction of thermodynamic tables. The  $\{H_m^o(T) - H_m^o(298.15 \text{ K})\}$  and

$\{S_m^o(T) - S_m^o(0 \text{ K})\}$  functions are calculated by numerical integration of the  $C_p^o(T)$  and

$C_p^o(T)/T$  functions, respectively. These functions are constructed using polynomial fit of the

$C_p^o(T)$  curve in small temperature ranges. The Gibbs energy function

$-\left\{\frac{G_m^o(T) - H_m^o(298.15 \text{ K})}{T}\right\}$  is calculated using the relation:

$$-\left(\frac{G_m^o(T) - H_m^o(298.15)}{T}\right) = S_m^o(T) - \frac{(H_m^o(T) - H_m^o(298.15))}{T} \quad (2.14)$$

$$\text{Where; } H_m^o(T) - H_m^o(298.15) = \int_{298.15}^T (C_{p,m}^o) dT \quad (2.15)$$

$$\text{and } S_m^o(T) = S_m^o(298.15) + \int_{298.15}^T \left(\frac{C_{p,m}^o(T)}{T}\right) dT \quad (2.16)$$

In order to make full use of the thermodynamic data,  $G_m^o(T)$  should be evaluated which requires a known value of  $H_m^o(0 \text{ K})$ . However, absolute value of  $H_m^o(0 \text{ K})$  is difficult to determine or calculate. Therefore, first  $H_m^o(T)$  is calculated using the relation:

$$H_m^{\circ}(T) = \Delta_f H_{298.15\text{K}}^{\circ} + \int_{298.15}^T C_{p,m}^{\circ}(T) dT \quad (2.17)$$

The absolute value of  $S_m^{\circ}(T)$  is calculated using the  $S_m^{\circ}(0\text{ K}) = 0$  and the relation (2.16). Now  $G_m^{\circ}(T)$  can be calculated using the relation:

$$G_m^{\circ}(T) = H_m^{\circ}(T) - T \cdot S_m^{\circ}(T) \quad (2.18)$$

After calculation of all the thermodynamic functions, the values are tabulated at selected temperatures. The thermodynamic functions which are usually tabulated in tables are:  $C_{p,m}^{\circ}(T)$ ,  $S_m^{\circ}(T)$ ,  $H_m^{\circ}(T)$ ,  $G_m^{\circ}(T)$ ,  $H_m^{\circ}(T) - H_m^{\circ}(298.15\text{ K})$ ,  $\Phi_m^{\circ}(T)$ ,  $\Delta H_{f,m}^{\circ}(T)$  and  $\Delta G_{f,m}^{\circ}(T)$ .

A knowledge of the heat capacity of a material as a function of temperature is the basis for determination of any thermodynamic quantity which helps in construction of thermodynamic tables.

### 2.5.3. Computation of Phase diagram

The phase equilibria and the underlying thermodynamics is crucial for the understanding of materials and their transformations under various conditions. For materials development, phase diagrams are frequently described as roadmaps. The graphical representation of more than two or three components by experiment is challenging and thereby limiting their usefulness. Furthermore, phase diagrams of multi-component (four/more components) systems, are only partially known. However, computational thermodynamics methods are helpful to fill these gaps.

Although the general idea of calculating phase equilibria from the thermodynamics is more than a century old [132], it took almost 50 years, before it was applied to the calculation of a real system. In 1970, Kaufman and Bernstein [133], known as father of phase diagram, provided the foundation for what today is known as the CALPHAD (CALculation of PHase

Diagrams) method. It was observed that the development of thermodynamic database was essential along with computer program. The thermodynamic calculations of phase equilibria have been developed during 1970s and 1980s [134] recognizing CALPHAD method as a valuable tool for material development. Activities in Europe for the development of a common database eventually resulted in the formation of SGTE (Scientific Group Thermodata Europe) [135]. Dinsdale [136] compiled the reference data for the pure elements which are the foundation of today's multicomponent databases. It is the strength of the CALPHAD method which is currently the only method available for efficient calculations in multi-component, multi-phase systems needed for practical applications.

## Software and Databases

A variety of software packages are available for the calculation of phase diagrams. In the early days of CALPHAD, available software was dominated by free source codes, such as SOLGASMIX [137] or the Lukas programs [138]. First commercial software began to appear shortly thereafter. Today a number of fully integrated, commercial software packages are available, a few of the more well-known are:

*i)* MatCalc [139], *ii)* MTDATA [140], *iii)* Pandat [141], *iv)* JMatPro [142], *v)* Thermo-Calc [143] and *vi)* FactSage [144].

Some of these softwares integrate thermodynamic equilibrium calculations with the simulation of kinetic processes, but basic calculation of equilibrium is based on minimization of Gibbs energy is common to all. This study used FactSage software to compute various properties of phosphate-based matrix.

## FactSage software

FactSage began in 1976 as F\*A\*C\*T–Facility for the Analysis of Chemical Thermodynamics

and in 1984 the Centre for Research in Computational Thermochemistry (CRCT) was formed and during 1990s F\*A\*C\*T migrated to personal computers running in a Windows, as operating system. In 2001, there was a fusion between F\*A\*C\*T/FACT-Win and ChemSage (formerly SOLGASMIX) resulting present FactSages software. Since then FactSage has expanded into a fully integrated thermochemical software and database package that is being used in worldwide.

### **CALPHAD-type databases**

The FactSage software contains FACT Databases—FactPS, FToxid, FTsalt, FTmisc, FToxCN, FTfritz and FTnucl databases. The CALPHAD method has been used in FactSage software to obtain thermodynamic description of the phase through an optimization procedure, if the Gibbs energy functions for a phase are not known, but their experimental phase equilibrium data or thermodynamic properties exist. A consistent description of the phase diagram and the thermodynamic properties are used to predict reliably the set of stable phases and their thermodynamic properties. This method is based on a semi-empirical approach and sequential modelling from simpler to complicated systems. Therefore, reliable experimental thermodynamic and phase properties for unary and binary systems are necessary for reliable prediction and assessment of higher order systems. Generally, the thermodynamic properties of each phase are described with adjustable parameters in a mathematical model. The parameters are evaluated by fitting all the information to the model. The thermodynamic functions of solution phases are expressed as polynomials of chemical composition and temperature. The numerical values of coefficients of polynomials are obtained by optimization technique. Finally, thermochemical databases contain parameters giving the Gibbs energy,  $G$ , of all compounds/solutions as a function of  $T$ ,  $P$  and composition. This is a complete database because all the other thermodynamic properties ( $H$ ,  $C_p$ ,  $m$ , etc.) can be calculated by taking the

appropriate derivatives of G functions, for a given set of constraints such as temperature/ total pressure/ total mass of each element.

### **Methodology of calculations of phase diagram**

The Gibbs energy data of phases viz. REPO<sub>4</sub> (RE = La, Nd, Sm and Gd), (La<sub>1-x</sub>M<sub>x/2</sub>Th<sub>x/2</sub>)PO<sub>4</sub> ( $0 \leq x \leq 1$ ) ( $M = \text{Ca, Sr and Ba}$ ) and Th<sub>4</sub>(PO<sub>4</sub>)<sub>2</sub>P<sub>2</sub>O<sub>7</sub> (TPD) are not reported in the literature and their database can be created by:

- Establishing a mathematical model for  $G(T, P, \text{Composition})$  for each phase.
- Optimizing model parameters using all available thermodynamic and phase equilibrium data such as activities, solubilities, vapour pressures, heat capacity, enthalpy of formation and chemical potentials of co-existing phase ect. from the literature/ measured experimentally.
- Estimating properties of multi-component systems (ternaries, quaternaries,..) from the generated database.

Finally, FactSage software calculates the equilibrium conditions by minimizing the total Gibbs energy of the system. This is mathematically equivalent to solving all the equilibrium constant equations simultaneously. Data are automatically extracted as required from the inbuilt and created database. The phase diagram and plots of a wide variety of axes of Th-P-O system (explained in Chapter 6) has been calculated using FactSage 7.2 software.

### **2.6. Chemical durability studies**

Chemical leaching is one of the important properties which used to determine durability and long-term stability of the glasses and ceramic materials. Several experimental test conditions

have been proposed to determine the chemical durability and broadly they can be categorized in two groups, viz. static and dynamic. Under static methods, ASTM - standard product consistency test (PCT) is most commonly used.

### **Leach resistance test**

In present study, the Product Consistency Test (PCT) as per the procedure described in ASTM-C1285-02, was followed to measure the chemical durability of the ceramic matrix. In this method, the sample is crushed and sieved to standard -100 to +200 mesh ASTM [145]. Powders were washed and ultrasonicated three times in Ultra-High Quality (UHQ) water and acetone to remove adhered fines. The powder was subsequently dried overnight. Particle surface area was determined geometrically, based upon the measured density and assuming spherical particle shape. A known quantity of powdered sample (~ 1 g) was placed into Teflon lined stainless steel 304 L vessels with 10 ml of UHQ water was added and sealed as shown in **Fig. 2.12**.



**Fig. 2.12:** Teflon-lined stainless-steel container used in leaching study.

Triplicate sample vessels and duplicate blanks containing UHQ only were placed in a 363 K ( $\pm 1$  K) oven and removed after 7 days. The clear leachate obtained after centrifugation was used for measurement of pH as well as the concentrations of the leached elements using ICP-AES technique.

From the measured concentration of the element, the normalized elemental leach rate ( $NR_i$ ) was determined as  $\text{g}\cdot\text{cm}^{-2}\cdot\text{d}^{-1}$  using the following equation:

$$NR_i = \frac{C_i}{f_i \times (SA/V) \times t} \quad (2.19)$$

where  $C_i$  = the concentration of  $i^{\text{th}}$  element in the leachate ( $\mu\text{g}/\text{cm}^3$ ),  $f_i$  = the mass fraction of the  $i^{\text{th}}$  element in sample (unit less) calculated from batch composition as taken,  $SA$  = the calculated surface area of the sample considering their spherical geometry ( $\text{cm}^2$ ),  $V$  = the volume of leachant ( $\text{cm}^3$ ) and  $t$  = the duration of leaching (day).

# ***CHAPTER-3***

---

## ***THERMODYNAMIC INVESTIGATIONS OF RARE EARTH ORTHOPHOSPHATES REPO<sub>4</sub> (RE = La, Nd, Sm and Gd)***

### 3.1. INTRODUCTION

Monazite mineral (light rare earth orthophosphates, REPO<sub>4</sub>) present in nature shows high radiation stability and chemical durability. Materials based on monazite mineral have been proposed as potential host matrices for safe immobilization of long-lived radionuclides arising due to the reprocessing of spent nuclear fuel [146]. The prediction of the long-term durability and chemical reactivity of REPO<sub>4</sub> in the geological repository conditions require accurate determination of their thermodynamic parameters such as Gibbs energy data, which can be evaluated from their standard molar enthalpy of formation values. The present study contributes towards the important thermodynamic function of the phosphate-based compounds. The work also provides an additional support for the existing knowledge of long-term stability of the monazite waste matrices. Despite the wide interest, their thermodynamic data is limited and scattered in the literature [147-159]. The thermodynamic data need to be measured using different methods to select the true value. The solution calorimetry offers an effective methodology for the determination of standard molar enthalpies of formation for different crystalline materials. In the present work, an isoperibol solution calorimeter has been used to perform a systematic study on synthetic monazite phases viz. REPO<sub>4</sub> (RE = La, Nd, Sm and Gd) in order to determine their standard molar enthalpy of formation. Subsequently, a correlation between the measured enthalpy of formation and ionic radii of the rare earth elements was drawn. The thermodynamic stabilities of these orthophosphates were assessed for the development of a stable host matrix and discussed.

### 3.2. EXPERIMENTAL

#### 3.2.1. Material Synthesis

##### 3.2.1.1. Synthesis of rhabdophane phase, REPO<sub>4</sub>·nH<sub>2</sub>O(s) (RE = La, Nd, Sm and Gd)

Solution route was used for the preparation of hydrated rare earth orthophosphates (rhabdophane phase) using aqueous solutions of lanthanum (III) chloride, neodymium (III) chloride, samarium (III) chloride and gadolinium (III) chloride from M/s Sigma Aldrich, 99.99% purity and ammonium dihydrogen phosphate from M/s Alfa Aesar, 99.99% purity. Solutions of known concentration of these ( $\text{RECl}_3(\text{aq.})$ ) ( $\text{RE} = \text{La, Nd, Sm and Gd}$ ) and  $\text{NH}_4\text{H}_2\text{PO}_4(\text{aq.})$  were thoroughly mixed in 1:1 molar ratio at room temperature which resulted in precipitation of their respective rhabdophane phases,  $\text{REPO}_4 \cdot n\text{H}_2\text{O}$  ( $\text{RE} = \text{La, Nd, Sm and Gd}$ ), where  $n$  = water of hydration. The resulted precipitates were filtered, thoroughly washed with double distilled water, dried under Infra-red (IR) lamp and stored under inert atmosphere for further studies.

### **3.2.1.2. Synthesis of monazite phases, $\text{REPO}_4(\text{s})$ ( $\text{RE} = \text{La, Nd, Sm and Gd}$ )**

The rhabdophane phases,  $\text{REPO}_4 \cdot n\text{H}_2\text{O}$  ( $\text{RE} = \text{La, Nd, Sm and Gd}$ ) precipitated at room temperature were used as a precursor for the preparation of their corresponding anhydrous rare earth orthophosphates i.e. monazite phases,  $\text{REPO}_4$  ( $\text{RE} = \text{La, Nd, Sm and Gd}$ ). The precipitates were kept in a sintered alumina boat, placed inside a muffle furnace and heat treated in a controlled manner under air atmosphere. The temperature of furnace was raised to 673 K to remove the volatile species. The resultant powders were ground, calcined at 1073 K for 6 h and compacted into pellets by applying uniaxial pressure of 500 MPa using hardened steel die and plunger. The pellets so formed were then finally heated at 1473 K for 10 h in air atmosphere.

## **3.2.2. Characterization methods**

### **3.2.2.1. Thermogravimetric analysis (TGA)**

Thermogravimetric analysis (TGA) was carried out employing Netzsch STA 409 PC, NETZSCH-Geratebau GmbH, Germany instrument. The description of the TGA technique is

provided in Section 2.3.5 of Chapter 2. This technique was used to quantitatively ascertain the water of crystallization in precursor materials such as rare earth chlorides and ammonium dihydrogen phosphate prior to the synthesis of rhabdophane phases. The method is also used to determine the extent of hydration of the room temperature rhabdophane phases viz.  $REPO_4 \cdot nH_2O$  (RE = La, Nd, Sm and Gd). The thermograms obtained for all precursors and corresponding precipitated products were recorded at a heating rate of  $2 \text{ K} \cdot \text{min}^{-1}$  under  $20 \text{ ml} \cdot \text{min}^{-1}$  flow rate of argon gas.

### 3.2.2.2. X-ray diffraction (XRD)

The products were characterized using X-ray diffraction technique by recording room temperature diffraction data on Stoe, Germany, X-ray diffractometer with monochromatic  $CuK_{\alpha}$  radiation ( $\lambda = 1.5406 \text{ \AA}$ ) and a nickel filter. The XRD patterns were recorded in the  $2\theta$  range from  $10^\circ$  to  $80^\circ$  with a step width of  $0.02^\circ$ . For determination of the structural parameters, diffraction pattern was recorded in the  $2\theta$  range of  $10-100^\circ$  with step size of  $0.01^\circ$  with a counting time of 5 s at each step. The detailed description of the XRD technique is given in Section 2.3.2 of Chapter 2. The observed diffraction data was analyzed using Fullprof-2000 Rietveld refinement program [160] in which peak profile was fitted with Pseudo-Voigt profile function and U, V, W parameters were refined. The computational details are given in Section 2.5.1 of Chapter 2.

### 3.2.3. Solution calorimeter

The enthalpy of precipitation of rhabdophane phases were measured using isoperibol solution calorimeter at room temperature. The detailed description of the calorimeter is provided in Section 2.4.2 of Chapter 2. A known quantity (10-20 mg) of rare earths chloride as solute were taken inside an ampoule which was then placed inside a 25 ml reaction vessel containing 0.02

$\text{mol}\cdot\text{dm}^{-3}$   $\text{NH}_4\text{H}_2\text{PO}_4(\text{aq.})$  as a solvent. The whole assembly was then placed inside a solution calorimeter kept at 298 K. The temperature of the calorimeter was continuously recorded as a function of time. The molar ratio of solute to solvent present in calorimetric vessel was more than 1:2500 to ensure infinite dilution condition. The reaction was commenced by breaking the ampoule containing solute inside the reaction vessel. Using the thermistor secured inside the reaction vessel, an instantaneous change in temperature was measured which correspond to the enthalpy of reaction resulted due to the precipitation of rhabdophane phase of rare earth phosphates. The enthalpy of reaction was calibrated electrically before and after each precipitation reaction as shown in **Fig. 3.1**. The methodology was applied for all rhabdophane phases,  $\text{REPO}_4\cdot n\text{H}_2\text{O}$  ( $\text{RE} = \text{La}, \text{Nd}, \text{Sm}$  and  $\text{Gd}$ ) to determine their enthalpy of precipitation at room temperature. The measured enthalpy of precipitation was used for the calculation of standard molar enthalpy of formation of rhabdophane and monazite phases.

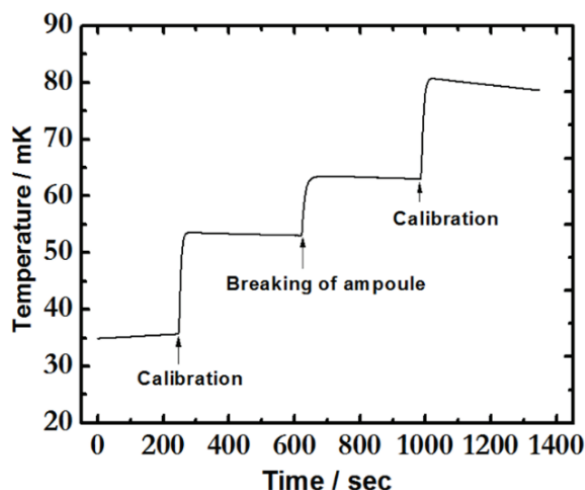


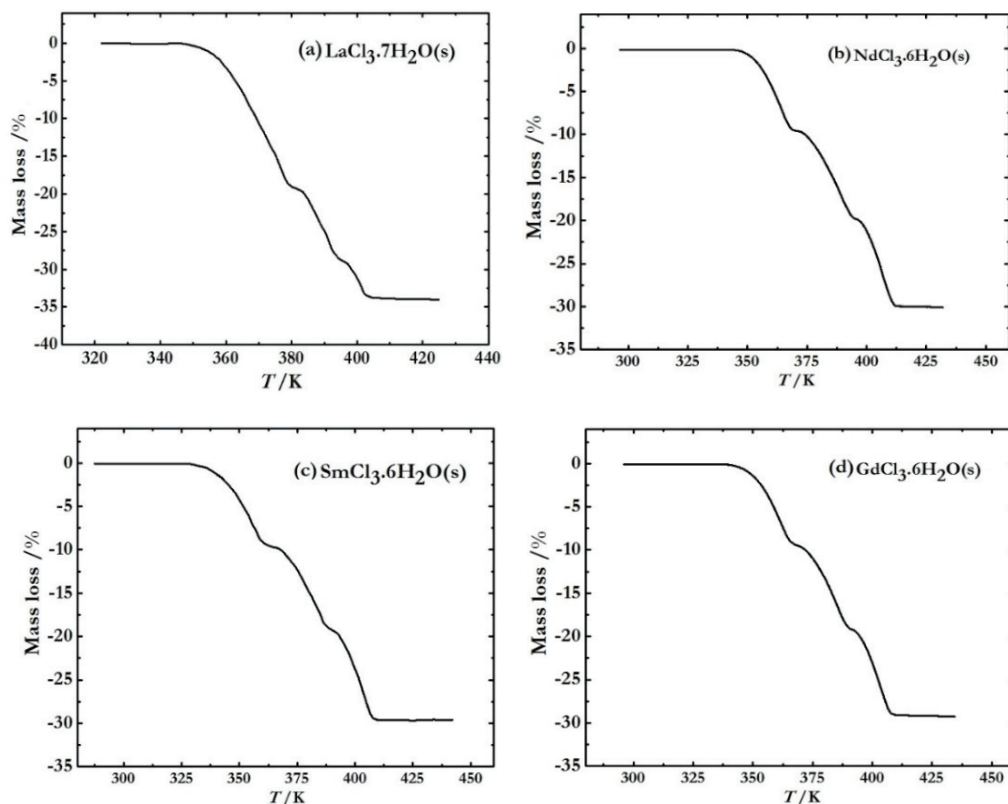
**Fig. 3.1:** Schematic plot of ampoule breaking inside reaction vessel.

### 3.3. RESULTS & DISCUSSIONS

#### 3.3.1. Thermogravimetry analysis (TGA)

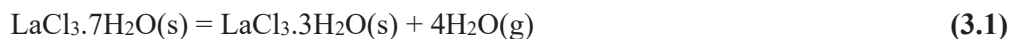
##### 3.3.1.1. Rare earth chlorides, $\text{RECl}_3\cdot n\text{H}_2\text{O}(\text{s})$ ( $\text{RE} = \text{La}, \text{Nd}, \text{Sm}$ and $\text{Gd}$ )

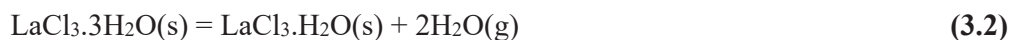
The observed thermograms of rare earth chlorides are given in **Fig. 3.2 (a-d)**. It could be observed that the hydrated rare earth chlorides decompose in three successive steps in the different temperature ranges with varying moles of water of crystallization.



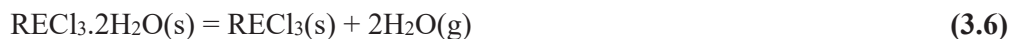
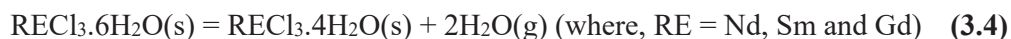
**Fig. 3.2:** Thermal dehydration of (a)  $\text{LaCl}_3 \cdot 7\text{H}_2\text{O}(\text{s})$ , (b)  $\text{NdCl}_3 \cdot 6\text{H}_2\text{O}(\text{s})$ , (c)  $\text{SmCl}_3 \cdot 6\text{H}_2\text{O}(\text{s})$  and (d)  $\text{GdCl}_3 \cdot 6\text{H}_2\text{O}(\text{s})$ .

**(a) Dehydration of  $\text{LaCl}_3 \cdot 7\text{H}_2\text{O}$ :** The dehydration takes place in three temperature intervals viz. 347-379 K, 382-394 and 396-407 K with 19.6 %, 9.9 % and 4.9 % mass loss respectively. The 19.6 % mass loss in the first step is attributed to loss of four water molecules. In the same way, 9.9 and 4.9 % mass loss observed in second and third steps correspond to the loss of two and one water molecules, respectively. The observed steps of dehydration of  $\text{LaCl}_3 \cdot 7\text{H}_2\text{O}$  can be written as:



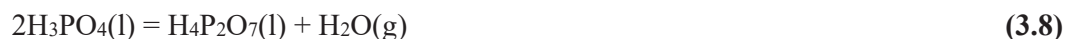


(b) **Dehydration of  $\text{NdCl}_3 \cdot 6\text{H}_2\text{O}$ ,  $\text{SmCl}_3 \cdot 6\text{H}_2\text{O}$  and  $\text{GdCl}_3 \cdot 6\text{H}_2\text{O}$ :** The observed dehydration of  $\text{NdCl}_3 \cdot 6\text{H}_2\text{O}$ ,  $\text{SmCl}_3 \cdot 6\text{H}_2\text{O}$  and  $\text{GdCl}_3 \cdot 6\text{H}_2\text{O}$  took place in nearly similar temperature range viz. 340-370 K, 372-395 K and 398-416 K. The mass loss corresponds to these temperature ranges are roughly 10 %. Each mass loss step is equivalent to two water molecules. The observed steps of dehydration of  $\text{NdCl}_3 \cdot 6\text{H}_2\text{O}$ ,  $\text{SmCl}_3 \cdot 6\text{H}_2\text{O}$  and  $\text{GdCl}_3 \cdot 6\text{H}_2\text{O}$  can be generally written as:



### 3.3.1.2. Ammonium dihydrogen phosphate (ADP), $\text{NH}_4\text{H}_2\text{PO}_4(\text{s})$

From **Fig. 3.3**, it is observed that no water of crystallization was present in ammonium dihydrogen phosphate (ADP) though a continuous mass loss starting from 473 K was noted. The continuous mass loss could be ascribed to the melting process and decomposition of ADP sample. The ADP sample decomposed to orthophosphoric acid,  $\text{H}_3\text{PO}_4$ , with evolution of ammonia gas.  $\text{H}_3\text{PO}_4$  transformed to pyrophosphoric acid,  $\text{H}_4\text{P}_2\text{O}_7$  with loss of a water molecule. The pyrophosphoric acid then converted to metaphosphoric acid,  $\text{HPO}_3$  followed by  $\text{P}_2\text{O}_5$ . The thermal decomposition of ADP can be represented according to the following reactions:





Thermogram also shows that mass is practically zero at 825 K which indicates that ADP sample totally decomposes into gaseous products at this temperature.

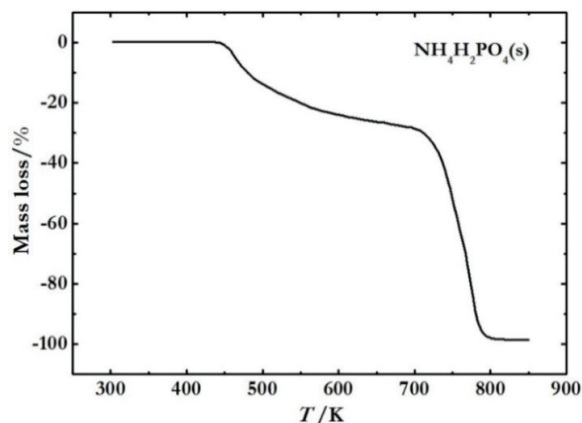


Fig. 3.3: Thermal decomposition of  $\text{NH}_4\text{H}_2\text{PO}_4(\text{s})$ .

### 3.3.1.3. Rhabdophane phase ( $\text{REPO}_4 \cdot n\text{H}_2\text{O}$ (RE = La, Nd, Sm and Gd))

The thermal decomposition of different rhabdophane products were carried out from room temperature to 823 K. The thermograms showed different degree of dehydration of rhabdophane products and the observed plots are given in Fig. 3.4.

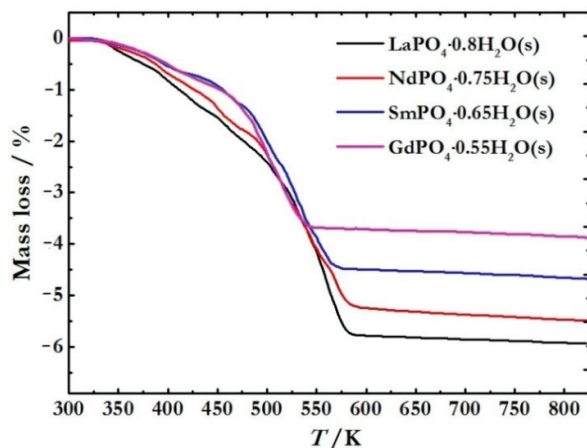


Fig. 3.4: Thermal decomposition of hydrated rhabdophane phases.

The plot shows that the water of crystallization in the rhabdophane phase varied from 0.8-0.55 viz.  $\text{LaPO}_4 \cdot 0.8\text{H}_2\text{O}(\text{s})$ ,  $\text{NdPO}_4 \cdot 0.75\text{H}_2\text{O}(\text{s})$ ,  $\text{SmPO}_4 \cdot 0.65\text{H}_2\text{O}(\text{s})$  and  $\text{GdPO}_4 \cdot 0.55\text{H}_2\text{O}(\text{s})$ . The water of hydrations measured in the present study are found in reasonable agreement with that of reported data [147, 161]. Shelyug et al. [147] carried out extensive studies on hydrated rare earths phosphates and their reported values were ranged from 0.804 (La) to 0.533 (Gd). Whereas values reported by Mesbah et al. [161] were varied from 0.6 to 1.0 mole of water.

### 3.3.2. X-ray diffraction (XRD)

XRD plots of the monazite phases are well matched with that reported pattern of  $\text{LaPO}_4(\text{s})$  (JCPDS file no: 83-651),  $\text{NdPO}_4(\text{s})$  (JCPDS file no: 83-654),  $\text{SmPO}_4(\text{s})$  (JCPDS file no: 83-655) and  $\text{GdPO}_4(\text{s})$  (JCPDS file no: 83-657) [162]. The results of the refined structural parameters using Rietveld analysis of a representative monazite phase i.e.  $\text{LaPO}_4$  which crystallizes in monoclinic lattice with  $P2_1/n$  space group. The Rietveld plot of  $\text{LaPO}_4$  is given in Fig. 3.5 and its refined structural parameters are provided in Table 3.1.

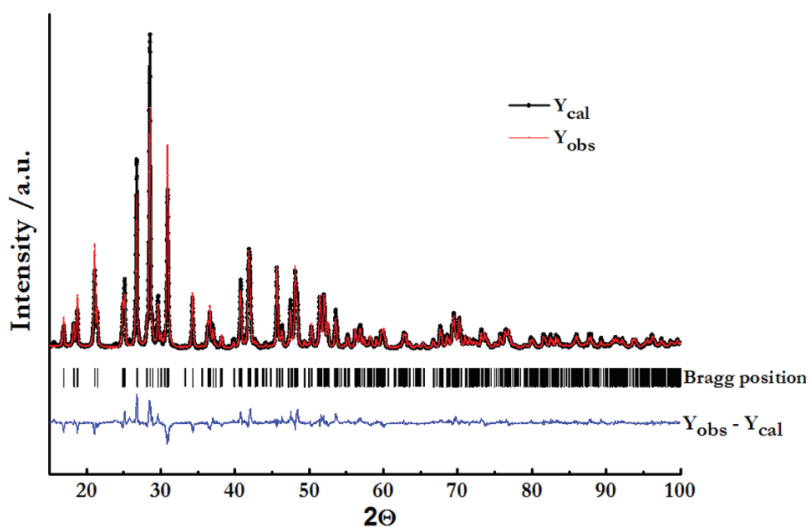


Fig. 3.5: Rietveld plot for  $\text{LaPO}_4$ .

**Table 3.1:** Refined structural parameters of LaPO<sub>4</sub>(s).

Sample	LaPO <sub>4</sub>
a <sup>a</sup> (Å)	6.8396(2)
b <sup>a</sup> (Å)	7.0792(2)
c <sup>a</sup> (Å)	6.5088(2)
β <sup>a</sup> (°)	103.271(2)
V <sup>a</sup> (Å <sup>3</sup> )	306.71(2)
ρ <sup>a,b</sup> (g·cm <sup>-3</sup> )	5.065(2)
U <sup>a</sup>	0.075(1)
V <sup>a</sup>	-0.087(2)
W <sup>a</sup>	0.051(1)
χ <sup>2</sup>	3.54
R <sub>p</sub>	12.7
R <sub>wp</sub>	15.3
R <sub>exp</sub>	7.27

<sup>a</sup>The numbers in the parenthesis represent the standard uncertainties.

<sup>b</sup>Density was estimated using the formula:  $\rho = (Z \cdot M) / (V \cdot N_A)$

Where,  $\rho$  = density in g·cm<sup>-3</sup>

Z = No. of formula units per unit cell

M = Formula weight of the compound in g·mol<sup>-1</sup>

V = unit cell volume in cm<sup>3</sup>

N<sub>A</sub> = Avogadro number in mol<sup>-1</sup>

### 3.3.3. Solution calorimeter

The enthalpy of precipitation ( $\Delta H_r$ ) of hydrated rhabdophane phases were measured for the following chemical reaction:



where, RE= La, Nd, Sm and Gd; x (water of crystallization in chloride precursors) = 7 (La), 6 (Nd, Sm and Gd); n (water of crystallization in rhabdophane phases) = 0.8 (La), 0.75 (Nd), 0.65 (Sm) and 0.55 (Gd). The measured values of the enthalpy of reaction using isoperibol solution calorimeter at 298 K are given in **Table 3.2**.

**Table 3.2:** Enthalpy of reaction<sup>a</sup> data using solution calorimeter experiment for LaCl<sub>3</sub>·7H<sub>2</sub>O(s), NdCl<sub>3</sub>·6H<sub>2</sub>O(s), SmCl<sub>3</sub>·6H<sub>2</sub>O(s) and GdCl<sub>3</sub>·6H<sub>2</sub>O(s) in solution of NH<sub>4</sub>H<sub>2</sub>PO<sub>4</sub>(aq.)<sup>b</sup> at 298 K.

Reactants	Sample wt. /mg	Q <sup>c</sup> /J	$\Delta H_r(298\text{ K})^d$ /kJ.mol <sup>-1</sup>	Mean $\Delta H_{ri}$ /kJ.mol <sup>-1</sup>
LaCl <sub>3</sub> ·7H <sub>2</sub> O(s)	19.7	1.024	19.3	$\Delta H_{r1}$
+	17.9	1.084	22.5	20.1±1.5
Soln A	19.4	1.029	19.7	
	20.3	1.006	18.4	
	18.6	1.032	20.6	
NdCl <sub>3</sub> ·6H <sub>2</sub> O(s)	10.3	0.359	12.5	
+	9.8	0.284	10.4	11.4±0.8
Soln A	11.6	0.372	11.5	
	11.9	0.358	10.8	
	10.5	0.348	11.9	
SmCl <sub>3</sub> ·6H <sub>2</sub> O(s)	11.5	0.192	6.1	
+	11.7	0.154	4.8	5.4±0.6
Soln A	10.8	0.166	5.6	
	12.5	0.199	5.8	
	12.3	0.162	4.8	
GdCl <sub>3</sub> ·6H <sub>2</sub> O(s)	10.6	0.202	7.1	
+	12.2	0.223	6.8	7.2±0.6
Soln A	12.4	0.250	7.5	
	11.1	0.197	6.6	
	10.8	0.235	8.1	

<sup>a</sup>The heat effect associated to precipitation reaction.

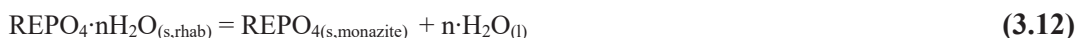
<sup>b</sup>25 ml of solvent was used in each ampoule break experiment.

<sup>c</sup>The heat effect correspond to the dissolution of solute.

<sup>d</sup>Expanded uncertainties for  $\Delta H$  with 0.95 level of confidence ( $k \approx 2$ ).

Standard molar enthalpy of formation,  $\Delta H_{f,m}^0$  was calculated for the rhabdophane phases viz. LaPO<sub>4</sub>·0.8H<sub>2</sub>O(s), NdPO<sub>4</sub>·0.75H<sub>2</sub>O(s), SmPO<sub>4</sub>·0.65H<sub>2</sub>O(s) and GdPO<sub>4</sub>·0.55H<sub>2</sub>O(s) using the measured enthalpy of precipitation,  $\Delta H_r$  and other auxiliary thermodynamic data from the literature employing suitable thermochemical cycles based on the Hess's law. The thermochemical cycles are given in **Tables 3.3-3.6**. The corresponding values of enthalpy of formation are -1959.7±3.0, -1950.0±2.9, -1951.8±2.8 and -1945.8±2.8 kJ·mol<sup>-1</sup>, respectively. The standard molar enthalpy of formation of rare earth orthophosphates ( $\Delta H_{f,monazite}^0$ ) viz. LaPO<sub>4</sub>(s), NdPO<sub>4</sub>(s), SmPO<sub>4</sub>(s) and GdPO<sub>4</sub>(s) is determined using the calculated standard

molar enthalpy of formation of corresponding rhabdophane phases ( $\Delta H_{f,rhab}^{\circ}$ ) and the enthalpy involved in the dehydration ( $\Delta H_{r,dehyd}^{\circ}$ ) of rhabdophane to monazite phase. The enthalpy of following dehydration reaction has been calculated from the results of Shelyug et al. [147].



The standard molar enthalpy of formation of monazite phases ( $\Delta H_{f,monazite}^{\circ}$ ) are calculated employing a thermochemical reaction schemes given in **Tables 3.3-3.6**. The calculated enthalpy of formation values of  $\text{LaPO}_4(s)$ ,  $\text{NdPO}_4(s)$ ,  $\text{SmPO}_4(s)$  and  $\text{GdPO}_4(s)$  are  $-1962.9 \pm 3.4$ ,  $-1949.2 \pm 3.4$ ,  $-1942.4 \pm 3.2$  and  $-1935.2 \pm 3.1$ , respectively.

**Table 3.3:** Thermo-chemical reaction scheme for standard molar enthalpy of formation of  $\text{LaPO}_4 \cdot 0.8\text{H}_2\text{O}_{(s,rhab)}$  at 298 K.

$$\Delta H_{f,rhab}^{\circ} = \Delta H_{r1} + \Delta H_1 + \Delta H_2 + \Delta H_3 - \Delta H_4 - 2 \cdot \Delta H_5 + \Delta H_6 - \Delta H_7 - 2 \cdot \Delta H_8$$

$$\Delta H_{f,monazite}^{\circ} = \Delta H_{f,rhab}^{\circ} + \Delta H_{r,dehyd}^{\circ}$$

Reactions	$\Delta H_i$	$\Delta H_r / \text{kJ} \cdot \text{mol}^{-1}$
$\text{LaCl}_3 \cdot 7\text{H}_2\text{O}_{(s)} + \text{NH}_4\text{H}_2\text{PO}_4_{(aq)} = \text{LaPO}_4 \cdot 0.8\text{H}_2\text{O}_{(s,rhab)} + \text{NH}_4\text{Cl}_{(aq)} + 2 \cdot \text{HCl}_{(aq)} + 6.2 \cdot \text{H}_2\text{O}_{(l)}$	$\Delta H_{r1}$	$20.1 \pm 1.5^{a,b}$
$\text{La}_{(s)} + 3/2 \cdot \text{Cl}_2_{(g)} = \text{LaCl}_3_{(s)}$	$\Delta H_1$	$-1071.1 \pm 1.5^{[163]}$
$\text{LaCl}_3_{(s)} + 7 \cdot \text{H}_2\text{O}_{(l)} = \text{LaCl}_3 \cdot 7\text{H}_2\text{O}_{(s)}$	$\Delta H_2$	$-106.9 \pm 1.3^{[163]}$
$1/2 \cdot \text{N}_2_{(g)} + 3 \cdot \text{H}_2_{(g)} + \text{P}_{(s)} + 2 \cdot \text{O}_2_{(g)} = \text{NH}_4\text{H}_2\text{PO}_4_{(s)}$	$\Delta H_3$	$-1452.5 \pm 1.2^{[164]}$
$1/2 \cdot \text{N}_2_{(g)} + 2 \cdot \text{H}_2_{(g)} + 1/2 \cdot \text{Cl}_2_{(g)} = \text{NH}_4\text{Cl}_{(s)}$	$\Delta H_4$	$-314.9 \pm 0.3^{[164]}$
$1/2 \cdot \text{H}_2_{(g)} + 1/2 \cdot \text{Cl}_2_{(g)} = \text{HCl}_{(g)}$	$\Delta H_5$	$-92.3 \pm 0.1^{[164]}$
$\text{NH}_4\text{H}_2\text{PO}_4_{(s)} = \text{NH}_4\text{H}_2\text{PO}_4_{(aq)}$	$\Delta H_6$	$16.3 \pm 1.2^{[164]}$
$\text{NH}_4\text{Cl}_{(s)} = \text{NH}_4\text{Cl}_{(aq)}$	$\Delta H_7$	$14.7 \pm 0.01^{[164]}$
$\text{HCl}_{(g)} = \text{HCl}_{(aq)}$	$\Delta H_8$	$-74.8 \pm 0.01^{[164]}$
$\text{La}_{(s)} + \text{P}_{(s)} + 2 \cdot \text{O}_2_{(g)} + 0.8 \cdot \text{H}_2\text{O}_{(l)} = \text{LaPO}_4 \cdot 0.8\text{H}_2\text{O}_{(s,rhab)}$	$\Delta H_{f,rhab}^{\circ}$	$-1959.7 \pm 3.0^c$
$\text{LaPO}_4 \cdot 0.8\text{H}_2\text{O}_{(s,rhab)} = \text{LaPO}_4_{(s,monazite)} + 0.8 \cdot \text{H}_2\text{O}_{(l)}$	$\Delta H_{r,dehyd}^{\circ}$	$-3.2 \pm 1.5^{[147]}$
$\text{La}_{(s)} + \text{P}_{(s)} + 2 \cdot \text{O}_2_{(g)} = \text{LaPO}_4_{(s,monazite)}$	$\Delta H_{f,monazite}^{\circ}$	$-1962.9 \pm 3.4^c$

<sup>a</sup>Expanded uncertainties for  $\Delta H$  with 0.95 level of confidence ( $k \approx 2$ ); <sup>b</sup>This work; <sup>c</sup>Uncertainty of the combined reaction is estimated as the square root of the sum of the squares of uncertainty of each individual reaction.

**Table 3.4:** Thermo-chemical reaction scheme for standard molar enthalpy of formation of  $\text{NdPO}_4 \cdot 0.75\text{H}_2\text{O}_{(\text{s,rhab})}$  at 298 K.

$$\Delta H_{\text{f,rhab}}^{\circ} = \Delta H_{\text{r}2} + \Delta H_9 + \Delta H_{10} + \Delta H_{11} - \Delta H_{12} - 2 \cdot \Delta H_{13} + \Delta H_{14} - \Delta H_{15} - 2 \cdot \Delta H_{16}$$

$$\Delta H_{\text{f,monazite}}^{\circ} = \Delta H_{\text{f,rhab}}^{\circ} + \Delta H_{\text{r,dehyd}}^{\circ}$$

Reactions	$\Delta H_i$	$\Delta H_r / \text{kJ} \cdot \text{mol}^{-1}$
$\text{NdCl}_3 \cdot 6\text{H}_2\text{O}_{(\text{s})} + \text{NH}_4\text{H}_2\text{PO}_4(\text{aq.}) = \text{NdPO}_4 \cdot 0.75\text{H}_2\text{O}_{(\text{s,rhab})} + \text{NH}_4\text{Cl}_{(\text{aq.})} + 2 \cdot \text{HCl}_{(\text{aq.})} + 5.25 \cdot \text{H}_2\text{O}_{(\text{l})}$	$\Delta H_{\text{r}2}$	$11.4 \pm 0.8^{\text{a,b}}$
$\text{Nd}_{(\text{s})} + 3/2 \cdot \text{Cl}_{2(\text{g})} = \text{NdCl}_{3(\text{s})}$	$\Delta H_9$	$-1041.0 \pm 1.5^{[163]}$
$\text{NdCl}_{3(\text{s})} + 6 \cdot \text{H}_2\text{O}_{(\text{l})} = \text{NdCl}_3 \cdot 6\text{H}_2\text{O}_{(\text{s})}$	$\Delta H_{10}$	$-118.6 \pm 1.6^{[163]}$
$1/2 \cdot \text{N}_{2(\text{g})} + 3 \cdot \text{H}_{2(\text{g})} + \text{P}_{(\text{s})} + 2 \cdot \text{O}_{2(\text{g})} = \text{NH}_4\text{H}_2\text{PO}_4(\text{s})$	$\Delta H_{11}$	$-1452.5 \pm 1.2^{[164]}$
$1/2 \cdot \text{N}_{2(\text{g})} + 2 \cdot \text{H}_{2(\text{g})} + 1/2 \cdot \text{Cl}_{2(\text{g})} = \text{NH}_4\text{Cl}_{(\text{s})}$	$\Delta H_{12}$	$-314.9 \pm 0.3^{[164]}$
$1/2 \cdot \text{H}_{2(\text{g})} + 1/2 \cdot \text{Cl}_{2(\text{g})} = \text{HCl}_{(\text{g})}$	$\Delta H_{13}$	$-92.3 \pm 0.1^{[164]}$
$\text{NH}_4\text{H}_2\text{PO}_4(\text{s}) = \text{NH}_4\text{H}_2\text{PO}_4(\text{aq.})$	$\Delta H_{14}$	$16.3 \pm 1.2^{[164]}$
$\text{NH}_4\text{Cl}_{(\text{s})} = \text{NH}_4\text{Cl}_{(\text{aq.})}$	$\Delta H_{15}$	$14.7 \pm 0.01^{[164]}$
$\text{HCl}_{(\text{g})} = \text{HCl}_{(\text{aq.})}$	$\Delta H_{16}$	$-74.8 \pm 0.01^{[164]}$
$\text{Nd}_{(\text{s})} + \text{P}_{(\text{s})} + 2 \cdot \text{O}_{2(\text{g})} + 0.75 \cdot \text{H}_2\text{O}_{(\text{l})} = \text{NdPO}_4 \cdot 0.75\text{H}_2\text{O}_{(\text{s,rhab})}$	$\Delta H_{\text{f,rhab}}^{\circ}$	$-1950.0 \pm 2.9^{\text{c}}$
$\text{NdPO}_4 \cdot 0.75\text{H}_2\text{O}_{(\text{s,rhab})} = \text{NdPO}_4(\text{s,monazite}) + 0.75 \cdot \text{H}_2\text{O}_{(\text{l})}$	$\Delta H_{\text{r,dehyd}}^{\circ}$	$0.8 \pm 1.8^{[147]}$
$\text{Nd}_{(\text{s})} + \text{P}_{(\text{s})} + 2 \cdot \text{O}_{2(\text{g})} = \text{NdPO}_4(\text{s,monazite})$	$\Delta H_{\text{f,monazite}}^{\circ}$	$-1949.2 \pm 3.4^{\text{c}}$

<sup>a</sup>Expanded uncertainties for  $\Delta H$  with 0.95 level of confidence ( $k \approx 2$ ); <sup>b</sup>This work; <sup>c</sup>Uncertainty of the combined reaction is estimated as the square root of the sum of the squares of uncertainty of each individual reaction.

**Table 3.5:** Thermo-chemical reaction scheme for standard molar enthalpy of formation of  $\text{SmPO}_4 \cdot 0.65\text{H}_2\text{O}_{(\text{s,rhab})}$  at 298 K.

$$\Delta H_{\text{f,rhab}}^{\circ} = \Delta H_{\text{r}3} + \Delta H_{17} + \Delta H_{18} + \Delta H_{19} - \Delta H_{20} - 2 \cdot \Delta H_{21} + \Delta H_{22} - \Delta H_{23} - 2 \cdot \Delta H_{24}$$

$$\Delta H_{\text{f,monazite}}^{\circ} = \Delta H_{\text{f,rhab}}^{\circ} + \Delta H_{\text{r,dehyd}}^{\circ}$$

Reactions	$\Delta H_i$	$\Delta H_r / \text{kJ} \cdot \text{mol}^{-1}$
$\text{SmCl}_3 \cdot 6\text{H}_2\text{O}_{(\text{s})} + \text{NH}_4\text{H}_2\text{PO}_4(\text{aq.}) = \text{SmPO}_4 \cdot 0.65\text{H}_2\text{O}_{(\text{s,rhab})} + \text{NH}_4\text{Cl}_{(\text{aq.})} + 2 \cdot \text{HCl}_{(\text{aq.})} + 5.35 \cdot \text{H}_2\text{O}_{(\text{l})}$	$\Delta H_{\text{r}3}$	$5.4 \pm 0.6^{\text{a,b}}$
$\text{Sm}_{(\text{s})} + 3/2 \cdot \text{Cl}_{2(\text{g})} = \text{SmCl}_{3(\text{s})}$	$\Delta H_{17}$	$-1025.9 \pm 1.5^{[163]}$
$\text{SmCl}_{3(\text{s})} + 6 \cdot \text{H}_2\text{O}_{(\text{l})} = \text{SmCl}_3 \cdot 6\text{H}_2\text{O}_{(\text{s})}$	$\Delta H_{18}$	$-129.5 \pm 1.4^{[163]}$
$1/2 \cdot \text{N}_{2(\text{g})} + 3 \cdot \text{H}_{2(\text{g})} + \text{P}_{(\text{s})} + 2 \cdot \text{O}_{2(\text{g})} = \text{NH}_4\text{H}_2\text{PO}_4(\text{s})$	$\Delta H_{19}$	$-1452.5 \pm 1.2^{[164]}$
$1/2 \cdot \text{N}_{2(\text{g})} + 2 \cdot \text{H}_{2(\text{g})} + 1/2 \cdot \text{Cl}_{2(\text{g})} = \text{NH}_4\text{Cl}_{(\text{s})}$	$\Delta H_{20}$	$-314.9 \pm 0.3^{[164]}$
$1/2 \cdot \text{H}_{2(\text{g})} + 1/2 \cdot \text{Cl}_{2(\text{g})} = \text{HCl}_{(\text{g})}$	$\Delta H_{21}$	$-92.3 \pm 0.1^{[164]}$
$\text{NH}_4\text{H}_2\text{PO}_4(\text{s}) = \text{NH}_4\text{H}_2\text{PO}_4(\text{aq.})$	$\Delta H_{22}$	$16.3 \pm 1.2^{[164]}$
$\text{NH}_4\text{Cl}_{(\text{s})} = \text{NH}_4\text{Cl}_{(\text{aq.})}$	$\Delta H_{23}$	$14.7 \pm 0.01^{[164]}$
$\text{HCl}_{(\text{g})} = \text{HCl}_{(\text{aq.})}$	$\Delta H_{24}$	$-74.8 \pm 0.01^{[164]}$
$\text{Sm}_{(\text{s})} + \text{P}_{(\text{s})} + 2 \cdot \text{O}_{2(\text{g})} + 0.65 \cdot \text{H}_2\text{O}_{(\text{l})} = \text{SmPO}_4 \cdot 0.65\text{H}_2\text{O}_{(\text{s,rhab})}$	$\Delta H_{\text{f,rhab}}^{\circ}$	$-1951.8 \pm 2.8^{\text{c}}$
$\text{SmPO}_4 \cdot 0.65\text{H}_2\text{O}_{(\text{s,rhab})} = \text{SmPO}_4(\text{s,monazite}) + 0.65 \cdot \text{H}_2\text{O}_{(\text{l})}$	$\Delta H_{\text{r,dehyd}}^{\circ}$	$9.4 \pm 1.6^{[147]}$
$\text{Sm}_{(\text{s})} + \text{P}_{(\text{s})} + 2 \cdot \text{O}_{2(\text{g})} = \text{SmPO}_4(\text{s,monazite})$	$\Delta H_{\text{f,monazite}}^{\circ}$	$-1942.4 \pm 3.2^{\text{c}}$

<sup>a</sup>Expanded uncertainties for  $\Delta H$  with 0.95 level of confidence ( $k \approx 2$ ); <sup>b</sup>This work; <sup>c</sup>Uncertainty of the combined reaction is estimated as the square root of the sum of the squares of uncertainty of each individual reaction.

**Table 3.6:** Thermo-chemical reaction scheme for standard molar enthalpy of formation of  $\text{GdPO}_4 \cdot 0.55\text{H}_2\text{O}_{(\text{s,rhab})}$  at 298.15 K.

$$\Delta H_{\text{f,rhab}}^{\circ} = \Delta H_{\text{r4}} + \Delta H_{25} + \Delta H_{26} + \Delta H_{27} - \Delta H_{28} - 2 \cdot \Delta H_{29} + \Delta H_{30} - \Delta H_{31} - 2 \cdot \Delta H_{32}$$

$$\Delta H_{\text{f,monazite}}^{\circ} = \Delta H_{\text{f,rhab}}^{\circ} + \Delta H_{\text{r,dehyd}}^{\circ}$$

Reactions	$\Delta H_i$	$\Delta H_r / \text{kJ} \cdot \text{mol}^{-1}$
$\text{GdCl}_3 \cdot 6\text{H}_2\text{O}_{(\text{s})} + \text{NH}_4\text{H}_2\text{PO}_4_{(\text{aq})} = \text{GdPO}_4 \cdot 0.55\text{H}_2\text{O}_{(\text{s,rhab})} + \text{NH}_4\text{Cl}_{(\text{aq})} + 2 \cdot \text{HCl}_{(\text{aq})} + 5.45 \cdot \text{H}_2\text{O}_{(\text{l})}$	$\Delta H_{\text{r4}}$	$7.2 \pm 0.6^{\text{a,b}}$
$\text{Gd}_{(\text{s})} + 3/2 \cdot \text{Cl}_{2(\text{g})} = \text{GdCl}_{3(\text{s})}$	$\Delta H_{25}$	$-1008.3 \pm 1.5^{[163]}$
$\text{GdCl}_{3(\text{s})} + 6 \cdot \text{H}_2\text{O}_{(\text{l})} = \text{GdCl}_3 \cdot 6\text{H}_2\text{O}_{(\text{s})}$	$\Delta H_{26}$	$-142.9 \pm 1.4^{[163]}$
$1/2 \cdot \text{N}_{2(\text{g})} + 3 \cdot \text{H}_{2(\text{g})} + \text{P}_{(\text{s})} + 2 \cdot \text{O}_{2(\text{g})} = \text{NH}_4\text{H}_2\text{PO}_4_{(\text{s})}$	$\Delta H_{27}$	$-1452.5 \pm 1.2^{[164]}$
$1/2 \cdot \text{N}_{2(\text{g})} + 2 \cdot \text{H}_{2(\text{g})} + 1/2 \cdot \text{Cl}_{2(\text{g})} = \text{NH}_4\text{Cl}_{(\text{s})}$	$\Delta H_{28}$	$-314.9 \pm 0.3^{[164]}$
$1/2 \cdot \text{H}_{2(\text{g})} + 1/2 \cdot \text{Cl}_{2(\text{g})} = \text{HCl}_{(\text{g})}$	$\Delta H_{29}$	$-92.3 \pm 0.1^{[164]}$
$\text{NH}_4\text{H}_2\text{PO}_4_{(\text{s})} = \text{NH}_4\text{H}_2\text{PO}_4_{(\text{aq})}$	$\Delta H_{30}$	$16.3 \pm 1.2^{[164]}$
$\text{NH}_4\text{Cl}_{(\text{s})} = \text{NH}_4\text{Cl}_{(\text{aq})}$	$\Delta H_{31}$	$14.7 \pm 0.01^{[164]}$
$\text{HCl}_{(\text{g})} = \text{HCl}_{(\text{aq})}$	$\Delta H_{32}$	$-74.8 \pm 0.01^{[164]}$
$\text{Gd}_{(\text{s})} + \text{P}_{(\text{s})} + 2 \cdot \text{O}_{2(\text{g})} + 0.55 \cdot \text{H}_2\text{O}_{(\text{l})} = \text{GdPO}_4 \cdot 0.55\text{H}_2\text{O}_{(\text{s,rhab})}$	$\Delta H_{\text{f,rhab}}^{\circ}$	$-1945.8 \pm 2.8^{\text{c}}$
$\text{GdPO}_4 \cdot 0.55\text{H}_2\text{O}_{(\text{s,rhab})} = \text{GdPO}_4_{(\text{s,monazite})} + 0.55 \cdot \text{H}_2\text{O}_{(\text{l})}$	$\Delta H_{\text{r,dehyd}}^{\circ}$	$10.6 \pm 1.3^{[147]}$
$\text{Gd}_{(\text{s})} + \text{P}_{(\text{s})} + 2 \cdot \text{O}_{2(\text{g})} = \text{GdPO}_4_{(\text{s,monazite})}$	$\Delta H_{\text{f,monazite}}^{\circ}$	$-1935.2 \pm 3.1^{\text{c}}$

<sup>a</sup>Expanded uncertainties for  $\Delta H$  with 0.95 level of confidence ( $k \approx 2$ ); <sup>b</sup>This work; <sup>c</sup>Uncertainty of the combined reaction is estimated as the square root of the sum of the squares of uncertainty of each individual reaction.

### 3.4. DISCUSSIONS

The standard molar enthalpy of formation,  $\Delta H_{\text{f,monazite}}^{\circ}$  of  $\text{LaPO}_4(\text{s})$ ,  $\text{NdPO}_4(\text{s})$ ,  $\text{SmPO}_4(\text{s})$  and  $\text{GdPO}_4(\text{s})$  were compared with the data reported in the literature [147-159] and provided in **Table 3.7**. The enthalpy of formation of  $\text{REPO}_4(\text{s})$  (RE = La, Nd, Sm and Gd) from their constituent oxides i.e.  $\Delta H_{\text{f,ox}}^{\circ}(\text{REPO}_4, \text{s}, 298 \text{ K})$  are calculated using the following relations:



$$\Delta H_{\text{f,ox}}^{\circ}(\text{REPO}_4, \text{s}, 298 \text{ K}) = \Delta H_{\text{f}}^{\circ}(\text{REPO}_4, \text{s}, 298 \text{ K}) - 1/2 \cdot \Delta H_{\text{f}}^{\circ}(\text{RE}_2\text{O}_3, \text{s}, 298 \text{ K}) - 1/2 \cdot \Delta H_{\text{f}}^{\circ}(\text{P}_2\text{O}_5, \text{l}, 298 \text{ K}) \quad (3.14)$$

The enthalpy of formation,  $\Delta H_{\text{f,ox}}^{\circ}(\text{REPO}_4, \text{s}, 298 \text{ K})$  (RE = La, Nd, Sm and Gd) determined in the present work was compared with that reported in the literature [147-159].

**Table 3.7:** Comparison of standard molar enthalpy of formation of LaPO<sub>4</sub>, NdPO<sub>4</sub>, SmPO<sub>4</sub> and GdPO<sub>4</sub> with that reported in the literature.

Authors	Techniques	$\Delta H_f^{\circ}$ , monazite			
		LaPO <sub>4</sub> /kJ.mol <sup>-1</sup>	NdPO <sub>4</sub> /kJ.mol <sup>-1</sup>	SmPO <sub>4</sub> /kJ.mol <sup>-1</sup>	GdPO <sub>4</sub> /kJ.mol <sup>-1</sup>
Shelyug et al. [147]	Oxide melt solution calorimetry at 973 K	-1994.4±4.3	-1964.7±5.1	-1965.7±5.3	-1956.1±7.2
Neumeier et al. [148]	Oxide melt solution calorimetry at 973 K	-1994.4±2.7			-1959.7±6.1
Yungman et al. [149]	Estimation method	-1913.8			-1888.2
Ushakov et al. [150]	Oxide melt solution calorimetry at 975 K	-1970.7±1.8	-1968.4±2.3	-1965.7±2.4	-1962.2±4.4
Popa et. al. [152]	Recalculated from experiment results of [151]	-1969.7±1.9	-1967.9±2.5	-1965.8±2.9	
Poitrasson et al. [153]	From the temperature dependence of solubility		-1928		
Wood and Williams-Jones [154]	Solubility		-1932		
Williamson et al. [155]	Estimated Data	-1955.2±2.1	-1960.4±2		
Cetiner et al. [156]	From the equilibrium constant	-1947	-1907±4	-1962	
Marinova and Yaglov [157]	Solubility products and estimated entropies	-1962±8	-1941	-1933	
Marinova et al. [158]	Acid Solution Calorimetry	-1949±4			
Ousbalyev et al. [159]	Calorimetry	-1942	-1930	-1925	
This work	Solution Calorimetry at 298 K	-1962.9±3.4	-1949.2±3.4	-1942.4±3.2	-1935.2±3.1

The  $\Delta H_{f,ox}^{\circ}(\text{REPO}_{4,s,298\text{ K}})$  values are plotted against ionic radii of trivalent rare earth ion in nine-fold coordination viz.  $\text{La}^{3+}$  (1.216 Å),  $\text{Nd}^{3+}$  (1.163 Å),  $\text{Sm}^{3+}$  (1.132 Å) and  $\text{Gd}^{3+}$  (1.107 Å) [165] and given in **Fig. 3.6**.

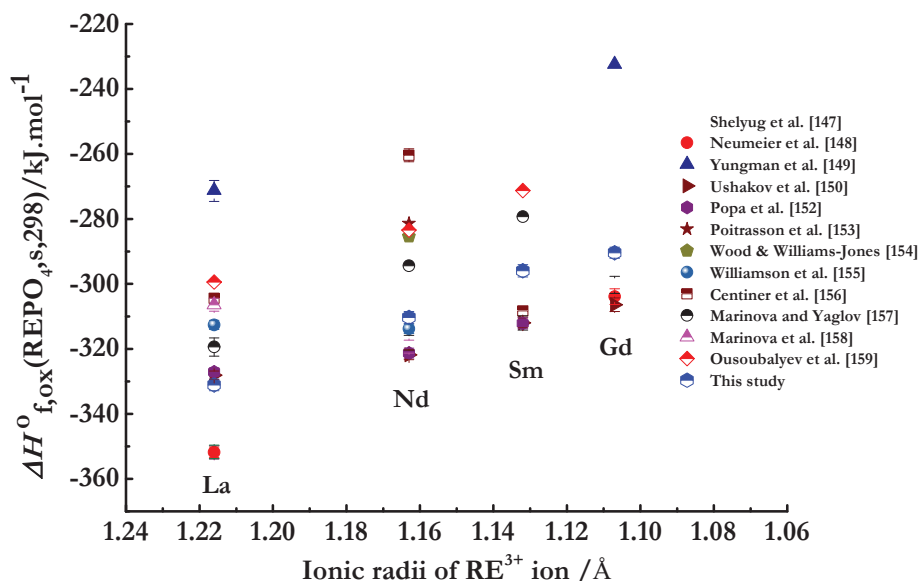


**Fig. 3.6:** Comparison of enthalpy of formation,  $\Delta H_{f,ox}^{\circ}$  of  $\text{REPO}_4$  ( $\text{RE} = \text{La}, \text{Nd}, \text{Sm}$  and  $\text{Gd}$ ) from their constituent oxides.

Shelyug et al. [147] measured the enthalpy of formation of rhabdophane and monazite phases using high temperature calorimeter with molten sodium molybdate ( $3\text{Na}_2\text{O}\cdot 4\text{MoO}_3$ ) as a solvent at 973 K (for all lanthanides except praseodymium) and lead borate ( $2\text{PbO}\cdot \text{B}_2\text{O}_3$ ) at 1073 K (for praseodymium). Using the data reported by Gausse et al. [166], the author determined a complete set of thermodynamic data for the rhabdophanes. Neumeier et al. [148] determined the enthalpy of formation of  $\text{LaPO}_4(\text{s})$ ,  $\text{GdPO}_4(\text{s})$  using molten  $3\text{Na}_2\text{O}\cdot 4\text{MoO}_3$  as a solvent in a platinum crucible in the calorimeter at 973 K. In contrary a difference of  $\sim 80$   $\text{kJ}\cdot\text{mol}^{-1}$  was observed to data reported by Yungman et al. [149].

Ushakov et al. [150] and Helean et al. [151] reported enthalpy of formation of  $\text{LaPO}_4(\text{s})$ ,  $\text{NdPO}_4(\text{s})$ , and  $\text{SmPO}_4(\text{s})$  using oxide melt solution calorimetry at 975 K performed in sodium

molybdate ( $3\text{Na}_2\text{O}\cdot 4\text{MoO}_3$ ) solvents at 975 K. Enthalpy of formation value of  $\text{REPO}_4(\text{s})$  (RE = La, Nd, Sm) were also recalculated by Popa et al. [152] using experimental results of Helean et al. [151]. Poitrasson et al. [153] derived  $\Delta H_f^\circ(\text{NdPO}_4, \text{s}, 298.15 \text{ K})$  from the temperature dependent solubility data and Wood & Williams-Jones [154] also derived this value from their solubility data. Williamson et al. [155] also reported the estimated enthalpy of formation value at 298.15 K for  $\text{LaPO}_4(\text{s})$  and  $\text{NdPO}_4(\text{s})$ . Cetiner et al. [156] derived the enthalpy of formation of  $\text{LaPO}_4(\text{s})$ ,  $\text{NdPO}_4(\text{s})$ , and  $\text{SmPO}_4(\text{s})$  from the temperature dependence of the solubility of these phosphates. Marinova and Yaglov [157] derived  $\Delta H_f^\circ(298.15 \text{ K})$  of  $\text{LaPO}_4(\text{s})$ ,  $\text{NdPO}_4(\text{s})$ , and  $\text{SmPO}_4(\text{s})$  from solubility products and estimated entropies of  $\text{REPO}_4(\text{s})$  (RE = La, Nd, Sm). Marinova et al. [158] measured the enthalpy of formation of  $\text{LaPO}_4(\text{s})$  using  $\text{LaCl}_3 + \text{H}_3\text{PO}_4$  reaction calorimetry. Ousoubalyev et al. [159] also reported enthalpy of formation of  $\text{LaPO}_4(\text{s})$ ,  $\text{NdPO}_4(\text{s})$ , and  $\text{SmPO}_4(\text{s})$  by calorimetry.

The comparison plot of  $\text{REPO}_4$  (RE = La, Nd, Sm and Gd) in **Fig. 3.6** shows that their  $\Delta H_{f,ox}^\circ$  values determined using oxide melt solution calorimeter [148, 150, 152] is lower than that of the present study. The standard molar enthalpies of formation,  $\Delta H_{f,m}^\circ$  of  $\text{REPO}_4$  (RE = La, Nd, Sm and Gd) showed the same trend with those reported by Ushakov et al. [150] and Neumeier et al. [148].

The data reported in different studies showed the similar trend i.e. the values of  $\Delta H_{f,ox}^\circ(\text{REPO}_4, \text{s}, 298 \text{ K})$  (RE = La, Nd, Sm and Gd) increases as the ionic radii of the trivalent rare earth ion in nine-fold coordination decreases. This revealed that more amount of heat is released on the formation of one mole of  $\text{LaPO}_4(\text{s})$  than that of  $\text{NdPO}_4(\text{s})$ ,  $\text{SmPO}_4(\text{s})$  and  $\text{GdPO}_4(\text{s})$  from their constituent oxides. This could be attributed to the fact that, substituting  $\text{Sm}^{3+}$  for  $\text{Gd}^{3+}$  stabilizes the structure by presumably better satisfying the bonding requirements of the  $\text{RE}^{3+}$ -site in  $\text{REPO}_4$ . This stabilization effect may continue until the  $\text{RE}^{3+}$ -site ion

becomes too large and begins to destabilize the structure. As there is no trivalent ion with ionic radii greater than  $\text{La}^{3+}$  available, the eventual destabilization of the  $\text{REPO}_4$  structure is experimentally not attained. Hence,  $\text{LaPO}_4(\text{s})$  exhibit thermodynamically the most stable structure than other rare earth phosphates and hence most suited for being used as a stable host matrix for immobilization of long-lived radionuclides.

### 3.5. CONCLUSIONS

The present work has described the synthesis of rhabdophane phase,  $\text{REPO}_4 \cdot n\text{H}_2\text{O}$  ( $\text{RE} = \text{La}, \text{Nd}, \text{Sm}, \text{Gd}; n = 0.8 - 0.55$ ) and monazite phase,  $\text{REPO}_4$  ( $\text{RE} = \text{La}, \text{Nd}, \text{Sm}$  and  $\text{Gd}$ ). The water of crystallization in rare earth chlorides, ammonium dihydrogen phosphate and rhabdophane phases have been determined using thermogravimetry analysis. Thermogravimetry results of rare earth chlorides,  $\text{RECl}_3 \cdot x\text{H}_2\text{O}(\text{s})$  ( $\text{RE} = \text{La}, \text{Nd}, \text{Sm}$  and  $\text{Gd}$ ) show the presence of water of crystallization. The dehydration of rare earth chlorides occurs in successive steps with varying moles of water of crystallization. Thermogravimetry analysis of rhabdophane phases,  $\text{REPO}_4 \cdot n\text{H}_2\text{O}$  ( $\text{RE} = \text{La}, \text{Nd}, \text{Sm}$  and  $\text{Gd}$ ) reveal different extent of water of crystallization viz.  $\text{LaPO}_4 \cdot 0.8\text{H}_2\text{O}(\text{s})$ ,  $\text{NdPO}_4 \cdot 0.75\text{H}_2\text{O}(\text{s})$ ,  $\text{SmPO}_4 \cdot 0.65\text{H}_2\text{O}(\text{s})$  and  $\text{GdPO}_4 \cdot 0.55\text{H}_2\text{O}(\text{s})$ .

XRD plots of the monazite phases,  $\text{REPO}_4$  ( $\text{RE} = \text{La}, \text{Nd}, \text{Sm}$  and  $\text{Gd}$ ) are well matched with that reported patterns in diffraction database. The refined structural parameters using Rietveld analysis for  $\text{LaPO}_4$  are presented and it found to crystallize in monoclinic lattice.

Standard molar enthalpies of formation,  $\Delta H_{\text{f,m}}^{\circ}$  are calculated for the rhabdophane phases viz.  $\text{LaPO}_4 \cdot 0.8\text{H}_2\text{O}(\text{s})$ ,  $\text{NdPO}_4 \cdot 0.75\text{H}_2\text{O}(\text{s})$ ,  $\text{SmPO}_4 \cdot 0.65\text{H}_2\text{O}(\text{s})$  and  $\text{GdPO}_4 \cdot 0.55\text{H}_2\text{O}(\text{s})$  and the corresponding calculated values are  $-1959.7 \pm 3.0$ ,  $-1950.0 \pm 2.9$ ,  $-1951.8 \pm 2.8$  and  $-1945.8 \pm 2.8 \text{ kJ} \cdot \text{mol}^{-1}$ , respectively. Whereas, the values for enthalpy of formation of  $\text{LaPO}_4(\text{s})$ ,  $\text{NdPO}_4(\text{s})$ ,  $\text{SmPO}_4(\text{s})$  and  $\text{GdPO}_4(\text{s})$  are determined to be  $-1962.9 \pm 3.4$ ,  $-1949.2 \pm 3.4$ ,

-1942.4±3.2 and -1935.2±3.1, respectively. A correlation has been drawn between the measured enthalpy of formation with the ionic radii of the rare earth elements. The values of  $\Delta H_{f,ox}^{\circ}(\text{REPO}_{4,s}, 298 \text{ K})$  (RE = La, Nd, Sm and Gd) are found to decrease with the ionic radii of  $\text{RE}^{3+}$  ion in nine-fold coordination and the value found to be most negative (i.e. exothermic) for  $\text{LaPO}_4$ . Hence,  $\text{LaPO}_4(s)$  is found to be thermodynamically most stable structure than other rare earth phosphates and can be considered as a stable host matrix for immobilization of long-lived radionuclides.

The study provided supporting results for the long-term stability of the monazite waste matrices. This study also demonstrates successful application of the calorimetric technique for measuring enthalpy of formation of ceramic crystalline materials and also elucidates energetic trends in rare earth phosphates. The formulated thermochemical cycle suggested in this study for rare earth phosphates can be employed for measurement of enthalpy of formation of other relevant actinide phosphates.

# CHAPTER-4

---

***THERMODYNAMIC  
INVESTIGATIONS OF CHARGE-  
COUPLED SUBSTITUTED MONAZITE  
SOLID SOLUTIONS  
(La<sub>1-x</sub>M<sub>x/2</sub>Th<sub>x/2</sub>)PO<sub>4</sub> (0 ≤ x ≤ 1)  
(M = Ca, Sr and Ba)***

## 4.1. INTRODUCTION

As the thermodynamic studies in previous chapter outlined that synthetic monazite  $\text{LaPO}_4$ , has the most negative enthalpy of formation i.e. most thermodynamically stable matrix and could be considered as the host matrix for the disposal of long-lived minor actinides. The substitution of these actinides into the synthetic monazite matrix results in the formation of monazite-cheralite solid solution. Thermodynamic investigations of monazite-cheralite solid solution would provide a fundamental understanding and insight into their stability and reactivity. Further, reliable thermodynamic data on these solid solutions are required to predict their long-term stability in order to use them as nuclear waste host matrices. Despite being one of the most suitable matrices for the nuclear waste disposal, information on thermodynamic properties of monazite-cheralite phosphate solid solutions are relatively scarce. A few experimental thermodynamic data are available for trivalent rare earth substituted monazite solid solution [167-170]. The thermodynamic data are even more limited in case of actinide substituted monazite solid solutions [171, 172]. This necessitates a thorough investigation on thermodynamic properties of such solid solutions.

In this chapter, synthesis, characterization and thermodynamic investigations of charge-coupled i.e.  $(M^{2+}, \text{Th}^{4+})$  ( $M = \text{Ca}, \text{Sr}$  and  $\text{Ba}$ ) substituted monazite-cheralite solid solutions are reported. The mechanism for the charge-coupled substitution of trivalent lanthanides with divalent and tetravalent radionuclides is described in Section 1.10.2. The resulted solid solution have general formula  $(\text{La}_{1-x}\text{M}_{x/2}\text{Th}_{x/2})\text{PO}_4$  ( $0 \leq x \leq 1$ ) ( $M = \text{Ca}, \text{Sr}$  and  $\text{Ba}$ ). The specific heat capacity ( $C_p^\circ$ ), the standard enthalpy of formation ( $\Delta H_{f,298\text{K}}^\circ$ ), Gibbs energy of formation and other thermodynamic parameters for the solid solutions are determined and discussed.

## 4.2. EXPERIMENTAL

### 4.2.1. Material Synthesis

Solid state synthesis route was used for the preparation of  $(\text{La}_{1-x}\text{M}_{x/2}\text{Th}_{x/2})\text{PO}_4$  ( $0 \leq x \leq 1$ ) ( $M = \text{Ca}, \text{Sr}$  and  $\text{Ba}$ ) solid solutions. In this method, stoichiometric amounts of  $\text{La}_2\text{O}_3$  (M/s Sigma Aldrich),  $\text{CaCO}_3$  (M/s Sigma Aldrich),  $\text{SrCO}_3$  (M/s Sigma Aldrich),  $\text{BaCO}_3$  (M/s Sigma Aldrich),  $\text{ThO}_2$  (NFC, Hyderabad) and ammonium dihydrogen phosphate  $\text{NH}_4\text{H}_2\text{PO}_4$  (M/s Alfa Aesar) are mixed thoroughly in an agate mortar. The mixed powders were heated at a heating rate  $5 \text{ K}\cdot\text{min}^{-1}$  up to  $973 \text{ K}$  and equilibrated for  $10 \text{ h}$ . The samples were then homogenized, pelletized and further heated at  $1500 \text{ K}$  for  $12 \text{ h}$  and program cooled to room temperature.

#### 4.2.2. Characterization methods

The elemental analyses of the solid solutions were carried out using inductively coupled plasma-atomic emission spectroscopy (ICP-AES) for the reactants and sintered products. The description of the ICP-AES technique is provided in Section 2.3.1 of Chapter 2.

The sintered samples of  $(\text{La}_{1-x}\text{M}_{x/2}\text{Th}_{x/2})\text{PO}_4$  ( $0 \leq x \leq 1$ ) ( $M = \text{Ca}, \text{Sr}$  and  $\text{Ba}$ ) solid solutions were analyzed by X-ray diffraction (XRD) technique using a Stoe, Germany, X-ray diffractometer with monochromatic  $\text{CuK}\alpha$  radiation ( $\lambda = 1.5406 \text{ \AA}$ ) and a nickel filter. The XRD patterns were recorded in the  $2\theta$  range from  $10^\circ$  to  $80^\circ$  with a step width of  $0.02^\circ$ . The observed X-ray powder diffraction patterns were refined using Rietveld method with the help of Fullprof-2k software program [173] in which peak profile was fitted to Pseudo-Voigt profile function and U, V, W parameters were refined. The background parameters were adjusted with sixth order polynomial and with an appropriate scale factor. The detailed description of the XRD technique is given in Section 2.3.2 of Chapter 2.

The specific heat capacity,  $C_p^o(T)$  of the solid solutions were measured in the temperature range of  $300\text{-}800 \text{ K}$  with a heating rate of  $7.5 \text{ K}\cdot\text{min}^{-1}$  using a pre-calibrated Mettler Toledo Differential Scanning Calorimeter (DSC I) under the flow of high purity argon gas.

Classical three-step method viz., blank, sapphire and sample run in a step heating mode was employed for measuring the heat capacity of each sample. The description of the technique and the classical three-step method is provided in Section 2.4.1 of Chapter 2. About 100 mg quantity of each sample of  $(\text{La}_{1-x}\text{M}_{x/2}\text{Th}_{x/2})\text{PO}_4$  ( $0 \leq x \leq 1$ ) ( $M = \text{Ca}, \text{Sr}$  and  $\text{Ba}$ ) solid solutions was taken in a sealed 40  $\mu\text{l}$  Al pan crucible for the heat capacity measurement and independently measured twice. For each experiment four consecutive measurements were done and the average of the last three superimposing DSC curve were considered for the calculation of heat capacity for the sample.

Standard molar enthalpy of formation,  $\Delta H_{f,m}^0(298.15 \text{ K})$  of  $(\text{La}_{1-x}\text{M}_{x/2}\text{Th}_{x/2})\text{PO}_4$  ( $0 \leq x \leq 1$ ) ( $M = \text{Ca}, \text{Sr}$  and  $\text{Ba}$ ) solid solutions were determined from the enthalpy of dissolution,  $\Delta H_{ds}$  data of each composition in molten  $\text{PbO} + \text{B}_2\text{O}_3$  (2:1 molar ratio) solvent at 1089 K. Enthalpy of dissolution was measured using a high temperature Calvet calorimeter (Setaram, Model HT-1000). The enthalpies of dissolution of the constituent oxides viz.  $\text{La}_2\text{O}_3$ ,  $\text{CaO}$ ,  $\text{SrO}$ ,  $\text{BaO}$  and  $\text{ThO}_2$  were also measured using similar technique. Details of the solvent preparation and dissolution studies are described in Section 2.4.2 of Chapter 2. A fresh solvent was used for dissolution of each composition and component oxides.

Microstructure analysis of the quenched  $\text{PbO} + \text{B}_2\text{O}_3$  (2:1 molar ratio) solvent of calorimeter containing  $(\text{La}_{0.4}\text{Sr}_{0.3}\text{Th}_{0.3})\text{PO}_4$  solute was carried out using Scanning Electron Microscope (SEM) to investigate the dissolution and distribution of the solute in the molten solvent. The microscope was operated at 20 kV potential. Prior to recording the micrographs, the surface of quenched solvent sample was sputter-coated with a thin layer of gold ( $\sim 10$ - $15 \text{ nm}$ ) in order to avoid charging interference during measurements. Image was taken in back scattered electron (BSE) mode (solid state back scattered electron detector). Energy dispersive spectroscopy (EDS,  $80 \text{ mm}^2$ , silicon drift detector) was used for X-ray dot mapping of elements. The detailed description of the technique is given in Section 2.3.4 of Chapter 2.

### 4.3. RESULTS & DISCUSSIONS

#### 4.3.1. Inductively Coupled Plasma-Atomic Emission Spectroscopy (ICP-AES)

The elemental analyses of  $(La_{1-x}M_{x/2}Th_{x/2})PO_4$  ( $0 \leq x \leq 1$ ) ( $M = Ca, Sr$  and  $Ba$ ) samples were carried out using inductively coupled plasma-atomic emission spectroscopy (ICP-AES). The results of the analysis for the reactants are tabulated in **Table 4.1** and for the sintered products in **Table 4.2**.

**Table 4.1:** Specifications of chemicals used for the synthesis.

Chemical	Source	Initial Mole Fraction purity	Final Mole Fraction purity	Analysis Method
$La_2O_3$	M/s Sigma Aldrich ChemieGmbH, Germany	0.9996		ICP-AES
$CaCO_3$	M/s Sigma Aldrich ChemieGmbH, Germany	0.9998		ICP-AES
$SrCO_3$	M/s Sigma Aldrich ChemieGmbH, Germany	0.9997		ICP-AES
$BaCO_3$	M/s Sigma Aldrich ChemieGmbH, Germany	0.9996		ICP-AES
$ThO_2$	NFC, Hyderabad	0.9998		ICP-AES
$NH_4H_2PO_4$	M/s Alfa Aesar, Germany	0.9997		ICP-AES
$ZrO_2$	M/s Johnson, Matthey & Co. Ltd	0.9995		ICP-AES

**Table 4.2:** Elementary composition of  $(La_{1-x}M_{x/2}Th_{x/2})PO_4$  ( $0 \leq x \leq 1$ ) ( $M = Ca, Sr$  and  $Ba$ ) compounds determined using ICP-AES<sup>a</sup> analysis.

Composition	La	$M$ ( $M = Ca/Sr/Ba$ )	Th	P/(La+M+Th)
<b><math>(La_{1-x}Ca_{x/2}Th_{x/2})PO_4</math> (<math>0 \leq x \leq 1</math>)</b>				
$LaPO_4$	1.00±0.01	-	-	1.01±0.01
$(La_{0.85}Ca_{0.075}Th_{0.075})PO_4$	0.85±0.01	0.074±0.001	0.076±0.001	1.06±0.02
$(La_{0.75}Ca_{0.125}Th_{0.125})PO_4$	0.75±0.01	0.123±0.002	0.127±0.001	1.04±0.01
$(La_{0.6}Ca_{0.2}Th_{0.2})PO_4$	0.61±0.01	0.19±0.01	0.20±0.01	1.06±0.01
$(La_{0.4}Ca_{0.3}Th_{0.3})PO_4$	0.39±0.02	0.29±0.02	0.32±0.01	1.07±0.02
$(La_{0.25}Ca_{0.375}Th_{0.375})PO_4$	0.25±0.01	0.374±0.001	0.376±0.001	1.01±0.01
$(La_{0.15}Ca_{0.425}Th_{0.425})PO_4$	0.15±0.01	0.427±0.001	0.423±0.002	1.02±0.01
$Ca_{0.5}Th_{0.5}PO_4$	-	0.35±0.01	0.35±0.01	1.04±0.02
<b><math>(La_{1-x}Sr_{x/2}Th_{x/2})PO_4</math> (<math>0 \leq x \leq 1</math>)</b>				
$(La_{0.9}Sr_{0.05}Th_{0.05})PO_4$	0.89±0.01	0.05±0.01	0.06±0.01	1.07±0.01
$(La_{0.8}Sr_{0.1}Th_{0.1})PO_4$	0.79±0.01	0.10±0.01	0.11±0.01	1.01±0.01
$(La_{0.7}Sr_{0.15}Th_{0.15})PO_4$	0.71±0.01	0.14±0.01	0.15±0.01	1.06±0.01
$(La_{0.6}Sr_{0.2}Th_{0.2})PO_4$	0.61±0.01	0.19±0.01	0.20±0.01	1.02±0.01
$(La_{0.5}Sr_{0.25}Th_{0.25})PO_4$	0.49±0.01	0.26±0.01	0.24±0.01	1.01±0.01
$(La_{0.4}Sr_{0.3}Th_{0.3})PO_4$	0.39±0.01	0.31±0.01	0.30±0.01	1.09±0.01
$(La_{0.3}Sr_{0.35}Th_{0.35})PO_4$	0.31±0.01	0.35±0.01	0.34±0.01	1.04±0.01
$(La_{0.2}Sr_{0.4}Th_{0.4})PO_4$	0.19±0.01	0.40±0.01	0.41±0.01	1.08±0.01
$(La_{0.1}Sr_{0.45}Th_{0.45})PO_4$	0.11±0.01	0.44±0.01	0.45±0.01	1.03±0.01



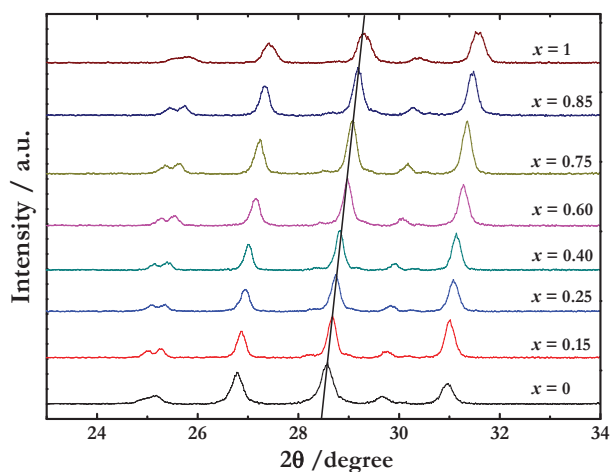


Fig. 4.2: Exaggerated view of the portion of XRD pattern in which solid line has been used to show the shift in peak position with variation in composition.

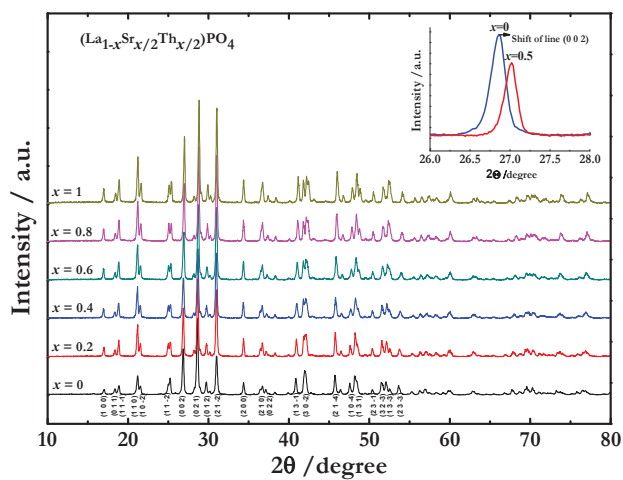


Fig. 4.3: XRD patterns of  $(\text{La}_{1-x}\text{Sr}_{x/2}\text{Th}_{x/2})\text{PO}_4$  ( $x = 0, 0.2, 0.4, 0.6, 0.8, 1$ ) solid solution.

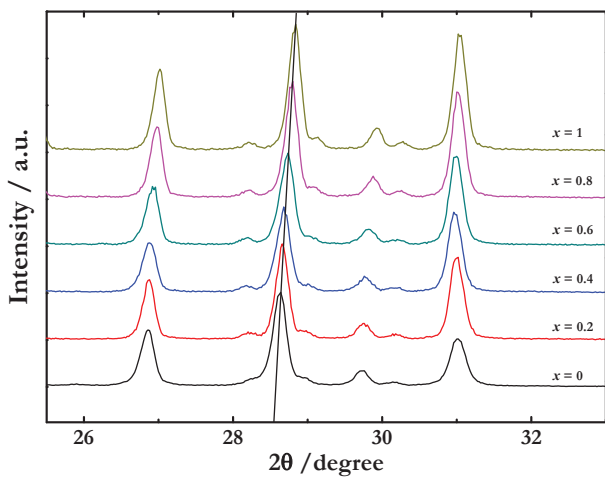
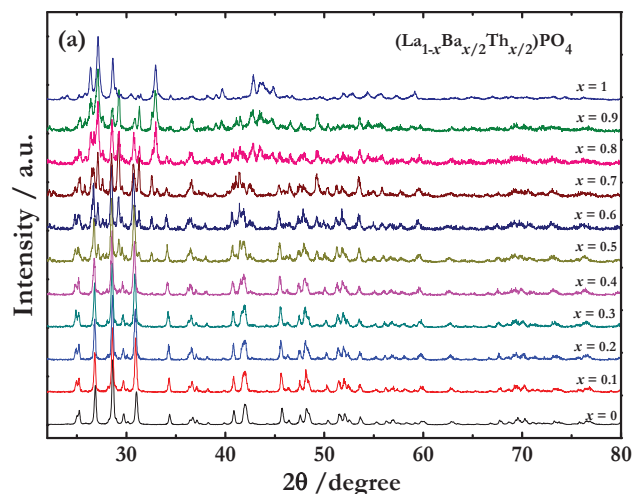
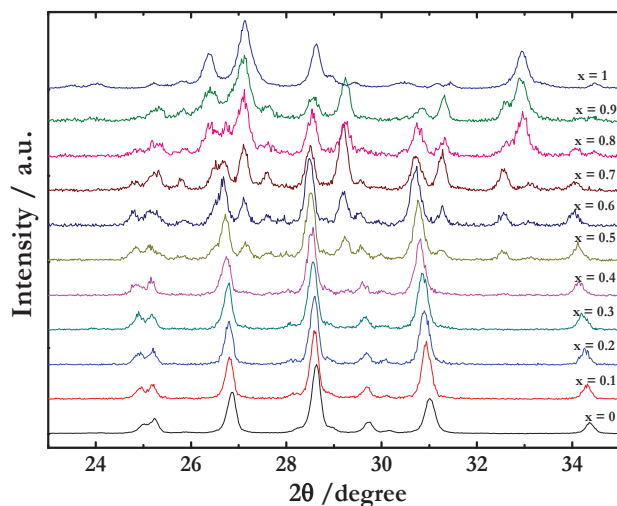


Fig. 4.4: Exaggerated view of the portion of XRD pattern in which solid line has been used to show the shift in peak position with variation in composition.



**Fig. 4.5:** XRD patterns of  $(\text{La}_{1-x}\text{Ba}_{x/2}\text{Th}_{x/2})\text{PO}_4$  ( $x = 0, 0.1, 0.2, 0.3, 0.4, 0.5, 0.6, 0.7, 0.8, 0.9, 1$ ) solid solution.



**Fig. 4.6:** Exaggerated view of the portion of XRD pattern showing phase separation beyond  $x = 0.3$ .

The unit cell parameters  $a$ ,  $b$  and  $c$  in the composition range  $(\text{La}_{1-x}\text{M}_{x/2}\text{Th}_{x/2})\text{PO}_4$  ( $0 \leq x \leq 1$ ) ( $M = \text{Ca}, \text{Sr}$  and  $\text{Ba}$ ) are found to systematically vary with increase in  $(\text{M}^{2+}, \text{Th}^{4+})$  ( $M = \text{Ca}, \text{Sr}$  and  $\text{Ba}$ ) coupled substitution. It indicates that the monoclinic monazite crystal has a wide range of solubility for charge coupled substitution  $(\text{M}^{2+}, \text{Th}^{4+})$  ( $M = \text{Ca}, \text{Sr}$  and  $\text{Ba}$ ). The variation of lattice parameters as a function of mole fraction of  $\text{M}_{0.5}\text{Th}_{0.5}\text{PO}_4$  ( $M = \text{Ca}, \text{Sr}$  and  $\text{Ba}$ ) is given in **Figs. 4.7–4.9**. The measured unit cell parameters of  $(\text{La}_{1-x}\text{Ca}_{x/2}\text{Th}_{x/2})\text{PO}_4$  ( $0 \leq x \leq 1$ ) at room temperature are well matched with that reported by Konings et. al. [171] and the comparison in the values are shown in **Fig. 4.7**.

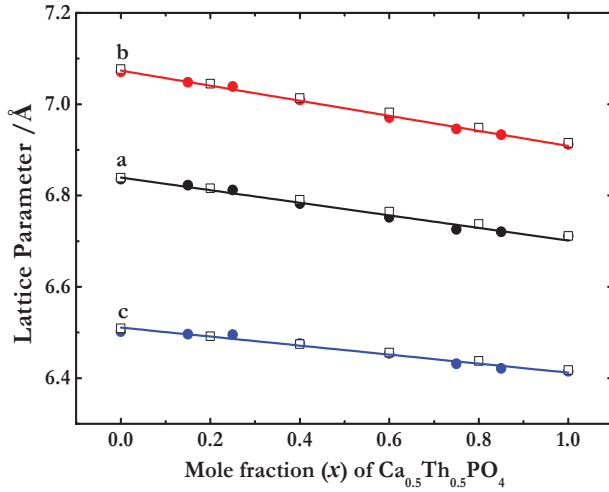


**Fig. 4.7:** Variation of unit cell parameters of  $(\text{La}_{1-x}\text{Ca}_{x/2}\text{Th}_{x/2})\text{PO}_4$  ( $x = 0, 0.15, 0.25, 0.40, 0.60, 0.75, 0.85, 1$ ) samples; (●) present study; (□) Konings et al. [171].

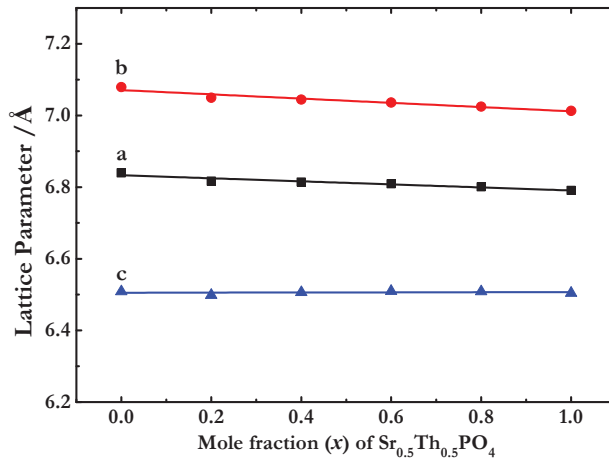


**Fig. 4.8:** Variation of unit cell parameter of  $(\text{La}_{1-x}\text{Sr}_{x/2}\text{Th}_{x/2})\text{PO}_4$  ( $x = 0, 0.2, 0.4, 0.6, 0.8, 1$ ) samples.

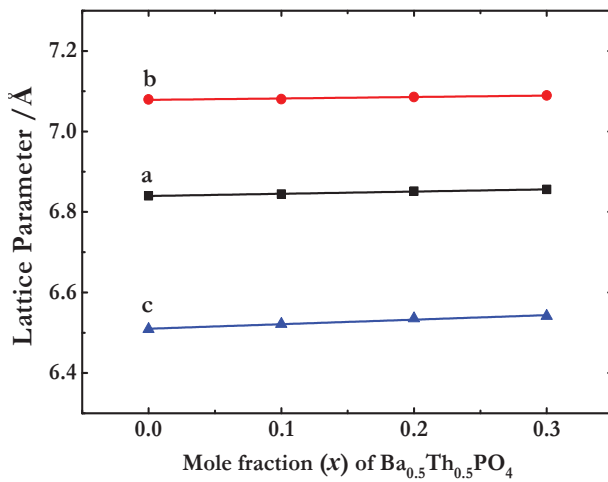


**Fig. 4.9:** Variation of unit cell parameter of  $(\text{La}_{1-x}\text{Ba}_{x/2}\text{Th}_{x/2})\text{PO}_4$  ( $x = 0, 0.1, 0.2, 0.3$ ) samples.

The unit cell parameters of  $(\text{La}_{1-x}\text{M}_{x/2}\text{Th}_{x/2})\text{PO}_4$  ( $0 \leq x \leq 1$ ) ( $M = \text{Ca}, \text{Sr}$  and  $\text{Ba}$ ) solid solutions were fitted to a first order linear equation with respect to mole fraction of  $\text{M}_{0.5}\text{Th}_{0.5}\text{PO}_4$  ( $M = \text{Ca}, \text{Sr}$  and  $\text{Ba}$ ) and the fitted linear equations 4.1–4.12 are given below:

**For  $(\text{La}_{1-x}\text{Ca}_{x/2}\text{Th}_{x/2})\text{PO}_4$  ( $0 \leq x \leq 1$ ):**

$$a(\text{\AA}) = 6.839(4) - 0.138(7) \cdot x \quad (4.1)$$

$$b(\text{\AA}) = 7.073(2) - 0.165(4) \cdot x \quad (4.2)$$

$$c(\text{\AA}) = 6.511(4) - 0.098(3) \cdot x \quad (4.3)$$

$$V(\text{\AA})^3 = 306.9(4) - 18.8(7) \cdot x \quad (4.4)$$

**For  $(\text{La}_{1-x}\text{Sr}_{x/2}\text{Th}_{x/2})\text{PO}_4$  ( $0 \leq x \leq 1$ ):**

$$a(\text{\AA}) = 6.833(4) - 0.042(6) \cdot x \quad (4.5)$$

$$b(\text{\AA}) = 7.071(2) - 0.059(7) \cdot x \quad (4.6)$$

$$c(\text{\AA}) = 6.505(4) - 0.002(5) \cdot x \quad (4.7)$$

$$V(\text{\AA})^3 = 306.5(3) - 5.4(4) \cdot x \quad (4.8)$$

**For  $(\text{La}_{1-x}\text{Ba}_{x/2}\text{Th}_{x/2})\text{PO}_4$  ( $0 \leq x \leq 0.3$ ):**

$$a(\text{\AA}) = 6.839(1) + 0.055(4) \cdot x \quad (4.9)$$

$$b(\text{\AA}) = 7.078(1) + 0.036(6) \cdot x \quad (4.10)$$

$$c(\text{\AA}) = 6.510(1) + 0.11(1) \cdot x \quad (4.11)$$

$$V(\text{\AA})^3 = 306.7(1) + 9.2(7) \cdot x \quad (4.12)$$

In  $(\text{La}_{1-x}\text{M}_{x/2}\text{Th}_{x/2})\text{PO}_4$  ( $0 \leq x \leq 1$ ) ( $M = \text{Ca}, \text{Sr}$  and  $\text{Ba}$ ) solid solutions,  $\text{Th}^{4+}$  and  $\text{M}^{2+}$  ( $M = \text{Ca}, \text{Sr}$  and  $\text{Ba}$ ) ions are randomly substituted at  $\text{La}^{3+}$  ion lattice sites. As the average ionic radii of  $(\text{Ca}^{2+}, \text{Th}^{4+})$  (1.135 Å) and  $(\text{Sr}^{2+}, \text{Th}^{4+})$  (1.2 Å) couple in nine fold co-ordination was less than that of  $\text{La}^{3+}$  ion (1.216 Å), it was observed that with increase in coupled substitution of these pairs, the lattice parameters were decreased [174], whereas the average ionic radii of  $(\text{Ba}^{2+}, \text{Th}^{4+})$  couple (1.28 Å) in nine fold co-ordination was more than that of  $\text{La}^{3+}$  ion, thus it resulted in increase of the lattice parameters on substitution of  $(\text{Ba}^{2+}, \text{Th}^{4+})$  couple as shown in **Figs. 4.1–4.6**. The XRD data were refined using Rietveld refinement method for various compositions of  $(\text{La}_{1-x}\text{M}_{x/2}\text{Th}_{x/2})\text{PO}_4$  ( $0 \leq x \leq 1$ ) ( $M = \text{Ca}, \text{Sr}$  and  $\text{Ba}$ ) solid solutions. The derived cell parameters and the refined structural parameters for the different solid solutions are listed in **Tables 4.3–4.5**.

**Table 4.3:** Refined structural parameters of  $(La_{1-x}Ca_x/2Th_{x/2})PO_4$  ( $x = 0, 0.15, 0.25, 0.40, 0.60, 0.75, 0.85, 1$ ) compositions at 298 K and pressure of 101.325 kPa<sup>a</sup>.

Sample	LaPO <sub>4</sub>	(La <sub>0.85</sub> Ca <sub>0.075</sub> Th <sub>0.075</sub> )PO <sub>4</sub>	(La <sub>0.75</sub> Ca <sub>0.125</sub> Th <sub>0.125</sub> )PO <sub>4</sub>	(La <sub>0.6</sub> Ca <sub>0.2</sub> Th <sub>0.2</sub> )PO <sub>4</sub>	(La <sub>0.4</sub> Ca <sub>0.3</sub> Th <sub>0.3</sub> )PO <sub>4</sub>	(La <sub>0.25</sub> Ca <sub>0.375</sub> Th <sub>0.375</sub> )PO <sub>4</sub>	(La <sub>0.15</sub> Ca <sub>0.425</sub> Th <sub>0.425</sub> )PO <sub>4</sub>	(Ca <sub>0.5</sub> Th <sub>0.5</sub> )PO <sub>4</sub>
a <sup>b</sup> (Å)	6.8399(2)	6.8231(2)	6.8140(2)	6.7821(2)	6.7522(2)	6.7261(2)	6.7203(2)	6.7073(2)
b <sup>b</sup> (Å)	7.0794(2)	7.0481(3)	7.0469(3)	7.0093(3)	6.9713(3)	6.9461(3)	6.9332(3)	6.9136(2)
c <sup>b</sup> (Å)	6.5087(2)	6.4963(2)	6.4932(2)	6.4762(2)	6.4541(2)	6.4312(2)	6.4211(2)	6.4134(2)
β <sup>b</sup> (°)	103.276(2)	103.341(2)	103.356(2)	103.432(2)	103.541(2)	103.614(2)	103.603(2)	103.715(1)
V <sup>b</sup> (Å <sup>3</sup> )	306.74(2)	303.97(2)	303.35(2)	299.44(2)	295.36(2)	292.02(2)	290.78(2)	288.92(1)
ρ <sup>b,c</sup> (g·cm <sup>-3</sup> )	5.063(3)	5.100(2)	5.104(2)	5.162(2)	5.220(2)	5.270(2)	5.286(2)	5.310(2)
U <sup>b</sup>	0.079(1)	0.22(1)	0.22(1)	0.22(1)	0.22(1)	0.22(1)	0.22(1)	0.126(7)
V <sup>b</sup>	-0.089(1)	-0.17(1)	-0.17(1)	-0.17(1)	-0.17(1)	-0.17(1)	-0.17(1)	-0.109(6)
W <sup>b</sup>	0.053(2)	0.074(2)	0.074(2)	0.074(2)	0.074(2)	0.074(2)	0.074(2)	0.053(1)
χ <sup>2</sup>	4.33	2.41	2.41	2.41	2.41	2.41	2.41	1.32
R <sub>p</sub>	16.6	9.43	9.43	9.43	9.43	9.43	9.43	10.1
R <sub>wp</sub>	19.9	11.8	11.8	11.8	11.8	11.8	11.8	11.4
R <sub>exp</sub>	9.54	7.59	7.59	7.59	7.59	7.59	7.59	9.96
Space group	P2 <sub>1</sub> /n	P2 <sub>1</sub> /n	P2 <sub>1</sub> /n	P2 <sub>1</sub> /n	P2 <sub>1</sub> /n	P2 <sub>1</sub> /n	P2 <sub>1</sub> /n	P2 <sub>1</sub> /n

<sup>a</sup>The standard uncertainty u(T) = 0.5 K, Expanded uncertainty U(P) = 4500 Pa (0.997 level of confidence).<sup>b</sup>The numbers in the parenthesis represent the standard uncertainties.<sup>c</sup>Density was estimated using the formula:  $\rho = (Z \cdot M) / (V \cdot N_A)$ Where,  $\rho$  = density in g·cm<sup>-3</sup>

Z = No. of formula units per unit cell

M = Formula weight of the compound in g·mol<sup>-1</sup>V = unit cell volume in cm<sup>3</sup>N<sub>A</sub> = Avogadro number in mol<sup>-1</sup>

**Table 4.4:** Refined structural parameters of  $(\text{La}_{1-x}\text{Sr}_x\text{Th}_{x/2})\text{PO}_4$  ( $x = 0, 0.2, 0.4, 0.6, 0.8, 1$ ) ( $0 \leq x \leq 1$ ) composition at 298 K and pressure of 101.325 kPa<sup>a</sup>.

Sample	$\text{LaPO}_4$	$(\text{La}_{0.8}\text{Sr}_{0.1}\text{Th}_{0.1})\text{PO}_4$	$(\text{La}_{0.6}\text{Sr}_{0.2}\text{Th}_{0.2})\text{PO}_4$	$(\text{La}_{0.4}\text{Sr}_{0.3}\text{Th}_{0.3})\text{PO}_4$	$(\text{La}_{0.2}\text{Sr}_{0.4}\text{Th}_{0.4})\text{PO}_4$	$(\text{Sr}_{0.5}\text{Th}_{0.5})\text{PO}_4$
$a^b(\text{Å})$	6.8399(2)	6.8168(2)	6.8141(2)	6.8093(2)	6.8009(1)	6.7909(1)
$b^b(\text{Å})$	7.0794(2)	7.0497(3)	7.0445(1)	7.0362(1)	7.0249(2)	7.0129(2)
$c^b(\text{Å})$	6.5087(2)	6.4986(2)	6.5063(3)	6.5097(2)	6.5086(1)	6.5045(1)
$\beta^b(^{\circ})$	103.276(2)	103.322(2)	103.385(2)	103.446(1)	103.503(2)	103.555(1)
$V^b(\text{Å}^3)$	306.74(2)	303.89(2)	303.83(1)	303.34(2)	302.36(1)	301.14(2)
$\rho^{b,c}(\text{g}\cdot\text{cm}^{-3})$	5.063(3)	5.203(2)	5.295(1)	5.395(1)	5.505(2)	5.619(1)
$U^b$	0.079(1)	0.25(1)	0.29(1)	0.29(1)	0.23(2)	0.21(1)
$V^b$	-0.089(1)	-0.24(1)	-0.19(1)	-0.21(2)	-0.20(1)	-0.17(2)
$W^b$	0.053(2)	0.086(2)	0.065(1)	0.075(2)	0.068(1)	0.057(1)
$\chi^2$	4.33	1.90	1.51	1.70	1.52	1.49
$R_p$	16.6	12.8	11.8	12.1	10.8	10.6
$R_{wp}$	19.9	16.9	12.7	15.6	13.9	13.3
$R_{exp}$	9.54	12.31	10.37	11.96	11.29	10.95
Space group	$P2_1/n$	$P2_1/n$	$P2_1/n$	$P2_1/n$	$P2_1/n$	$P2_1/n$

<sup>a</sup>The standard uncertainty  $u(T) = 0.5$  K, Expanded uncertainty  $U(P) = 4500$  Pa (0.997 level of confidence).<sup>b</sup>The numbers in the parenthesis represent the standard uncertainties.<sup>c</sup>Density was estimated using the formula:  $\rho = (Z \cdot M) / (V \cdot N_A)$ Where,  $\rho$  = density in  $\text{g}\cdot\text{cm}^{-3}$  $Z$  = No. of formula units per unit cell $M$  = Formula weight of the compound in  $\text{g}\cdot\text{mol}^{-1}$  $V$  = unit cell volume in  $\text{cm}^3$  $N_A$  = Avogadro number in  $\text{mol}^{-1}$

**Table 4.5:** Refined structural parameters of  $(\text{La}_{1-x}\text{Ba}_x/2\text{Th}_x/2)\text{PO}_4$  ( $x = 0, 0.1, 0.2, 0.3; x = 1$ ) compositions at 298 K and pressure of 101.325 kPa<sup>a</sup>.

Sample	$\text{LaPO}_4$	$(\text{La}_{0.9}\text{Ba}_{0.05}\text{Th}_{0.05})\text{PO}_4$	$(\text{La}_{0.8}\text{Ba}_{0.1}\text{Th}_{0.1})\text{PO}_4$	$(\text{La}_{0.7}\text{Ba}_{0.15}\text{Th}_{0.15})\text{PO}_4$	$(\text{Ba}_{0.5}\text{Th}_{0.5})\text{PO}_4$
$a^b(\text{\AA})$	6.8399(2)	6.8443(2)	6.8515(2)	6.8559(3)	12.8012(2)
$b^b(\text{\AA})$	7.0794(2)	7.0804(2)	7.0857(3)	7.0896(2)	5.4376(2)
$c^b(\text{\AA})$	6.5087(2)	6.5215(3)	6.5354(2)	6.5416(2)	9.4611(3)
$\beta^b(^{\circ})$	103.276(2)	103.291(2)	103.300(3)	103.307(2)	102.241(2)
$V^b(\text{\AA}^3)$	306.74(2)	307.57(3)	308.77(2)	309.42(2)	643.59(2)
$\rho^{b,c}(\text{g}\cdot\text{cm}^{-3})$	5.063(3)	5.148(2)	5.227(1)	5.314(1)	5.771(2)
$U^b$	0.079(1)	0.255(2)	0.259(1)	0.246(2)	0.287(2)
$V^b$	-0.089(1)	-0.237(1)	-0.206(1)	-0.195(2)	-0.157(2)
$W^b$	0.053(2)	0.086(2)	0.072(2)	0.069(1)	0.099(1)
$\chi^2$	4.33	1.35	1.43	1.44	2.31
$R_p$	16.6	10.5	10.7	10.6	11.7
$R_{\text{wip}}$	19.9	14.5	15.4	14.4	15.2
$R_{\text{exp}}$	9.54	12.4	12.8	12.0	14.5
Space group	$P2_1/n$	$P2_1/n$	$P2_1/n$	$P2_1/n$	$C2/c$

<sup>a</sup>The standard uncertainty  $u(T) = 0.5$  K, Expanded uncertainty  $U(P) = 4500$  Pa (0.997 level of confidence).

<sup>b</sup>The numbers in the parenthesis represent the standard uncertainties.

<sup>c</sup>Density was estimated using the formula:  $\rho = (Z \cdot M) / (V \cdot N_A)$

Where,  $\rho$  = density in  $\text{g}\cdot\text{cm}^{-3}$

$Z$  = No. of formula units per unit cell

$M$  = Formula weight of the compound in  $\text{g}\cdot\text{mol}^{-1}$

$V$  = unit cell volume in  $\text{cm}^3$

$N_A$  = Avogadro number in  $\text{mol}^{-1}$

The lattice parameters and densities for LaPO<sub>4</sub> measured in the present work have been compared with the reported values in **Table 4.6** and found to be in good agreement.

**Table 4.6:** Comparison of lattice parameters viz. a, b, c, unit-cell volume (V) and density ( $\rho$ ) of LaPO<sub>4</sub> and (M<sub>0.5</sub>Th<sub>0.5</sub>)PO<sub>4</sub> (M = Ca, Sr and Ba) at 298 K and pressure of 101.325 kPa<sup>a</sup> with that of the reported data in literature.

Compound	a <sup>b</sup> (Å)	b <sup>b</sup> (Å)	c <sup>b</sup> (Å)	V <sup>b</sup> (Å <sup>3</sup> )	$\rho^{b,c}$ (g.cm <sup>-3</sup> )
<b>LaPO<sub>4</sub></b>					
This work <sup>a</sup>	6.8399(2)	7.0794(2)	6.5087(2)	306.74(2)	5.063(3)
Neumeier et al. [168]	6.8421(1)	7.0782(1)	6.5121(1)	306.94(3)	5.060(5)
Gavrichev et al. [175]	6.841(3)	7.065(3)	6.503(2)	305.91(2)	5.077(3)
Mullica et al. [176]	6.825(4)	7.057(2)	6.482(2)	303.9(3)	5.120(4)
Ushakov et al. [177]	6.8242(6)	7.0792(5)	6.4919(6)	305.58(5)	5.082(8)
<b>Ca<sub>0.5</sub>Th<sub>0.5</sub>PO<sub>4</sub></b>					
This work <sup>a</sup>	6.7073(2)	6.9136(2)	6.4134(2)	288.92(1)	5.310(2)
Raison et al. [178]	6.7085(8)	6.9160(6)	6.4152(6)	289.16(1)	5.306(1)
Popa et al. [179]	6.7066(10)	6.9149(8)	6.4137(8)	289.3(1)	5.303(1)
Hikichi et al [180]	6.681	6.926	6.421	288.4	5.320
Rose [181]	6.708	6.914	6.409	288.7	5.314
Podor and Cuney [182]	6.706	6.918	6.417	289.3	5.303
Montel et al. [183]	6.714	6.921	6.424	290.0	5.291
<b>Sr<sub>0.5</sub>Th<sub>0.5</sub>PO<sub>4</sub></b>					
This work <sup>a</sup>	6.7909(1)	7.0129(2)	6.5045(1)	301.14(2)	5.619(1)
Keskar et al. [184]	6.8011(2)	7.0229(2)	6.5143(2)	302.52(1)	5.594(2)
<b>Ba<sub>0.5</sub>Th<sub>0.5</sub>PO<sub>4</sub></b>					
This work <sup>a</sup>	12.8012(2)	5.4376(2)	9.4611(3)	643.59(2)	5.771(2)
Wallez et al. [185]	12.8053(7)	5.4400(3)	9.4636(5)	644.2(1)	5.766(1)

<sup>a</sup>The standard uncertainty  $u(T) = 0.5$  K, Expanded uncertainty  $U(P) = 4500$  Pa (0.997 level of confidence).

<sup>b</sup>The numbers in the parenthesis represent the standard uncertainties.

<sup>c</sup>Density was estimated using the formula:  $\rho = (Z \cdot M) / (V \cdot N_A)$

Where,  $\rho$  = density in g.cm<sup>-3</sup>

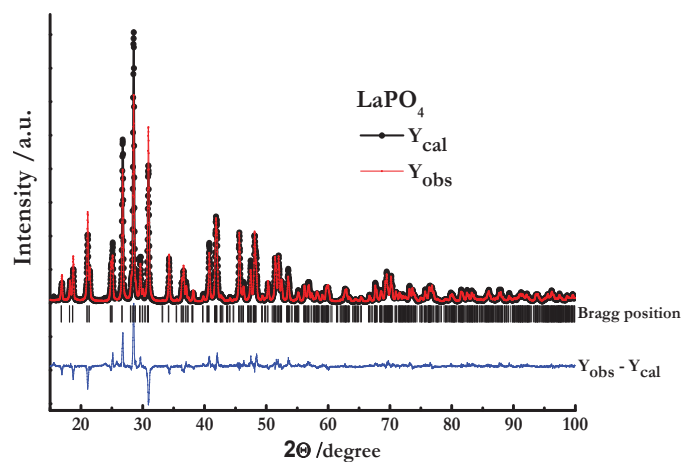
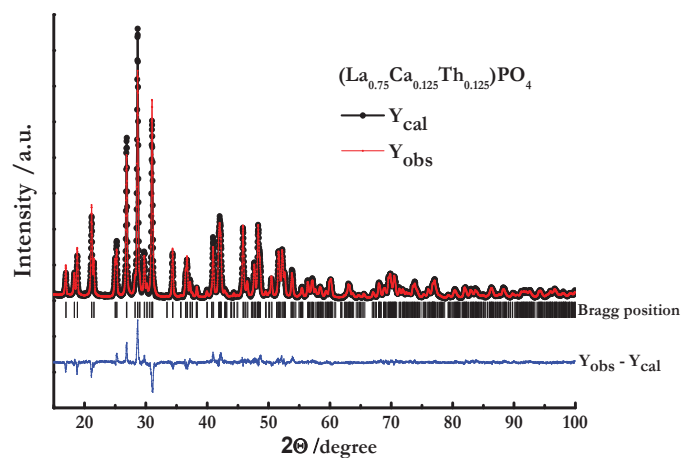
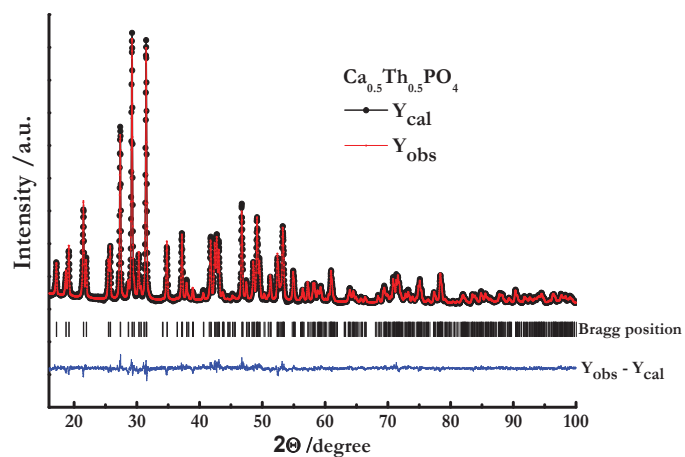
Z = No. of formula units per unit cell

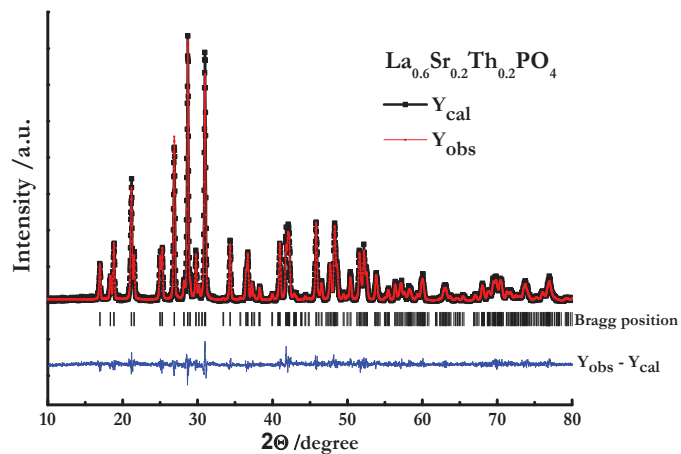
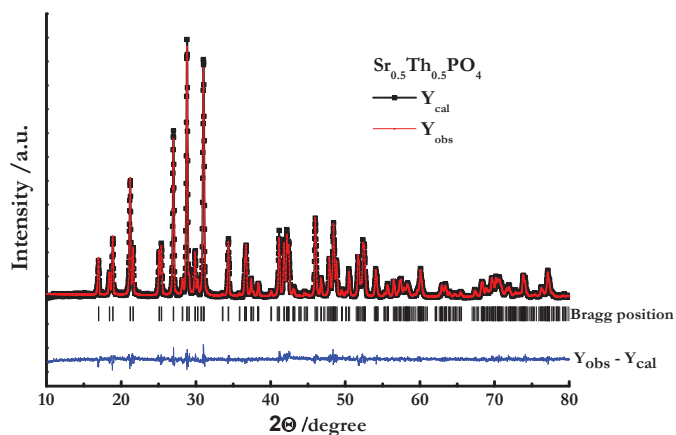
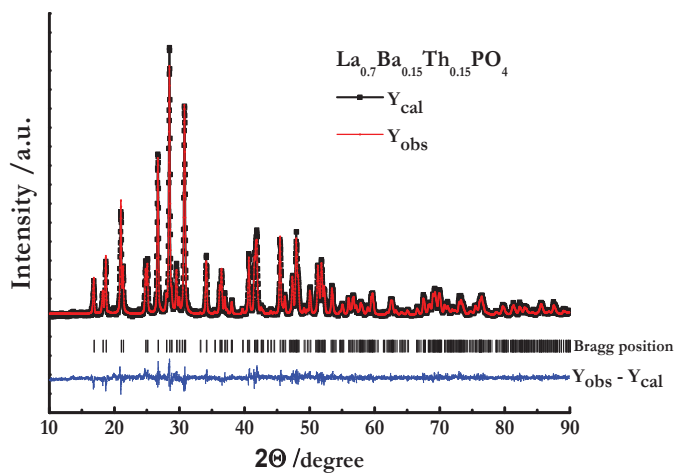
M = Formula weight of the compound in g.mol<sup>-1</sup>

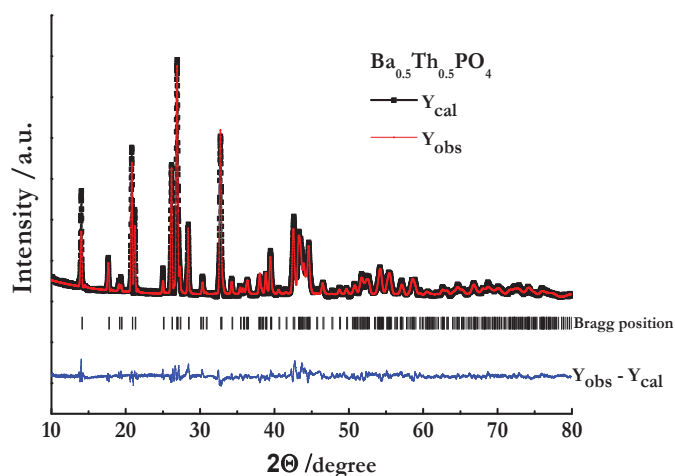
V = unit cell volume in cm<sup>3</sup>

N<sub>A</sub> = Avogadro number in mol<sup>-1</sup>

Rietveld refinement plots of representative compositions viz., LaPO<sub>4</sub>, (La<sub>0.75</sub>Ca<sub>0.125</sub>Th<sub>0.125</sub>)PO<sub>4</sub>, Ca<sub>0.5</sub>Th<sub>0.5</sub>PO<sub>4</sub>, (La<sub>0.6</sub>Sr<sub>0.2</sub>Th<sub>0.2</sub>)PO<sub>4</sub>, Sr<sub>0.5</sub>Th<sub>0.5</sub>PO<sub>4</sub>, (La<sub>0.7</sub>Ba<sub>0.15</sub>Th<sub>0.15</sub>)PO<sub>4</sub> and Ba<sub>0.5</sub>Th<sub>0.5</sub>PO<sub>4</sub> are shown in **Figs. 4.10–4.16**. The results indicate that the above compounds belong to monoclinic crystal structure.

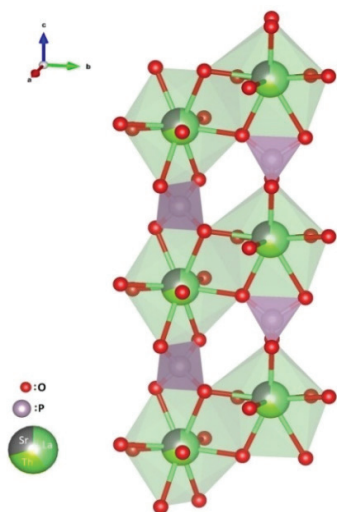
Fig. 4.10: Rietveld plot for LaPO<sub>4</sub>.Fig. 4.11: Rietveld plot for (La<sub>0.75</sub>Ca<sub>0.125</sub>Th<sub>0.125</sub>)PO<sub>4</sub>.Fig. 4.12: Rietveld plot for Ca<sub>0.5</sub>Th<sub>0.5</sub>PO<sub>4</sub>.

Fig. 4.13: Rietveld plot for  $(\text{La}_{0.6}\text{Sr}_{0.2}\text{Th}_{0.2})\text{PO}_4$ .Fig. 4.14: Rietveld plot for  $\text{Sr}_{0.5}\text{Th}_{0.5}\text{PO}_4$ .Fig. 4.15: Rietveld plot for  $(\text{La}_{0.7}\text{Ba}_{0.15}\text{Th}_{0.15})\text{PO}_4$ .



**Fig. 4.16:** Rietveld plot for  $\text{Ba}_{0.5}\text{Th}_{0.5}\text{PO}_4$ .

VESTA program [186] is used to draw the crystal structure of a representative composition i.e.  $(\text{La}_{0.4}\text{Sr}_{0.3}\text{Th}_{0.3})\text{PO}_4$  given in **Fig. 4.17** using Rietveld data as the input parameters.



**Fig. 4.17:** Crystal structure of  $(\text{La}_{0.4}\text{Sr}_{0.3}\text{Th}_{0.3})\text{PO}_4$  using VESTA program [186].

From the crystal structure of  $(\text{La}_{0.4}\text{Sr}_{0.3}\text{Th}_{0.3})\text{PO}_4$ , it can be observed that in solid solutions,  $\text{La}^{3+}$  ion is randomly substituted by either  $\text{Sr}^{2+}$  or  $\text{Th}^{4+}$  ion resulting in the formation of  $(\text{Sr,Th})\text{O}_9$  polyhedra. It can also be noted that  $\text{Sr}^{2+}$  and  $\text{Th}^{4+}$  ions form a regular solid solution in the entire composition range in conformity with the Vegard's law.

### 4.3.3. Heat capacity measurements

Heat capacity,  $C_p^{\circ}(T)$  measurements for  $\text{La}_{1-x}\text{M}_{x/2}\text{Th}_{x/2}\text{PO}_4$  ( $0 \leq x \leq 1$ ) ( $M = \text{Ca}, \text{Sr}$  and  $\text{Ba}$ ) samples were carried out in the temperature range 300–800 K at a heating rate of  $7.5 \text{ K}\cdot\text{min}^{-1}$ . The DSC data has been validated using the heat capacity values of high purity  $\text{ZrO}_2$  (monoclinic) as shown in **Fig. 4.18** and the measured data has been given in **Table 4.7**. The expected uncertainty in measured heat capacity values is less than 4%.

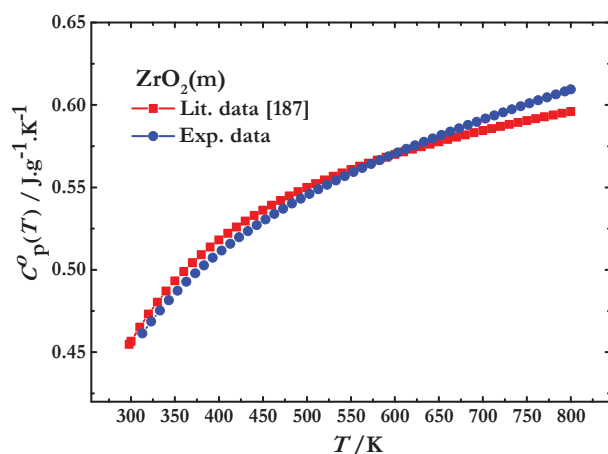


**Fig. 4.18:** Comparison of specific heat capacity of  $\text{ZrO}_2$  as a function of temperature with literature data [187].

**Table 4.7:** Experimentally observed data for specific heat capacity of  $\text{ZrO}_2$ .

$T/\text{K}$	$C_p^{\circ}$ $/\text{J}\cdot\text{g}^{-1}\cdot\text{K}^{-1}$	$^a u(C_p^{\circ})$ $/\text{J}\cdot\text{g}^{-1}\cdot\text{K}^{-1}$	$T/\text{K}$	$C_p^{\circ}$ $/\text{J}\cdot\text{g}^{-1}\cdot\text{K}^{-1}$	$^a u(C_p^{\circ})$ $/\text{J}\cdot\text{g}^{-1}\cdot\text{K}^{-1}$
313	0.46	0.02	573	0.56	0.02
333	0.48	0.02	593	0.57	0.02
353	0.49	0.01	613	0.57	0.02
373	0.50	0.02	633	0.58	0.02
393	0.51	0.02	653	0.58	0.02
413	0.52	0.02	673	0.59	0.01
433	0.52	0.01	693	0.59	0.02
453	0.53	0.02	713	0.59	0.02
473	0.54	0.02	733	0.60	0.02
493	0.54	0.01	753	0.60	0.02
513	0.55	0.02	773	0.60	0.02
533	0.55	0.02	793	0.61	0.02
553	0.56	0.01	800	0.61	0.02

<sup>a</sup>The standard uncertainty in heat capacity  $u(C_p^{\circ})$ .

The measured heat capacity values of  $\text{LaPO}_4$  and  $\text{Ca}_{0.5}\text{Th}_{0.5}\text{PO}_4$  along with that reported in the literature and estimated values using Neumann–Kopp rule in the temperature range of 298–800 K are shown in **Fig. 4.19** and **Fig. 4.20**, respectively. In both the cases, the observed deviation in the heat capacity values of the compounds from Neumann–Kopp rule could be due to the difference in co-ordination number of the metal cations in the constituent oxides compared to that in  $\text{LaPO}_4$  and  $\text{Ca}_{0.5}\text{Th}_{0.5}\text{PO}_4$ .

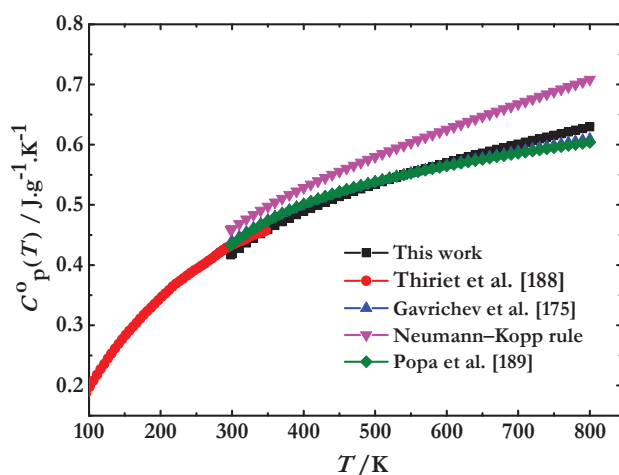


**Fig. 4.19:** Comparison of specific heat capacity of  $\text{LaPO}_4$  as a function of temperature.

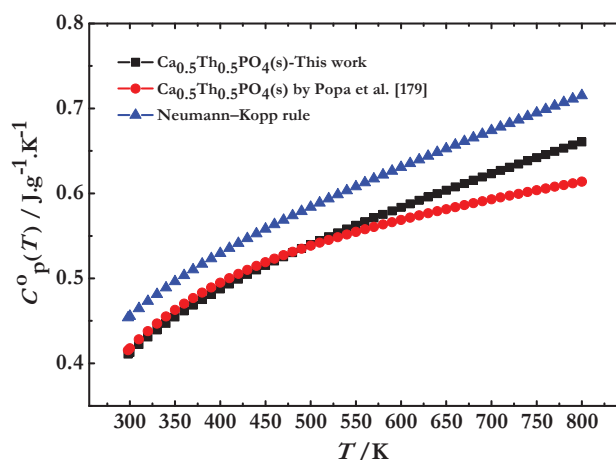


**Fig. 4.20:** A comparison of specific heat capacity of  $\text{Ca}_{0.5}\text{Th}_{0.5}\text{PO}_4$  with that reported by author [179].

The heat capacity data of  $\text{LaPO}_4$  measured in this study are in good agreement (within  $\pm 2.0\%$ ) with the reported values by Gavrichev et al. [175], Thiriet et al. [188] and Popa et al. [189].

The heat capacity data of  $\text{Ca}_{0.5}\text{Th}_{0.5}\text{PO}_4$  measured in this study has been compared with the reported values by Popa et al. [179]. It is apparent from **Fig. 4.20** that the measured data deviate from that of the reported values at higher temperature.

However, the maximum deviation from the reported data is about 7%. This deviation will hardly affect the values of standard molar enthalpy of formation and standard molar free energy of formation of the compounds. This deviation can be attributed to the difference in techniques used to measure the heat capacity of  $\text{Ca}_{0.5}\text{Th}_{0.5}\text{PO}_4$ . In the present study, the heat capacity was measured using DSC in a dynamic mode whereas Popa et al. [179] have carried out the measurements using drop calorimetry.

The experimentally measured specific heat capacity of  $(\text{La}_{1-x}\text{Ca}_{x/2}\text{Th}_{x/2})\text{PO}_4$  ( $x = 0, 0.15, 0.25, 0.40, 0.60, 0.75, 0.85, 1$ ),  $(\text{La}_{1-x}\text{Sr}_{x/2}\text{Th}_{x/2})\text{PO}_4$  ( $x = 0, 0.2, 0.4, 0.6, 0.8, 1$ ) and  $(\text{La}_{1-x}\text{Ba}_{x/2}\text{Th}_{x/2})\text{PO}_4$  ( $x = 0, 0.1, 0.2, 0.3; x = 1$ ) solid solutions are respectively shown in **Figs. 4.21–4.23**. Heat capacity data of  $(\text{La}_{1-x}\text{M}_{x/2}\text{Th}_{x/2})\text{PO}_4$  ( $0 \leq x \leq 1$ ) ( $M = \text{Ca}, \text{Sr}$  and  $\text{Ba}$ ) solid solutions are the mean values of three measurements for each sample. The error derived from the mean standard deviation for the measurements of each sample is less than 2 %.

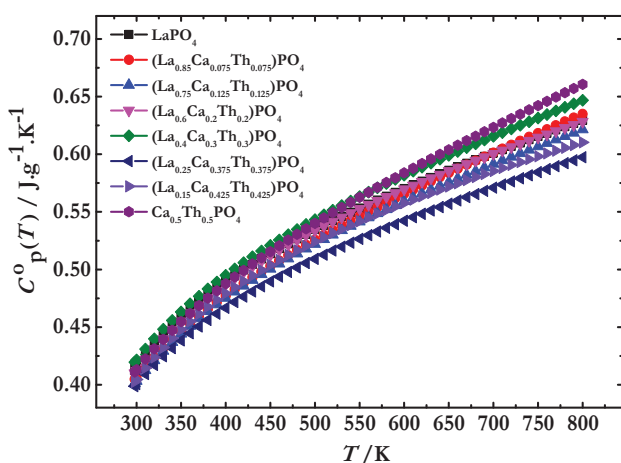


**Fig. 4.21:** Variation of specific heat capacity of  $(\text{La}_{1-x}\text{Ca}_{x/2}\text{Th}_{x/2})\text{PO}_4$  ( $x = 0, 0.15, 0.25, 0.40, 0.60, 0.75, 0.85, 1$ ) solid solutions as a function of temperature.

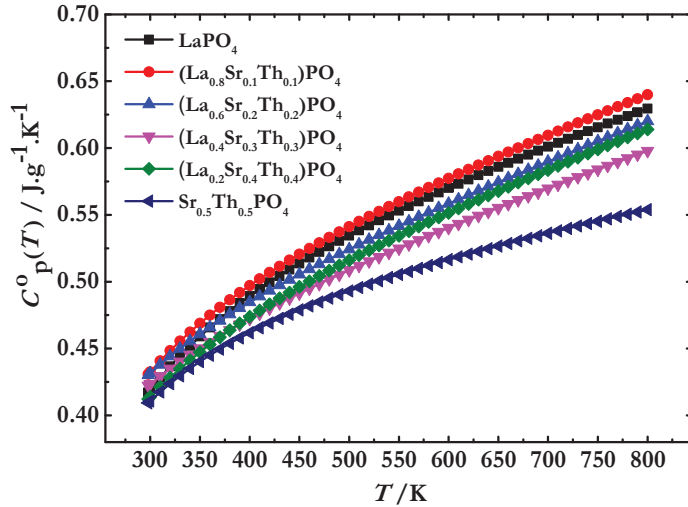


**Fig. 4.22:** Variation of specific heat capacity of  $(\text{La}_{1-x}\text{Sr}_{x/2}\text{Th}_{x/2})\text{PO}_4$  ( $x = 0, 0.2, 0.4, 0.6, 0.8, 1$ ) solid solutions as a function of temperature.

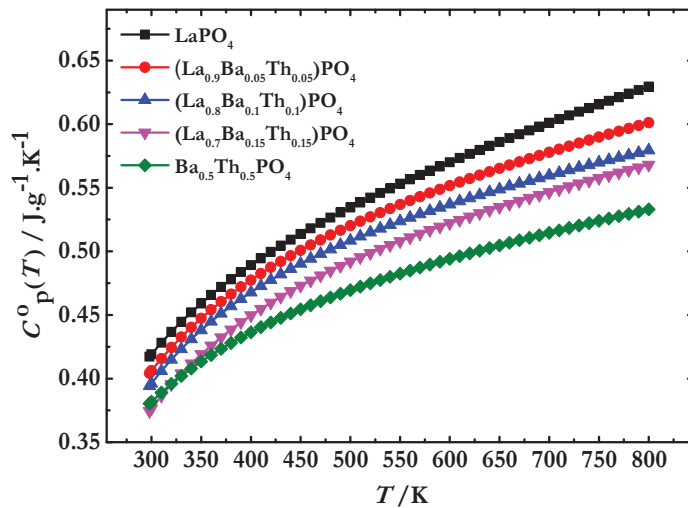


**Fig. 4.23:** Variation of specific heat capacity of  $(\text{La}_{1-x}\text{Ba}_{x/2}\text{Th}_{x/2})\text{PO}_4$  ( $x = 0, 0.1, 0.2, 0.3; x = 1$ ) solid solutions as a function of temperature.

The plots of the specific heat capacity for the intermediate compositions suggest that the heat capacity for the solid solutions is not a simple function of (Ca, Th) and (Sr, Th) content and the heat capacity is not compositionally weighted heat capacities of the constituent oxides [190, 191]. Xiao et al. [192] have also reported similar trend in the heat capacity values for the solid solutions. Konings et al. [171] also observed the excess heat content in  $\text{Ln}_{1-2x}\text{Ca}_x\text{Th}_x\text{PO}_4$  (Ln= La, Ce) solid solutions arising due to substitution using drop solution calorimetry

measurements. The experimental values of specific heat capacity of  $(\text{La}_{1-x}\text{M}_{x/2}\text{Th}_{x/2})\text{PO}_4$  ( $0 \leq x \leq 1$ ) ( $M = \text{Ca}, \text{Sr}$  and  $\text{Ba}$ ) solid solutions were least square fitted to  $a + b \cdot T + c \cdot T^2$  polynomials.

Where coefficients  $a$ ,  $b$ , and  $c$  are constants and ' $T$ ' is absolute temperature. The values of coefficients  $a$ ,  $b$ , and  $c$  in the temperature range 298-800 K are given in **Table 4.8**.

**Table 4.8:** Coefficients of specific heat capacity of  $(\text{La}_{1-x}\text{M}_{x/2}\text{Th}_{x/2})\text{PO}_4$  ( $0 \leq x \leq 1$ ) ( $M = \text{Ca}, \text{Sr}$  and  $\text{Ba}$ ) samples as a function of temperature ( $298 \leq T/\text{K} \leq 800$ ) at a pressure of 101.325 kPa<sup>a</sup>.

Composition	$C_p^0 / \text{J} \cdot \text{g}^{-1} \cdot \text{K}^{-1}$		
	$a$	$b \cdot 10^4$	$-c$
<b><math>(\text{La}_{1-x}\text{Ca}_{x/2}\text{Th}_{x/2})\text{PO}_4</math> (<math>0 \leq x \leq 1</math>)</b>			
$\text{LaPO}_4$	0.4528	2.4	9497
$(\text{La}_{0.85}\text{Ca}_{0.075}\text{Th}_{0.075})\text{PO}_4$	0.4117	3.0	8443
$(\text{La}_{0.75}\text{Ca}_{0.125}\text{Th}_{0.125})\text{PO}_4$	0.4340	2.5	9616
$(\text{La}_{0.6}\text{Ca}_{0.2}\text{Th}_{0.2})\text{PO}_4$	0.4628	2.3	10720
$(\text{La}_{0.4}\text{Ca}_{0.3}\text{Th}_{0.3})\text{PO}_4$	0.4482	2.7	9618
$(\text{La}_{0.25}\text{Ca}_{0.375}\text{Th}_{0.375})\text{PO}_4$	0.4354	2.2	9088
$(\text{La}_{0.15}\text{Ca}_{0.425}\text{Th}_{0.425})\text{PO}_4$	0.4725	1.9	11376
$\text{Ca}_{0.5}\text{Th}_{0.5}\text{PO}_4$	0.4086	3.3	8518
<b><math>(\text{La}_{1-x}\text{Sr}_{x/2}\text{Th}_{x/2})\text{PO}_4</math> (<math>0 \leq x \leq 1</math>)</b>			
$(\text{La}_{0.8}\text{Sr}_{0.1}\text{Th}_{0.1})\text{PO}_4$	0.4599	2.6	8447
$(\text{La}_{0.6}\text{Sr}_{0.2}\text{Th}_{0.2})\text{PO}_4$	0.4071	2.8	5272
$(\text{La}_{0.4}\text{Sr}_{0.3}\text{Th}_{0.3})\text{PO}_4$	0.3975	2.6	4675
$(\text{La}_{0.2}\text{Sr}_{0.4}\text{Th}_{0.4})\text{PO}_4$	0.4074	2.7	6755
$\text{Sr}_{0.5}\text{Th}_{0.5}\text{PO}_4$	0.4529	1.4	7614
<b><math>(\text{La}_{1-x}\text{Ba}_{x/2}\text{Th}_{x/2})\text{PO}_4</math> (<math>0 \leq x \leq 0.3, x = 1</math>)</b>			
$(\text{La}_{0.9}\text{Ba}_{0.05}\text{Th}_{0.05})\text{PO}_4$	0.4734	1.8	10941
$(\text{La}_{0.8}\text{Ba}_{0.1}\text{Th}_{0.1})\text{PO}_4$	0.4859	1.4	11852
$(\text{La}_{0.7}\text{Ba}_{0.15}\text{Th}_{0.15})\text{PO}_4$	0.4601	1.6	11789
$\text{Ba}_{0.5}\text{Th}_{0.5}\text{PO}_4$	0.4303	1.4	8264

<sup>a</sup>The standard uncertainty  $u(T) = 0.5$  K, Expanded uncertainty  $U(P) = 5000$  Pa (0.997 level of confidence).

#### 4.3.4. Enthalpy of dissolution ( $\Delta H_{\text{ds}}$ ) measurements

Standard molar enthalpy of formation,  $\Delta H_{\text{f,m}}^0(298 \text{ K})$  of  $(\text{La}_{1-x}\text{M}_{x/2}\text{Th}_{x/2})\text{PO}_4$  ( $0 \leq x \leq 1$ )

( $M = \text{Ca}, \text{Sr}$  and  $\text{Ba}$ ) compositions were derived from the molar enthalpy of dissolution,  $\Delta H_{\text{ds}}$

data of each of these compositions together with their component oxides viz.,  $\text{La}_2\text{O}_3$ ,  $\text{MO}$  ( $M = \text{Ca}, \text{Sr}$  and  $\text{Ba}$ ),  $\text{ThO}_2$  and  $\text{P}_2\text{O}_5$  in molten  $\text{PbO} + \text{B}_2\text{O}_3$  (2:1 molar ratio) solvent maintained at 1089 K. The details of the experimental measurements have been described in Section 2.4.2 of Chapter 2.

Since  $\text{P}_2\text{O}_5$  is highly hygroscopic and reactive material, the value of molar enthalpy of dissolution of  $\text{P}_2\text{O}_5$  was therefore, obtained indirectly by means of a separate thermo-chemical cycle using enthalpy of dissolution of  $\text{Ca}_3(\text{PO}_4)_2$ . **Table 4.9** gives the thermo-chemical cycle for derivation of standard molar enthalpies of dissolution of  $\text{P}_2\text{O}_5(s, 298\text{K})$ .

**Table 4.9:** Thermo-chemical cycles for calculation of standard molar enthalpy of dissolution<sup>a</sup> ( $\Delta H_{\text{ds}}$ ) of  $\text{P}_2\text{O}_5$  from temperature 298K ( $T_r$ ) to temperature of solvent<sup>b</sup> 1089 K ( $T_s$ ) at pressure  $P = 101.325 \text{ kPa}^c$ .

$$\Delta H_{\text{ds}}(\text{P}_2\text{O}_5) = \Delta H_1 + \Delta H_2 - 3\Delta H_3 - 3\Delta H_4 - \Delta H_5$$

Reactions	$\Delta H_i$	$\Delta H / \text{kJ} \cdot \text{mol}^{-1}$
$\text{Ca}_3(\text{PO}_4)_2(s, 298\text{K}) = 3\text{CaO}(s_{\text{ln}}, 1089\text{K}) + \text{P}_2\text{O}_5(s_{\text{ln}}, 1089\text{K})$	$\Delta H_1 = \Delta H_{\text{ds}}[\text{Ca}_3(\text{PO}_4)_2]$	$358.9 \pm 0.8^{\text{d,e}}$
$3\text{Ca}(s, 298\text{K}) + 2\text{P}(s, 298\text{K}) + 4\text{O}_2(g, 298\text{K}) = \text{Ca}_3(\text{PO}_4)_2(s, 298\text{K})$	$\Delta H_2 = \Delta H_{\text{f}}^\circ[\text{Ca}_3(\text{PO}_4)_2]$	$-4120.8 \pm 5.0^{[193]}$
$\text{CaO}(s, 298\text{K}) = \text{CaO}(s_{\text{ln}}, 1089\text{K})$	$\Delta H_3 = \Delta H_{\text{ds}}(\text{CaO})$	$-8.4 \pm 2.0^{\text{d,e}}$
$\text{Ca}(s, 298\text{K}) + 1/2 \cdot \text{O}_2(g, 298\text{K}) = \text{CaO}(s, 298\text{K})$	$\Delta H_4 = \Delta H_{\text{f}}^\circ(\text{CaO})$	$-635.1 \pm 0.9^{[193]}$
$2\text{P}(s, 298\text{K}) + 5/2 \cdot \text{O}_2(g, 298\text{K}) = \text{P}_2\text{O}_5(s, 298\text{K})$	$\Delta H_5 = \Delta H_{\text{f}}^\circ(\text{P}_2\text{O}_5)$	$-1504.9 \pm 0.5^{[193]}$
$\text{P}_2\text{O}_5(s, 298\text{K}) = \text{P}_2\text{O}_5(s_{\text{ln}}, 1089\text{K})$	$\Delta H_{\text{ds}}(\text{P}_2\text{O}_5)$	$-326.5 \pm 8.3^{\text{f}}$

<sup>a</sup>The heat effect associated to dissolution of solid at  $T_r$  in 10g of  $\text{PbO} + \text{B}_2\text{O}_3$  (2:1 molar ratio) at  $T_s$ .

<sup>b</sup>10g of  $\text{PbO} + \text{B}_2\text{O}_3$  (2:1 molar ratio) was used as solvent.

<sup>c</sup>Standard uncertainties  $u$  are  $u(p) = 5000 \text{ Pa}$ ,  $u(T_r) = 0.5 \text{ K}$ ,  $u(T_s) = 0.05 \text{ K}$ .

<sup>d</sup>Expanded uncertainties for  $\Delta H$  with 0.95 level of confidence ( $k \approx 2$ ).

<sup>e</sup>This work.

<sup>f</sup>Uncertainty of the combined reaction is estimated as the square root of the sum of the squares of uncertainty of each individual reaction.

Since  $\text{CaO}$ ,  $\text{SrO}$  and  $\text{BaO}$  are difficult to handle in ambient conditions, their molar enthalpy of dissolution was determined using the enthalpies of dissolution of  $\text{CaCO}_3$ ,  $\text{SrCO}_3$  and  $\text{BaCO}_3$  and other auxiliary data from the literature employing a separate thermo-chemical cycle given in **Table 4.10**.

**Table 4.10:** Thermo-chemical cycles for calculation of standard molar enthalpy of dissolution<sup>a</sup> ( $\Delta H_{ds}$ ) of  $MO$  ( $M = \text{Ca, Sr and Ba}$ ) from temperature 298K ( $T_r$ ) to temperature of solvent<sup>b</sup> 1089 K ( $T_s$ ) at pressure  $P = 101.325 \text{ kPa}^c$ .

$$\Delta H_{ds}(MO) = \Delta H_{ds}(MCO_3) + \Delta H_{f,ox}^0(MCO_3) - \Delta H_{298-1089}(CO_2)$$

Reactions	$\Delta H_i$	$\Delta H / \text{kJ}\cdot\text{mol}^{-1}$
$\text{CaCO}_3(\text{s}, 298 \text{ K}) = \text{CaO}(\text{sln}, 1089 \text{ K}) + \text{CO}_2(\text{sln}, 1089 \text{ K})$	$\Delta H_1 = \Delta H_{ds}(\text{CaCO}_3)$	$209.3 \pm 1.2^{\text{d,e}}$
$\text{SrCO}_3(\text{s}, 298 \text{ K}) = \text{SrO}(\text{sln}, 1089 \text{ K}) + \text{CO}_2(\text{sln}, 1089 \text{ K})$	$\Delta H_2 = \Delta H_{ds}(\text{SrCO}_3)$	$220.1 \pm 2.7^{\text{d,e}}$
$\text{BaCO}_3(\text{s}, 298 \text{ K}) = \text{BaO}(\text{sln}, 1089 \text{ K}) + \text{CO}_2(\text{sln}, 1089 \text{ K})$	$\Delta H_3 = \Delta H_{ds}(\text{BaCO}_3)$	$219.9 \pm 1.4^{\text{d,e}}$
$\text{CaO}(\text{s}, 298 \text{ K}) + \text{CO}_2(\text{g}, 298 \text{ K}) = \text{CaCO}_3(\text{s}, 298 \text{ K})$	$\Delta H_4 = \Delta H_{f,ox}^0(\text{CaCO}_3)$	$-178.8 \pm 1.6^{[193]}$
$\text{SrO}(\text{s}, 298 \text{ K}) + \text{CO}_2(\text{g}, 298 \text{ K}) = \text{SrCO}_3(\text{s}, 298 \text{ K})$	$\Delta H_5 = \Delta H_{f,ox}^0(\text{SrCO}_3)$	$-234.3 \pm 1.8^{[193]}$
$\text{BaO}(\text{s}, 298 \text{ K}) + \text{CO}_2(\text{g}, 298 \text{ K}) = \text{BaCO}_3(\text{s}, 298 \text{ K})$	$\Delta H_6 = \Delta H_{f,ox}^0(\text{BaCO}_3)$	$-269.2 \pm 1.6^{[193]}$
$\text{CO}_2(\text{g}, 298 \text{ K}) = \text{CO}_2(\text{sln}, 1089 \text{ K})$	$\Delta H_7 = \Delta H_{298-1089}(\text{CO}_2)$	$38.9^{[193]}$
$\text{CaO}(\text{s}, 298 \text{ K}) = \text{CaO}(\text{sln}, 1089 \text{ K})$	$\Delta H_8 = \Delta H_{ds}(\text{CaO})$	$-8.4 \pm 2.0^{\text{f}}$
$\text{SrO}(\text{s}, 298 \text{ K}) = \text{SrO}(\text{sln}, 1089 \text{ K})$	$\Delta H_9 = \Delta H_{ds}(\text{SrO})$	$-53.1 \pm 3.2^{\text{f}}$
$\text{BaO}(\text{s}, 298 \text{ K}) = \text{BaO}(\text{sln}, 1089 \text{ K})$	$\Delta H_{10} = \Delta H_{ds}(\text{BaO})$	$-88.2 \pm 2.1^{\text{f}}$

<sup>a</sup>The heat effect associated to dissolution of solid at  $T_r$  in 10g of  $\text{PbO} + \text{B}_2\text{O}_3$  (2:1 molar ratio) at  $T_s$ .

<sup>b</sup>10g of  $\text{PbO} + \text{B}_2\text{O}_3$  (2:1 molar ratio) was used as solvent.

<sup>c</sup>Standard uncertainties  $u$  are  $u(p) = 5000 \text{ Pa}$ ,  $u(T_r) = 0.5 \text{ K}$ ,  $u(T_s) = 0.05 \text{ K}$ .

<sup>d</sup>Expanded uncertainties for  $\Delta H$  with 0.95 level of confidence ( $k \approx 2$ ).

<sup>e</sup>This work.

<sup>f</sup>Uncertainty of the combined reaction is estimated as the square root of the sum of the squares of uncertainty of each individual reaction.

The values of molar enthalpy of dissolution ( $\Delta H_{ds}$ ) of relevant oxides, carbonates and phosphates in molten  $\text{PbO} + \text{B}_2\text{O}_3$  (2:1 molar ratio) solvent at 1089 K measured in this study were compared with the literature values under similar condition are given in **Table 4.11**.

**Table 4.11:** Comparison of enthalpy of dissolution ( $\Delta H_{ds}$ ) values of relevant oxides, carbonates and phosphates with that reported in literature by different authors.

Compounds	$\Delta H_{ds} / \text{kJ}\cdot\text{mol}^{-1}$			
	973–978 K	1073–1078 K	1080 K <sup>[199]</sup>	1089 K <sup>1</sup>
$\text{La}_2\text{O}_3$	$-42.3 \pm 4.4^{\text{d},[194]}$	$-30.91 \pm 0.61^{[197]}$		$-45.9 \pm 0.4^{\text{e}}$
$\text{ThO}_2$		$98.1 \pm 1.7^{[198]}$		$98.2 \pm 0.6$
$\text{CaCO}_3$			$209.51 \pm 1.64$	$209.3 \pm 1.2$
$\text{SrCO}_3$			$226.76 \pm 2.35$	$220.1 \pm 2.7$
$\text{BaCO}_3$	$209.9 \pm 1.7^{[195]}$			$219.9 \pm 1.3$
$\text{CaO}$	$-21.4 \pm 1.9^{\text{d},[196]}$		$-7.08 \pm 2.31$	$-8.4 \pm 2.0$
$\text{SrO}$	$-58.5 \pm 2.0^{\text{d},[194]}$		$-44.93 \pm 2.99$	$-53.1 \pm 3.2$
$\text{BaO}$	$-91.5 \pm 1.9^{[195]}$			$-88.2 \pm 2.1$
$\text{P}_2\text{O}_5$	$-326 \pm 1.21^{[177]}$			$-326.5 \pm 8.3$
$\text{Ca}_3(\text{PO}_4)_2$	$347.4 \pm 4.9^{[179]}$			$358.9 \pm 0.8$

LaPO <sub>4</sub>	141.70±1.25 <sup>[177]</sup>	131.4±1.0
CaTh(PO <sub>4</sub> ) <sub>2</sub>	255.3±4.4 <sup>[179]</sup>	279.6±1.6

<sup>1</sup>This work.

<sup>2</sup>Calculated from heat content and enthalpy of solution.

<sup>3</sup>Calculated from  $\Delta H_{\text{ds}}$  and  $\Delta H_{\text{f}}^{\circ}$  of corresponding carbonates.

The only noticeable difference is the heat of dissolution of La<sub>2</sub>O<sub>3</sub>, where our value  $-45.9 \pm 0.4$  kJ.mol<sup>-1</sup> differs with literature value i.e.  $-30.91 \pm 0.61$  kJ.mol<sup>-1</sup>. The reason for the difference could be due to dissimilar experimental conditions. The fact that our value is more negative indicates absence of any impurity phase like lanthanum oxycarbonate, as decomposition of oxycarbonate would have contributed to the endothermic effect. The enthalpy of dissolution of ThO<sub>2</sub> observed in our experiment  $98.2 \pm 0.6$  kJ.mol<sup>-1</sup> is in close agreement with the literature value  $98.1 \pm 1.7$  kJ.mol<sup>-1</sup> measured in temperature range 1073–1078 K. The enthalpies of dissolution of MCO<sub>3</sub> ( $M = \text{Ca, Sr and Ba}$ ) measured in our experiment are also in good agreement with the corresponding literature values.

The heat of dissolution of CaO in temperature range 973–978 K reported in the literature is  $-21.4 \pm 1.9$  kJ.mol<sup>-1</sup>, whereas the corresponding value in our measurement is  $-8.4 \pm 2.0$  kJ.mol<sup>-1</sup>. The lower negative value is attributed to the higher measurement temperature of 1089 K. At higher temperature there is endothermic contribution due to heat capacity and lower exothermic effect due to lower heat of formation. It can be observed here that similar decrease in exothermic heat effect is observed for La<sub>2</sub>O<sub>3</sub> measured at 975 and 1075 K. The decrease is about 11.4 kJ.mol<sup>-1</sup>. Applying similar effect for CaO dissolution the expected lit value will be around  $-10$  kJ.mol<sup>-1</sup>, which is closer to our value. The heat of dissolution of P<sub>2</sub>O<sub>5</sub> derived from thermodynamic cycle (**Table 4.9**) is also found in agreement with the reported data.

### 4.3.5. Standard molar enthalpy of formation ( $\Delta H_{f,m}^0$ ) of $(La_{1-x}M_{x/2}Th_{x/2})PO_4$ ( $0 \leq x \leq 1$ ) ( $M = Ca, Sr$ and $Ba$ )

#### 4.3.5.1. $(La_{1-x}Ca_{x/2}Th_{x/2})PO_4$ ( $0 \leq x \leq 1$ ) solid solutions:

The molar enthalpy of dissolution ( $\Delta H_{ds}$ ) data measured using oxide melt solution calorimetric study for  $(La_{1-x}Ca_{x/2}Th_{x/2})PO_4$  ( $x = 0, 0.15, 0.25, 0.40, 0.60, 0.75, 0.85, 1$ ) samples,  $La_2O_3$ ,  $CaCO_3$ ,  $ThO_2$  and  $Ca_3(PO_4)_2$  in molten  $PbO+B_2O_3$  (2:1 molar ratio) solvent at 1089 K are provided in **Table 4.12**. The calculation of enthalpy of dissolution for  $CaO$  and  $P_2O_5$  is mentioned in Section 4.3.4 using the values of  $CaCO_3$  and  $Ca_3(PO_4)_2$ , respectively.

**Table 4.12:** The molar enthalpies of dissolution<sup>a</sup> of  $(La_{1-x}Ca_{x/2}Th_{x/2})PO_4$  ( $x = 0, 0.15, 0.25, 0.40, 0.60, 0.75, 0.85, 1$ ),  $La_2O_3$ ,  $CaO$ ,  $ThO_2$  and  $Ca_3(PO_4)_2$  with mass  $m$ , from temperature 298 K ( $T_r$ ) to temperature of solvent<sup>b</sup> 1089 K ( $T_s$ ) at pressure  $P = 101.325$  kPa<sup>c</sup>.

Sample	$m$ /mg	$\Delta H^d$ /J·g <sup>-1</sup>	$\Delta H_{ds}^e$ /kJ·mol <sup>-1</sup>	Ref.
LaPO <sub>4</sub> (233.88 g·mol <sup>-1</sup> )	8.6	562.0	131.4	This work
	7.3	556.3	130.1	
	8.8	563.5	131.8	
	10.0	566.0	132.4	
			<b>Avg.:</b> 131.4±1.0	
$(La_{0.85}Ca_{0.075}Th_{0.075})PO_4$ (233.45 g·mol <sup>-1</sup> )	6.4	683.2	159.5	This work
	8.7	678.9	158.5	
	7.9	685.4	160.0	
	10.0	678.1	158.3	
			<b>Avg.:</b> 159.1±0.8	
$(La_{0.75}Ca_{0.125}Th_{0.125})PO_4$ (233.16 g·mol <sup>-1</sup> )	5.3	744.6	173.6	This work
	10.0	737.3	171.9	
	8.9	745.0	173.7	
	12.1	740.3	172.6	
			<b>Avg.:</b> 173.0±0.9	
$(La_{0.6}Ca_{0.2}Th_{0.2})PO_4$ (232.74 g·mol <sup>-1</sup> )	7.8	696.1	162.0	This work
	8.9	700.8	163.1	
	9.3	690.5	160.7	
	10.0	693.9	161.5	
			<b>Avg.:</b> 161.8±1.0	
$(La_{0.4}Ca_{0.3}Th_{0.3})PO_4$ (232.17 g·mol <sup>-1</sup> )	9.8	668.5	155.2	This work
	7.6	670.2	155.6	
	10.0	662.4	153.8	

	8.3	664.6	154.3	
			<b>Avg.:</b> 154.7±0.8	This work
(La <sub>0.25</sub> Ca <sub>0.375</sub> Th <sub>0.375</sub> )PO <sub>4</sub> (231.74 g·mol <sup>-1</sup> )	4.4	636.9	147.6	
	5.3	639.9	148.3	
	7.8	633.5	146.8	
	10.0	630.0	146.0	
			<b>Avg.:</b> 147.2±1.0	This work
(La <sub>0.15</sub> Ca <sub>0.425</sub> Th <sub>0.425</sub> )PO <sub>4</sub> (231.45 g·mol <sup>-1</sup> )	6.9	599.7	138.8	
	7.2	601.4	139.2	
	10.0	595.8	137.9	
	8.7	594.9	137.7	
			<b>Avg.:</b> 138.4±0.7	This work
Ca <sub>0.5</sub> Th <sub>0.5</sub> PO <sub>4</sub> (231.03 g·mol <sup>-1</sup> )	10.0	606.8	140.2	
	5.8	608.1	140.5	
	10.5	600.8	138.8	
	13.2	603.8	139.5	
			<b>Avg.:</b> 139.8±0.8	This work
La <sub>2</sub> O <sub>3</sub> (325.81 g·mol <sup>-1</sup> )	16.7	-142.8	-46.5	
	13.7	-141.1	-46.0	
	21.6	-140.2	-45.7	
	14.9	-139.9	-45.6	
			<b>Avg.:</b> -45.9 ± 0.4	This work
CaCO <sub>3</sub> (100.08 g·mol <sup>-1</sup> )	15.8	2083.5	208.5	
	16.6	2095.4	209.7	
	15.3	2080.2	208.2	
	17.2	2107.5	210.9	
			<b>Avg.:</b> 209.33±1.2	This work
ThO <sub>2</sub> (264.04 g·mol <sup>-1</sup> )	6.6	374.8	98.8	
	4.6	373.1	98.5	
	3.2	369.1	97.5	
	2.3	371.1	98.0	
			<b>Avg.:</b> 98.2 ± 0.6	This work
Ca <sub>3</sub> (PO <sub>4</sub> ) <sub>2</sub> (310.18 g·mol <sup>-1</sup> )	4.6	1160.3	359.9	
	4.5	1155.3	358.3	
	16.8	1158.2	359.3	
	21.5	1154.5	358.1	
			<b>Avg.:</b> 358.9±0.8	This work

<sup>a</sup>The heat effect associated to dissolution of solid at  $T_r$  in 10g of PbO + B<sub>2</sub>O<sub>3</sub> (2:1 molar ratio) at  $T_s$ .

<sup>b</sup>10g of PbO + B<sub>2</sub>O<sub>3</sub> (2:1 molar ratio) was used as solvent.

<sup>c</sup>Standard uncertainties  $u$  are  $u(p) = 5000$  Pa,  $u(m) = 0.1$  mg,  $u(T_r) = 0.5$  K,  $u(T_s) = 0.05$  K.

<sup>d</sup>The heat effect correspond to the dissolution of solute per unit mass.

<sup>e</sup>Expanded uncertainties for  $\Delta H$  with 0.95 level of confidence ( $k \approx 2$ ).

Heat flow signal plots measured during the drop experiment of (La<sub>1-x</sub>Ca<sub>x/2</sub>Th<sub>x/2</sub>)PO<sub>4</sub> ( $x = 0, 0.15, 0.25, 0.40, 0.60, 0.75, 0.85, 1$ ) samples from room temperature to molten PbO+B<sub>2</sub>O<sub>3</sub> (2:1 molar ratio) solvent at 1089 K are shown in **Fig. 4.24**.

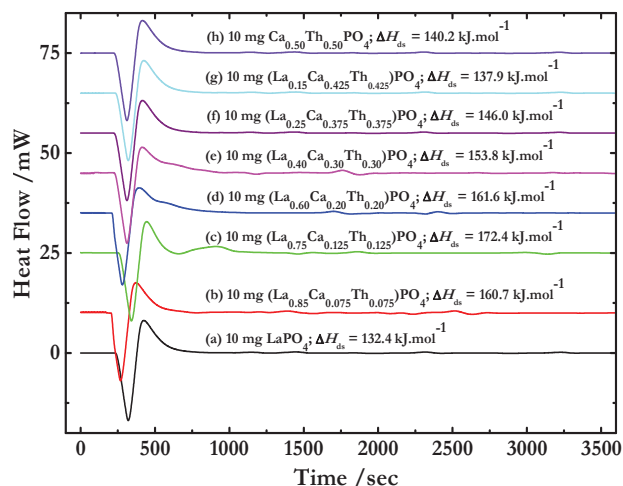


**Fig. 4.24:** Plots of heat flow signals measured for the drop experiments of  $\text{La}_{1-x}\text{Ca}_{x/2}\text{Th}_{x/2}\text{PO}_4$  ( $x = 0, 0.15, 0.25, 0.40, 0.60, 0.75, 0.85, 1$ ) samples.

Endothermic peaks were observed in each of the drop experiment except for  $\text{La}_2\text{O}_3$  and  $\text{CaO}$ . The endothermic enthalpy signal was attributed to the sum of the three heat effects i.e. absorption of heat by the sample heating from 298–1089 K, lattice dissociation energy and dissolution energy. The first two effects are in general endothermic in nature, while the dissolution energy can be either endothermic or exothermic depending on the nature of the solvent-solute interactions. The overall heat effect for dissolution in molten  $\text{PbO}+\text{B}_2\text{O}_3$  (2:1 molar ratio) solvent was calculated using the SETSOFT software supplied along with the instrument. The completion of the reaction between the reactants and the solvent was monitored by recording the heat flow signal for different time intervals. Steady base line in the heat flow signal was observed after one hour of sample dropping beyond which no significant change in the heat flow values could be noticed. Molten  $\text{PbO}+\text{B}_2\text{O}_3$  (2:1 molar ratio) solvent is quite viscous. The rate of dissolution of solute in the solvent depends on the local concentration of the solute. The geometry of the solute particle and extent of compactness determines the rate of diffusion of the solute in the solvent. The ceramic phosphate samples dissolve slowly in the solvent over one hour and depending on conditions they often dissolve over a range of temperature. This effect is probably responsible for appearance of multiple

small exothermic peaks in the dissolution experiments of some samples. When plotted the molar heats of dissolution for all the samples in molten  $\text{PbO}+\text{B}_2\text{O}_3$  (2:1 molar ratio) solvent at 1089 K against their respective molar concentration showed no significant dilution effect and thus the experiments were effectively carried out under infinite dilution conditions. In each sample, the average values of four measurements were considered.

The standard molar enthalpy of formation ( $\Delta H_f^\circ$ ) of each composition of  $(\text{La}_{1-x}\text{Ca}_{x/2}\text{Th}_{x/2})\text{PO}_4$  ( $x = 0, 0.15, 0.25, 0.40, 0.60, 0.75, 0.85, 1$ ) at 298 K was derived using the thermo-chemical cycle based on Hess's law given in **Table 4.13**. The thermochemical cycle involves values of molar enthalpy of dissolution of  $(\text{La}_{1-x}\text{Ca}_{x/2}\text{Th}_{x/2})\text{PO}_4$  ( $x = 0, 0.15, 0.25, 0.40, 0.60, 0.75, 0.85, 1$ ),  $\text{La}_2\text{O}_3$ ,  $\text{CaO}$ ,  $\text{ThO}_2$  and  $\text{P}_2\text{O}_5$  along with other auxiliary data from the literature [193], such as standard molar enthalpies of formation of constituent oxides viz.  $\text{La}_2\text{O}_3$ ,  $\text{CaO}$ ,  $\text{ThO}_2$  and  $\text{P}_2\text{O}_5$ .

**Table 4.13:** Thermo-chemical cycles for derivation of standard molar enthalpies of formation of  $(\text{La}_{1-x}\text{Ca}_{x/2}\text{Th}_{x/2})\text{PO}_4$  ( $x = 0, 0.15, 0.25, 0.40, 0.60, 0.75, 0.85, 1$ ) at temperature 298 K ( $T_r$ ) using enthalpy of dissolution<sup>a</sup> data at temperature of solvent<sup>b</sup> 1089 K ( $T_s$ ) and pressure  $P = 101.325$  kPa<sup>c</sup>.

Reactions	$\Delta H_i$	$\Delta H / \text{kJ}\cdot\text{mol}^{-1}$
$\text{LaPO}_4(\text{monazite}, 298\text{K}) = 1/2\cdot\text{La}_2\text{O}_3(\text{sln}, 1089\text{K}) + 1/2\cdot\text{P}_2\text{O}_5(\text{sln}, 1089\text{K})$	$\Delta H_1$	$131.4 \pm 1.0^{\text{d,e}}$
$\text{La}_{1-x}\text{Ca}_{x/2}\text{Th}_{x/2}\text{PO}_4(\text{s}, 298\text{K}) = (1-x)/2\cdot\text{La}_2\text{O}_3(\text{sln}, 1089\text{K}) + x/2\cdot\text{CaO}(\text{sln}, 1089\text{K})$ $+ x/2\cdot\text{ThO}_2(\text{sln}, 1089\text{K}) + 1/2\cdot\text{P}_2\text{O}_5(\text{sln}, 1089\text{K})$	$\Delta H_{2i}$	
$x = 0.15$	$i = 1$	$159.1 \pm 0.8^{\text{d,e}}$
$x = 0.25$	$i = 2$	$173.0 \pm 0.9^{\text{d,e}}$
$x = 0.4$	$i = 3$	$161.8 \pm 1.0^{\text{d,e}}$
$x = 0.6$	$i = 4$	$154.7 \pm 0.8^{\text{d,e}}$
$x = 0.75$	$i = 5$	$147.2 \pm 1.0^{\text{d,e}}$
$x = 0.85$	$i = 6$	$138.4 \pm 0.7^{\text{d,e}}$
$\text{Ca}_{0.5}\text{Th}_{0.5}\text{PO}_4(\text{s}, 298\text{K}) = 1/2\cdot\text{CaO}(\text{sln}, 1089\text{K}) + 1/2\cdot\text{ThO}_2(\text{sln}, 1089\text{K})$ $+ 1/2\cdot\text{P}_2\text{O}_5(\text{sln}, 1089\text{K})$	$\Delta H_3$	$139.8 \pm 0.8^{\text{d,e}}$
$\text{La}_2\text{O}_3(\text{s}, 298\text{K}) = \text{La}_2\text{O}_3(\text{sln}, 1089\text{K})$	$\Delta H_4$	$-45.9 \pm 0.4^{\text{d,e}}$
$\text{CaO}(\text{s}, 298\text{K}) = \text{CaO}(\text{sln}, 1089\text{K})$	$\Delta H_5$	$-8.4 \pm 2.0^{\text{d,e}}$
$\text{ThO}_2(\text{s}, 298\text{K}) = \text{ThO}_2(\text{sln}, 1089\text{K})$	$\Delta H_6$	$98.2 \pm 0.6^{\text{d,e}}$
$\text{P}_2\text{O}_5(\text{s}, 298\text{K}) = \text{P}_2\text{O}_5(\text{sln}, 1089\text{K})$	$\Delta H_7$	$-326.5 \pm 8.3^{\text{d,e}}$
$2\cdot\text{La}(\text{s}, 298\text{K}) + 3/2\cdot\text{O}_2(\text{g}, 298\text{K}) = \text{La}_2\text{O}_3(\text{s}, 298\text{K})$	$\Delta H_8$	$-1793.7 \pm 1.6^{[193]}$
$\text{Ca}(\text{s}, 298\text{K}) + 1/2\cdot\text{O}_2(\text{g}, 298\text{K}) = \text{CaO}(\text{s}, 298\text{K})$	$\Delta H_9$	$-635.1 \pm 0.9^{[193]}$

$\text{Th}_{(s, 298\text{K})} + \text{O}_{2(g, 298\text{K})} = \text{ThO}_{2(s, 298\text{K})}$	$\Delta H_{10}$	$-1226.4 \pm 3.5^{[193]}$
$2 \cdot \text{P}_{(s, 298\text{K})} + 5/2 \cdot \text{O}_{2(g, 298\text{K})} = \text{P}_2\text{O}_{5(s, 298\text{K})}$	$\Delta H_{11}$	$-1504.9 \pm 0.5^{[193]}$
$\text{La}_{(s, 298\text{K})} + \text{P}_{(s, 298\text{K})} + 2 \cdot \text{O}_{2(g, 298\text{K})} = \text{LaPO}_{4(s, 298\text{K})}$	$\Delta H_{f,m}^{\circ}$	$-1966.9 \pm 4.4^f$
$(1-x) \cdot \text{La}_{(s, 298\text{K})} + x/2 \cdot \text{Ca}_{(s, 298\text{K})} + x/2 \cdot \text{Th}_{(s, 298\text{K})} + \text{P}_{(s, 298\text{K})} + 2 \cdot \text{O}_{2(g, 298\text{K})} = \text{La}_{1-x}\text{Ca}_{x/2}\text{Th}_{x/2}\text{PO}_{4(s, 298\text{K})}$		
$x = 0.15$	$i = 1$	$-1989.5 \pm 4.3^f$
$x = 0.25$	$i = 2$	$-2000.0 \pm 4.3^f$
$x = 0.4$	$i = 3$	$-1983.7 \pm 4.4^f$
$x = 0.6$	$i = 4$	$-1969.8 \pm 4.4^f$
$x = 0.75$	$i = 5$	$-1957.2 \pm 4.6^f$
$x = 0.85$	$i = 6$	$-1945.0 \pm 4.6^f$
$1/2 \cdot \text{Ca}_{(s, 298\text{K})} + 1/2 \cdot \text{Th}_{(s, 298\text{K})} + \text{P}_{(s, 298\text{K})} + 2 \cdot \text{O}_{2(g, 298\text{K})} = \text{Ca}_{0.5}\text{Th}_{0.5}\text{PO}_{4(s, 298\text{K})}$	$\Delta H_{f,m}^{\circ}$	$-1941.4 \pm 4.7^f$

Here,  $\Delta H_{f,m}^{\circ}[\text{LaPO}_{4(s, 298\text{K})}] = -\Delta H_1 + 1/2 \cdot \Delta H_4 + 1/2 \cdot \Delta H_7 + 1/2 \cdot \Delta H_8 + 1/2 \cdot \Delta H_{11}$ ;

$\Delta H_{f,m}^{\circ}[\text{La}_{1-x}\text{Ca}_{x/2}\text{Th}_{x/2}\text{PO}_{4(s, 298\text{K})}] = -\Delta H_{2i} + (1-x)/2 \cdot \Delta H_4 + x/2 \cdot \Delta H_5 + x/2 \cdot \Delta H_6 + 1/2 \cdot \Delta H_7 + (1-x)/2 \cdot \Delta H_8 + x/2 \cdot \Delta H_9 + x/2 \cdot \Delta H_{10} + 1/2 \cdot \Delta H_{11}$ ;

$\Delta H_{f,m}^{\circ}[\text{Ca}_{0.5}\text{Th}_{0.5}\text{PO}_{4(s, 298\text{K})}] = -\Delta H_3 + 1/2 \cdot \Delta H_5 + 1/2 \cdot \Delta H_6 + 1/2 \cdot \Delta H_7 + 1/2 \cdot \Delta H_9 + 1/2 \cdot \Delta H_{10} + 1/2 \cdot \Delta H_{11}$ .

<sup>a</sup>The heat effect associated to dissolution of solid at  $T_r$  in 10g of  $\text{PbO} + \text{B}_2\text{O}_3$  (2:1 molar ratio) at  $T_s$ .

<sup>b</sup>10g of  $\text{PbO} + \text{B}_2\text{O}_3$  (2:1 molar ratio) was used as solvent.

<sup>c</sup>Standard uncertainties  $u$  are  $u(p) = 5000 \text{ Pa}$ ,  $u(T_r) = 0.5 \text{ K}$ ,  $u(T_s) = 0.05 \text{ K}$ .

<sup>d</sup>Expanded uncertainties for  $\Delta H$  with 0.95 level of confidence ( $k \approx 2$ ).

<sup>e</sup>This work.

<sup>f</sup>Uncertainty of the combined reaction is estimated as the square root of the sum of the squares of uncertainty of each individual reaction.

The variation of standard molar enthalpy of formation for  $(\text{La}_{1-x}\text{Ca}_{x/2}\text{Th}_{x/2})\text{PO}_4$  ( $x = 0, 0.15, 0.25, 0.40, 0.60, 0.75, 0.85, 1$ ) with respect to their constituent elements ( $\Delta H_f^{\circ}$ ) and to their constituent oxides ( $\Delta H_{f,ox}^{\circ}$ ) as a function of mole fraction of  $\text{Ca}_{0.5}\text{Th}_{0.5}\text{PO}_4$  are shown in

**Fig. 4.25** and **Fig. 4.26**, respectively and the corresponding values are listed in **Table 4.14**.

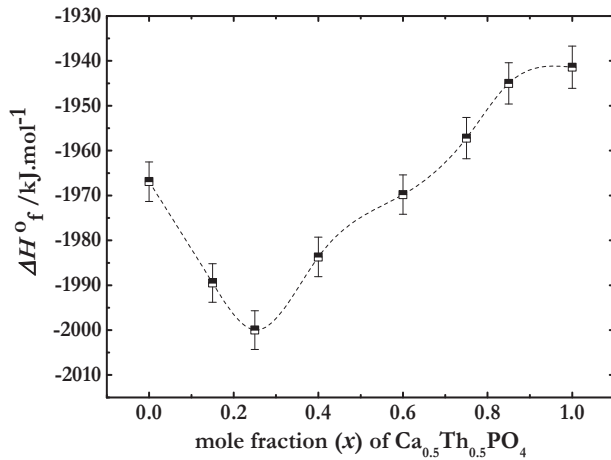


**Fig. 4.25:** Variation of standard molar enthalpy of formation of  $(\text{La}_{1-x}\text{Ca}_{x/2}\text{Th}_{x/2})\text{PO}_4$  ( $x = 0, 0.15, 0.25, 0.40, 0.60, 0.75, 0.85, 1$ ) as a function of mole fraction of  $\text{Ca}_{0.5}\text{Th}_{0.5}\text{PO}_4$  (with dashed line as a guide to the eye).

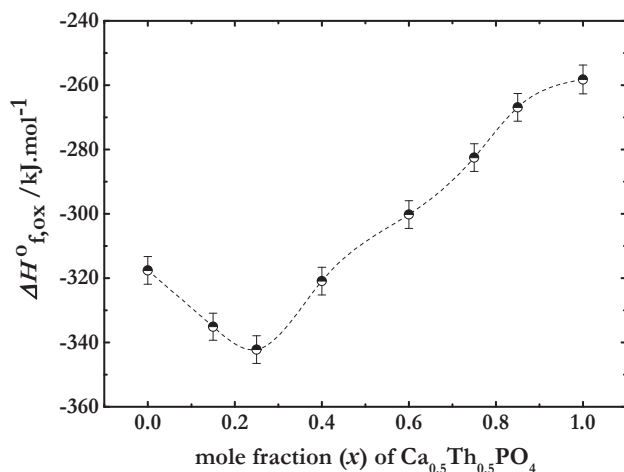


**Fig. 4.26:** Trend of molar enthalpy of formation from constituent oxides ( $\Delta H_{f,ox}^{\circ}$ ) of  $(La_{1-x}Ca_{x/2}Th_{x/2})PO_4$  ( $x = 0, 0.15, 0.25, 0.40, 0.60, 0.75, 0.85, 1$ ) as a function of mole fraction of  $Ca_{0.5}Th_{0.5}PO_4$  (with dashed line as a guide to the eye).

**Table 4.14:** Measured values of enthalpy of formation from the constituent element and from the constituent oxides for  $(La_{1-x}Ca_{x/2}Th_{x/2})PO_4$  ( $x = 0, 0.15, 0.25, 0.40, 0.60, 0.75, 0.85, 1$ ).

Samples (x)	$\Delta H_f^{\circ} / \text{kJ.mol}^{-1}$	$\Delta H_{f,ox}^{\circ} / \text{kJ.mol}^{-1}$
0	-1966.9±4.4	-317.6±4.3
0.15	-1989.5±4.3	-335.1±4.2
0.25	-2000.0±4.3	-342.2±4.3
0.4	-1983.7±4.4	-320.9±4.3
0.6	-1969.8±4.4	-300.2±4.3
0.75	-1957.2±4.6	-282.5±4.3
0.85	-1945.0±4.6	-266.9±4.3
1	-1941.4±4.7	-258.2±4.5

The standard molar enthalpy of formation of studied solid solutions with respect to oxide ( $\Delta H_{f,ox}^{\circ}$ ) was calculated by subtracting the sum of the enthalpy of formation of constituent oxides [193] taken in stoichiometric proportion from the enthalpy of formation of the corresponding compositions derived from experimental results. The reasons for such variation of standard molar enthalpy of formation with a minimum are discussed in Section 4.4.

#### 4.3.5.1.1. SEM analysis of quenched solute and $2\text{PbO}\cdot\text{B}_2\text{O}_3$ solvent

Microstructure analysis of the quenched  $\text{PbO} + \text{B}_2\text{O}_3$  (2:1 molar ratio) solvent of calorimeter containing  $(\text{La}_{0.4}\text{Ca}_{0.3}\text{Th}_{0.3})\text{PO}_4$  solute was carried out to evaluate the dissolution of sample in solvent at 1089 K. Back scattered electron (BSE) imaging of the specimen and elemental mapping for La, Ca and Th are given in **Fig. 4.27**. No undissolved fragments of solute were observed in BSE image and X-ray dot map of the solvent showed that the constituent elements of the sample are homogeneously distributed in the molten solvent.

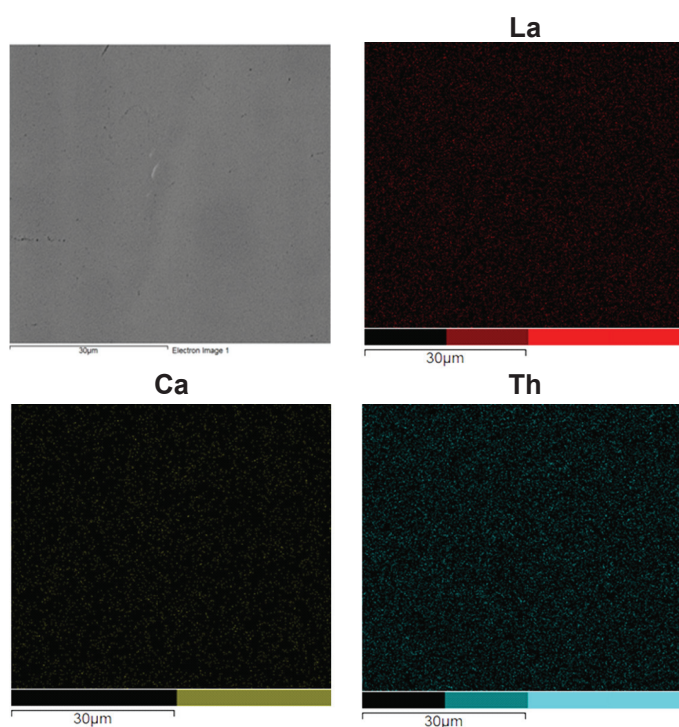


**Fig. 4.27:** Backscattered electron SEM image of the surface of quenched  $\text{PbO} + \text{B}_2\text{O}_3$  (2:1 molar ratio) calorimeter solvent with dissolved  $(\text{La}_{0.4}\text{Ca}_{0.3}\text{Th}_{0.3})\text{PO}_4$  sample and corresponding elemental maps for La, Ca and Th.

#### 4.3.5.1.2. Correlation of thermodynamic data with thorium content in natural monazite mineral on earth's crust

A correlation is drawn between the thermodynamic data of synthetic monazite  $(\text{La}_{1-x}\text{Ca}_{x/2}\text{Th}_{x/2})\text{PO}_4$  ( $0 \leq x \leq 1$ ) solid solutions and the composition of monazite mineral present

on earth's crust. The beach sands in India, Brazil, USA, Malaysia, Korea, and Sri Lanka contain 3.1-14.32 wt. % ThO<sub>2</sub> and 40.7-65.0 wt. % RE<sub>2</sub>O<sub>3</sub> (rare earth oxides) [200]. However, monazite from granitic rocks could comprise higher percentage of ThO<sub>2</sub>. The range of composition of thorium and rare earth oxides present in the beach sands corresponds to the minima of the enthalpy of formation  $\Delta H_{f,ox}^{\circ}$  curve determined in the present work. The enthalpy minima of (La<sub>1-x</sub>Ca<sub>x/2</sub>Th<sub>x/2</sub>)PO<sub>4</sub> ( $0 \leq x \leq 1$ ) solid solutions corresponds to  $x = 0.25$  i.e. 14.1 wt. % ThO<sub>2</sub>, 3.1 wt. % CaO and 52.4 wt. % La<sub>2</sub>O<sub>3</sub> and shown in **Fig. 4.28**.

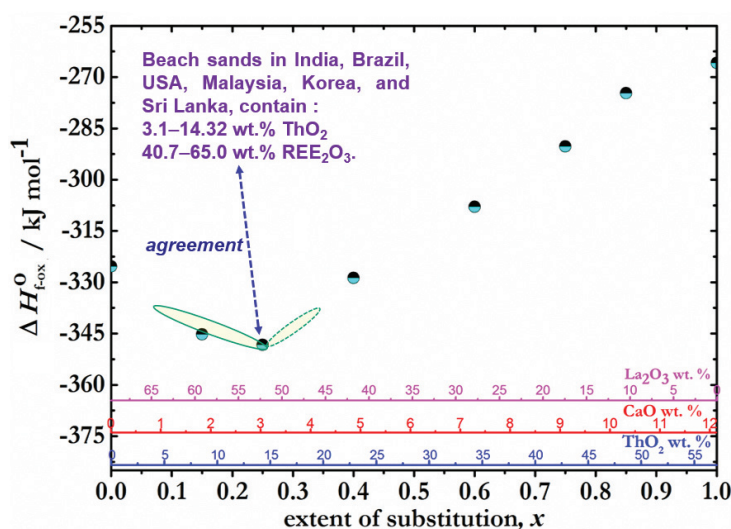


**Fig. 4.28:** Correlation curve between enthalpies of formation of synthetic monazite with the natural composition of monazite present in beach sands.

Thus, the enthalpy of formation  $\Delta H_{f,ox}^{\circ}$  plot of (La<sub>1-x</sub>Ca<sub>x/2</sub>Th<sub>x/2</sub>)PO<sub>4</sub> ( $0 \leq x \leq 1$ ) solid solutions as a function of thorium content may also explain why only monazite with 3.1-14.32 wt. % ThO<sub>2</sub> and 40.7-65.0 wt. % RE<sub>2</sub>O<sub>3</sub> concentrations are most abundant in the earth's crust.

### 4.3.5.2. (La<sub>1-x</sub>Sr<sub>x/2</sub>Th<sub>x/2</sub>)PO<sub>4</sub> (0 ≤ x ≤ 1) solid solutions:

The molar enthalpy of dissolution ( $\Delta H_{ds}$ ) observed in the present calorimetric study for (La<sub>1-x</sub>Sr<sub>x/2</sub>Th<sub>x/2</sub>)PO<sub>4</sub> ( $x = 0.1, 0.2, 0.3, 0.4, 0.5, 0.6, 0.7, 0.8, 0.9, 1$ ) samples and SrCO<sub>3</sub> in molten PbO+B<sub>2</sub>O<sub>3</sub> (2:1 molar ratio) solvent at 1089 K are given in **Table 4.15**. The values of enthalpy of dissolution for SrO, ThO<sub>2</sub> and P<sub>2</sub>O<sub>5</sub> is provided in Section 4.3.4.

**Table 4.15:** The molar enthalpies of dissolution<sup>a</sup> ( $\Delta H_{ds}$ ) of (La<sub>1-x</sub>Sr<sub>x/2</sub>Th<sub>x/2</sub>)PO<sub>4</sub> ( $x = 0.1, 0.2, 0.3, 0.4, 0.5, 0.6, 0.7, 0.8, 0.9, 1$ ) and SrCO<sub>3</sub> with mass  $m$ , from temperature 298 K ( $T_r$ ) to temperature of solvent<sup>b</sup> 1089 K ( $T_s$ ) at pressure  $P = 101.325$  kPa<sup>c</sup>.

Sample	$m$ /mg	$\Delta H^d$ /J·g <sup>-1</sup>	$\Delta H_{ds}^e$ /kJ·mol <sup>-1</sup>	Ref.
(La <sub>0.9</sub> Sr <sub>0.05</sub> Th <sub>0.05</sub> )PO <sub>4</sub> (235.97 g·mol <sup>-1</sup> )	11.2	636.1	150.1	This work
	13.1	644.6	152.1	
	9.8	642.9	151.7	
	10.4	638.2	150.6	
			<b>Avg.:</b> 151.1±0.9	
(La <sub>0.8</sub> Sr <sub>0.1</sub> Th <sub>0.1</sub> )PO <sub>4</sub> (238.06 g·mol <sup>-1</sup> )	9.5	701.9	167.1	This work
	10.4	695.6	165.6	
	9.7	700.7	166.8	
	11.4	696.5	165.8	
			<b>Avg.:</b> 166.3±0.7	
(La <sub>0.7</sub> Sr <sub>0.15</sub> Th <sub>0.15</sub> )PO <sub>4</sub> (240.15 g·mol <sup>-1</sup> )	10.2	729.5	175.2	This work
	11.3	723.7	173.8	
	8.6	732.0	175.8	
	9.5	721.2	173.2	
			<b>Avg.:</b> 174.5±1.2	
(La <sub>0.6</sub> Sr <sub>0.2</sub> Th <sub>0.2</sub> )PO <sub>4</sub> (242.25 g·mol <sup>-1</sup> )	9.5	688.1	166.7	This work
	11.1	690.2	167.2	
	9.3	684.4	165.8	
	10.5	681.9	165.2	
			<b>Avg.:</b> 166.2±0.9	
(La <sub>0.5</sub> Sr <sub>0.25</sub> Th <sub>0.25</sub> )PO <sub>4</sub> (244.34 g·mol <sup>-1</sup> )	10.2	660.6	161.4	This work
	12.1	663.8	162.2	
	10.7	665.9	162.7	
	11.2	666.3	162.8	
			<b>Avg.:</b> 162.3±0.6	
(La <sub>0.4</sub> Sr <sub>0.3</sub> Th <sub>0.3</sub> )PO <sub>4</sub> (246.43 g·mol <sup>-1</sup> )	11.1	644.4	158.8	This work
	9.4	639.1	157.5	
	8.6	642.4	158.3	
	10.3	640.3	157.8	
			<b>Avg.:</b> 158.1±0.6	
(La <sub>0.3</sub> Sr <sub>0.35</sub> Th <sub>0.35</sub> )PO <sub>4</sub>	9.8	620.1	154.1	

(248.52 g·mol <sup>-1</sup> )	10.3	624.9	155.3	
	8.8	623.7	155.0	
	11.4	620.5	154.2	
			<b>Avg.:</b> 154.7±0.6	This work
(La <sub>0.2</sub> Sr <sub>0.4</sub> Th <sub>0.4</sub> )PO <sub>4</sub> (250.62 g·mol <sup>-1</sup> )	10.7	602.9	151.1	
	8.6	595.3	149.2	
	11.3	597.7	149.8	
	9.5	601.7	150.8	
			<b>Avg.:</b> 150.2±0.9	This work
(La <sub>0.1</sub> Sr <sub>0.45</sub> Th <sub>0.45</sub> )PO <sub>4</sub> (252.71 g·mol <sup>-1</sup> )	11.6	592.0	149.6	
	10.8	584.9	147.8	
	9.4	590.4	149.2	
	10.7	586.0	148.1	
			<b>Avg.:</b> 148.7±0.9	This work
Sr <sub>0.5</sub> Th <sub>0.5</sub> PO <sub>4</sub> (254.8 g·mol <sup>-1</sup> )	9.8	577.7	147.2	
	10.1	574.2	146.3	
	8.7	579.3	147.6	
	11.2	572.6	145.9	
			<b>Avg.:</b> 146.8±0.8	This work
SrCO <sub>3</sub> (147.63 g·mol <sup>-1</sup> )	14.5	1482.8	218.9	
	11.5	1474.7	217.7	
	10.7	1488.9	219.8	
	14.2	1516.6	223.9	
			<b>Avg.:</b> 220.1±2.7	This work

<sup>a</sup>The heat effect associated to dissolution of solid at  $T_r$  in 10g of PbO + B<sub>2</sub>O<sub>3</sub> (2:1 molar ratio) at  $T_s$ .

<sup>b</sup>10g of PbO + B<sub>2</sub>O<sub>3</sub> (2:1 molar ratio) was used as solvent.

<sup>c</sup>Standard uncertainties  $u$  are  $u(p) = 5000$  Pa,  $u(m) = 0.1$  mg,  $u(T_r) = 0.5$  K,  $u(T_s) = 0.05$  K.

<sup>d</sup>The heat effect correspond to the dissolution of solute per unit mass.

<sup>e</sup>Expanded uncertainties for  $\Delta H$  with 0.95 level of confidence ( $k \approx 2$ ).

The standard molar enthalpy of formation ( $\Delta H_f^\circ$ ) of each composition of (La<sub>1-x</sub>Sr<sub>x/2</sub>Th<sub>x/2</sub>)PO<sub>4</sub> ( $x = 0, 0.1, 0.2, 0.3, 0.4, 0.5, 0.6, 0.7, 0.8, 0.9, 1$ ) at 298 K was derived using the thermochemical cycle given in **Table 4.16**. The thermochemical cycle includes values of molar enthalpy of dissolution of (La<sub>1-x</sub>Sr<sub>x/2</sub>Th<sub>x/2</sub>)PO<sub>4</sub> ( $x = 0, 0.1, 0.2, 0.3, 0.4, 0.5, 0.6, 0.7, 0.8, 0.9, 1$ ), La<sub>2</sub>O<sub>3</sub>, SrO, ThO<sub>2</sub> and P<sub>2</sub>O<sub>5</sub> together with data of standard molar enthalpies of formation of constituent oxides viz. La<sub>2</sub>O<sub>3</sub>, SrO, ThO<sub>2</sub> and P<sub>2</sub>O<sub>5</sub> from the literature.

**Table 4.16:** Thermo-chemical cycles for derivation of standard molar enthalpies of formation of  $(\text{La}_{1-x}\text{Sr}_x/2\text{Th}_{x/2})\text{PO}_4$  ( $x = 0, 0.1, 0.2, 0.3, 0.4, 0.5, 0.6, 0.7, 0.8, 0.9, 1$ ) at temperature 298 K ( $T_r$ ) using enthalpy of dissolution<sup>a</sup> data at temperature of solvent<sup>b</sup> 1089 K ( $T_s$ ) and pressure  $P = 101.325$  kPa<sup>c</sup>.

Reactions	$\Delta H_i$	$\Delta H / \text{kJ}\cdot\text{mol}^{-1}$
$\text{LaPO}_4(\text{monazite}, 298\text{K}) = 1/2\cdot\text{La}_2\text{O}_3(\text{sln}, 1089\text{K}) + 1/2\cdot\text{P}_2\text{O}_5(\text{sln}, 1089\text{K})$	$\Delta H_1$	$131.4 \pm 1.0^{\text{d,e}}$
$\text{La}_{1-x}\text{Sr}_x/2\text{Th}_{x/2}\text{PO}_4(\text{s}, 298\text{K}) = (1-x)/2\cdot\text{La}_2\text{O}_3(\text{sln}, 1089\text{K}) + x/2\cdot\text{SrO}(\text{sln}, 1089\text{K})$ $+ x/2\cdot\text{ThO}_2(\text{sln}, 1089\text{K}) + 1/2\cdot\text{P}_2\text{O}_5(\text{sln}, 1089\text{K})$	$\Delta H_{2i}$	
$x = 0.1$	$i = 1$	$151.1 \pm 0.9^{\text{d,e}}$
$x = 0.2$	$i = 2$	$166.3 \pm 0.7^{\text{d,e}}$
$x = 0.3$	$i = 3$	$174.5 \pm 1.2^{\text{d,e}}$
$x = 0.4$	$i = 4$	$166.2 \pm 0.9^{\text{d,e}}$
$x = 0.5$	$i = 5$	$162.3 \pm 0.6^{\text{d,e}}$
$x = 0.6$	$i = 6$	$158.1 \pm 0.6^{\text{d,e}}$
$x = 0.7$	$i = 7$	$154.7 \pm 0.6^{\text{d,e}}$
$x = 0.8$	$i = 8$	$150.2 \pm 0.9^{\text{d,e}}$
$x = 0.9$	$i = 9$	$148.7 \pm 0.9^{\text{d,e}}$
$\text{Sr}_{0.5}\text{Th}_{0.5}\text{PO}_4(\text{s}, 298\text{K}) = 1/2\cdot\text{SrO}(\text{sln}, 1089\text{K}) + 1/2\cdot\text{ThO}_2(\text{sln}, 1089\text{K})$ $+ 1/2\cdot\text{P}_2\text{O}_5(\text{sln}, 1089\text{K})$	$\Delta H_3$	$146.8 \pm 0.8^{\text{d,e}}$
$\text{La}_2\text{O}_3(\text{s}, 298\text{K}) = \text{La}_2\text{O}_3(\text{sln}, 1089\text{K})$	$\Delta H_4$	$-45.9 \pm 0.4^{\text{d,e}}$
$\text{SrO}(\text{s}, 298\text{K}) = \text{SrO}(\text{sln}, 1089\text{K})$	$\Delta H_5$	$-53.1 \pm 3.2^{\text{d,e}}$
$\text{ThO}_2(\text{s}, 298\text{K}) = \text{ThO}_2(\text{sln}, 1089\text{K})$	$\Delta H_6$	$98.2 \pm 0.6^{\text{d,e}}$
$\text{P}_2\text{O}_5(\text{s}, 298\text{K}) = \text{P}_2\text{O}_5(\text{sln}, 1089\text{K})$	$\Delta H_7$	$-326.5 \pm 8.3^{\text{d,e}}$
$2\cdot\text{La}(\text{s}, 298\text{K}) + 3/2\cdot\text{O}_2(\text{g}, 298\text{K}) = \text{La}_2\text{O}_3(\text{s}, 298\text{K})$	$\Delta H_8$	$-1793.7 \pm 1.6^{[193]}$
$\text{Sr}(\text{s}, 298\text{K}) + 1/2\cdot\text{O}_2(\text{g}, 298\text{K}) = \text{SrO}(\text{s}, 298\text{K})$	$\Delta H_9$	$-591.3 \pm 1.0^{[193]}$
$\text{Th}(\text{s}, 298\text{K}) + \text{O}_2(\text{g}, 298\text{K}) = \text{ThO}_2(\text{s}, 298\text{K})$	$\Delta H_{10}$	$-1226.4 \pm 3.5^{[193]}$
$2\cdot\text{P}(\text{s}, 298\text{K}) + 5/2\cdot\text{O}_2(\text{g}, 298\text{K}) = \text{P}_2\text{O}_5(\text{s}, 298\text{K})$	$\Delta H_{11}$	$-1504.9 \pm 0.5^{[193]}$
$\text{La}(\text{s}, 298\text{K}) + \text{P}(\text{s}, 298\text{K}) + 2\cdot\text{O}_2(\text{g}, 298\text{K}) = \text{LaPO}_4(\text{s}, 298\text{K})$	$\Delta H_{\text{f,m}}^{\text{o}}$	$-1966.9 \pm 4.4^{\text{f}}$
$(1-x)\cdot\text{La}(\text{s}, 298\text{K}) + x/2\cdot\text{Sr}(\text{s}, 298\text{K}) + x/2\cdot\text{Th}(\text{s}, 298\text{K}) + \text{P}(\text{s}, 298\text{K})$ $+ 2\cdot\text{O}_2(\text{g}, 298\text{K}) = \text{La}_{1-x}\text{Sr}_x/2\text{Th}_{x/2}\text{PO}_4(\text{s}, 298\text{K})$		
$x = 0.1$	$i = 1$	$-1983.3 \pm 4.3^{\text{f}}$
$x = 0.2$	$i = 2$	$-1995.1 \pm 4.3^{\text{f}}$
$x = 0.3$	$i = 3$	$-1999.9 \pm 4.4^{\text{f}}$
$x = 0.4$	$i = 4$	$-1988.3 \pm 4.4^{\text{f}}$
$x = 0.5$	$i = 5$	$-1981.1 \pm 4.4^{\text{f}}$
$x = 0.6$	$i = 6$	$-1973.5 \pm 4.5^{\text{f}}$
$x = 0.7$	$i = 7$	$-1966.8 \pm 4.5^{\text{f}}$
$x = 0.8$	$i = 8$	$-1958.9 \pm 4.6^{\text{f}}$
$x = 0.9$	$i = 9$	$-1954.1 \pm 4.8^{\text{f}}$
$1/2\cdot\text{Sr}(\text{s}, 298\text{K}) + 1/2\cdot\text{Th}(\text{s}, 298\text{K}) + \text{P}(\text{s}, 298\text{K}) + 2\cdot\text{O}_2(\text{g}, 298\text{K}) =$ $\text{Sr}_{0.5}\text{Th}_{0.5}\text{PO}_4(\text{s}, 298\text{K})$	$\Delta H_{\text{f,m}}^{\text{o}}$	$-1948.8 \pm 4.8^{\text{f}}$

Here,  $\Delta H_{\text{f,m}}^{\text{o}}[\text{LaPO}_4(\text{s}, 298\text{K})] = -\Delta H_1 + 1/2\cdot\Delta H_4 + 1/2\cdot\Delta H_7 + 1/2\cdot\Delta H_8 + 1/2\cdot\Delta H_{11}$ ;

$\Delta H_{\text{f,m}}^{\text{o}}[\text{La}_{1-x}\text{Sr}_x/2\text{Th}_{x/2}\text{PO}_4(\text{s}, 298\text{K})] = -\Delta H_{2i} + (1-x)/2\cdot\Delta H_4 + x/2\cdot\Delta H_5 + x/2\cdot\Delta H_6 + 1/2\cdot\Delta H_7 + (1-x)/2\cdot\Delta H_8$   
 $+ x/2\cdot\Delta H_9 + x/2\cdot\Delta H_{10} + 1/2\cdot\Delta H_{11}$ ;

$\Delta H_{\text{f,m}}^{\text{o}}[\text{Sr}_{0.5}\text{Th}_{0.5}\text{PO}_4(\text{s}, 298\text{K})] = -\Delta H_3 + 1/2\cdot\Delta H_5 + 1/2\cdot\Delta H_6 + 1/2\cdot\Delta H_7 + 1/2\cdot\Delta H_9 + 1/2\cdot\Delta H_{10} + 1/2\cdot\Delta H_{11}$ .

<sup>a</sup>The heat effect associated to dissolution of solid at  $T_r$  in 10g of  $\text{PbO} + \text{B}_2\text{O}_3$  (2:1 molar ratio) at  $T_s$ .

<sup>b</sup>10g of  $\text{PbO} + \text{B}_2\text{O}_3$  (2:1 molar ratio) was used as solvent.

<sup>c</sup>Standard uncertainties  $u$  are  $u(p) = 5000$  Pa,  $u(T_r) = 0.5$  K,  $u(T_s) = 0.05$  K.

<sup>d</sup>Expanded uncertainties for  $\Delta H$  with 0.95 level of confidence ( $k \approx 2$ ).

<sup>e</sup>This work.

<sup>f</sup>Uncertainty of the combined reaction is estimated as the square root of the sum of the squares of uncertainty of each individual reaction.

The variation of standard molar enthalpy of formation for  $(\text{La}_{1-x}\text{Sr}_{x/2}\text{Th}_{x/2})\text{PO}_4$  ( $x = 0, 0.1, 0.2, 0.3, 0.4, 0.5, 0.6, 0.7, 0.8, 0.9, 1$ ) from their constituent elements ( $\Delta H_f^\circ$ ) and from their oxides ( $\Delta H_{f,\text{ox}}^\circ$ ) as a function of mole fraction of end member viz.  $\text{Sr}_{0.5}\text{Th}_{0.5}\text{PO}_4$  are given in **Fig. 4.29** and **Fig. 4.30**, respectively and the individual values are listed in **Table 4.17**.

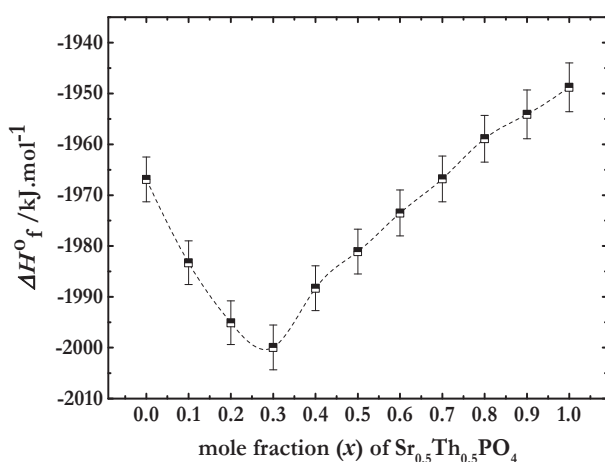


**Fig. 4.29:** Variation of standard molar enthalpy of formation of  $(\text{La}_{1-x}\text{Sr}_{x/2}\text{Th}_{x/2})\text{PO}_4$  ( $x = 0, 0.1, 0.2, 0.3, 0.4, 0.5, 0.6, 0.7, 0.8, 0.9, 1$ ) as a function of mole fraction of  $\text{Sr}_{0.5}\text{Th}_{0.5}\text{PO}_4$  (with dashed line as a guide to the eye).

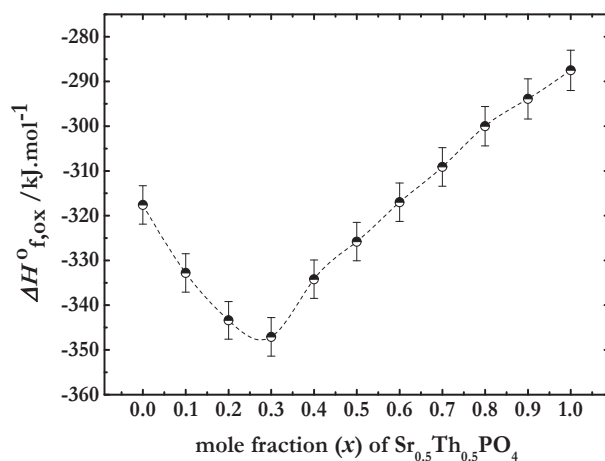


**Fig. 4.30:** Trend of molar enthalpy of formation from constituent oxides ( $\Delta H_{f,\text{ox}}^\circ$ ) of  $(\text{La}_{1-x}\text{Sr}_{x/2}\text{Th}_{x/2})\text{PO}_4$  ( $x = 0, 0.1, 0.2, 0.3, 0.4, 0.5, 0.6, 0.7, 0.8, 0.9, 1$ ) as a function of mole fraction of  $\text{Sr}_{0.5}\text{Th}_{0.5}\text{PO}_4$  (with dashed line as a guide to the eye).

**Table 4.17:** Measured values of enthalpy of formation from the constituent elements and from the constituent oxides for  $(\text{La}_{1-x}\text{Sr}_{x/2}\text{Th}_{x/2})\text{PO}_4$  ( $x = 0, 0.1, 0.2, 0.3, 0.4, 0.5, 0.6, 0.7, 0.8, 0.9, 1$ ).

Samples (x)	$\Delta H_f^0(298\text{ K})$ /kJ.mol <sup>-1</sup>	$\Delta H_{f,\text{ox}}^0(298\text{ K})$ /kJ.mol <sup>-1</sup>
0	-1966.9±4.4	-317.6±4.3
0.1	-1983.3±4.3	-332.8±4.3
0.2	-1995.1±4.3	-343.4±4.2
0.3	-1999.9±4.4	-347.1±4.3
0.4	-1988.3±4.4	-334.2±4.3
0.5	-1981.1±4.4	-325.8±4.3
0.6	-1973.5±4.5	-317.0±4.3
0.7	-1966.8±4.5	-309.1±4.3
0.8	-1958.9±4.6	-300.0±4.4
0.9	-1954.1±4.8	-293.9±4.5
1	-1948.8±4.8	-287.5±4.5

The enthalpy value,  $\Delta H_{f,\text{ox}}^0$  at 298 K was calculated by subtracting the sum of the enthalpy of formation of constituent oxides [193] taken in stoichiometric proportion from the enthalpy of formation of the corresponding compositions derived from experimental results. The reason for such behavior of standard molar enthalpy of formation are discussed in Section 4.4.

### 4.3.5.3. (La<sub>1-x</sub>Ba<sub>x/2</sub>Th<sub>x/2</sub>)PO<sub>4</sub> (x = 0, 0.1, 0.2, 0.3; x = 1) solid solutions:

The measured values of molar enthalpy of dissolution ( $\Delta H_{ds}$ ) for (La<sub>1-x</sub>Ba<sub>x/2</sub>Th<sub>x/2</sub>)PO<sub>4</sub> (x = 0.1, 0.2, 0.3; x = 1) (0.1 ≤ x ≤ 0.3; x = 1) samples and BaCO<sub>3</sub> in molten PbO+B<sub>2</sub>O<sub>3</sub> (2:1 molar ratio) solvent at 1089 K are provided in **Table 4.18**. The values of enthalpy of dissolution for BaO, ThO<sub>2</sub> and P<sub>2</sub>O<sub>5</sub> is provided in Section 4.3.4.

**Table 4.18:** The molar enthalpies of dissolution<sup>a</sup> ( $\Delta H_{ds}$ ) of (La<sub>1-x</sub>Ba<sub>x/2</sub>Th<sub>x/2</sub>)PO<sub>4</sub> (x = 0.1, 0.2, 0.3; x = 1) and BaCO<sub>3</sub> with mass m, from temperature 298 K ( $T_r$ ) to temperature of solvent<sup>b</sup> 1089 K ( $T_s$ ) at pressure P = 101.325 kPa<sup>c</sup>.

Sample	m /mg	$\Delta H^d$ /J·g <sup>-1</sup>	$\Delta H_{ds}^e$ /kJ·mol <sup>-1</sup>	Ref.
(La <sub>0.90</sub> Ba <sub>0.05</sub> Th <sub>0.05</sub> )PO <sub>4</sub> (238.45 g·mol <sup>-1</sup> )	15.1	670.6	159.9	
	14.8	661.8	157.8	
	13.4	658.8	157.1	
	14.7	666.0	158.8	
			<b>Avg.:</b> 158.4±1.2	This work
(La <sub>0.8</sub> Ba <sub>0.1</sub> Th <sub>0.1</sub> )PO <sub>4</sub> (243.03 g·mol <sup>-1</sup> )	13.2	672.3	163.4	
	14.6	659.6	160.3	
	15.6	665.3	161.7	
	17.1	670.3	162.9	
			<b>Avg.:</b> 162.1±1.4	This work
(La <sub>0.70</sub> Ba <sub>0.15</sub> Th <sub>0.15</sub> )PO <sub>4</sub> (247.61 g·mol <sup>-1</sup> )	14.2	636.1	157.5	
	18.1	638.9	158.2	
	16.3	645.4	159.8	
	14.5	639.7	158.4	
			<b>Avg.:</b> 158.5±1.0	This work
Ba <sub>0.50</sub> Th <sub>0.50</sub> PO <sub>4</sub> (279.65 g·mol <sup>-1</sup> )	12.7	526.4	147.2	
	11.8	520.7	145.6	
	13.2	517.8	144.8	
	14.6	523.5	146.4	
			<b>Avg.:</b> 146.0±1.1	This work
BaCO <sub>3</sub> (197.33 g·mol <sup>-1</sup> )	17.5	1110.8	219.2	
	16.9	1106.3	218.3	
	18.5	1122.0	221.4	
	11.8	1118.4	220.7	
			<b>Avg.:</b> 219.9±1.4	This work

<sup>a</sup>The heat effect associated to dissolution of solid at  $T_r$  in 10g of PbO + B<sub>2</sub>O<sub>3</sub> (2:1 molar ratio) at  $T_s$ .

<sup>b</sup>10g of PbO + B<sub>2</sub>O<sub>3</sub> (2:1 molar ratio) was used as solvent.

<sup>c</sup>Standard uncertainties u are u(p) = 5000 Pa, u(m) = 0.1 mg, u( $T_r$ ) = 0.5 K, u( $T_s$ ) = 0.05 K.

<sup>d</sup>The heat effect correspond to the dissolution of solute per unit mass.

<sup>e</sup>Expanded uncertainties for  $\Delta H$  with 0.95 level of confidence ( $k \approx 2$ ).

The standard molar enthalpy of formation,  $\Delta H_{f,m}^0(298\text{ K})$  of each composition of  $(\text{La}_{1-x}\text{Ba}_{x/2}\text{Th}_{x/2})\text{PO}_4$  ( $x = 0, 0.1, 0.2, 0.3; x = 1$ ) at 298 K was derived using the thermo-chemical cycle given in **Table 4.19**. The thermo-chemical cycle comprises values of molar enthalpy of dissolution of  $(\text{La}_{1-x}\text{Ba}_{x/2}\text{Th}_{x/2})\text{PO}_4$  ( $x = 0, 0.1, 0.2, 0.3; x = 1$ )  $\text{La}_2\text{O}_3$ ,  $\text{BaO}$ ,  $\text{ThO}_2$  and  $\text{P}_2\text{O}_5$  together with data of standard molar enthalpies of formation of constituent oxides viz.  $\text{La}_2\text{O}_3$ ,  $\text{BaO}$ ,  $\text{ThO}_2$  and  $\text{P}_2\text{O}_5$  from the literature.

**Table 4.19:** Thermo-chemical cycle for derivation of standard molar enthalpies of formation of  $(\text{La}_{1-x}\text{Ba}_{x/2}\text{Th}_{x/2})\text{PO}_4$  ( $x = 0, 0.1, 0.2, 0.3; x = 1$ ) at temperature 298 K ( $T_r$ ) using enthalpy of dissolution<sup>a</sup> data at temperature of solvent<sup>b</sup> 1089 K ( $T_s$ ) and pressure  $P = 101.325\text{ kPa}$ .

Reactions	$\Delta H_i$	$\Delta H / \text{kJ}\cdot\text{mol}^{-1}$
$\text{LaPO}_4(\text{monazite}, 298\text{K}) = 1/2\cdot\text{La}_2\text{O}_3(\text{sln}, 1089\text{K}) + 1/2\cdot\text{P}_2\text{O}_5(\text{sln}, 1089\text{K})$	$\Delta H_1$	$131.4 \pm 1.0^{\text{d,e}}$
$\text{La}_{1-x}\text{Ba}_{x/2}\text{Th}_{x/2}\text{PO}_4(\text{s}, 298\text{K}) = (1-x)/2\cdot\text{La}_2\text{O}_3(\text{sln}, 1089\text{K}) + x/2\cdot\text{BaO}(\text{sln}, 1089\text{K})$ $+ x/2\cdot\text{ThO}_2(\text{sln}, 1089\text{K}) + 1/2\cdot\text{P}_2\text{O}_5(\text{sln}, 1089\text{K})$	$\Delta H_{2i}$	
$x = 0.1$	$i = 1$	$158.4 \pm 1.5^{\text{d,e}}$
$x = 0.2$	$i = 2$	$162.1 \pm 1.4^{\text{d,e}}$
$x = 0.3$	$i = 3$	$158.5 \pm 1.0^{\text{d,e}}$
$\text{Ba}_{0.5}\text{Th}_{0.5}\text{PO}_4(\text{s}, 298\text{K}) = 1/2\cdot\text{BaO}(\text{sln}, 1089\text{K}) + 1/2\cdot\text{ThO}_2(\text{sln}, 1089\text{K})$ $+ 1/2\cdot\text{P}_2\text{O}_5(\text{sln}, 1089\text{K})$	$\Delta H_3$	$146.0 \pm 1.2^{\text{d,e}}$
$\text{La}_2\text{O}_3(\text{s}, 298\text{K}) = \text{La}_2\text{O}_3(\text{sln}, 1089\text{K})$	$\Delta H_4$	$-45.9 \pm 0.4^{\text{d,e}}$
$\text{BaO}(\text{s}, 298\text{K}) = \text{BaO}(\text{sln}, 1089\text{K})$	$\Delta H_5$	$-88.2 \pm 2.1^{\text{d,e}}$
$\text{ThO}_2(\text{s}, 298\text{K}) = \text{ThO}_2(\text{sln}, 1089\text{K})$	$\Delta H_6$	$98.2 \pm 0.6^{\text{d,e}}$
$\text{P}_2\text{O}_5(\text{s}, 298\text{K}) = \text{P}_2\text{O}_5(\text{sln}, 1089\text{K})$	$\Delta H_7$	$-326.5 \pm 8.3^{\text{d,e}}$
$2\cdot\text{La}(\text{s}, 298\text{K}) + 3/2\cdot\text{O}_2(\text{g}, 298\text{K}) = \text{La}_2\text{O}_3(\text{s}, 298\text{K})$	$\Delta H_8$	$-1793.7 \pm 1.6^{[193]}$
$\text{Ba}(\text{s}, 298\text{K}) + 1/2\cdot\text{O}_2(\text{g}, 298\text{K}) = \text{BaO}(\text{s}, 298\text{K})$	$\Delta H_9$	$-548.1 \pm 2.1^{[193]}$
$\text{Th}(\text{s}, 298\text{K}) + \text{O}_2(\text{g}, 298\text{K}) = \text{ThO}_2(\text{s}, 298\text{K})$	$\Delta H_{10}$	$-1226.4 \pm 3.5^{[193]}$
$2\cdot\text{P}(\text{s}, 298\text{K}) + 5/2\cdot\text{O}_2(\text{g}, 298\text{K}) = \text{P}_2\text{O}_5(\text{s}, 298\text{K})$	$\Delta H_{11}$	$-1504.9 \pm 0.5^{[193]}$
$\text{La}(\text{s}, 298\text{K}) + \text{P}(\text{s}, 298\text{K}) + 2\cdot\text{O}_2(\text{g}, 298\text{K}) = \text{LaPO}_4(\text{s}, 298\text{K})$	$\Delta H_{f,m}^0$	$-1966.9 \pm 4.4^{\text{f}}$
$(1-x)\cdot\text{La}(\text{s}, 298\text{K}) + x/2\cdot\text{Ba}(\text{s}, 298\text{K}) + x/2\cdot\text{Th}(\text{s}, 298\text{K}) + \text{P}(\text{s}, 298\text{K})$ $+ 2\cdot\text{O}_2(\text{g}, 298\text{K}) = \text{La}_{1-x}\text{Ba}_{x/2}\text{Th}_{x/2}\text{PO}_4(\text{s}, 298\text{K})$		
$x = 0.1$	$i = 1$	$-1990.1 \pm 4.6^{\text{f}}$
$x = 0.2$	$i = 2$	$-1990.1 \pm 4.5^{\text{f}}$
$x = 0.3$	$i = 3$	$-1982.7 \pm 4.4^{\text{f}}$
$1/2\cdot\text{Ba}(\text{s}, 298\text{K}) + 1/2\cdot\text{Th}(\text{s}, 298\text{K}) + \text{P}(\text{s}, 298\text{K}) + 2\cdot\text{O}_2(\text{g}, 298\text{K}) =$ $\text{Ba}_{0.5}\text{Th}_{0.5}\text{PO}_4(\text{s}, 298\text{K})$	$\Delta H_{f,m}^0$	$-1944.0 \pm 4.9^{\text{f}}$

Here,  $\Delta H_{f,m}^0[\text{LaPO}_4(\text{s}, 298\text{K})] = -\Delta H_1 + 1/2\cdot\Delta H_4 + 1/2\cdot\Delta H_7 + 1/2\cdot\Delta H_8 + 1/2\cdot\Delta H_{11}$ ;

$\Delta H_{f,m}^0[\text{La}_{1-x}\text{Ba}_{x/2}\text{Th}_{x/2}\text{PO}_4(\text{s}, 298\text{K})] = -\Delta H_{2i} + (1-x)/2\cdot\Delta H_4 + x/2\cdot\Delta H_5 + x/2\cdot\Delta H_6 + 1/2\cdot\Delta H_7 + (1-x)/2\cdot\Delta H_8$   
 $+ x/2\cdot\Delta H_9 + x/2\cdot\Delta H_{10} + 1/2\cdot\Delta H_{11}$ ;

$\Delta H_{f,m}^0[\text{Ba}_{0.5}\text{Th}_{0.5}\text{PO}_4(\text{s}, 298\text{K})] = -\Delta H_3 + 1/2\cdot\Delta H_5 + 1/2\cdot\Delta H_6 + 1/2\cdot\Delta H_7 + 1/2\cdot\Delta H_9 + 1/2\cdot\Delta H_{10} + 1/2\cdot\Delta H_{11}$ .

<sup>a</sup>The heat effect associated to dissolution of solid at  $T_r$  in 10g of  $\text{PbO} + \text{B}_2\text{O}_3$  (2:1 molar ratio) at  $T_s$ .

<sup>b</sup>10g of  $\text{PbO} + \text{B}_2\text{O}_3$  (2:1 molar ratio) was used as solvent.

<sup>c</sup>Standard uncertainties  $u$  are  $u(p) = 5000$  Pa,  $u(T_r) = 0.5$  K,  $u(T_s) = 0.05$  K.

<sup>d</sup>Expanded uncertainties for  $\Delta H$  with 0.95 level of confidence ( $k \approx 2$ ).

<sup>e</sup>This work.

<sup>f</sup>Uncertainty of the combined reaction is estimated as the square root of the sum of the squares of uncertainty of each individual reaction.

The variation of standard molar enthalpy of formation for  $(\text{La}_{1-x}\text{Ba}_{x/2}\text{Th}_{x/2})\text{PO}_4$  ( $x = 0, 0.1, 0.2, 0.3; x = 1$ ) from their constituent elements,  $\Delta H_{f,m}^{\circ}(298\text{ K})$  and from their oxides,  $\Delta H_{f,ox}^{\circ}(298\text{ K})$  as a function of mole fraction of end member viz.  $\text{Ba}_{0.5}\text{Th}_{0.5}\text{PO}_4$  are given in **Fig. 4.31** and **Fig. 4.32**, respectively and the individual values are listed in **Table 4.20**.

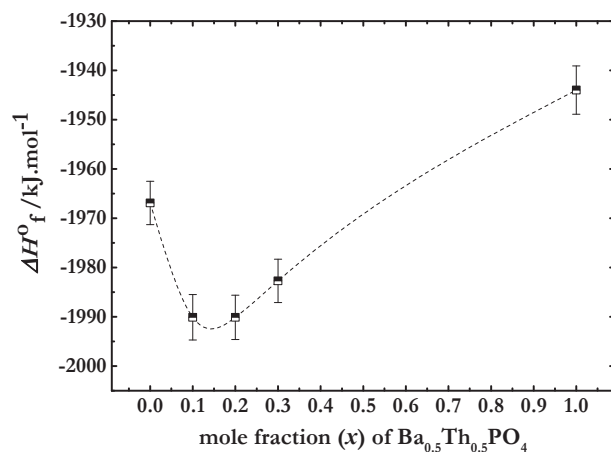


**Fig. 4.31:** Variation of standard molar enthalpy of formation,  $\Delta H_f^{\circ}(298\text{ K})$  of  $(\text{La}_{1-x}\text{Ba}_{x/2}\text{Th}_{x/2})\text{PO}_4$  ( $x = 0, 0.1, 0.2, 0.3; x = 1$ ) as a function of mole fraction of  $\text{Ba}_{0.5}\text{Th}_{0.5}\text{PO}_4$  (with dashed line as a guide to the eye).

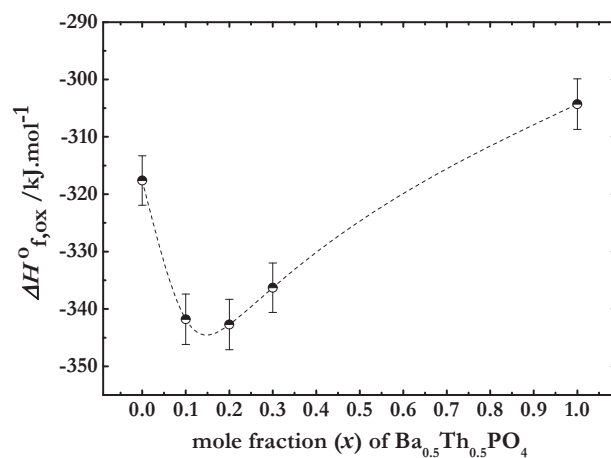


**Fig. 4.32:** Trend of molar enthalpy of formation from constituent oxides,  $\Delta H_{f,ox}^{\circ}(298\text{ K})$  of  $(\text{La}_{1-x}\text{Ba}_{x/2}\text{Th}_{x/2})\text{PO}_4$  ( $x = 0, 0.1, 0.2, 0.3; x = 1$ ) as a function of mole fraction of  $\text{Ba}_{0.5}\text{Th}_{0.5}\text{PO}_4$  (with dashed line as a guide to the eye).

**Table 4.20:** Measured values of enthalpy of formation from the constituent elements and from the constituent oxides for  $(\text{La}_{1-x}\text{Ba}_{x/2}\text{Th}_{x/2})\text{PO}_4$  ( $x = 0, 0.1, 0.2, 0.3; x = 1$ ).

Samples ( $x$ )	$\Delta H_f^0$ /kJ.mol <sup>-1</sup>	$\Delta H_{f,ox}^0$ /kJ.mol <sup>-1</sup>
0	-1966.9±4.4	-317.6±4.3
0.1	-1990.1±4.6	-341.8±4.4
0.2	-1990.1±4.5	-342.7±4.4
0.3	-1982.7±4.4	-336.3±4.3
1	-1944.0±4.9	-304.3±4.4

The cause for such variation of standard molar enthalpy of formation for the solid solution and extent of substitution from the energetic point of view are described in Section 4.4.

#### 4.3.6. Enthalpy of mixing ( $\Delta H_{\text{mix}}$ ) of $(\text{La}_{1-x}\text{M}_{x/2}\text{Th}_{x/2})\text{PO}_4$ ( $0 \leq x \leq 1$ ) ( $M = \text{Ca}, \text{Sr}$ and $\text{Ba}$ )

The enthalpy of mixing,  $\Delta H_{\text{mix}}$  of  $(\text{La}_{1-x}\text{M}_{x/2}\text{Th}_{x/2})\text{PO}_4$  ( $0 \leq x \leq 1$ ) ( $M = \text{Ca}, \text{Sr}$  and  $\text{Ba}$ ) solid solutions relative to their end members viz.  $\text{LaPO}_4$  and  $\text{M}_{0.5}\text{Th}_{0.5}\text{PO}_4$  ( $M = \text{Ca}, \text{Sr}$  and  $\text{Ba}$ ) were derived from the drop solution enthalpies at 1089 K employing the following relation (4.13):

$$\Delta H_{\text{mix}} = -\Delta H_{\text{ds}}(\text{La}_{1-x}\text{M}_{x/2}\text{Th}_{x/2}\text{PO}_4) + (1-x) \cdot \Delta H_{\text{ds}}(\text{LaPO}_4) + x \cdot \Delta H_{\text{ds}}(\text{M}_{0.5}\text{Th}_{0.5}\text{PO}_4) \quad (4.13)$$

Using the above relation, enthalpy of mixing  $\Delta H_{\text{mix}}$  for the solid solutions was calculated relative to their end members and listed in **Table 4.21**. Further, the variation of  $\Delta H_{\text{mix}}$  of  $(\text{La}_{1-x}\text{M}_{x/2}\text{Th}_{x/2})\text{PO}_4$  ( $0 \leq x \leq 1$ ) ( $M = \text{Ca}, \text{Sr}$  and  $\text{Ba}$ ) as a function of mole fraction of end-member  $\text{M}_{0.5}\text{Th}_{0.5}\text{PO}_4$  ( $M = \text{Ca}, \text{Sr}$  and  $\text{Ba}$ ) was shown in **Figs. 4.33–4.35**.

**Table 4.21:** Calculated values of enthalpy of mixing,  $\Delta H_{\text{mix}}$  of  $(\text{La}_{1-x}\text{M}_{x/2}\text{Th}_{x/2})\text{PO}_4$  ( $0 \leq x \leq 1$ ) ( $M = \text{Ca}, \text{Sr}$  and  $\text{Ba}$ ) solid solutions relative to their end members.

$(\text{La}_{1-x}\text{Ca}_{x/2}\text{Th}_{x/2})\text{PO}_4$		$(\text{La}_{1-x}\text{Sr}_{x/2}\text{Th}_{x/2})\text{PO}_4$		$(\text{La}_{1-x}\text{Ba}_{x/2}\text{Th}_{x/2})\text{PO}_4$	
$x$	$\Delta H_{\text{mix}}$	$x$	$\Delta H_{\text{mix}}$	$x$	$\Delta H_{\text{mix}}$
0	0	0	0	0.8	-6.5
0.15	-26.4	0.1	-18.2	0.9	-3.4
0.25	-39.5	0.2	-31.8	1	0
				0.2	-27.8

0.4	-27.0	0.3	-38.5	0.3	-22.7
0.6	-18.3	0.4	-28.6	1	0
0.75	-9.5	0.5	-23.2		
0.85	0.14	0.6	-17.5		
1	0	0.7	-12.5		

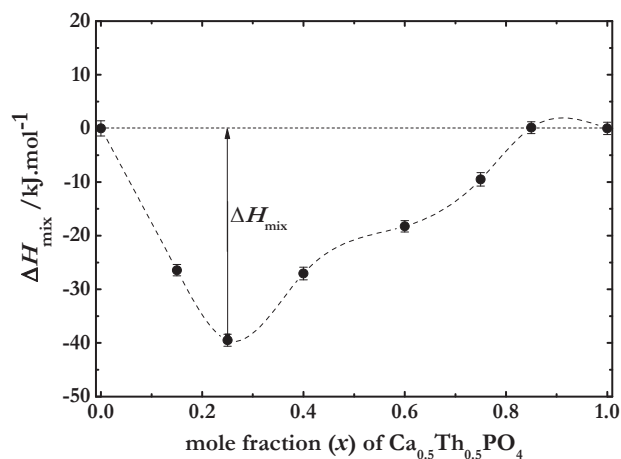


**Fig. 4.33:** Variation of enthalpy of mixing,  $\Delta H_{\text{mix}}$  of  $(\text{La}_{1-x}\text{Ca}_{x/2}\text{Th}_{x/2})\text{PO}_4$  ( $x = 0, 0.15, 0.25, 0.40, 0.60, 0.75, 0.85, 1$ ) as a function of mole fraction of  $\text{Ca}_{0.5}\text{Th}_{0.5}\text{PO}_4$  (with dashed line as a guide to the eye).

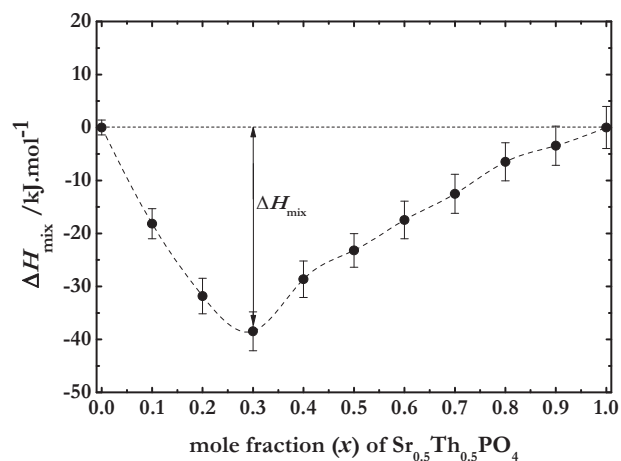


**Fig. 4.34:** Variation of enthalpy of mixing,  $\Delta H_{\text{mix}}$  of  $(\text{La}_{1-x}\text{Sr}_{x/2}\text{Th}_{x/2})\text{PO}_4$  ( $x = 0, 0.1, 0.2, 0.3, 0.4, 0.5, 0.6, 0.7, 0.8, 0.9, 1$ ) as a function of mole fraction of  $\text{Sr}_{0.5}\text{Th}_{0.5}\text{PO}_4$  (with dashed line as a guide to the eye).

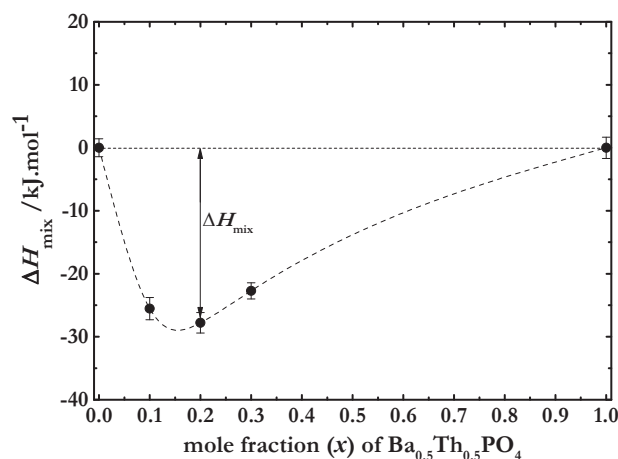


**Fig. 4.35:** Variation of enthalpy of mixing,  $\Delta H_{\text{mix}}$  of  $(\text{La}_{1-x}\text{Ba}_{x/2}\text{Th}_{x/2})\text{PO}_4$  ( $x = 0, 0.1, 0.2, 0.3; x = 1$ ) as a function of mole fraction of  $\text{Ba}_{0.5}\text{Th}_{0.5}\text{PO}_4$  (with dashed line as a guide to the eye).

The strongly negative value of  $\Delta H_{\text{mix}}$  shows that the charge-coupled substitution of La with (Ca, Th), (Sr, Th) and (Ba, Th) pairs in the monazite host matrix lead to an overall exothermic effect. The substitution results in thermodynamically more stable intermediate compositions than a mixture of the two end-members and discussed in Section 4.4.

### 4.3.7. Calculation of thermodynamic functions

The standard molar enthalpies of formation  $\Delta H_f^\circ(298 \text{ K})$  and specific heat capacity  $C_p^\circ(T)$  of  $(\text{La}_{1-x}\text{M}_{x/2}\text{Th}_{x/2})\text{PO}_4$  ( $0 \leq x \leq 1$ ) ( $M = \text{Ca}, \text{Sr}$  and  $\text{Ba}$ ) sample have been determined by high temperature solution calorimeter and differential scanning calorimeter. The standard molar entropy  $S_m^\circ(298 \text{ K})$  of the solid solutions has been estimated by adding the standard molar entropies  $S_m^\circ(298 \text{ K})$  of component oxides in their respective molar ratio from the literature [187]. The standard molar entropy  $S_m^\circ(T)$  of  $(\text{La}_{1-x}\text{M}_{x/2}\text{Th}_{x/2})\text{PO}_4$  ( $0 \leq x \leq 1$ ) ( $M = \text{Ca}, \text{Sr}$  and  $\text{Ba}$ ) samples at any temperature were calculated by using the relation:

$$S_m^\circ(\text{La}_{1-x}\text{M}_{x/2}\text{Th}_{x/2}\text{PO}_{4,\text{s}}, T) = S_m^\circ(\text{La}_{1-x}\text{M}_{x/2}\text{Th}_{x/2}\text{PO}_{4,\text{s}}, 298 \text{ K}) + \int_{298}^T \left( \frac{\Delta C_{p,\text{f}}^\circ(\text{La}_{1-x}\text{M}_{x/2}\text{Th}_{x/2}\text{PO}_{4,\text{s}}, T)}{T} \right) dT \quad (4.14)$$

The standard molar enthalpy of each composition of the solid solutions at any temperature can be calculated by the relation:

$$H_m^{\circ}(\text{La}_{1-x}\text{M}_{x/2}\text{Th}_{x/2}\text{PO}_{4,s},T) = H_m^{\circ}(\text{La}_{1-x}\text{M}_{x/2}\text{Th}_{x/2}\text{PO}_{4,s},298\text{ K}) + \int_{298}^T C_p^{\circ}(\text{La}_{1-x}\text{M}_{x/2}\text{Th}_{x/2}\text{PO}_{4,s},T)dT \quad (4.15)$$

$H_m^{\circ}(\text{La}_{1-x}\text{M}_{x/2}\text{Th}_{x/2}\text{PO}_{4,s},298\text{ K})$  can be equated to its standard molar enthalpy of formation  $\Delta H_{f,m}^{\circ}(\text{La}_{1-x}\text{M}_{x/2}\text{Th}_{x/2}\text{PO}_{4,s},298\text{ K})$  according to the following relation:

$$\Delta H_{f,m}^{\circ}(\text{La}_{1-x}\text{M}_{x/2}\text{Th}_{x/2}\text{PO}_{4,s},298\text{ K}) = H_m^{\circ}(\text{La}_{1-x}\text{M}_{x/2}\text{Th}_{x/2}\text{PO}_{4,s},298\text{ K}) - (1-x) \cdot H_m^{\circ}(\text{La},s) - x/2 \cdot H_m^{\circ}(\text{M},s) - x/2 \cdot H_m^{\circ}(\text{Th},s) - H_m^{\circ}(\text{P},s) - 2 \cdot H_m^{\circ}(\text{O}_2,g) \quad (4.16)$$

Since the values of the molar enthalpy of the elements in their standard state at 298 K [i.e.  $H_m^{\circ}(\text{La},s)$ ,  $H_m^{\circ}(\text{M},s)$ ,  $H_m^{\circ}(\text{Th},s)$ ,  $H_m^{\circ}(\text{P},s)$ ,  $H_m^{\circ}(\text{O}_2,g)$ ] are zero as per the convention. Hence, eqn. (4.15) could be expressed as:

$$H_m^{\circ}(\text{La}_{1-x}\text{M}_{x/2}\text{Th}_{x/2}\text{PO}_{4,s},T) = \Delta H_{f,m}^{\circ}(\text{La}_{1-x}\text{M}_{x/2}\text{Th}_{x/2}\text{PO}_{4,s},298\text{ K}) + \int_{298}^T C_{p,m}^{\circ}(\text{La}_{1-x}\text{M}_{x/2}\text{Th}_{x/2}\text{PO}_{4,s},T)dT \quad (4.17)$$

The Gibbs energies of the compounds at any temperature ‘ $T$ ’ were calculated from the combined values of standard molar enthalpies and standard molar entropies for the compounds using the relation:

$$G_m^{\circ}(T) = H_m^{\circ}(T) - T \cdot S_m^{\circ}(T) \quad (4.18)$$

The energy functions  $\Phi_m^{\circ}(T)$  for each composition of  $(\text{La}_{1-x}\text{M}_{x/2}\text{Th}_{x/2})\text{PO}_4$  ( $0 \leq x \leq 1$ ) ( $M = \text{Ca}$ ,  $\text{Sr}$  and  $\text{Ba}$ ) solid solutions are derived from the values of  $G_m^{\circ}(T)$  and  $\Delta H_{f,m}^{\circ}(298\text{ K})$  using the relation:

$$\Phi_m^{\circ}(T) = - \left( \frac{G_m^{\circ}(T) - H_m^{\circ}(298.15\text{ K})}{T} \right) \quad (4.19)$$

The values of free energy functions at the experimental temperatures for the different compositions for  $(\text{La}_{1-x}\text{M}_{x/2}\text{Th}_{x/2})\text{PO}_4$  ( $0 \leq x \leq 1$ ) ( $M = \text{Ca}$ ,  $\text{Sr}$  and  $\text{Ba}$ ) solid solutions are listed in **Tables 4.22-4.38**.

**Table 4.22:** Thermodynamic data for LaPO<sub>4</sub>, where  $T$  = temperature,  $C_p^\circ$  = standard molar heat capacity,  $S_T^\circ$  = standard molar entropy,  $H_T^\circ$  = standard molar enthalpy,  $G_T^\circ$  = standard Gibbs energy,  $-(G_T^\circ - H_{298}^\circ)/T$  = free energy function,  $\Delta H_f^\circ$  = standard molar enthalpy of formation,  $\Delta G_f^\circ$  = standard molar free energy of formation as a function of temperature at a pressure of 101.325 kPa<sup>a</sup>.

$T$ (K)	$C_p^\circ$ (J·mol <sup>-1</sup> ·K <sup>-1</sup> )	$S_T^\circ$ (J·mol <sup>-1</sup> ·K <sup>-1</sup> )	$-H_T^\circ$ (kJ·mol <sup>-1</sup> )	$-G_T^\circ$ (kJ·mol <sup>-1</sup> )	$-(G_T^\circ - H_{298}^\circ)/T$ (J·mol <sup>-1</sup> ·K <sup>-1</sup> )	$\Delta H_f^\circ$ (kJ·mol <sup>-1</sup> )	$\Delta G_f^\circ$ (kJ·mol <sup>-1</sup> )
298	97.6	120.8	1966.9	2002.9	120.9	-1966.9	-1851.4
300	98.0	121.5	1966.7	2003.2	120.8	-1966.9	-1850.6
350	107.4	137.3	1961.6	2009.7	122.2	-1967.3	-1831.2
400	114.4	152.1	1956.0	2016.9	124.9	-1967.3	-1811.8
450	120.1	165.9	1950.1	2024.8	128.7	-1967.2	-1792.3
500	125.0	178.9	1944.0	2033.5	133.1	-1966.8	-1772.9
550	129.4	191.0	1937.6	2042.7	137.8	-1966.3	-1753.6
600	133.3	202.4	1931.1	2052.6	142.8	-1965.6	-1734.2
650	137.0	213.2	1924.3	2062.9	147.7	-1964.9	-1715.0
700	140.6	223.5	1917.4	2073.9	152.9	-1964.0	-1695.8
750	144.0	233.3	1910.3	2085.3	157.9	-1962.9	-1676.7
800	147.2	242.7	1902.9	2097.1	162.8	-1961.8	-1657.6

<sup>a</sup>The standard uncertainty  $u(T) = 0.5$  K, Expanded uncertainty  $U(P) = 5000$  Pa (0.997 level of confidence).

**Table 4.23:** Thermodynamic data for (La<sub>0.85</sub>Ca<sub>0.075</sub>Th<sub>0.075</sub>)PO<sub>4</sub>, where  $T$  = temperature,  $C_p^\circ$  = standard molar heat capacity,  $S_T^\circ$  = standard molar entropy,  $H_T^\circ$  = standard molar enthalpy,  $G_T^\circ$  = standard Gibbs energy,  $-(G_T^\circ - H_{298}^\circ)/T$  = free energy function,  $\Delta H_f^\circ$  = standard molar enthalpy of formation,  $\Delta G_f^\circ$  = standard molar free energy of formation as a function of temperature at a pressure of 101.325 kPa<sup>a</sup>.

$T$ (K)	$C_p^\circ$ (J·mol <sup>-1</sup> ·K <sup>-1</sup> )	$S_T^\circ$ (J·mol <sup>-1</sup> ·K <sup>-1</sup> )	$-H_T^\circ$ (kJ·mol <sup>-1</sup> )	$-G_T^\circ$ (kJ·mol <sup>-1</sup> )	$-(G_T^\circ - H_{298}^\circ)/T$ (J·mol <sup>-1</sup> ·K <sup>-1</sup> )	$\Delta H_f^\circ$ (kJ·mol <sup>-1</sup> )	$\Delta G_f^\circ$ (kJ·mol <sup>-1</sup> )
298	94.5	119.0	1989.5	2025.0	119.0	-1989.5	-1873.9
300	94.9	119.6	1989.3	2025.2	118.9	-1989.5	-1873.1
350	104.2	135.0	1984.3	2031.6	120.1	-1990.1	-1853.7
400	111.4	149.4	1978.9	2038.7	122.9	-1990.3	-1834.2
450	117.4	162.9	1973.2	2046.5	126.7	-1990.2	-1814.6
500	122.7	175.5	1967.2	2055.0	130.9	-1990.1	-1795.3
550	127.5	187.5	1960.9	2064.0	135.5	-1989.6	-1775.7
600	132.0	198.7	1954.5	2073.7	140.4	-1989.1	-1756.4
650	136.3	209.5	1947.7	2083.9	145.2	-1988.3	-1736.9
700	140.4	219.7	1940.8	2094.6	150.1	-1987.5	-1717.7
750	144.3	229.6	1933.7	2105.9	155.2	-1986.5	-1698.4
800	148.2	239.0	1926.4	2117.6	160.1	-1985.4	-1679.3

<sup>a</sup>The standard uncertainty  $u(T) = 0.5$  K, Expanded uncertainty  $U(P) = 5000$  Pa (0.997 level of confidence).

**Table 4.24:** Thermodynamic data for  $(\text{La}_{0.75}\text{Ca}_{0.125}\text{Th}_{0.125})\text{PO}_4$ , where  $T$  = temperature,  $C_p^\circ$  = standard molar heat capacity,  $S_T^\circ$  = standard molar entropy,  $H_T^\circ$  = standard molar enthalpy,  $G_T^\circ$  = standard Gibbs energy,  $-(G_T^\circ - H_{298}^\circ)/T$  = free energy function,  $\Delta H_f^\circ$  = standard molar enthalpy of formation,  $\Delta G_f^\circ$  = standard molar free energy of formation as a function of temperature at a pressure of 101.325 kPa<sup>a</sup>.

$T$ (K)	$C_p^\circ$ ( $\text{J}\cdot\text{mol}^{-1}\cdot\text{K}^{-1}$ )	$S_T^\circ$ ( $\text{J}\cdot\text{mol}^{-1}\cdot\text{K}^{-1}$ )	$-H_T^\circ$ ( $\text{kJ}\cdot\text{mol}^{-1}$ )	$-G_T^\circ$ ( $\text{kJ}\cdot\text{mol}^{-1}$ )	$-(G_T^\circ - H_{298}^\circ)/T$ ( $\text{J}\cdot\text{mol}^{-1}\cdot\text{K}^{-1}$ )	$\Delta H_f^\circ$ ( $\text{kJ}\cdot\text{mol}^{-1}$ )	$\Delta G_f^\circ$ ( $\text{kJ}\cdot\text{mol}^{-1}$ )
298	93.5	117.8	2000.0	2035.1	117.8	-2000.0	-1884.4
300	94.0	118.4	1999.8	2035.3	117.7	-2000.1	-1883.7
350	103.5	133.7	1994.8	2041.6	118.8	-2000.6	-1864.1
400	110.8	148.0	1989.5	2048.7	121.8	-2000.8	-1844.5
450	116.7	161.4	1983.8	2056.4	125.4	-2000.9	-1825.1
500	121.7	174.0	1977.8	2064.8	129.6	-2000.6	-1805.5
550	126.2	185.8	1971.6	2073.8	134.2	-2000.3	-1786.0
600	130.4	196.9	1965.2	2083.3	138.9	-1999.8	-1766.5
650	134.2	207.5	1958.6	2093.5	143.8	-1999.2	-1747.2
700	137.9	217.6	1951.8	2104.1	148.7	-1998.5	-1727.8
750	141.5	227.3	1944.8	2115.3	153.7	-1997.6	-1708.5
800	144.9	236.5	1937.7	2126.9	158.6	-1996.7	-1689.3

<sup>a</sup>The standard uncertainty  $u(T) = 0.5$  K, Expanded uncertainty  $U(P) = 5000$  Pa (0.997 level of confidence).

**Table 4.25:** Thermodynamic data for  $(\text{La}_{0.60}\text{Ca}_{0.20}\text{Th}_{0.20})\text{PO}_4$ , where  $T$  = temperature,  $C_p^\circ$  = standard molar heat capacity,  $S_T^\circ$  = standard molar entropy,  $H_T^\circ$  = standard molar enthalpy,  $G_T^\circ$  = standard Gibbs energy,  $-(G_T^\circ - H_{298}^\circ)/T$  = free energy function,  $\Delta H_f^\circ$  = standard molar enthalpy of formation,  $\Delta G_f^\circ$  = standard molar free energy of formation as a function of temperature at a pressure of 101.325 kPa<sup>a</sup>.

$T$ (K)	$C_p^\circ$ ( $\text{J}\cdot\text{mol}^{-1}\cdot\text{K}^{-1}$ )	$S_T^\circ$ ( $\text{J}\cdot\text{mol}^{-1}\cdot\text{K}^{-1}$ )	$-H_T^\circ$ ( $\text{kJ}\cdot\text{mol}^{-1}$ )	$-G_T^\circ$ ( $\text{kJ}\cdot\text{mol}^{-1}$ )	$-(G_T^\circ - H_{298}^\circ)/T$ ( $\text{J}\cdot\text{mol}^{-1}\cdot\text{K}^{-1}$ )	$\Delta H_f^\circ$ ( $\text{kJ}\cdot\text{mol}^{-1}$ )	$\Delta G_f^\circ$ ( $\text{kJ}\cdot\text{mol}^{-1}$ )
298	95.4	116.0	1983.8	2018.4	116.1	-1983.8	-1868.0
300	95.9	116.7	1983.6	2018.6	116.0	-1983.8	-1867.2
350	105.9	132.2	1978.6	2024.9	117.4	-1984.2	-1847.8
400	113.3	146.9	1973.1	2031.9	120.2	-1984.4	-1828.3
450	119.2	160.6	1967.2	2039.5	123.7	-1984.3	-1808.7
500	124.2	173.4	1961.2	2047.9	128.3	-1984.0	-1789.3
550	128.6	185.5	1954.8	2056.8	132.8	-1983.5	-1769.8
600	132.6	196.8	1948.3	2066.4	137.7	-1982.9	-1750.4
650	136.3	207.6	1941.6	2076.6	142.7	-1982.2	-1731.1
700	139.7	217.8	1934.7	2087.2	147.7	-1981.3	-1711.8
750	143.0	227.6	1927.6	2098.3	152.7	-1980.4	-1692.6
800	146.2	236.9	1920.4	2110.0	157.7	-1979.4	-1673.4

<sup>a</sup>The standard uncertainty  $u(T) = 0.5$  K, Expanded uncertainty  $U(P) = 5000$  Pa (0.997 level of confidence).

**Table 4.26:** Thermodynamic data for  $(\text{La}_{0.40}\text{Ca}_{0.30}\text{Th}_{0.30})\text{PO}_4$ , where  $T$  = temperature,  $C_p^\circ$  = standard molar heat capacity,  $S_T^\circ$  = standard molar entropy,  $H_T^\circ$  = standard molar enthalpy,  $G_T^\circ$  = standard Gibbs energy,  $-(G_T^\circ - H_{298}^\circ)/T$  = free energy function,  $\Delta H_f^\circ$  = standard molar enthalpy of formation,  $\Delta G_f^\circ$  = standard molar free energy of formation as a function of temperature at a pressure of 101.325 kPa<sup>a</sup>.

$T$ (K)	$C_p^\circ$ ( $\text{J}\cdot\text{mol}^{-1}\cdot\text{K}^{-1}$ )	$S_T^\circ$ ( $\text{J}\cdot\text{mol}^{-1}\cdot\text{K}^{-1}$ )	$-H_T^\circ$ ( $\text{kJ}\cdot\text{mol}^{-1}$ )	$-G_T^\circ$ ( $\text{kJ}\cdot\text{mol}^{-1}$ )	$-(G_T^\circ - H_{298}^\circ)/T$ ( $\text{J}\cdot\text{mol}^{-1}\cdot\text{K}^{-1}$ )	$\Delta H_f^\circ$ ( $\text{kJ}\cdot\text{mol}^{-1}$ )	$\Delta G_f^\circ$ ( $\text{kJ}\cdot\text{mol}^{-1}$ )
298	97.4	113.6	1969.8	2003.7	113.7	-1969.8	-1853.9
300	97.8	114.3	1969.6	2003.9	113.6	-1969.8	-1853.1
350	107.5	130.1	1964.5	2010.1	115.0	-1970.1	-1833.6
400	114.9	145.0	1958.9	2016.9	117.8	-1970.2	-1814.1
450	120.9	158.9	1952.9	2024.4	121.3	-1970.0	-1794.6
500	126.1	171.9	1946.8	2032.8	125.9	-1969.6	-1775.1
550	130.8	184.1	1940.4	2041.7	130.7	-1969.1	-1755.7
600	135.1	195.7	1933.7	2051.1	135.6	-1968.4	-1736.3
650	139.1	206.6	1926.9	2061.2	140.7	-1967.5	-1717.0
700	142.9	217.1	1919.8	2071.8	145.7	-1966.6	-1697.8
750	146.6	227.1	1912.6	2082.9	150.9	-1965.5	-1678.6
800	150.2	236.7	1905.2	2094.6	156.0	-1964.3	-1659.5

<sup>a</sup>The standard uncertainty  $u(T) = 0.5$  K, Expanded uncertainty  $U(P) = 5000$  Pa (0.997 level of confidence).

**Table 4.27:** Thermodynamic data for  $(\text{La}_{0.25}\text{Ca}_{0.375}\text{Th}_{0.375})\text{PO}_4$ , where  $T$  = temperature,  $C_p^\circ$  = standard molar heat capacity,  $S_T^\circ$  = standard molar entropy,  $H_T^\circ$  = standard molar enthalpy,  $G_T^\circ$  = standard Gibbs energy,  $-(G_T^\circ - H_{298}^\circ)/T$  = free energy function,  $\Delta H_f^\circ$  = standard molar enthalpy of formation,  $\Delta G_f^\circ$  = standard molar free energy of formation as a function of temperature at a pressure of 101.325 kPa<sup>a</sup>.

$T$ (K)	$C_p^\circ$ ( $\text{J}\cdot\text{mol}^{-1}\cdot\text{K}^{-1}$ )	$S_T^\circ$ ( $\text{J}\cdot\text{mol}^{-1}\cdot\text{K}^{-1}$ )	$-H_T^\circ$ ( $\text{kJ}\cdot\text{mol}^{-1}$ )	$-G_T^\circ$ ( $\text{kJ}\cdot\text{mol}^{-1}$ )	$-(G_T^\circ - H_{298}^\circ)/T$ ( $\text{J}\cdot\text{mol}^{-1}\cdot\text{K}^{-1}$ )	$\Delta H_f^\circ$ ( $\text{kJ}\cdot\text{mol}^{-1}$ )	$\Delta G_f^\circ$ ( $\text{kJ}\cdot\text{mol}^{-1}$ )
298	92.4	111.8	1957.2	1990.5	111.9	-1957.2	-1841.2
300	92.8	112.4	1957.0	1990.7	111.8	-1957.2	-1840.4
350	101.6	127.4	1952.1	1996.7	112.9	-1957.8	-1820.9
400	108.1	141.4	1946.9	2003.5	115.7	-1958.2	-1801.3
450	113.5	154.5	1941.4	2010.9	119.4	-1958.4	-1781.6
500	118.0	166.7	1935.6	2019.0	123.5	-1958.4	-1762.0
550	122.0	178.1	1929.6	2027.6	128.0	-1958.2	-1742.3
600	125.7	188.9	1923.6	2037.0	132.9	-1958.0	-1722.7
650	129.1	199.1	1917.0	2046.4	137.3	-1957.7	-1703.1
700	132.3	208.8	1910.5	2056.7	142.1	-1957.2	-1683.6
750	135.4	218.0	1903.8	2067.3	146.9	-1956.7	-1664.1
800	138.4	226.9	1896.9	2078.4	151.5	-1956.1	-1644.6

<sup>a</sup>The standard uncertainty  $u(T) = 0.5$  K, Expanded uncertainty  $U(P) = 5000$  Pa (0.997 level of confidence).

**Table 4.28:** Thermodynamic data for  $(\text{La}_{0.15}\text{Ca}_{0.425}\text{Th}_{0.425})\text{PO}_4$ , where  $T$  = temperature,  $C_p^\circ$  = standard molar heat capacity,  $S_T^\circ$  = standard molar entropy,  $H_T^\circ$  = standard molar enthalpy,  $G_T^\circ$  = standard Gibbs energy,  $-(G_T^\circ - H_{298}^\circ)/T$  = free energy function,  $\Delta H_f^\circ$  = standard molar enthalpy of formation,  $\Delta G_f^\circ$  = standard molar free energy of formation as a function of temperature at a pressure of 101.325 kPa<sup>a</sup>.

$T$ (K)	$C_p^\circ$ ( $\text{J}\cdot\text{mol}^{-1}\cdot\text{K}^{-1}$ )	$S_T^\circ$ ( $\text{J}\cdot\text{mol}^{-1}\cdot\text{K}^{-1}$ )	$-H_T^\circ$ ( $\text{kJ}\cdot\text{mol}^{-1}$ )	$-G_T^\circ$ ( $\text{kJ}\cdot\text{mol}^{-1}$ )	$-(G_T^\circ - H_{298}^\circ)/T$ ( $\text{J}\cdot\text{mol}^{-1}\cdot\text{K}^{-1}$ )	$\Delta H_f^\circ$ ( $\text{kJ}\cdot\text{mol}^{-1}$ )	$\Delta G_f^\circ$ ( $\text{kJ}\cdot\text{mol}^{-1}$ )
298	93.1	110.6	1945.0	1978.0	110.7	-1945.0	-1828.9
300	93.6	111.2	1944.8	1978.2	110.6	-1945.0	-1828.1
350	103.6	126.5	1939.9	1984.2	111.9	-1945.5	-1808.6
400	110.9	140.8	1934.5	1990.8	114.6	-1945.8	-1789.0
450	116.6	154.2	1928.8	1998.2	118.2	-1945.8	-1769.4
500	121.3	166.7	1922.8	2006.2	122.4	-1945.6	-1749.8
550	125.4	178.5	1916.7	2014.9	127.1	-1945.4	-1730.2
600	129.1	189.6	1910.3	2024.1	131.8	-1945.0	-1710.7
650	132.4	200.0	1903.8	2033.8	136.7	-1944.5	-1691.2
700	135.5	210.0	1897.1	2044.1	141.6	-1943.9	-1671.7
750	138.4	219.4	1890.2	2054.8	146.4	-1943.2	-1652.3
800	141.3	228.4	1883.2	2066.0	151.2	-1942.5	-1632.9

<sup>a</sup>The standard uncertainty  $u(T) = 0.5$  K, Expanded uncertainty  $U(P) = 5000$  Pa (0.997 level of confidence).

**Table 4.29:** Thermodynamic data for  $\text{Ca}_{0.5}\text{Th}_{0.5}\text{PO}_4$ , where  $T$  = temperature,  $C_p^\circ$  = standard molar heat capacity,  $S_T^\circ$  = standard molar entropy,  $H_T^\circ$  = standard molar enthalpy,  $G_T^\circ$  = standard Gibbs energy,  $-(G_T^\circ - H_{298}^\circ)/T$  = free energy function,  $\Delta H_f^\circ$  = standard molar enthalpy of formation,  $\Delta G_f^\circ$  = standard molar free energy of formation as a function of temperature at a pressure of 101.325 kPa<sup>a</sup>.

$T$ (K)	$C_p^\circ$ ( $\text{J}\cdot\text{mol}^{-1}\cdot\text{K}^{-1}$ )	$S_T^\circ$ ( $\text{J}\cdot\text{mol}^{-1}\cdot\text{K}^{-1}$ )	$-H_T^\circ$ ( $\text{kJ}\cdot\text{mol}^{-1}$ )	$-G_T^\circ$ ( $\text{kJ}\cdot\text{mol}^{-1}$ )	$-(G_T^\circ - H_{298}^\circ)/T$ ( $\text{J}\cdot\text{mol}^{-1}\cdot\text{K}^{-1}$ )	$\Delta H_f^\circ$ ( $\text{kJ}\cdot\text{mol}^{-1}$ )	$\Delta G_f^\circ$ ( $\text{kJ}\cdot\text{mol}^{-1}$ )
298	95.0	108.8	1941.4	1973.8	108.9	-1941.4	-1825.2
300	95.4	109.5	1941.2	1974.0	108.8	-1941.4	-1824.4
350	105.0	124.9	1936.2	1979.9	110.1	-1941.9	-1804.8
400	112.6	139.5	1930.7	1986.5	112.7	-1942.0	-1785.2
450	119.0	153.1	1924.9	1993.8	116.5	-1941.9	-1765.7
500	124.6	165.9	1918.8	2001.8	120.8	-1941.6	-1746.1
550	129.8	178.1	1912.5	2010.5	125.6	-1941.2	-1726.6
600	134.7	189.6	1905.8	2019.6	130.3	-1940.5	-1707.1
650	139.3	200.6	1899.1	2029.3	135.2	-1939.7	-1687.6
700	143.7	211.1	1891.9	2039.7	140.4	-1938.7	-1668.3
750	148.1	221.1	1884.6	2050.5	145.5	-1937.6	-1649.0
800	152.3	230.8	1877.1	2061.8	150.6	-1936.4	-1629.8

<sup>a</sup>The standard uncertainty  $u(T) = 0.5$  K, Expanded uncertainty  $U(P) = 5000$  Pa (0.997 level of confidence).

**Table 4.30:** Thermodynamic data for  $(\text{La}_{0.8}\text{Sr}_{0.1}\text{Th}_{0.1})\text{PO}_4$ , where  $T$  = temperature,  $C_p^\circ$  = standard molar heat capacity,  $S_T^\circ$  = standard molar entropy,  $H_T^\circ$  = standard molar enthalpy,  $G_T^\circ$  = standard Gibbs energy,  $-(G_T^\circ - H_{298}^\circ)/T$  = free energy function,  $\Delta H_f^\circ$  = standard molar enthalpy of formation,  $\Delta G_f^\circ$  = standard molar free energy of formation as a function of temperature at a pressure of 101.325 kPa<sup>a</sup>.

$T$ (K)	$C_p^\circ$ ( $\text{J}\cdot\text{mol}^{-1}\cdot\text{K}^{-1}$ )	$S_T^\circ$ ( $\text{J}\cdot\text{mol}^{-1}\cdot\text{K}^{-1}$ )	$-H_T^\circ$ ( $\text{kJ}\cdot\text{mol}^{-1}$ )	$-G_T^\circ$ ( $\text{kJ}\cdot\text{mol}^{-1}$ )	$-(G_T^\circ - H_{298}^\circ)/T$ ( $\text{J}\cdot\text{mol}^{-1}\cdot\text{K}^{-1}$ )	$\Delta H_f^\circ$ ( $\text{kJ}\cdot\text{mol}^{-1}$ )	$\Delta G_f^\circ$ ( $\text{kJ}\cdot\text{mol}^{-1}$ )
298	102.6	120.2	1995.1	2030.9	120.2	-1995.1	-1879.6
300	103.0	120.9	1994.9	2031.2	120.2	-1995.1	-1878.8
350	111.6	137.4	1989.5	2037.6	121.4	-1995.3	-1859.5
400	118.3	152.8	1983.7	2044.8	124.3	-1995.2	-1840.1
450	123.9	167.1	1977.7	2052.9	128.4	-1994.8	-1820.7
500	128.8	180.4	1971.4	2061.6	133.0	-1994.3	-1801.4
550	133.3	192.9	1964.8	2070.9	137.8	-1993.6	-1782.2
600	137.4	204.6	1958.1	2080.9	142.9	-1992.7	-1763.0
650	141.4	215.8	1951.1	2091.4	148.1	-1991.7	-1743.8
700	145.1	226.4	1943.9	2102.4	153.3	-1990.6	-1724.8
750	148.8	236.6	1936.6	2114.1	158.6	-1989.4	-1705.9
800	152.3	246.3	1929.1	2126.1	163.8	-1988.0	-1687.0

<sup>a</sup>The standard uncertainty  $u(T) = 0.5$  K, Expanded uncertainty  $U(P) = 5000$  Pa (0.997 level of confidence).

**Table 4.31:** Thermodynamic data for  $(\text{La}_{0.6}\text{Sr}_{0.2}\text{Th}_{0.2})\text{PO}_4$ , where  $T$  = temperature,  $C_p^\circ$  = standard molar heat capacity,  $S_T^\circ$  = standard molar entropy,  $H_T^\circ$  = standard molar enthalpy,  $G_T^\circ$  = standard Gibbs energy,  $-(G_T^\circ - H_{298}^\circ)/T$  = free energy function,  $\Delta H_f^\circ$  = standard molar enthalpy of formation,  $\Delta G_f^\circ$  = standard molar free energy of formation as a function of temperature at a pressure of 101.325 kPa<sup>a</sup>.

$T$ (K)	$C_p^\circ$ ( $\text{J}\cdot\text{mol}^{-1}\cdot\text{K}^{-1}$ )	$S_T^\circ$ ( $\text{J}\cdot\text{mol}^{-1}\cdot\text{K}^{-1}$ )	$-H_T^\circ$ ( $\text{kJ}\cdot\text{mol}^{-1}$ )	$-G_T^\circ$ ( $\text{kJ}\cdot\text{mol}^{-1}$ )	$-(G_T^\circ - H_{298}^\circ)/T$ ( $\text{J}\cdot\text{mol}^{-1}\cdot\text{K}^{-1}$ )	$\Delta H_f^\circ$ ( $\text{kJ}\cdot\text{mol}^{-1}$ )	$\Delta G_f^\circ$ ( $\text{kJ}\cdot\text{mol}^{-1}$ )
298	104.2	119.5	1988.3	2023.9	119.5	-1988.3	-1872.8
300	104.5	120.2	1988.1	2024.2	119.5	-1988.3	-1872.0
350	111.6	136.9	1982.7	2030.6	120.9	-1988.4	-1852.6
400	117.4	152.2	1976.9	2037.8	123.7	-1988.3	-1833.2
450	122.5	166.3	1970.9	2045.7	127.6	-1988.1	-1813.9
500	127.0	179.4	1964.7	2054.4	132.2	-1987.6	-1794.6
550	131.2	191.7	1958.3	2063.7	137.2	-1987.0	-1775.3
600	135.3	203.3	1951.6	2073.6	142.1	-1986.3	-1756.1
650	139.1	214.3	1944.7	2084.0	147.2	-1985.4	-1736.9
700	142.9	224.7	1937.7	2095.0	152.4	-1984.4	-1717.8
750	146.6	234.7	1930.5	2106.5	157.6	-1983.3	-1698.8
800	150.2	244.3	1923.0	2118.4	162.7	-1982.1	-1679.9

<sup>a</sup>The standard uncertainty  $u(T) = 0.5$  K, Expanded uncertainty  $U(P) = 5000$  Pa (0.997 level of confidence).

**Table 4.32:** Thermodynamic data for  $(\text{La}_{0.4}\text{Sr}_{0.3}\text{Th}_{0.3})\text{PO}_4$ , where  $T$  = temperature,  $C_p^\circ$  = standard molar heat capacity,  $S_T^\circ$  = standard molar entropy,  $H_T^\circ$  = standard molar enthalpy,  $G_T^\circ$  = standard Gibbs energy,  $-(G_T^\circ - H_{298}^\circ)/T$  = free energy function,  $\Delta H_f^\circ$  = standard molar enthalpy of formation,  $\Delta G_f^\circ$  = standard molar free energy of formation as a function of temperature at a pressure of 101.325 kPa<sup>a</sup>.

$T$ (K)	$C_p^\circ$ ( $\text{J}\cdot\text{mol}^{-1}\cdot\text{K}^{-1}$ )	$S_T^\circ$ ( $\text{J}\cdot\text{mol}^{-1}\cdot\text{K}^{-1}$ )	$-H_T^\circ$ ( $\text{kJ}\cdot\text{mol}^{-1}$ )	$-G_T^\circ$ ( $\text{kJ}\cdot\text{mol}^{-1}$ )	$-(G_T^\circ - H_{298}^\circ)/T$ ( $\text{J}\cdot\text{mol}^{-1}\cdot\text{K}^{-1}$ )	$\Delta H_f^\circ$ ( $\text{kJ}\cdot\text{mol}^{-1}$ )	$\Delta G_f^\circ$ ( $\text{kJ}\cdot\text{mol}^{-1}$ )
298	104.0	118.8	1973.5	2008.9	118.9	-1973.5	-1858.0
300	104.4	119.5	1973.3	2009.2	118.9	-1973.5	-1857.2
350	110.9	136.1	1967.9	2015.6	120.2	-1973.6	-1837.8
400	116.4	151.3	1962.2	2022.7	123.1	-1973.6	-1818.4
450	121.1	165.3	1956.3	2030.7	127.1	-1973.4	-1799.1
500	125.3	178.3	1950.1	2039.3	131.5	-1973.0	-1779.7
550	129.3	190.4	1943.7	2048.4	136.3	-1972.6	-1760.4
600	133.2	201.8	1937.2	2058.3	141.4	-1971.9	-1741.1
650	136.8	212.6	1930.4	2068.6	146.4	-1971.2	-1721.9
700	140.4	222.9	1923.5	2079.6	151.5	-1970.3	-1702.8
750	143.9	232.7	1916.4	2091.0	156.6	-1969.3	-1683.7
800	147.4	242.1	1909.1	2102.8	161.6	-1968.2	-1664.7

<sup>a</sup>The standard uncertainty  $u(T) = 0.5$  K, Expanded uncertainty  $U(P) = 5000$  Pa (0.997 level of confidence).

**Table 4.33:** Thermodynamic data for  $(\text{La}_{0.2}\text{Sr}_{0.4}\text{Th}_{0.4})\text{PO}_4$ , where  $T$  = temperature,  $C_p^\circ$  = standard molar heat capacity,  $S_T^\circ$  = standard molar entropy,  $H_T^\circ$  = standard molar enthalpy,  $G_T^\circ$  = standard Gibbs energy,  $-(G_T^\circ - H_{298}^\circ)/T$  = free energy function,  $\Delta H_f^\circ$  = standard molar enthalpy of formation,  $\Delta G_f^\circ$  = standard molar free energy of formation as a function of temperature at a pressure of 101.325 kPa<sup>a</sup>.

$T$ (K)	$C_p^\circ$ ( $\text{J}\cdot\text{mol}^{-1}\cdot\text{K}^{-1}$ )	$S_T^\circ$ ( $\text{J}\cdot\text{mol}^{-1}\cdot\text{K}^{-1}$ )	$-H_T^\circ$ ( $\text{kJ}\cdot\text{mol}^{-1}$ )	$-G_T^\circ$ ( $\text{kJ}\cdot\text{mol}^{-1}$ )	$-(G_T^\circ - H_{298}^\circ)/T$ ( $\text{J}\cdot\text{mol}^{-1}\cdot\text{K}^{-1}$ )	$\Delta H_f^\circ$ ( $\text{kJ}\cdot\text{mol}^{-1}$ )	$\Delta G_f^\circ$ ( $\text{kJ}\cdot\text{mol}^{-1}$ )
298	103.3	118.2	1958.9	1994.1	118.2	-1958.9	-1843.4
300	103.7	118.9	1958.7	1994.4	118.2	-1958.9	-1842.6
350	112.1	135.5	1953.3	2000.7	119.6	-1959.0	-1823.2
400	118.7	150.9	1947.5	2007.9	122.5	-1958.9	-1803.8
450	124.3	165.2	1941.4	2015.8	126.4	-1958.6	-1784.5
500	129.3	178.6	1935.1	2024.4	131.0	-1958.0	-1765.1
550	133.9	191.1	1928.5	2033.7	135.9	-1957.4	-1745.9
600	138.2	203.0	1921.7	2043.5	141.0	-1956.5	-1726.7
650	142.3	214.2	1914.7	2054.0	146.3	-1955.5	-1707.6
700	146.3	224.9	1907.5	2065.0	151.5	-1954.4	-1688.6
750	150.1	235.1	1900.1	2076.5	156.8	-1953.1	-1669.7
800	153.9	244.9	1892.5	2088.5	162.0	-1951.7	-1650.8

<sup>a</sup>The standard uncertainty  $u(T) = 0.5$  K, Expanded uncertainty  $U(P) = 5000$  Pa (0.997 level of confidence).

**Table 4.34:** Thermodynamic data for  $\text{Sr}_{0.5}\text{Th}_{0.5}\text{PO}_4$ , where  $T$  = temperature,  $C_p^\circ$  = standard molar heat capacity,  $S_T^\circ$  = standard molar entropy,  $H_T^\circ$  = standard molar enthalpy,  $G_T^\circ$  = standard Gibbs energy,  $-(G_T^\circ - H_{298}^\circ)/T$  = free energy function,  $\Delta H_f^\circ$  = standard molar enthalpy of formation,  $\Delta G_f^\circ$  = standard molar free energy of formation as a function of temperature at a pressure of 101.325 kPa<sup>a</sup>.

$T$ (K)	$C_p^\circ$ ( $\text{J}\cdot\text{mol}^{-1}\cdot\text{K}^{-1}$ )	$S_T^\circ$ ( $\text{J}\cdot\text{mol}^{-1}\cdot\text{K}^{-1}$ )	$-H_T^\circ$ ( $\text{kJ}\cdot\text{mol}^{-1}$ )	$-G_T^\circ$ ( $\text{kJ}\cdot\text{mol}^{-1}$ )	$-(G_T^\circ - H_{298}^\circ)/T$ ( $\text{J}\cdot\text{mol}^{-1}\cdot\text{K}^{-1}$ )	$\Delta H_f^\circ$ ( $\text{kJ}\cdot\text{mol}^{-1}$ )	$\Delta G_f^\circ$ ( $\text{kJ}\cdot\text{mol}^{-1}$ )
298	104.2	117.5	1948.8	1983.8	117.5	-1948.8	-1833.3
300	104.5	118.2	1948.6	1984.1	117.5	-1948.8	-1832.5
350	112.0	134.9	1943.2	1990.4	118.9	-1948.9	-1813.1
400	117.5	150.2	1937.4	1997.5	121.7	-1948.8	-1793.7
450	121.8	164.3	1931.4	2005.3	125.6	-1948.6	-1774.4
500	125.4	177.4	1925.3	2014.0	130.4	-1948.2	-1755.0
550	128.6	189.5	1918.9	2023.1	135.1	-1947.8	-1735.7
600	131.4	200.8	1912.4	2032.9	140.1	-1947.3	-1716.5
650	133.9	211.4	1905.8	2043.2	145.2	-1946.6	-1697.2
700	136.4	221.4	1899.0	2054.0	150.3	-1945.9	-1678.0
750	138.6	230.9	1892.1	2065.3	155.3	-1945.2	-1658.9
800	140.8	239.9	1885.2	2077.1	160.4	-1944.4	-1639.9

<sup>a</sup>The standard uncertainty  $u(T) = 0.5$  K, Expanded uncertainty  $U(P) = 5000$  Pa (0.997 level of confidence).

**Table 4.35:** Thermodynamic data for  $(\text{La}_{0.9}\text{Ba}_{0.05}\text{Th}_{0.05})\text{PO}_4$ , where  $T$  = temperature,  $C_p^\circ$  = standard molar heat capacity,  $S_T^\circ$  = standard molar entropy,  $H_T^\circ$  = standard molar enthalpy,  $G_T^\circ$  = standard Gibbs energy,  $-(G_T^\circ - H_{298}^\circ)/T$  = free energy function,  $\Delta H_f^\circ$  = standard molar enthalpy of formation,  $\Delta G_f^\circ$  = standard molar free energy of formation as a function of temperature at a pressure of 101.325 kPa<sup>a</sup>.

$T$ (K)	$C_p^\circ$ ( $\text{J}\cdot\text{mol}^{-1}\cdot\text{K}^{-1}$ )	$S_T^\circ$ ( $\text{J}\cdot\text{mol}^{-1}\cdot\text{K}^{-1}$ )	$-H_T^\circ$ ( $\text{kJ}\cdot\text{mol}^{-1}$ )	$-G_T^\circ$ ( $\text{kJ}\cdot\text{mol}^{-1}$ )	$-(G_T^\circ - H_{298}^\circ)/T$ ( $\text{J}\cdot\text{mol}^{-1}\cdot\text{K}^{-1}$ )	$\Delta H_f^\circ$ ( $\text{kJ}\cdot\text{mol}^{-1}$ )	$\Delta G_f^\circ$ ( $\text{kJ}\cdot\text{mol}^{-1}$ )
298	96.4	121.3	1990.1	2026.2	121.3	-1990.1	-1874.8
300	96.9	122.0	1989.9	2026.5	121.3	-1990.1	-1874.0
350	106.7	137.7	1984.8	2033.0	122.6	-1990.6	-1854.7
400	113.9	152.4	1979.3	2040.3	125.4	-1990.7	-1835.2
450	119.4	166.2	1973.4	2048.2	129.1	-1990.6	-1815.8
500	124.0	179.0	1967.4	2056.9	133.6	-1990.3	-1796.4
550	128.0	191.0	1961.1	2066.2	138.3	-1989.8	-1776.9
600	131.6	202.3	1954.6	2076.0	143.1	-1989.3	-1757.7
650	134.8	212.9	1947.9	2086.3	148.0	-1988.6	-1738.3
700	137.8	223.0	1941.1	2097.2	153.0	-1987.9	-1719.1
750	140.6	232.7	1934.1	2108.6	158.0	-1987.1	-1700.0
800	143.4	241.8	1927.0	2120.4	162.9	-1986.2	-1680.9

<sup>a</sup>The standard uncertainty  $u(T) = 0.5$  K, Expanded uncertainty  $U(P) = 5000$  Pa (0.997 level of confidence).

**Table 4.36:** Thermodynamic data for  $(\text{La}_{0.8}\text{Ba}_{0.1}\text{Th}_{0.1})\text{PO}_4$ , where  $T$  = temperature,  $C_p^\circ$  = standard molar heat capacity,  $S_T^\circ$  = standard molar entropy,  $H_T^\circ$  = standard molar enthalpy,  $G_T^\circ$  = standard Gibbs energy,  $-(G_T^\circ - H_{298}^\circ)/T$  = free energy function,  $\Delta H_f^\circ$  = standard molar enthalpy of formation,  $\Delta G_f^\circ$  = standard molar free energy of formation as a function of temperature at a pressure of 101.325 kPa<sup>a</sup>.

$T$ (K)	$C_p^\circ$ ( $\text{J}\cdot\text{mol}^{-1}\cdot\text{K}^{-1}$ )	$S_T^\circ$ ( $\text{J}\cdot\text{mol}^{-1}\cdot\text{K}^{-1}$ )	$-H_T^\circ$ ( $\text{kJ}\cdot\text{mol}^{-1}$ )	$-G_T^\circ$ ( $\text{kJ}\cdot\text{mol}^{-1}$ )	$-(G_T^\circ - H_{298}^\circ)/T$ ( $\text{J}\cdot\text{mol}^{-1}\cdot\text{K}^{-1}$ )	$\Delta H_f^\circ$ ( $\text{kJ}\cdot\text{mol}^{-1}$ )	$\Delta G_f^\circ$ ( $\text{kJ}\cdot\text{mol}^{-1}$ )
298	97.2	121.8	1990.1	2026.4	121.9	-1990.1	-1874.9
300	97.8	122.5	1989.9	2026.7	121.8	-1990.1	-1874.1
350	108.6	138.4	1984.7	2033.2	123.0	-1990.5	-1854.8
400	116.0	153.4	1979.1	2040.5	126.0	-1990.5	-1835.4
450	121.4	167.4	1973.2	2048.6	129.9	-1990.3	-1816.0
500	125.5	180.4	1966.9	2057.1	134.1	-1989.9	-1796.6
550	128.8	192.5	1960.6	2066.5	139.0	-1989.5	-1777.3
600	131.5	203.9	1954.1	2076.5	143.9	-1988.9	-1758.0
650	133.8	214.5	1947.5	2087.0	149.0	-1988.4	-1738.9
700	135.9	224.5	1940.7	2097.9	154.0	-1987.7	-1719.7
750	137.7	233.9	1933.9	2109.4	159.0	-1987.1	-1700.6
800	139.4	242.9	1926.9	2121.2	163.9	-1986.3	-1681.5

<sup>a</sup>The standard uncertainty  $u(T) = 0.5$  K, Expanded uncertainty  $U(P) = 5000$  Pa (0.997 level of confidence).

**Table 4.37:** Thermodynamic data for  $(\text{La}_{0.7}\text{Ba}_{0.15}\text{Th}_{0.15})\text{PO}_4$ , where  $T$  = temperature,  $C_p^\circ$  = standard molar heat capacity,  $S_T^\circ$  = standard molar entropy,  $H_T^\circ$  = standard molar enthalpy,  $G_T^\circ$  = standard Gibbs energy,  $-(G_T^\circ - H_{298}^\circ)/T$  = free energy function,  $\Delta H_f^\circ$  = standard molar enthalpy of formation,  $\Delta G_f^\circ$  = standard molar free energy of formation as a function of temperature at a pressure of 101.325 kPa<sup>a</sup>.

$T$ (K)	$C_p^\circ$ ( $\text{J}\cdot\text{mol}^{-1}\cdot\text{K}^{-1}$ )	$S_T^\circ$ ( $\text{J}\cdot\text{mol}^{-1}\cdot\text{K}^{-1}$ )	$-H_T^\circ$ ( $\text{kJ}\cdot\text{mol}^{-1}$ )	$-G_T^\circ$ ( $\text{kJ}\cdot\text{mol}^{-1}$ )	$-(G_T^\circ - H_{298}^\circ)/T$ ( $\text{J}\cdot\text{mol}^{-1}\cdot\text{K}^{-1}$ )	$\Delta H_f^\circ$ ( $\text{kJ}\cdot\text{mol}^{-1}$ )	$\Delta G_f^\circ$ ( $\text{kJ}\cdot\text{mol}^{-1}$ )
298	92.7	122.3	1982.7	2019.2	122.4	-1982.7	-1867.7
300	93.2	122.9	1982.5	2019.4	122.3	-1982.7	-1866.9
350	103.8	138.1	1977.6	2026.0	123.6	-1983.4	-1847.6
400	111.3	152.5	1972.2	2033.2	126.3	-1983.6	-1828.1
450	117.1	166.0	1966.5	2041.2	130.0	-1983.7	-1808.7
500	121.8	178.6	1960.5	2049.8	134.2	-1983.6	-1789.3
550	125.8	190.4	1954.3	2059.0	138.8	-1983.3	-1769.8
600	129.3	201.5	1947.9	2068.8	143.5	-1982.9	-1750.4
650	132.4	211.9	1941.4	2079.2	148.5	-1982.4	-1731.0
700	135.3	221.9	1934.7	2090.0	153.3	-1981.9	-1711.8
750	138.1	231.3	1927.8	2101.3	158.2	-1981.2	-1692.5
800	140.6	240.3	1920.9	2113.2	163.1	-1980.5	-1673.3

<sup>a</sup>The standard uncertainty  $u(T) = 0.5$  K, Expanded uncertainty  $U(P) = 5000$  Pa (0.997 level of confidence).

**Table 4.38:** Thermodynamic data for  $\text{Ba}_{0.5}\text{Th}_{0.5}\text{PO}_4$ , where  $T$  = temperature,  $C_p^\circ$  = standard molar heat capacity,  $S_T^\circ$  = standard molar entropy,  $H_T^\circ$  = standard molar enthalpy,  $G_T^\circ$  = standard Gibbs energy,  $-(G_T^\circ - H_{298}^\circ)/T$  = free energy function,  $\Delta H_f^\circ$  = standard molar enthalpy of formation,  $\Delta G_f^\circ$  = standard molar free energy of formation as a function of temperature at a pressure of 101.325 kPa<sup>a</sup>.

$T$ (K)	$C_p^\circ$ ( $\text{J}\cdot\text{mol}^{-1}\cdot\text{K}^{-1}$ )	$S_T^\circ$ ( $\text{J}\cdot\text{mol}^{-1}\cdot\text{K}^{-1}$ )	$-H_T^\circ$ ( $\text{kJ}\cdot\text{mol}^{-1}$ )	$-G_T^\circ$ ( $\text{kJ}\cdot\text{mol}^{-1}$ )	$-(G_T^\circ - H_{298}^\circ)/T$ ( $\text{J}\cdot\text{mol}^{-1}\cdot\text{K}^{-1}$ )	$\Delta H_f^\circ$ ( $\text{kJ}\cdot\text{mol}^{-1}$ )	$\Delta G_f^\circ$ ( $\text{kJ}\cdot\text{mol}^{-1}$ )
298	106.0	125.9	1944.0	1981.5	125.9	-1944.0	-1830.0
300	106.4	125.6	1943.8	1981.5	124.9	-1944.0	-1829.2
350	115.2	143.7	1938.2	1988.5	127.1	-1944.1	-1810.1
400	121.6	159.5	1932.3	1996.1	130.3	-1943.9	-1790.9
450	126.5	174.1	1926.1	2004.4	134.3	-1943.7	-1771.8
500	130.7	187.6	1919.7	2013.5	139.0	-1943.3	-1752.7
550	134.2	200.3	1913.0	2023.2	143.9	-1942.8	-1733.7
600	137.4	212.1	1906.3	2033.6	149.3	-1942.2	-1714.7
650	140.3	223.2	1899.3	2044.4	154.4	-1941.6	-1695.8
700	143.0	233.7	1892.2	2055.8	159.7	-1940.8	-1676.9
750	145.6	243.7	1885.0	2067.8	165.0	-1939.9	-1658.0
800	148.0	253.1	1877.7	2080.2	170.2	-1939.0	-1639.3

<sup>a</sup>The standard uncertainty  $u(T) = 0.5$  K, Expanded uncertainty  $U(P) = 5000$  Pa (0.997 level of confidence).

The standard molar free energy of formation  $\Delta G_f^\circ(T)$  of  $(\text{La}_{1-x}\text{M}_{x/2}\text{Th}_{x/2})\text{PO}_4$  ( $0 \leq x \leq 1$ ) ( $M = \text{Ca}, \text{Sr}$  and  $\text{Ba}$ ) solid solutions as a function of temperature are determined using the experimental values of standard molar enthalpy of formation  $\Delta H_f^\circ(298 \text{ K})$ , the estimated standard molar entropy of formation  $\Delta S_f^\circ(298 \text{ K})$  and molar heat capacity change for the formation  $\Delta C_p^\circ$  of compounds. The plots of Gibbs energy of formation as a function of temperature are shown in **Figs. 4.36–4.38** and the coefficients of linear least square fitted equation for the Gibbs energy of formation are given in **Table 4.39**.

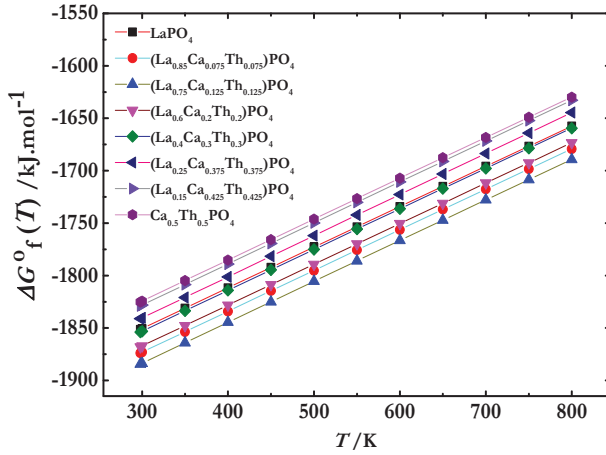


**Fig. 4.36:** Plots of Gibbs energy of formation of  $\text{La}_{1-x}\text{Ca}_{x/2}\text{Th}_{x/2}\text{PO}_4$  ( $x = 0, 0.15, 0.25, 0.40, 0.60, 0.75, 0.85, 1$ ) as a function of temperature.

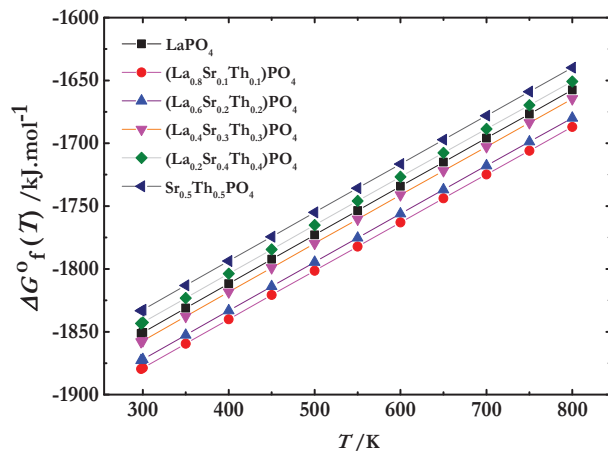


**Fig. 4.37:** Plots of Gibbs energy of formation of  $\text{La}_{1-x}\text{Sr}_{x/2}\text{Th}_{x/2}\text{PO}_4$  ( $x = 0, 0.2, 0.4, 0.6, 0.8, 1$ ) as a function of temperature.

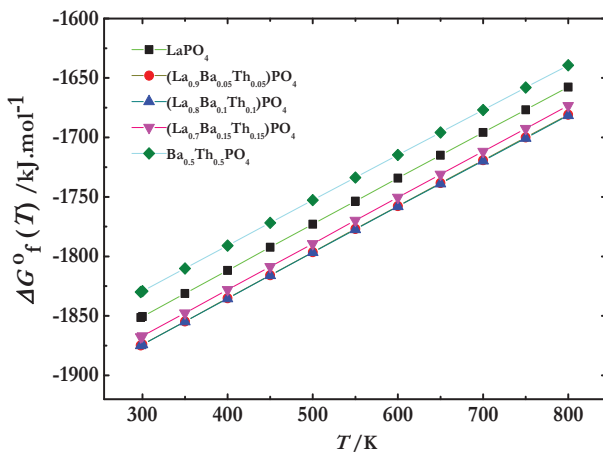


**Fig. 4.38:** Plots of Gibbs energy of formation of  $\text{La}_{1-x}\text{Ba}_{x/2}\text{Th}_{x/2}\text{PO}_4$  ( $x = 0, 0.1, 0.2, 0.3; x = 1$ ) as a function of temperature.

**Table 4.39:** The coefficients of Gibbs energy of formation of  $\text{La}_{1-x}\text{M}_{x/2}\text{Th}_{x/2}\text{PO}_4$  ( $0 \leq x \leq 1$ ) ( $M = \text{Ca}, \text{Sr}$  and  $\text{Ba}$ ) as a function of temperature at  $P = 101.325 \text{ kPa}^a$ .

Composition	${}^b\Delta G_f^0(T) / \text{kJ}\cdot\text{mol}^{-1} = A + B\cdot T$	
	A	B
<b>(La<sub>1-x</sub>Ca<sub>x/2</sub>Th<sub>x/2</sub>)PO<sub>4</sub> (<math>0 \leq x \leq 1</math>)</b>		
LaPO <sub>4</sub>	-1966.3	0.3864
(La <sub>0.85</sub> Ca <sub>0.075</sub> Th <sub>0.075</sub> )PO <sub>4</sub>	-1989.4	0.3881
(La <sub>0.75</sub> Ca <sub>0.125</sub> Th <sub>0.125</sub> )PO <sub>4</sub>	-2000.2	0.3891
(La <sub>0.6</sub> Ca <sub>0.2</sub> Th <sub>0.2</sub> )PO <sub>4</sub>	-1983.5	0.3881
(La <sub>0.4</sub> Ca <sub>0.3</sub> Th <sub>0.3</sub> )PO <sub>4</sub>	-1969.2	0.3876
(La <sub>0.25</sub> Ca <sub>0.375</sub> Th <sub>0.375</sub> )PO <sub>4</sub>	-1957.9	0.3919
(La <sub>0.15</sub> Ca <sub>0.425</sub> Th <sub>0.425</sub> )PO <sub>4</sub>	-1945.2	0.3907
Ca <sub>0.5</sub> Th <sub>0.5</sub> PO <sub>4</sub>	-1941.1	0.3896
<b>(La<sub>1-x</sub>Sr<sub>x/2</sub>Th<sub>x/2</sub>)PO<sub>4</sub> (<math>0.2 \leq x \leq 1</math>)</b>		
(La <sub>0.8</sub> Sr <sub>0.1</sub> Th <sub>0.1</sub> )PO <sub>4</sub>	-1993.8	0.3842
(La <sub>0.6</sub> Sr <sub>0.2</sub> Th <sub>0.2</sub> )PO <sub>4</sub>	-1987.2	0.3847
(La <sub>0.4</sub> Sr <sub>0.3</sub> Th <sub>0.3</sub> )PO <sub>4</sub>	-1972.6	0.3854
(La <sub>0.2</sub> Sr <sub>0.4</sub> Th <sub>0.4</sub> )PO <sub>4</sub>	-1957.5	0.3841
Sr <sub>0.5</sub> Th <sub>0.5</sub> PO <sub>4</sub>	-1948.0	0.3856
<b>(La<sub>1-x</sub>Ba<sub>x/2</sub>Th<sub>x/2</sub>)PO<sub>4</sub> (<math>0.1 \leq x \leq 0.3, x = 1</math>)</b>		
(La <sub>0.90</sub> Ba <sub>0.05</sub> Th <sub>0.05</sub> )PO <sub>4</sub>	-1989.9	0.3867
(La <sub>0.8</sub> Ba <sub>0.1</sub> Th <sub>0.1</sub> )PO <sub>4</sub>	-1989.6	0.3856
(La <sub>0.70</sub> Ba <sub>0.15</sub> Th <sub>0.15</sub> )PO <sub>4</sub>	-1983.1	0.3876
Ba <sub>0.5</sub> Th <sub>0.5</sub> PO <sub>4</sub>	-1943.1	0.3802

<sup>a</sup>Standard uncertainties  $u$  are  $u(P) = 5000 \text{ Pa}$ .

<sup>b</sup>estimated in this study, the uncertainty in the values are within 3 percent.

The calculated Gibbs energy data for the solid solutions indicates that the stability of substituted LaPO<sub>4</sub> is mainly governed by the enthalpy factor as the change in entropy among the compositions is negligible.

#### 4.4. DISCUSSIONS

The specific heat capacity data of LaPO<sub>4</sub> and  $M_{0.5}\text{Th}_{0.5}\text{PO}_4$  ( $M = \text{Ca}, \text{Sr}$  and  $\text{Ba}$ ) have been compared and plotted in **Fig. 4.39**. The specific heat capacity of Ca<sub>0.5</sub>Th<sub>0.5</sub>PO<sub>4</sub> is found to be slightly higher than that of LaPO<sub>4</sub>. This could be due to the effect of substitution of charge coupled ( $\text{Ca}^{2+}, \text{Th}^{4+}$ ) ( ${}^{\text{IX}}\text{rCa}^{2+} = 1.18 \text{ \AA}$ ,  ${}^{\text{IX}}\text{rTh}^{4+} = 1.09 \text{ \AA}$ ) in place of  $\text{La}^{3+}$  ( ${}^{\text{IX}}\text{rLa}^{3+} = 1.216 \text{ \AA}$ ), decreases the average M-O bond length and increases the average bond strength than La-O

bond in  $\text{LaPO}_4$ . This fact also corroborated by their lattice parameter variations using X-ray diffraction data. On the other hand, the specific heat capacity of  $\text{Sr}_{0.5}\text{Th}_{0.5}\text{PO}_4$  and  $\text{Ba}_{0.5}\text{Th}_{0.5}\text{PO}_4$  is slightly less than that of  $\text{LaPO}_4$  as the average M-O bond length in  $(\text{Sr}^{2+}, \text{Th}^{4+})$  and  $(\text{Ba}^{2+}, \text{Th}^{4+})$  couple substituted solid solution are higher than La-O bond length in  $\text{LaPO}_4$ . The heat capacity of  $M_{0.5}\text{Th}_{0.5}\text{PO}_4$  ( $M = \text{Ca}, \text{Sr}$  and  $\text{Ba}$ ) are found to be lower than that estimated value obtained by Neumann-Kopp rule. The deviation from the Neumann-Kopp rule for these compounds can be explained on the basis of the difference in the coordination number of the metal atom in substituted monazite as compared to their respective metal oxides.

The enthalpy of formation,  $\Delta H_f^\circ(298 \text{ K})$  for  $\text{LaPO}_4$  and  $M_{0.5}\text{Th}_{0.5}\text{PO}_4$  ( $M = \text{Ca}, \text{Sr}$  and  $\text{Ba}$ ) derived from this work was compared with the literature data. The values are listed in **Table 4.40** and plotted in **Fig. 4.40**. The standard enthalpies of formation for  $\text{LaPO}_4$  measured in the present work are compared to values reported in the literature [168, 177, 189, 201, 202].

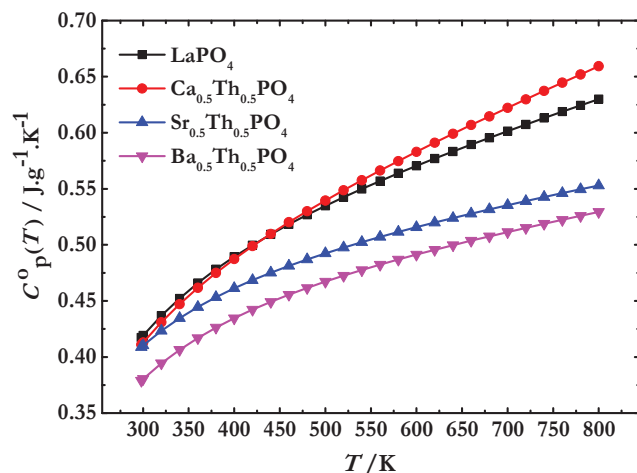


**Figure 4.39:** Heat capacity plots of  $\text{LaPO}_4$  and  $M_{0.5}\text{Th}_{0.5}\text{PO}_4$  ( $M = \text{Ca}, \text{Sr}$  and  $\text{Ba}$ ).

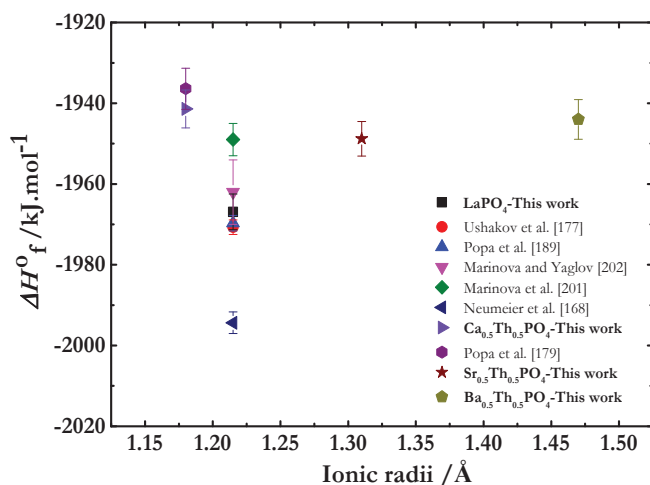


**Fig. 4.40:** Comparison of the standard molar enthalpies of formation values of  $\text{LaPO}_4$  and  $M_{0.5}\text{Th}_{0.5}\text{PO}_4$  ( $M = \text{Ca}, \text{Sr}$  and  $\text{Ba}$ ) with that the values reported in the literature.

The standard molar enthalpy of formation found to vary from  $-1949 \pm 4 \text{ kJ}\cdot\text{mol}^{-1}$  to  $-1994.4 \pm 2.7 \text{ kJ}\cdot\text{mol}^{-1}$ . Deviation in the measurement from the literature values reported by Marinova et al. [201] and Neumeier et al. [168] could not be identified. However, the value of enthalpy of formation for  $\text{LaPO}_4$  reported in the present work is found to be well within the experimental uncertainty of the values reported by three different measurements viz. Ushakov et al. [177], Popa et al. [189] and Marinova & Yaglov et al. [202]. The  $\Delta H_f^0(298 \text{ K})$  value for  $\text{Ca}_{0.5}\text{Th}_{0.5}\text{PO}_4$  is found to be in good agreement with that of Popa et al. [179]. The corresponding  $\Delta H_f^0(298 \text{ K})$  values for  $\text{Sr}_{0.5}\text{Th}_{0.5}\text{PO}_4$  and  $\text{Ba}_{0.5}\text{Th}_{0.5}\text{PO}_4$  were measured for the first time in this work and hence could not be compared with the literature values.

**Table 4.40:** Comparison of the standard molar enthalpies of formation values of  $\text{LaPO}_4$  and  $\text{Ca}_{0.5}\text{Th}_{0.5}\text{PO}_4$  with that reported in the literature.

Authors	Methods	$\Delta H_f^0$ [ $\text{LaPO}_4$ , 298 K] / $\text{kJ}\cdot\text{mol}^{-1}$
<b>LaPO<sub>4</sub></b>		
This work	Oxide melt calorimeter at 1089 K	$-1966.9 \pm 4.4^a$
Ushakov et al. [177]	Oxide melt solution calorimetry at 976 K	$-1970.7 \pm 1.8$
Popa et. al. [189]	Recalculated from results of Ushakov et al. [177]	$-1969.7 \pm 1.9$
Marinova et al. [201]	Acid solution calorimetry	$-1949 \pm 4$
Marinova and Yaglov [202]	Solubility products and estimated entropies	$-1962 \pm 8$
Neumeier et al. [168]	Oxide melt solution calorimetry at 973 K	$-1994.36 \pm 2.68$

<b>Ca<sub>0.5</sub>Th<sub>0.5</sub>PO<sub>4</sub></b>		
This work	Oxide melt calorimeter at 1089 K	-1941.4±4.7
Popa et al. [179]	Oxide melt calorimeter at 1080 K	-1936.4±5.1
<b>Sr<sub>0.5</sub>Th<sub>0.5</sub>PO<sub>4</sub></b>		
This work	Oxide melt calorimeter at 1089 K	-1948.8±4.3
<b>Ba<sub>0.5</sub>Th<sub>0.5</sub>PO<sub>4</sub></b>		
This work	Oxide melt calorimeter at 1089 K	-1944.0±4.9

The standard molar enthalpy of formation  $\Delta H_f^0(298\text{ K})$  of  $M_{0.5}\text{Th}_{0.5}\text{PO}_4$  ( $M = \text{Ca}, \text{Sr}$  and  $\text{Ba}$ ) are found to be in the order:  $\text{Ca}_{0.5}\text{Th}_{0.5}\text{PO}_4$  ( $-1941.4 \pm 4.7\text{ kJ}\cdot\text{mol}^{-1}$ ) <  $\text{Ba}_{0.5}\text{Th}_{0.5}\text{PO}_4$  ( $-1944.0 \pm 4.9\text{ kJ}\cdot\text{mol}^{-1}$ ) <  $\text{Sr}_{0.5}\text{Th}_{0.5}\text{PO}_4$  ( $-1948.8 \pm 4.3\text{ kJ}\cdot\text{mol}^{-1}$ ). The variation of enthalpy of formation of  $M_{0.5}\text{Th}_{0.5}\text{PO}_4$  ( $M = \text{Ca}, \text{Sr}$  and  $\text{Ba}$ ) can be explained by the match of the ionic radii of metal ion with the cavity size. The ionic radii of  $\text{Sr}^{2+}$  (1.31 Å) matches well with the lattice site of  $\text{La}^{3+}$  ion (1.216 Å) formed by the phosphate tetrahedral. The radii of the  $\text{Ba}^{2+}$  ion (1.47 Å) are slightly higher than the cavity, whereas that of  $\text{Ca}^{2+}$  (1.18 Å) is less. Therefore, substitution of these ions at  $\text{La}^{3+}$  site creates lattice strain and decreases the stability.

**Fig. 4.41** gives the variation of standard molar enthalpy of formation for  $(\text{La}_{1-x}\text{M}_{x/2}\text{Th}_{x/2})\text{PO}_4$  ( $0 \leq x \leq 1$ ) ( $M = \text{Ca}, \text{Sr}$  and  $\text{Ba}$ ) with respect to their binary oxides ( $\Delta H_{f,\text{ox}}^0$ ) as a function of mole-fraction of charge coupled substitution. It shows that on substitution of charge couple ( $M^{2+}, \text{Th}^{4+}$ ) ( $M = \text{Ca}, \text{Sr}$  and  $\text{Ba}$ ) in  $\text{LaPO}_4$  forming  $(\text{La}_{1-x}\text{M}_{x/2}\text{Th}_{x/2})\text{PO}_4$  solid solution increases the thermodynamically stability the host matrix up to  $x = 0.25$  for  $(\text{La}_{1-x}\text{Ca}_{x/2}\text{Th}_{x/2})\text{PO}_4$ ,  $x = 0.3$  for  $(\text{La}_{1-x}\text{Sr}_{x/2}\text{Th}_{x/2})\text{PO}_4$  and  $x = 0.2$  for  $(\text{La}_{1-x}\text{Ba}_{x/2}\text{Th}_{x/2})\text{PO}_4$ . On further substitution, the stabilities of the solid solutions decreases and the values of  $\Delta H_{f,\text{ox}}^0$  become less negative.

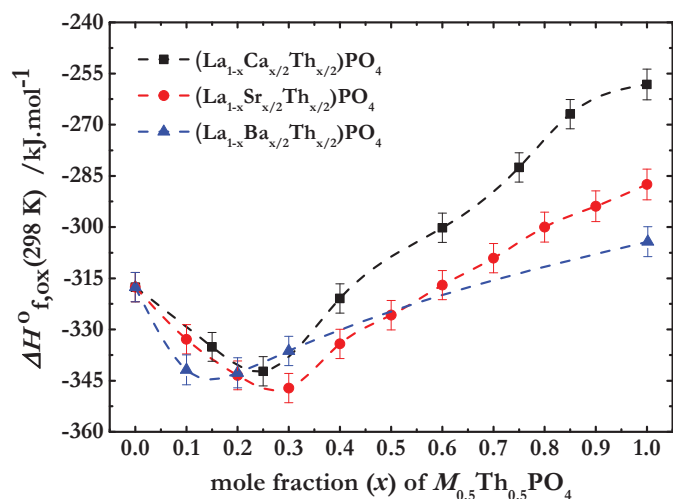


**Fig. 4.41:** Combined plot of standard molar enthalpy of formation of  $(\text{La}_{1-x}\text{M}_{x/2}\text{Th}_{x/2})\text{PO}_4$  ( $0 \leq x \leq 1$ ) ( $M = \text{Ca}, \text{Sr}$  and  $\text{Ba}$ ) from their constituent oxides.

The observed minima for the solid solutions could be interpreted in terms of the interplay between two opposite factors:

- (a) The increase in stabilization of the solid solution with the increase in basic strength of the Group-II metal-oxide (**Fig. 4.42**).
- (b) The destabilization of the solid solution caused by the sublattice strain arising due to size mismatch of the substituted ions as compared to  $\text{La}^{3+}$  ion in the crystal lattice (**Fig. 4.43**).

The stabilization of  $\text{LaPO}_4$  matrix by the charge couple ( $M^{2+}, \text{Th}^{4+}$ ) ( $M = \text{Ca}, \text{Sr}$  and  $\text{Ba}$ ) substitution, can be explained by the extent of acid-base reaction between basic oxides viz.  $\text{MO}$  ( $M = \text{Ca}, \text{Sr}$  and  $\text{Ba}$ ),  $\text{ThO}_2$  and acidic oxide  $\text{P}_2\text{O}_5$  as given in the eqn. (20).



As reported by Zhang et al. [203], the basicity of Group-II oxides increases with their ionic radius and their basic strength follows the order:  $\text{CaO} < \text{SrO} < \text{BaO}$ . Thus, the enthalpy of formation ( $\Delta H_{f,ox}^0$ ) of phosphates at 298 K increases in the order  $\text{Ca}_{0.5}\text{Th}_{0.5}\text{PO}_4$  ( $-258.2 \pm 4.5$   $\text{kJ}\cdot\text{mol}^{-1}$ )  $<$   $\text{Sr}_{0.5}\text{Th}_{0.5}\text{PO}_4$  ( $-287.5 \pm 4.2$   $\text{kJ}\cdot\text{mol}^{-1}$ )  $<$   $\text{Ba}_{0.5}\text{Th}_{0.5}\text{PO}_4$  ( $-304.3 \pm 4.4$   $\text{kJ}\cdot\text{mol}^{-1}$ ) as shown in **Fig. 4.42**.

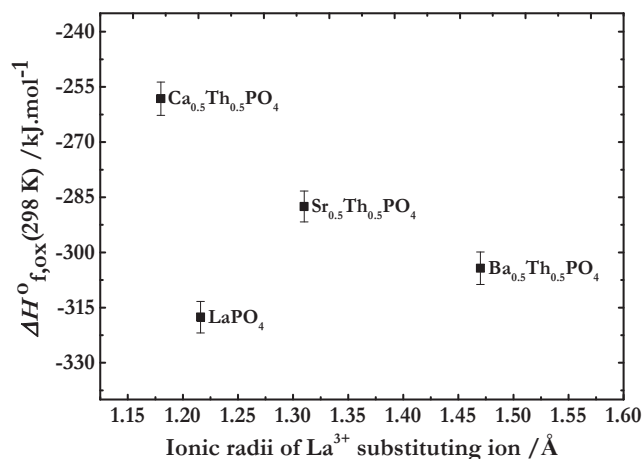


**Fig. 4.42:** Enthalpy of formation from oxides of LaPO<sub>4</sub> and M<sub>0.5</sub>Th<sub>0.5</sub>PO<sub>4</sub> (M = Ca, Sr and Ba) as a function of ionic radii of La<sup>3+</sup> substituting ion.

Similarly, the enthalpy of formation ( $\Delta H_{f,ox}^{\circ}$ ) of (La<sub>1-x</sub>M<sub>x/2</sub>Th<sub>x/2</sub>)PO<sub>4</sub> (0 ≤ x ≤ 1) (M = Ca, Sr and Ba) solid solution from their binary oxides at 298 K can be represented by the eqn. (4.21)



The basic strength of the metal oxide follows the order: ThO<sub>2</sub> < La<sub>2</sub>O<sub>3</sub> < CaO < SrO < BaO [203]. Therefore, enthalpy of formation ( $\Delta H_{f,ox}^{\circ}$ ) for the solid solution at 298 K is most negative or exothermic for (Ba, Th)-substituted followed by (Sr, Th) and then (Ca, Th)-substituted solid solutions.

On the other hand, the destabilization of (La<sub>1-x</sub>M<sub>x/2</sub>Th<sub>x/2</sub>)PO<sub>4</sub> (0 ≤ x ≤ 1) (M = Ca, Sr and Ba) solid solution arises due to mismatch in size between the charge couple (M<sup>2+</sup>, Th<sup>4+</sup>) (M = Ca, Sr and Ba) and that of La<sup>3+</sup> ion. The size mismatch causes strain in the crystal lattice and decreases the enthalpy of formation,  $\Delta H_{f,ox}^{\circ}$ (298 K) of solid solutions. The charge coupled (Ca<sup>2+</sup>, Th<sup>4+</sup>) and (Sr<sup>2+</sup>, Th<sup>4+</sup>) substitution shrink the crystal lattice of pure LaPO<sub>4</sub> host matrix, whereas the crystal lattice expands in case of charge coupled (Ba<sup>2+</sup>, Th<sup>4+</sup>) substitution as shown in Fig. 4.43.

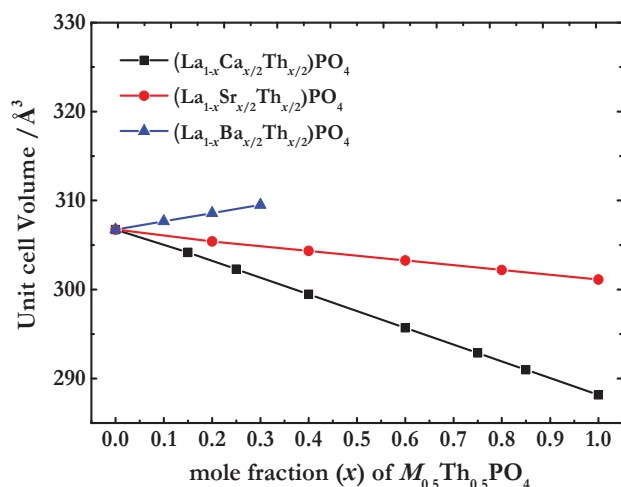


**Fig. 4.43:** Variations of unit cell volume of the solid solutions on substitution.

Further, it was observed that the enthalpy of formation,  $\Delta H_{f,ox}^0(298\text{ K})$  of  $(Sr^{2+}, Th^{4+})$  substituted solid solution is more negative than  $(Ca^{2+}, Th^{4+})$  and  $(Ba^{2+}, Th^{4+})$  substituted solid solution (**Fig. 4.44**). In case of  $(Sr^{2+}, Th^{4+})$  charge couple, the average ionic radius of  $(Sr^{2+}, Th^{4+})$  couple matches well with that of  $La^{3+}$  host ion whereas average ionic radii in case of  $(Ca^{2+}, Th^{4+})$  and  $(Ba^{2+}, Th^{4+})$  charge couples differs.

It is also observed that the lattice strain arising due to ion size mismatch is the main contributor to the excess enthalpy of mixing,  $\Delta H_{mix}$  in these solid solutions and shown in **Fig. 4.44**. This effect of the ion size mismatch on the excess enthalpy of mixing of substituted phosphates solid solutions was also reported by Neumeier et al. [168] and Konings et al. [171]. The strong negative value of  $\Delta H_{mix}$  shows that the mixing of  $(Ca^{2+}, Th^{4+})$ ,  $(Sr^{2+}, Th^{4+})$  and  $(Ba^{2+}, Th^{4+})$  couple at lattice site of  $La^{3+}$  in  $LaPO_4$  (monazite) host structure is highly favorable. Therefore, solid solution so formed are thermodynamically more stable than the end members i.e.  $LaPO_4$  and  $(M_{0.5}Th_{0.5})PO_4$ .

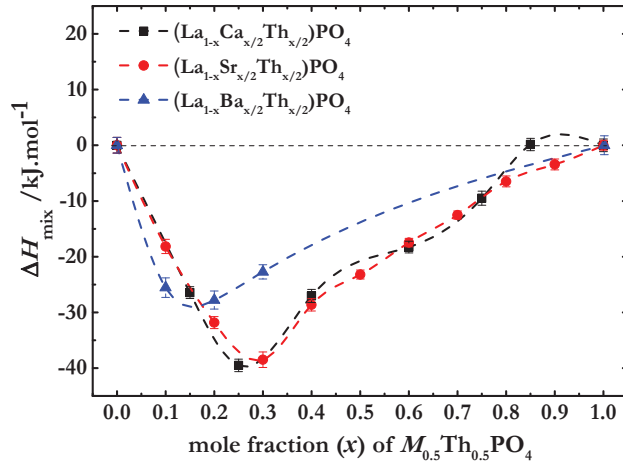


**Fig. 4.44:** Combined plot of enthalpy of mixing for  $(\text{La}_{1-x}\text{M}_{x/2}\text{Th}_{x/2})\text{PO}_4$  ( $0 \leq x \leq 1$ ) ( $M = \text{Ca}, \text{Sr}$  and  $\text{Ba}$ ) as a function of mole fraction of their respective end member.

Hence, the interplay of these two opposite factors i.e. the stabilization of the solid solution with the basic strength of the metal oxides and the destabilization of the solid solution due to ions size mismatch, results in the enthalpy minima observed for the solid solutions. The compositions correspond to the enthalpy minima found to be most thermodynamically stable. The enthalpy of formation data for the solid solution indicates that the compositions corresponding to  $x = 0.25$  for  $(\text{La}_{1-x}\text{Ca}_{x/2}\text{Th}_{x/2})\text{PO}_4$ ,  $x = 0.3$  for  $(\text{La}_{1-x}\text{Sr}_{x/2}\text{Th}_{x/2})\text{PO}_4$  and  $x = 0.2$  for  $(\text{La}_{1-x}\text{Ba}_{x/2}\text{Th}_{x/2})\text{PO}_4$  solid solutions in the (Ca, Th) (Sr, Th) and (Ba, Th) charge couple substitution series are thermodynamically most stable.

## 4.5. CONCLUSIONS

X-ray diffraction results for  $(\text{La}_{1-x}\text{M}_{x/2}\text{Th}_{x/2})\text{PO}_4$  ( $0 \leq x \leq 1$ ) ( $M = \text{Ca}, \text{Sr}$  and  $\text{Ba}$ ) suggest that a homogeneous solid solution are formed for  $M = \text{Ca}$  and  $\text{Sr}$  in the entire range of composition. Phase separation was observed for (Ba, Th) was observed above  $x = 0.3$ . Unit cell parameters and the density of the solid solutions hold linear relations in the homogeneity range. This indicates excellent ability of monazite to accommodate minor actinides along with alkaline earth metals.

Heat capacities of the solid solutions do not vary linearly with the composition. This could be due to the small difference in heat capacities between the end-member of solid solutions. High-temperature oxide drop solution calorimetry shows that the energetic of monazite-cheralite solid solutions depend on the radii and the concentration of the ions occupying the lanthanide sites in host matrix. All three solid solution systems showed minima for a certain extent of substitution, which found to be interplay of two opposite effects. The strong negative value of enthalpy of mixing,  $\Delta H_{\text{mix}}$  suggests that the mixing of  $\text{Ca}^{2+}/\text{Sr}^{2+}/\text{Ba}^{2+}$  and  $\text{Th}^{4+}$  at lattice site of  $\text{La}^{3+}$  ions in the synthetic monazite structure results in more thermodynamically stable intermediate composition than the corresponding end-members, which is an important information in view of the long-term stability of the monazite-cheralite waste matrix.

The results of the present study evoke to explore the thermodynamic stabilities of other possible charge couple substitutions involving tetravalent ( $\text{An}^{4+}$ ) actinides/divalent ( $\text{M}^{2+}$ ) radionuclides as well we trivalent ( $\text{An}^{3+}$ ) actinides/trivalent ( $\text{M}^{3+}$ ) radionuclides in monazite-cheralite matrix. A list of possible divalent/tetravalent and trivalent/trivalent charge couples having average ionic radii within 15 % ionic radii of  $\text{La}^{3+}$  ion in nine-fold coordination are provided in **Table 4.41**. Since most of these elements are highly radioactive and difficult to handle in normal laboratory conditions, the surrogate elements can be considered for their thermodynamic investigations. The list of surrogate elements having physical and chemical properties similar to the minor actinides are also given in **Table 4.42**.

**Table 4.41:** List of possible combinations of tetravalent/divalent and trivalent/trivalent charge coupled ions for synthetic monazite.

Charge couple substitution	Avg. ionic radii ( $r_{\text{avg.}}^a$ ) / Å	Difference in radii (Å) <sup>b</sup>	Percentage difference in ionic radii
<b><i>Tetravalent substitution: (<math>\text{M}^{2+}</math>, <math>\text{An}^{4+}</math>)</i></b>			
$\text{Ca}^{2+}$ , $\text{Th}^{4+}$	1.135	-0.081	6.7
$\text{Ca}^{2+}$ , $\text{U}^{4+}$	1.115	-0.101	8.3
$\text{Ca}^{2+}$ , $\text{Np}^{4+}$	1.105	-0.111	9.1

Ca <sup>2+</sup> , Pu <sup>4+</sup>	1.085	-0.131	10.8
Sr <sup>2+</sup> , Th <sup>4+</sup>	1.20	-0.016	1.3
Sr <sup>2+</sup> , U <sup>4+</sup>	1.18	-0.036	3.0
Sr <sup>2+</sup> , Np <sup>4+</sup>	1.17	-0.046	3.8
Sr <sup>2+</sup> , Pu <sup>4+</sup>	1.15	-0.066	5.4
Sr <sup>2+</sup> , Zr <sup>4+</sup>	1.10	-0.116	9.5
Ba <sup>2+</sup> , Th <sup>4+</sup>	1.28	0.064	5.0
Ba <sup>2+</sup> , U <sup>4+</sup>	1.26	0.044	3.5
Ba <sup>2+</sup> , Np <sup>4+</sup>	1.25	0.034	2.7
Ba <sup>2+</sup> , Pu <sup>4+</sup>	1.23	0.014	1.1
Ba <sup>2+</sup> , Zr <sup>4+</sup>	1.18	-0.036	3.1

---

**Trivalent substitution: (M<sup>3+</sup>, An<sup>3+</sup>)**

---

La <sup>3+</sup> , Pu <sup>3+</sup>	1.201	-0.015	1.2
La <sup>3+</sup> , Am <sup>3+</sup>	1.185	-0.031	2.5
La <sup>3+</sup> , Cm <sup>3+</sup>	1.179	-0.037	3.0
Sm <sup>3+</sup> , Pu <sup>3+</sup>	1.159	-0.057	4.7
Sm <sup>3+</sup> , Am <sup>3+</sup>	1.143	-0.073	6.0
Sm <sup>3+</sup> , Cm <sup>3+</sup>	1.137	-0.079	6.5
Gd <sup>3+</sup> , Pu <sup>3+</sup>	1.146	-0.069	5.7
Gd <sup>3+</sup> , Am <sup>3+</sup>	1.130	-0.085	7.0
Gd <sup>3+</sup> , Cm <sup>3+</sup>	1.125	-0.091	7.5

---

<sup>a</sup>r<sub>avg.</sub> = (I<sub>X</sub>rM<sup>2+</sup> + I<sub>X</sub>rAn<sup>4+</sup>)/2 or (I<sub>X</sub>rM<sup>3+</sup> + I<sub>X</sub>rAn<sup>3+</sup>)/2.

<sup>b</sup>Difference is calculated with respect to the ionic radii of La<sup>3+</sup> ion (1.216 Å) in nine-fold coordination.

**Table 4.42:** List of surrogate elements for trivalent and tetravalent actinides [204-208].

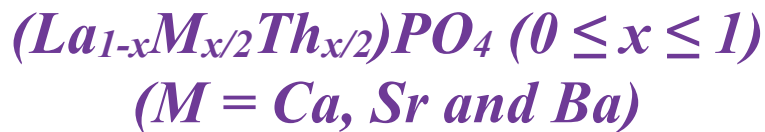
Actinides	Surrogates
Np <sup>4+</sup>	Th <sup>4+</sup> /U <sup>4+</sup>
Pu <sup>3+</sup>	Sm <sup>3+</sup> /Eu <sup>3+</sup>
Pu <sup>4+</sup>	Hf <sup>4+</sup> /Ce <sup>4+</sup>
Am <sup>3+</sup>	Nd <sup>3+</sup> /Eu <sup>3+</sup>
Cm <sup>3+</sup>	Nd <sup>3+</sup> /Gd <sup>3+</sup>

The thermodynamic data for these charge couple substituted monazite-cheralite solid solutions or their suitable surrogates will provide the comprehensive knowledge about the use of monazite-cheralite matrix for the disposal of long-lived radionuclide elements involving above ions.

# **CHAPTER-5**

---

## ***LEACHING STUDIES OF CHARGE- COUPLED SUBSTITUTED MONAZITE SOLID SOLUTIONS***



## 5.1. INTRODUCTION

The thermodynamic data reported in Chapter 4 suggests that thorium and alkaline earth metal charge couple substituted  $\text{LaPO}_4$  (monazite) forming  $(\text{La}_{1-x}\text{M}_{x/2}\text{Th}_{x/2})\text{PO}_4$  ( $0 \leq x \leq 1$ ) ( $M = \text{Ca}$ ,  $\text{Sr}$  and  $\text{Ba}$ ) solid solution have higher thermodynamic stability than the host matrix ( $\text{LaPO}_4$ ). Since in the present work, a systematic study on synthesis, characterization and thermodynamic stabilities of charge-coupled substituted monazite-cherhalite solid solution are carried out. The chemical durability studies on these solid solution series would be of great scientific interest. There are no data present on the leaching behavior of these substituted solid solutions series in aqueous medium under off-normal conditions. Studies on leaching behaviour and rate of release of radionuclides from the waste matrix are of prime importance for long term geological disposal of minor actinides and other nuclear waste constituents.

Despite the wide interest in charge-coupled substituted synthetic monazite-cherhalite solid solutions as a suitable host matrix for HLW disposal, literature dealing with their chemical durability studies is very limited. Few dissolution studies were carried out on natural samples of monazite-cherhalite solid solutions by Sales et al. [209] and Oelkers and Poitrasson [210]. A few results were lately reported on the dissolution studies of homogeneous and single phase  $\text{Ca}_{0.5}\text{Th}^{4+}_{0.5-x}\text{U}^{4+}_x(\text{PO}_4)$  at 363 K in  $10^{-1}$  and  $10^{-4}$  M  $\text{HNO}_3$  by Terra et al. [211], du Fou de Kerdaniel et al. [212] and Veilly et al. [213]. Dissolution of  $\text{La}_{0.4}\text{Eu}_{0.1}\text{Ca}_{0.25}\text{Th}_{0.25}\text{PO}_4$  and  $\text{La}_{0.4}\text{Eu}_{0.1}\text{Ca}_{0.25}\text{U}_{0.25}\text{PO}_4$  were measured in  $10^{-1}$  M  $\text{HNO}_3$  at 363 K and compared by Dacheux et al. [214]. The same author also studied several  $\text{Ca}_{0.5}\text{Th}_{0.5-x}\text{U}_x\text{PO}_4$  solid solutions in dynamic conditions to account for the influence on normalized leaching rates caused by the rapid precipitation of neo-formed phases.

In the present chapter, the aqueous leaching behaviour of monazite-cherhalite solid solutions with compositions  $(\text{La}_{1-x}\text{Ca}_{x/2}\text{Th}_{x/2})\text{PO}_4$  ( $x = 0.1, 0.25, 0.4$ ),  $(\text{La}_{1-x}\text{Sr}_{x/2}\text{Th}_{x/2})\text{PO}_4$  ( $x = 0.1, 0.3, 0.5$ ) and  $(\text{La}_{1-x}\text{Ba}_{x/2}\text{Th}_{x/2})\text{PO}_4$  ( $x = 0.2$ ) are investigated. These mentioned

compositions correspond to the enthalpy minima compositions, as outlined in previous chapter. So, the present work makes an effort to draw a correlation between the results of thermodynamic studies and chemical durability studies. The standard Product Consistency Test (PCT) approved by the American Society of Testing Materials (ASTM) [215] has been used to determine the leach rate behavior of the solid solutions. The procedure and experimental details of the PCT method was described in Section 2.6 of Chapter 2.

## **5.2. EXPERIMENTAL**

### **5.2.1. Material Synthesis & Characterization**

Selected compositions of solid solutions were prepared by the solid-state synthesis method described in Section 4.2.1 of Chapter 4. The chemical analysis of the products was carried out using ICP-AES techniques and phase characterization by powder X-ray diffraction (XRD) as described in Section 4.3.1 and 4.3.2. The technical details of the ICP-AES and XRD instruments have been described in Section 2.3.1 and 2.3.2, respectively.

### **5.2.2. Density and surface area determination**

The bulk density of each sample of solid solutions was determined using a hydrostatic balance based on the Archimedes' principle. The density was measured with around 1 g sample having grain size ASTM 100 to 200 mesh (0.149–0.074 mm) and water as immersing liquid. Density measurements for each sample were made in triplicate and the average value is considered.

Using the measured bulk density of the sample and assuming spherical geometry for the particles, surface area (SA) of the given mass of sample was calculated using the relation,  $SA = 3 \cdot w / \rho \cdot r$ , where,  $w$  is the mass of the sample (g),  $\rho$  is the density of sample ( $\text{g} \cdot \text{cm}^{-3}$ ) and  $r$  is radius of the sample particle (cm).

### 5.2.3. Product Consistency Test (PCT)

In order to determine the chemical durability of  $(\text{La}_{1-x}\text{Ca}_{x/2}\text{Th}_{x/2})\text{PO}_4$  ( $x = 0.1, 0.25, 0.4$ ),  $(\text{La}_{1-x}\text{Sr}_{x/2}\text{Th}_{x/2})\text{PO}_4$  ( $x = 0.1, 0.3, 0.5$ ) and  $(\text{La}_{1-x}\text{Ba}_{x/2}\text{Th}_{x/2})\text{PO}_4$  ( $x = 0.2$ ) solid solution matrix, Product Consistency Test-A (PCT-A) method was performed. In this method, the selected compositions of the solid solution were crushed to powder and sieved in a standard ASTM 100 to 200 mesh (i.e. 0.149–0.074 mm sieve). A known quantity of powdered sample (~1 g) was placed into Teflon lined stainless steel 304 L vessel. 10 ml of double distilled water as leachant was added to the vessel for dissolution of ions. Triplicate sample vessels and duplicate blanks containing demineralized water were placed inside an oven. The ovens are kept at  $363 \pm 1$  K to enhance the rate of dissolution. The objective for such experimental conditions is to generate leach rate data within realistic time frame and use them as input in suitable mathematical models to have prediction of release of radionuclides into the biosphere. The vessels should be kept at constant temperature so that there is ample convection around the samples and heat distribution. After seven days the vessels are removed from the oven and cooled to ambient temperature. The pH and the temperature of the aliquot were measured. The clear leachate obtained after centrifugation of the aliquot was used for quantitative elemental analysis using ICP-AES technique.

### 5.2.4. Elemental analysis using ICP-AES technique

After a period of seven days, the leachate was examined for the quantitative measurement of dissolved elements into the aqueous medium using Jobin–Yvon Ultima high resolution ICP-AES instrument. It has resolution of 0.005 nm and a continuous wave length coverage in the range of 200–800 nm. The optimized instrumental and experimental conditions are summarized in **Table 5.1**.

**Table 5.1:** ICP-AES instrumental parameters and operational conditions.

<b>Parameters</b>	<b>Operational conditions</b>
Focal length	1 m
Grating	Holographic
Groove density	4320/2400 lines/mm
Wavelength range	120–800 nm
Frequency	40.68 MHz
Resolution (FWHM)	< 6 pm from 120 to 430 nm < 11 pm from 430 to 800 nm
Nebulizer	Concentric nebulizer with cyclonic spray
Pump	Dual channel peristaltic pump
ICP-torch	Demountable, radial viewing
Detector	High dynamic PMT detector
<b>Operating conditions:</b>	
Input power	230 V AC
RF power output	1.0 kW
Total time of measurement	36 s
Coolant flow	12 L/min
Auxiliary flow	0.2 L/min
Pump speed	20 Rpm

Standard solutions for analytes were prepared from CertiPUR® ICP standard procured from E-Merck, Darmstadt, Germany. Suprapur® HNO<sub>3</sub> from E-Merck, Darmstadt, Germany and quartz double distilled Milli-Q® water were used for all the samples.

Multi-point standardization was carried out for each elemental line after proper peak search, profiling and auto-attenuation. The analysis of blank and standard solutions for different elements are carried out and the calibration curve for each element is established. Elemental analysis on a blank solution was carried out to determine the concentration of foreign ions in the leachant water used during this study and found below the detection limit of the instrument. The calibration curves acquired for the best analytical lines of each element are used for the determination of the analytes in the samples. The diluted sample is analyzed and concentration corresponding to the signal of each element in the sample is measured in

mg·L<sup>-1</sup>. Each sample was done in triplicate with different aliquots. The values of obtained analytical lines (nm), limit of detection (LOD) and relative standard deviation (RSD) are given in **Table 5.2**.

**Table 5.2:** Analytical line of elements obtained using ICP-AES technique.

Element	Analytical line /nm	LOD /ng·ml <sup>-1</sup>	RSD /%
La	394.910	0.0121±0.0001	2.3
Th	283.730	0.0048±0.0001	3.1

From the measured concentration of leached ions present in the leachate, the normalized leach rate ( $NR_i$ , g·cm<sup>-2</sup>·d<sup>-1</sup>) was determined employing the relation:

$$NR_i = \frac{C_i(\text{sample})}{f_i \times (SA/V) \times t} \quad (5.1)$$

where  $C_i(\text{sample})$  = the concentration of  $i^{\text{th}}$  element in the leachate (mg·L<sup>-1</sup>),  $f_i$  = the mass fraction of the  $i^{\text{th}}$  element in sample (unit less) calculated from batch composition as taken, SA= the calculated surface area of the sample considering spherical geometry (cm<sup>2</sup>), V= volume of the leachate (cm<sup>3</sup>) and t = duration of leaching (day).

### 5.3. RESULTS & DISCUSSIONS

The elemental analysis of the samples of solid solution were performed using ICP-AES technique and phase characterized using the X-ray diffraction analysis. All the samples are found to be in single monoclinic phase. Density of each sample was measured four times and the mean value of density is used for the calculation of normalized leach rate. Density of the samples was found to be in the range of 4.2-4.7 g·cm<sup>-3</sup> and showed systematic variation with

composition of the samples. The pH of the leachant was found to be in the range of 6.3-6.5. The individual error in pH value was  $\pm 0.2$ .

The concentration of the leached ions measured over a period of 7 days was found to be below the detection limit of the ICP-AES instrument. The normalized leaching rate  $NR(La)$  and  $NR(Th)$  obtained at 363 K in static conditions are reported in **Table 5.3**. The normalized leach rate for the elements are calculated by considering their detection limit values i.e. The observed normalized leach rates values for the ions in the solid solution are found to be well within the internationally accepted limits of the vitrified waste matrix [216]. Generally, the  $NR_i$  values in the range of  $10^{-8}$  to  $10^{-10}$   $\text{g}\cdot\text{cm}^{-2}\cdot\text{day}^{-1}$  calculated using PCT method for a proposed waste matrix are considered to be reasonable for nuclear waste management [217, 218].

The results showed that the normalized leach rates ( $NR_i$ ) values in the present work are less than that reported for currently used borosilicate glass [219]. Thus, monazite-cheralite solid solutions showed improved chemical durability than borosilicate glasses and consequently could be considered as an alternate waste form for the immobilization of radionuclides present in HLW.

**Table 5.3:** Normalized leaching rates of monazite-cherhalite solid solutions leached in aqueous medium under static conditions at 363 K for 7 days.

Samples	SA/V /m <sup>2</sup> ·L <sup>-1</sup>	pH	<sup>a</sup> Normalized leach rate, NR <sub>i</sub> /g·cm <sup>-2</sup> ·d <sup>-1</sup>	
			La <sup>3+</sup>	Th <sup>4+</sup>
<b>(La<sub>1-x</sub>Ca<sub>x/2</sub>Th<sub>x/2</sub>)PO<sub>4</sub> (x = 0.1, 0.25, 0.4)</b>				
(La <sub>0.9</sub> Ca <sub>0.05</sub> Th <sub>0.05</sub> )PO <sub>4</sub>	1.23	6.5	< 1.31 x 10 <sup>-10</sup>	< 7.89 x 10 <sup>-10</sup>
(La <sub>0.75</sub> Ca <sub>0.125</sub> Th <sub>0.125</sub> )PO <sub>4</sub>	1.24	6.4	< 1.57 x 10 <sup>-10</sup>	< 3.14 x 10 <sup>-10</sup>
(La <sub>0.6</sub> Ca <sub>0.2</sub> Th <sub>0.2</sub> )PO <sub>4</sub>	1.25	6.5	< 1.94 x 10 <sup>-10</sup>	< 1.95 x 10 <sup>-10</sup>
<b>(La<sub>1-x</sub>Sr<sub>x/2</sub>Th<sub>x/2</sub>)PO<sub>4</sub> (x = 0.1, 0.3, 0.5)</b>				
(La <sub>0.9</sub> Sr <sub>0.05</sub> Th <sub>0.05</sub> )PO <sub>4</sub>	1.21	6.3	< 1.36 x 10 <sup>-10</sup>	< 8.17 x 10 <sup>-10</sup>
(La <sub>0.7</sub> Sr <sub>0.15</sub> Th <sub>0.15</sub> )PO <sub>4</sub>	1.18	6.5	< 1.83 x 10 <sup>-10</sup>	< 2.84 x 10 <sup>-10</sup>
(La <sub>0.5</sub> Sr <sub>0.25</sub> Th <sub>0.25</sub> )PO <sub>4</sub>	1.15	6.4	< 2.66 x 10 <sup>-10</sup>	< 1.78 x 10 <sup>-10</sup>
<b>(La<sub>1-x</sub>Ba<sub>x/2</sub>Th<sub>x/2</sub>)PO<sub>4</sub> (x = 0.2)</b>				
(La <sub>0.8</sub> Ba <sub>0.1</sub> Th <sub>0.1</sub> )PO <sub>4</sub>	1.09	6.4	< 1.74 x 10 <sup>-10</sup>	< 4.64 x 10 <sup>-10</sup>

<sup>a</sup>Normalized leach rate, NR<sub>i</sub> values are calculated by considering the detection limit for each ion.

## 5.4. CONCLUSIONS

The leaching behavior of  $(\text{La}_{1-x}\text{M}_{x/2}\text{Th}_{x/2})\text{PO}_4$  ( $0 \leq x \leq 1$ ) ( $M = \text{Ca}, \text{Sr}$  and  $\text{Ba}$ ) solid solutions have been studied for the selected compositions at 363 K for a period of 7 days. The chemical durability of monazite-cheralite solid solutions to aqueous alteration indicates that the normalized leach rate  $NR(\text{La})$  and  $NR(\text{Th})$  was below  $10^{-10} \text{ g}\cdot\text{cm}^{-2}\cdot\text{d}^{-1}$ . The complementary results of thermodynamic studies and chemical durability studies of monazite-cheralite solid solutions suggest that such materials could be considered as a potential candidate for suitable immobilization of long-lived trivalent and tetravalent actinides.

# ***CHAPTER-6***

---

***THERMODYNAMIC STUDIES OF  
THORIUM PHOSPHATE-  
DIPHOSPHATE (TPD)  
AND  
PHASE INVESTIGATIONS OF  
Th-P-O, Th-P-H<sub>2</sub>O SYSTEMS***

## 6.1. INTRODUCTION

As discussed in Section 1.8, among the various phosphate-based crystalline matrix, thorium phosphate diphosphate (TPD) viz.  $\text{Th}_4(\text{PO}_4)_4\text{P}_2\text{O}_7$ , TPD,  $\text{Th}_4\text{P}_6\text{O}_{23}$ , has also been proposed as a potential host matrix for long-lived tetravalent actinides. The thermophysical and thermochemical properties viz. heat capacity  $C_{p,m}^\circ(T)$  and standard enthalpy of formation  $\Delta H_f^\circ(T)$  of waste forms are important parameters that decide the maximum waste loading based on the decay heat from the radioactive elements in HLW. Alpha ( $\alpha$ ) decay of actinides loaded in TPD host matrix could alter its chemical reactivity by modifying the thermodynamic stability of the material [220]. This in turn could modify the long-term performance of TPD as a host matrix.

The present study deals with the thorough investigations of thermodynamic properties of TPD which enables to evaluate its long-term durability and reactivity. To the best of our knowledge, no experimental data is available for standard enthalpy of formation of TPD. In this chapter, the determination of the standard molar enthalpy of formation and heat capacity of TPD are reported. The important thermodynamic functions of TPD, Gibbs phase diagram, predominant area diagram for Th-P-O system and  $E_H$ -pH diagram for Th-P- $\text{H}_2\text{O}$  system have also been calculated using FactSage software [221] and discussed in this chapter.

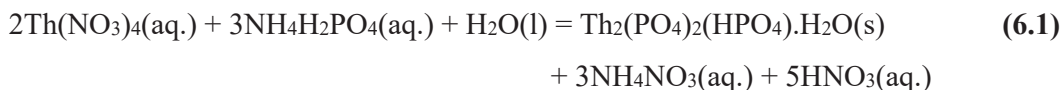
## 6.2. EXPERIMENTAL

### 6.2.1. Material Synthesis

#### 6.2.1.1. Synthesis of $\text{Th}_2(\text{PO}_4)_2(\text{HPO}_4)\cdot\text{H}_2\text{O}$ (TPHPH)

Solution chemistry route was used for the preparation of  $\text{Th}_2(\text{PO}_4)_2(\text{HPO}_4)\cdot\text{H}_2\text{O}$  (TPHPH) compound using the mixture of thorium nitrate (NFC, Hyderabad; 99.99 % purity) and ammonium dihydrogen phosphate (M/s Alfa Aesar, 99.9 % purity) taken in stoichiometric amount. Aqueous solution of  $\text{Th}(\text{NO}_3)_4(\text{aq.})$  and  $\text{NH}_4\text{H}_2\text{PO}_4(\text{aq.})$  were taken in 2:3 mole ratio.

Addition of aqueous solutions of  $\text{Th}(\text{NO}_3)_4(\text{aq.})$  to ammoniacal solution of  $\text{NH}_4\text{H}_2\text{PO}_4(\text{aq.})$  with continuous stirring resulted in precipitate of respective hydrated thorium phosphate diphosphate viz.  $\text{Th}_2(\text{PO}_4)_2(\text{HPO}_4)\cdot\text{H}_2\text{O}$  according to the following reaction:



The resulting precipitates were filtered and washed in distilled water until the filtrate was neutral. The precipitates thus obtained were dried using infra-red lamp and stored under argon atmosphere.

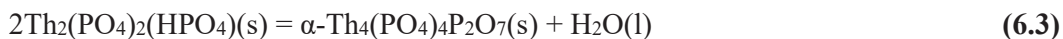
#### 6.2.1.2. Synthesis of $\text{Th}_2(\text{PO}_4)_2(\text{HPO}_4)$ (TPHP)

The dried precipitate of  $\text{Th}_2(\text{PO}_4)_2(\text{HPO}_4)\cdot\text{H}_2\text{O}$  (TPHPH) was heated at 500 K for 30 h under flowing argon resulted its dehydrated form as  $\text{Th}_2(\text{PO}_4)_2(\text{HPO}_4)$  (TPHP) as per the reaction:



#### 6.2.1.3. Synthesis of $\alpha\text{-Th}_4(\text{PO}_4)_4\text{P}_2\text{O}_7$ ( $\alpha$ -TPD)

$\alpha$ -TPD was prepared by heating dehydrated  $\text{Th}_2(\text{PO}_4)_2(\text{HPO}_4)$  (TPHP) compound at 1000 K for 24 h under argon flow. The corresponding reaction can be written as:



#### 6.2.1.4. Synthesis of $\beta\text{-Th}_4(\text{PO}_4)_4\text{P}_2\text{O}_7$ ( $\beta$ -TPD)

$\beta\text{-Th}_4(\text{PO}_4)_4\text{P}_2\text{O}_7$  ( $\beta$ -TPD) was prepared through transition from its  $\alpha$ -phase. The sample of  $\alpha$ -TPD was ground, pelletized and heated to 1373 K for 24 h. The  $\beta$ -TPD was formed as per the reaction given below:



The  $\beta$ -TPD pellets were then gradually cooled to room temperature and stored inside a desiccator for further studies. The purity of TPHPH, TPHP,  $\alpha$ -TPD and  $\beta$ -TPD prepared in this study has been taken similar to that of constituent precursors.

## 6.2.2. Characterization methods

### 6.2.2.1. Thermogravimetric analysis (TGA)

The accurate weight of thorium nitrate and ammonium dihydrogen phosphate was required for the determination of  $\Delta H_f^\circ(298.15\text{ K})$  for  $\text{Th}_2(\text{PO}_4)_2(\text{HPO}_4)\cdot\text{H}_2\text{O}$  (TPHPH). In order to obtain the number of waters of hydration in thorium nitrate, ammonium dihydrogen phosphate and resulting precipitate, thorium phosphate-hydrogenphosphate hydrate, thermogravimetric analysis (TG) of these compounds were carried out in Netzsch STA 409 PC, NETZSCH-Geratebau GmbH, Germany. Thermogravimetric studies on thorium nitrate, ammonium dihydrogen phosphate and thorium phosphate-hydrogenphosphate hydrate were carried out at the heating rate of  $2\text{ K}\cdot\text{min}^{-1}$  under flowing argon with flow rate of  $20\text{ ml}\cdot\text{min}^{-1}$  in the temperature range 303-1273 K. The method is described in Section 2.3.5 of Chapter 2.

### 6.2.2.2. X-ray diffraction (XRD)

$\beta$ -TPD was analyzed by X-ray diffraction (XRD) technique using a Stoe, Germany, X-ray diffractometer with monochromatic  $\text{CuK}\alpha$  radiation ( $\lambda = 1.5406\text{ \AA}$ ) and a nickel filter. The XRD patterns were recorded in the  $2\theta$  range from  $10^\circ$  to  $90^\circ$  with a step width of  $0.02^\circ$  at 298 K. The description of the technique is given in Section 2.3.2 of Chapter 2. X-ray powder diffraction pattern of  $\beta$ -TPD was indexed by LATPAR program [222].

### 6.2.2.3. Fourier transform infrared (FT-IR) spectroscopy

The Infrared (IR) absorption spectra of  $\text{Th}_2(\text{PO}_4)_2(\text{HPO}_4)\cdot\text{H}_2\text{O}$  (TPHPH) and  $\beta\text{-Th}_4(\text{PO}_4)_4\text{P}_2\text{O}_7$  ( $\beta$ -TPD) were recorded from  $500$  to  $4000\text{ cm}^{-1}$  using diamond ATR, employing IR Affinity-1

FT-IR spectrophotometer, Shimadzu. The details of the instrument are described in Section 2.3.3 of Chapter 2. FT-IR spectrophotometer measured the infrared spectrum resulting from irradiating samples with an interference pattern generated from a light source. The infrared light was transmitted through the beam splitter to generate the interference pattern from the light. The attenuated total reflectance (ATR) method was used to obtain infrared spectra from samples in a variety of forms.

#### 6.2.2.4. Enthalpy of dehydration

The enthalpies of reaction, correspond to dehydration of  $\text{Th}_2(\text{PO}_4)_2(\text{HPO}_4)\cdot\text{H}_2\text{O}$  (TPHPH) to  $\text{Th}_2(\text{PO}_4)_2(\text{HPO}_4)$  (TPHP) and further dehydration to  $\alpha\text{-Th}_4(\text{PO}_4)_4\text{P}_2\text{O}_7$  ( $\alpha$ -TPD) were measured using continuous scanning mode of Differential Scanning Calorimeter (DSC). The enthalpy of dehydration was measured using a heating rate of  $5\text{ K}\cdot\text{min}^{-1}$  with a pre-calibrated Mettler Toledo Differential Scanning Calorimeter (DSC I) under the flow of high purity argon gas. About 250 mg of sample was taken in a sealed 100  $\mu\text{l}$  Al pan crucible for the measurement. The details of both DSC techniques are provided in Section 2.4.1 of Chapter 2.

#### 6.2.2.5. Heat capacity

The transition enthalpy and heat capacity,  $C_p^\circ(T)$  of the samples were measured in the temperature range of 300-800 K with a heating rate of  $5\text{ K}\cdot\text{min}^{-1}$  using Differential Scanning Calorimeter (DSC) under a constant flow of argon gas. Classical three-step method viz., blank, sapphire and sample run in a step heating mode was used to measure the heat capacity of each sample. The descriptions of the classical three-step method are provided in Section 2.4.1.4 of Chapter 2. About 200 mg quantity of each sample was taken in a sealed 40  $\mu\text{l}$  Al pan crucible for the heat capacity measurement and independently measured twice. Four consecutive runs

were performed for each sample and the average of the last three superimposing DSC curve were considered for the calculation of heat capacity for the sample.

#### **6.2.2.6. Enthalpy of formation**

The enthalpy of reaction between  $\text{Th}(\text{NO}_3)_4(\text{aq.})$  and  $\text{NH}_4\text{H}_2\text{PO}_4(\text{aq.})$  was measured in ampoule break experiment in which known quantity of thorium nitrate was loaded into the Isoperibol calorimetric ampoule. Calorimetric solvent contained  $\text{NH}_4\text{H}_2\text{PO}_4$  in 25 g (1.388 mol) of double distilled water. The mole ratio of solute to solvent present in calorimetric vessel was more than 1:4000. The sample containing ampoule was equilibrated in the calorimeter containing solvent. The calorimetric temperature was recorded as a function of time before the ampoule was broken. The reaction inside the calorimeter was initiated by breaking the ampoule containing thorium nitrate. The reaction was observed as an instantaneous change in the calorimetric temperature. The measured temperature change for dissolution of thorium nitrate in calorimetric solvent was due to both enthalpy of solution at infinite dilution and enthalpy of precipitation of TPHPH. The details of the method is provided in Section 2.4.2 of Chapter 2.

### **6.3. RESULTS & DISCUSSIONS**

#### **6.3.1. Thermogravimetric analysis (TGA)**

Thermogravimetric analysis of the precursor material i.e. hydrated thorium nitrate and room temperature precipitated product i.e.  $\text{Th}_2(\text{PO}_4)_2(\text{HPO}_4) \cdot \text{H}_2\text{O}$  (TPHPH) were carried out and the observed thermograms were given in **Fig. 6.1** and **Fig. 6.2**, respectively. The thermogram for hydrated thorium nitrate represents the stepwise mass loss of equivalent to five water molecules. The detailed dehydration study of second precursor material i.e.  $\text{NH}_4\text{H}_2\text{PO}_4$  has already been discussed in Section 3.3.1.2. of Chapter 3.

The observed results of the thermogram of decomposition of room temperature precipitate  $\text{Th}_2(\text{PO}_4)_2(\text{HPO}_4)\cdot\text{H}_2\text{O}$  (TPHPH) was found to be in agreement with the observation of Dacheux et al. [223]. They have thoroughly studied TGA and DTA analysis of TPHPH and found presence of one water molecule. The final product obtained at 1250 was characterized as  $\beta\text{-Th}_4(\text{PO}_4)_4\text{P}_2\text{O}_7$  (TPD).

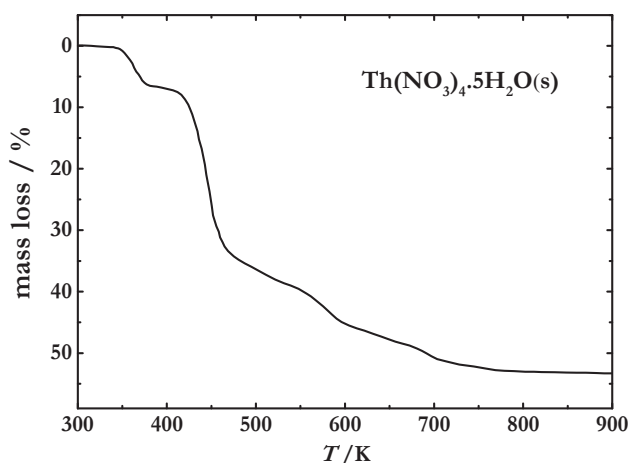


Fig. 6.1: Thermal decomposition of  $\text{Th}(\text{NO}_3)_4\cdot 5\text{H}_2\text{O}$ .

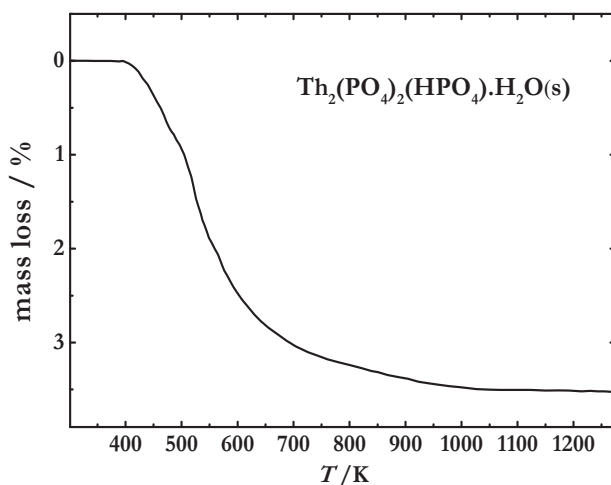
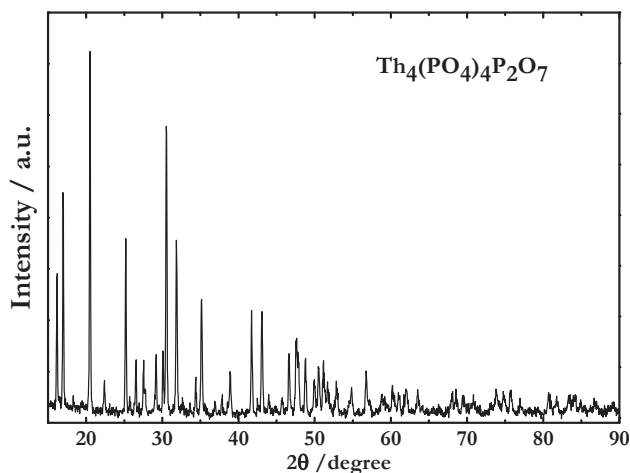


Fig. 6.2: Thermal decomposition of  $\text{Th}_2(\text{PO}_4)_2(\text{HPO}_4)\cdot\text{H}_2\text{O}$ .

### 6.3.2. X-ray diffraction (XRD)

XRD pattern of the product was matched well with the reported pattern of  $\beta$ - $\text{Th}_4(\text{PO}_4)_4\text{P}_2\text{O}_7$  (TPD) given in JCPDS file no: 86-0669 [224] which is given in **Fig. 6.3**. Indexing of the powder diffraction pattern using the LATPAR program [222] resulted in an orthorhombic unit cell.



**Fig. 6.3:** X-ray powder diffraction pattern of  $\beta$ - $\text{Th}_4(\text{PO}_4)_4\text{P}_2\text{O}_7$ .

The least square refinement of the unit cell parameters leads to  $a = 12.8607(24) \text{ \AA}$ ,  $b = 10.4302(15) \text{ \AA}$ ,  $c = 7.0646(11) \text{ \AA}$  and  $V = 947.64(27) \text{ \AA}^3$ . The least squares analyzed X-ray powder diffraction data of  $\beta$ - $\text{Th}_4(\text{PO}_4)_4\text{P}_2\text{O}_7$  are provided in **Table 6.1**.

**Table 6.1:** X-ray powder diffraction data for  $\beta$ -  $\text{Th}_4(\text{PO}_4)_4\text{P}_2\text{O}_7$ .

h k l	$2\theta_{\text{obs}}/\text{deg}$	$2\theta_{\text{calc}}/\text{deg}$	$d_{\text{obs}}/\text{\AA}$	$I/I_0$
2 0 0	13.730	13.760	6.444	10.0
2 1 0	16.160	16.180	5.480	50.1
0 2 0	16.970	16.988	5.221	67.2
1 2 0	18.360	18.343	4.828	7.6
2 1 1	20.500	20.510	4.329	100
3 1 0	22.400	22.404	3.966	14.3
0 0 2	25.180	25.192	3.534	43.6
3 1 1	25.750	25.745	3.457	10.7
1 3 0	26.550	26.537	3.355	14.5
1 1 2	27.520	27.526	3.239	16.8
2 3 0	29.170	29.176	3.059	17.9
2 1 2	30.070	30.085	2.969	19.8

4 0 1	30.530	30.523	2.926	76.0
2 3 1	31.860	31.859	2.807	52.0
4 2 0	32.700	32.694	2.736	10.3
0 4 0	34.370	34.364	2.607	12.0
4 2 1	35.130	35.136	2.552	33.0
2 3 2	38.890	38.921	2.314	14.0
2 1 3	41.730	41.722	2.163	25.0
0 4 2	43.070	43.084	2.099	28.0
4 4 1	46.640	46.616	1.946	17.0
2 5 1	47.570	47.561	1.910	22.0
2 3 3	48.770	48.767	1.866	20.0
6 3 0	49.930	49.945	1.825	14.3
6 1 2	50.540	50.530	1.804	18.0
4 2 3	51.110	51.129	1.786	14.8
0 0 4	51.730	51.717	1.766	13.0
2 5 2	52.880	52.881	1.730	10.1
1 6 1	54.810	54.806	1.674	11.9
5 5 0	56.770	56.776	1.620	13.2
6 1 3	58.910	58.883	1.566	9.0

### 6.3.3. Fourier transform infrared (FT-IR) spectroscopy

The observed FT-IR spectrum of the room temperature precipitate i.e.  $\text{Th}_2(\text{PO}_4)_2(\text{HPO}_4)\cdot\text{H}_2\text{O}$  and high temperature product i.e.  $\beta\text{-Th}_4(\text{PO}_4)_4\text{P}_2\text{O}_7$  are given in **Fig. 6.4** and the corresponding infra-red vibrational frequencies are provided in **Table 6.2**.

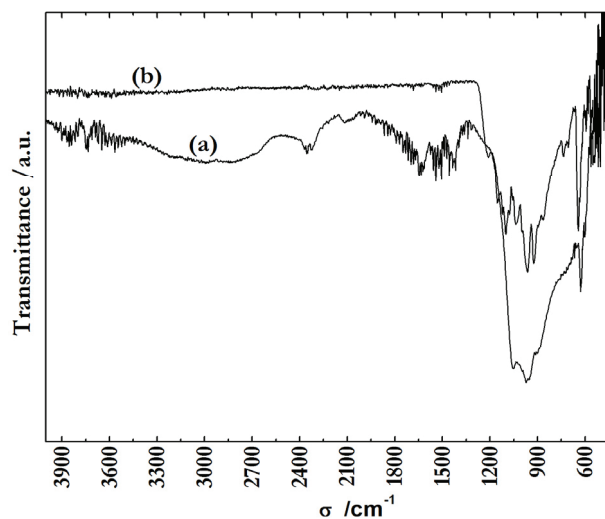


**Fig. 6.4:** Infrared spectra of (a)  $\text{Th}_2(\text{PO}_4)_2(\text{HPO}_4)\cdot\text{H}_2\text{O}$  and (b)  $\beta\text{-Th}_4(\text{PO}_4)_4\text{P}_2\text{O}_7$  recorded at room temperature.

**Table 6.2:** Assignments of the vibrational frequencies of  $\text{Th}_2(\text{PO}_4)_2(\text{HPO}_4)\cdot\text{H}_2\text{O}$  and  $\beta\text{-Th}_4(\text{PO}_4)_4\text{P}_2\text{O}_7$  at room temperature.

Assignments	$\text{Th}_2(\text{PO}_4)_2(\text{HPO}_4)\cdot\text{H}_2\text{O}$ $\sigma / \text{cm}^{-1}$	$\beta\text{-Th}_4(\text{PO}_4)_4\text{P}_2\text{O}_7$ $\sigma / \text{cm}^{-1}$
stretching O-H and (P)-O-H	3650-2700	-
stretching (P)-O-H	~ 2400 shoulder	-
bending $\text{H}_2\text{O}$	1638	-
bending (P)-O-H	~ 1400 shoulder	-
$\nu\text{P-O}$	1140-940	1150-860
$\delta\text{P-O}$	628-506	640-620
stretching P-O-P	-	740

The IR spectra of  $\text{Th}_2(\text{PO}_4)_2(\text{HPO}_4)\cdot\text{H}_2\text{O}$  showed O-H stretching, H-O-H bending vibrations [225-227], P-O and (P)-O-H bands. The broad band observed from 3650 to 2700  $\text{cm}^{-1}$  consist of O-H stretching modes of the water molecule and that of the (P)-O-H group [225, 228], while the band observed at 1638  $\text{cm}^{-1}$  is the characteristic bending mode of  $\text{H}_2\text{O}$ . The stretching and bending vibrations of (P)-O-H are detected as a shoulder at ~2400  $\text{cm}^{-1}$  and ~1400  $\text{cm}^{-1}$ , respectively [229, 230].

The P-O bonds vibrations are observed in the wavelength range 640-506  $\text{cm}^{-1}$  ( $\delta_{\text{as}}$ ) and from 1150-860  $\text{cm}^{-1}$  ( $\nu_{\text{s}}$  and  $\nu_{\text{as}}$ ) in the infrared spectra of  $\text{Th}_2(\text{PO}_4)_2(\text{HPO}_4)\cdot\text{H}_2\text{O}$  and  $\beta\text{-Th}_4(\text{PO}_4)_4\text{P}_2\text{O}_7$ . The signature of  $\text{P}_2\text{O}_7$  group (P-O-P) bridge (720-770  $\text{cm}^{-1}$ ) is not generally so intense [231], but can be seen in case of  $\beta\text{-Th}_4(\text{PO}_4)_4\text{P}_2\text{O}_7$  and absent in  $\text{Th}_2(\text{PO}_4)_2(\text{HPO}_4)\cdot\text{H}_2\text{O}$ .

The observations confirm the presence of hydrogenphosphate group and absence of  $\text{P}_2\text{O}_7$  group in  $\text{Th}_2(\text{PO}_4)_2(\text{HPO}_4)\cdot\text{H}_2\text{O}$ . The bands corresponding to the stretching mode of O-H, (P)-O-H, or bending mode of H-O-H are not observed for  $\beta\text{-Th}_4(\text{PO}_4)_4\text{P}_2\text{O}_7$ . These bands might have disappeared when  $\text{Th}_2(\text{PO}_4)_2(\text{HPO}_4)\cdot\text{H}_2\text{O}$  was heated at 1273 K due to formation of  $\beta\text{-Th}_2(\text{PO}_4)_2(\text{HPO}_4)\cdot\text{H}_2\text{O}$ .

### 6.3.4. Enthalpy of dehydration

DSC measurements showed two endothermic peaks at 450 K and 638 K with corresponding enthalpy of transitions  $88.5$  and  $101.4 \text{ J}\cdot\text{g}^{-1}$ , respectively. These peaks correspond to different events in the temperature range 350-555 K and 555-750 K shown in **Fig. 6.5**. The first peak corresponds to the full dehydration of  $\text{Th}_2(\text{PO}_4)_2(\text{HPO}_4)\cdot\text{H}_2\text{O}$  into  $\text{Th}_2(\text{PO}_4)_2(\text{HPO}_4)$  whereas the second peak correspond to the loss of one mole of water for the formation of  $\text{P}_2\text{O}_7$  from two  $\text{HPO}_4$  groups. This rearrangement resulted in low temperature form:  $\alpha\text{-Th}_2(\text{PO}_4)_2(\text{HPO}_4)\cdot\text{H}_2\text{O}$ . Dacheux et al. [232] have measured DTA-TGA of curves of  $\text{Th}_2(\text{PO}_4)_2(\text{HPO}_4)\cdot\text{H}_2\text{O}$  using Setaram TG 92-16 apparatus under dry argon in the temperature range 300-1473 K. From their measurements the enthalpy of transition of  $\alpha$  to  $\beta$  phase of  $\text{Th}_2(\text{PO}_4)_2(\text{HPO}_4)\cdot\text{H}_2\text{O}$  has been calculated as  $-53.1 \text{ kJ}\cdot\text{mol}^{-1}$ .

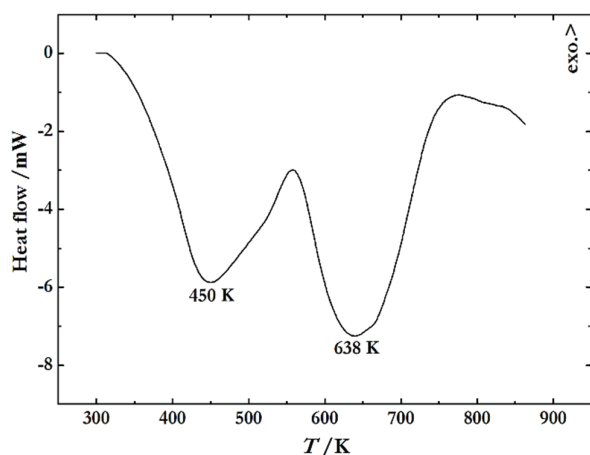


**Fig. 6.5:** Heat flow curve of  $\text{Th}_2(\text{PO}_4)_2(\text{HPO}_4)\cdot\text{H}_2\text{O}$ .

### 6.3.5. Heat capacity measurements

The molar heat capacity data for  $\text{Th}_2(\text{PO}_4)_2(\text{HPO}_4)\cdot\text{H}_2\text{O}$ ,  $\text{Th}_2(\text{PO}_4)_2(\text{HPO}_4)$ ,  $\alpha\text{-Th}_4(\text{PO}_4)_4\text{P}_2\text{O}_7$  ( $\alpha\text{-TPD}$ ) and  $\beta\text{-Th}_4(\text{PO}_4)_4\text{P}_2\text{O}_7$  ( $\beta\text{-TPD}$ ) are calculated based on classical three steps method and are tabulated in **Tables 6.3-6.5**. These molar heat capacity data are least square fitted to

$A + B \cdot T + C \cdot T^2$  polynomial expressions and the results along with the temperature range are given below:

**Th<sub>2</sub>(PO<sub>4</sub>)<sub>2</sub>(HPO<sub>4</sub>)·H<sub>2</sub>O (TPHPH)**

$$C_{p,m}^{\circ}(T) / \text{J} \cdot \text{mol}^{-1} \cdot \text{K}^{-1} = 426.93 + 0.49486 \cdot (T/\text{K}) - 17.248 \cdot 10^6 \cdot (\text{K}/T)^2 \quad (298.15 \leq T/\text{K} \leq 450) \quad (6.5)$$

**Th<sub>2</sub>(PO<sub>4</sub>)<sub>2</sub>(HPO<sub>4</sub>) (TPHP)**

$$C_{p,m}^{\circ}(T) / \text{J} \cdot \text{mol}^{-1} \cdot \text{K}^{-1} = 371.32 + 0.03583 \cdot (T/\text{K}) - 6.946 \cdot 10^6 \cdot (\text{K}/T)^2 \quad (473 \leq T/\text{K} \leq 638) \quad (6.6)$$

**α-Th<sub>4</sub>(PO<sub>4</sub>)<sub>4</sub>P<sub>2</sub>O<sub>7</sub> (α-TPD)**

$$C_{p,m}^{\circ}(T) / \text{J} \cdot \text{mol}^{-1} \cdot \text{K}^{-1} = 574.046 + 0.04001 \cdot (T/\text{K}) - 8.483 \cdot 10^6 \cdot (\text{K}/T)^2 \quad (303 \leq T/\text{K} \leq 791) \quad (6.7)$$

**β-Th<sub>4</sub>(PO<sub>4</sub>)<sub>4</sub>P<sub>2</sub>O<sub>7</sub> (β-TPD)**

$$C_{p,m}^{\circ}(T) / \text{J} \cdot \text{mol}^{-1} \cdot \text{K}^{-1} = 422.75 + 1.5253 \cdot (T/\text{K}) - 6.44 \cdot 10^{-3} \cdot (T/\text{K})^2 + 1.0 \cdot 10^{-5} \cdot (T/\text{K})^3 - 10.395 \cdot 10^5 \cdot (\text{K}/T)^2 - 35.112 \cdot 10^7 \cdot (\text{K}/T)^3 \quad (127 \leq T/\text{K} \leq 304) \quad (6.8)$$

$$C_{p,m}^{\circ}(T) / \text{J} \cdot \text{mol}^{-1} \cdot \text{K}^{-1} = 718.17 + 0.01135 \cdot (T/\text{K}) - 12.43 \cdot 10^6 \cdot (\text{K}/T)^2 \quad (303 \leq T/\text{K} \leq 791) \quad (6.9)$$

**Table 6.3:** Heat capacity data of Th<sub>2</sub>(PO<sub>4</sub>)<sub>2</sub>(HPO<sub>4</sub>)·H<sub>2</sub>O and Th<sub>2</sub>(PO<sub>4</sub>)<sub>2</sub>(HPO<sub>4</sub>).

Th <sub>2</sub> (PO <sub>4</sub> ) <sub>2</sub> (HPO <sub>4</sub> )·H <sub>2</sub> O		Th <sub>2</sub> (PO <sub>4</sub> ) <sub>2</sub> (HPO <sub>4</sub> )			
T/K	C <sub>p,m</sub> <sup>o</sup> (T) /J·mol <sup>-1</sup> ·K <sup>-1</sup>	T/K	C <sub>p,m</sub> <sup>o</sup> (T) /J·mol <sup>-1</sup> ·K <sup>-1</sup>	T/K	C <sub>p,m</sub> <sup>o</sup> (T) /J·mol <sup>-1</sup> ·K <sup>-1</sup>
300.0	391.5	310.0	310.0	482.7	358.6
316.4	408.4	317.2	312.8	490.3	360.3
323.9	416.1	324.9	315.5	497.8	361.7
331.5	427.8	332.6	318.6	505.3	361.7
339.0	444.9	340.2	322.6	512.8	362.8
346.4	454.3	347.7	325.3	520.3	363.5
353.6	465.6	355.2	331.4	527.8	364.2

360.9	474.1	362.7	333.5	535.4	365.3
368.2	483.0	370.1	336.0	542.8	366.4
375.5	490.6	377.6	337.8	550.4	367.0
382.9	502.2	385.0	339.1	557.9	368.1
390.4	509.2	392.5	341.6	565.4	368.9
397.9	515.4	399.9	343.4	572.8	371.2
405.4	523.0	407.4	345.2	580.3	372.3
413.0	530.5	414.9	346.1	587.8	373.2
420.6	538.0	422.4	347.6	595.4	373.4
428.3	546.5	429.9	348.8	602.9	374.3
435.9	550.6	437.4	350.0	610.5	375.5
443.5	557.5	444.9	351.9	618.0	375.5
451.1	563.0	452.5	352.5	625.6	376.0
		460.0	353.4	633.2	377.3
		467.6	355.3	640.8	378.0
		475.1	357.1	482.7	358.6

**Table 6.4:** Heat capacity data of  $\alpha$ -Th<sub>4</sub>(PO<sub>4</sub>)<sub>4</sub>P<sub>2</sub>O<sub>7</sub> ( $\alpha$ -TPD).

$\alpha$ -Th <sub>4</sub> (PO <sub>4</sub> ) <sub>4</sub> P <sub>2</sub> O <sub>7</sub> ( $\alpha$ -TPD)							
$T/K$	$C_{\text{pm}}^{\circ}(T)$ /J·mol <sup>-1</sup> ·K <sup>-1</sup>	$T/K$	$C_{\text{pm}}^{\circ}(T)$ /J·mol <sup>-1</sup> ·K <sup>-1</sup>	$T/K$	$C_{\text{pm}}^{\circ}(T)$ /J·mol <sup>-1</sup> ·K <sup>-1</sup>	$T/K$	$C_{\text{pm}}^{\circ}(T)$ /J·mol <sup>-1</sup> ·K <sup>-1</sup>
303.3	493.9	437.0	548.5	580.2	571.5	723.6	585.8
304.5	496.5	444.5	550.4	587.7	573.4	731.1	587.6
309.8	497.6	452.0	552.5	595.3	573.4	738.7	587.6
317.0	503.6	459.6	552.0	602.8	574.3	746.2	587.6
324.6	505.1	467.1	553.2	610.4	575.3	753.8	590.1
332.2	510.2	474.7	556.0	617.9	575.0	761.4	589.7
339.8	515.0	482.3	558.9	625.4	576.5	768.9	590.9
347.4	516.5	489.8	559.2	633.0	577.7	776.5	590.9
354.8	520.0	497.3	560.3	640.5	578.1	784.0	593.1
362.3	521.7	504.8	559.6	648.1	579.3	791.5	593.5
369.7	524.5	512.4	562.3	655.6	579.8	799.1	593.4
377.1	527.6	519.9	563.4	663.2	581.7	806.6	594.3
384.6	529.1	527.5	564.3	670.8	580.9	814.1	594.3
392.0	533.2	535.0	565.1	678.3	582.1	818.2	594.7
399.5	538.7	542.5	567.5	685.9	583.6	819.0	593.8
406.9	540.6	550.0	568.6	693.4	582.4	819.1	595.0
414.4	542.4	557.5	568.6	701.0	584.0	819.1	593.5
421.9	546.6	565.1	569.8	708.5	584.5	819.1	593.4
429.4	548.2	572.6	571.5	716.1	586.4	819.0	595.9

**Table 6.5:** Heat capacity data of  $\beta$ -Th<sub>4</sub>(PO<sub>4</sub>)<sub>4</sub>P<sub>2</sub>O<sub>7</sub> ( $\beta$ -TPD).

<b><math>\beta</math>-TPD</b>							
Low temperature heat capacity data				High temperature heat capacity data			
$T/K$	$C_{\text{pm}}^{\circ}(T)$ /J·mol <sup>-1</sup> ·K <sup>-1</sup>	$T/K$	$C_{\text{pm}}^{\circ}(T)$ /J·mol <sup>-1</sup> ·K <sup>-1</sup>	$T/K$	$C_{\text{pm}}^{\circ}(T)$ /J·mol <sup>-1</sup> ·K <sup>-1</sup>	$T/K$	$C_{\text{pm}}^{\circ}(T)$ /J·mol <sup>-1</sup> ·K <sup>-1</sup>
126.8	299.2	249.0	540.4	302.4	590.4	602.3	691.2
134.1	336.1	256.8	547.2	310.4	593.7	621.0	693.2
141.6	365.3	264.6	553.5	326.8	606.0	640.8	695.3
149.1	391.2	272.4	560.0	348.9	617.0	660.7	697.7
156.6	414.5	280.2	570.7	367.7	624.9	679.4	699.7
164.2	434.2	288.0	570.4	387.5	636.1	700.4	700.7
172.0	450.0	295.8	578.1	408.5	645.6	716.8	702.7
180.6	462.7	303.6	591.0	427.2	653.4	738.9	703.4
187.1	472.9			447.1	662.2	752.9	704.7
194.8	484.7			464.6	668.6	766.9	705.4
202.5	495.6			485.0	672.7	775.1	705.4
210.2	502.4			504.6	677.0	779.8	705.5
217.9	513.4			524.1	681.1	780.9	706.0
225.7	518.5			543.7	684.1	784.5	706.5
233.5	526.9			563.2	685.5	790.2	707.1
241.2	533.7			582.8	687.8		

The heat capacity data of  $\beta$ -Th<sub>4</sub>(PO<sub>4</sub>)<sub>4</sub>P<sub>2</sub>O<sub>7</sub> measured in this study matched well with that reported by Dacheux et al. [232]. The heat capacity data determined for Th<sub>2</sub>(PO<sub>4</sub>)<sub>2</sub>(HPO<sub>4</sub>)·H<sub>2</sub>O, Th<sub>2</sub>(PO<sub>4</sub>)<sub>2</sub>(HPO<sub>4</sub>) and  $\alpha$ -Th<sub>4</sub>(PO<sub>4</sub>)<sub>4</sub>P<sub>2</sub>O<sub>7</sub> in the present study could not be compared as no data was reported in the literature. A comparison of specific heat of  $\alpha$ -Th<sub>4</sub>(PO<sub>4</sub>)<sub>4</sub>P<sub>2</sub>O<sub>7</sub> and  $\beta$ -Th<sub>4</sub>(PO<sub>4</sub>)<sub>4</sub>P<sub>2</sub>O<sub>7</sub> obtained in this study with that of Dacheux et al. [232] is shown in **Fig. 6.6**. The difference between the specific heat capacity values of the present study and that of Dacheux et al. [232] is well within 5% at 800°C.

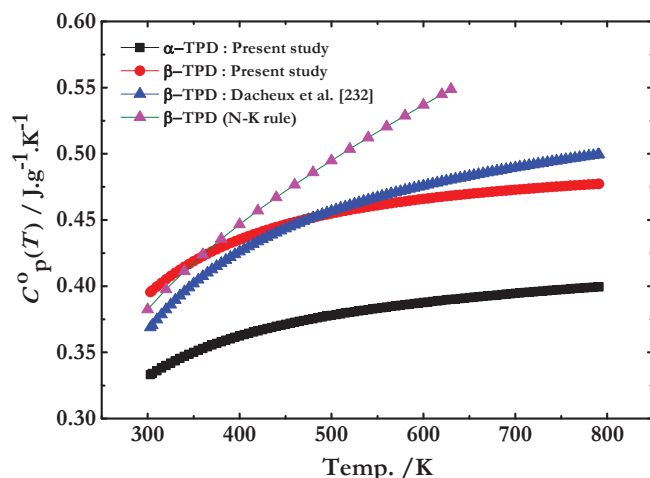


**Fig. 6.6:** A comparison of specific heat capacities of  $\alpha$ -TPD and  $\beta$ -TPD.

### 6.3.6. Enthalpy of formation

The results of the enthalpy of reaction of thorium nitrate with ammoniacal solution of ammonium dihydrogen phosphate are given in **Table 6.6**. Applying Hess's law, the value of standard molar enthalpy of formation,  $\Delta H_{f,m}^0$  for TPHPH is calculated to be  $-5754.2 \pm 5.1$   $\text{kJ}\cdot\text{mol}^{-1}$ . The required enthalpy data for the thermo-chemical reaction scheme for the formation of  $\text{Th}_2(\text{PO}_4)_2(\text{HPO}_4)\cdot\text{H}_2\text{O}$  are given in **Table 6.7**.

**Table 6.6:** Enthalpy of reaction data using solution calorimeter experiment for  $\text{Th}(\text{NO}_3)_4\cdot 5\text{H}_2\text{O}(\text{s})$  in solution of  $\text{NH}_4\text{H}_2\text{PO}_4(\text{aq.})$  at 298 K. (where, Soln A =  $1.4 \times 10^{-4}$  mol  $\text{NH}_4\text{H}_2\text{PO}_4$  in 25 g (1.388 mol) of double distilled water).

Reactant	Sample wt. /mg	$Q$ /J	$\Delta H_r^0$ /kJ·mol <sup>-1</sup>	Mean $\Delta H_r^0$ /kJ·mol <sup>-1</sup>
$\text{Th}(\text{NO}_3)_4\cdot 5\text{H}_2\text{O}(\text{s})$	11.9	-0.622	-29.8	
+	12.7	-0.648	-29.1	$-29.8 \pm 0.6^{\text{a,b}}$
Soln A	11.8	-0.629	-30.4	

<sup>a</sup>Uncertainty is twice the standard deviation.

<sup>b</sup>Molar enthalpy of solution based on the molar mass of  $570.134$   $\text{g}\cdot\text{mol}^{-1}$  for  $\text{Th}(\text{NO}_3)_4\cdot 5\text{H}_2\text{O}$ .

**Table 6.7:** Thermochemical-cycle for calculation of standard molar enthalpy of formation,  $\Delta H_{f,m}^{\circ}$  of  $\text{Th}_2(\text{PO}_4)_2(\text{HPO}_4) \cdot \text{H}_2\text{O}$  (TPHPH) at 298 K.

$$(\Delta H_{f,m}^{\circ} = \Delta H_1 + \Delta H_2 + \Delta H_3 + \Delta H_4 + \Delta H_5 + \Delta H_6 + \Delta H_7 + \Delta H_8 + \Delta H_9 + \Delta H_{10} + \Delta H_{11}).$$

Reactions	$\Delta H_i$	$\Delta H_r / \text{kJ} \cdot \text{mol}^{-1}$
$2 \cdot \text{Th}(\text{NO}_3)_4 \cdot 5\text{H}_2\text{O}_{(s)} = 2 \cdot \text{Th}(\text{NO}_3)_{4(aq)} + 10 \cdot \text{H}_2\text{O}_{(l)}$		
$2 \cdot \text{Th}(\text{NO}_3)_{4(aq)} + 3 \cdot \text{NH}_4\text{H}_2\text{PO}_{4(aq)} + \text{H}_2\text{O}_{(l)} = \text{Th}_2(\text{PO}_4)_2(\text{HPO}_4) \cdot \text{H}_2\text{O}_{(s)}$ $+ 3 \cdot \text{NH}_4\text{NO}_{3(aq)} + 5 \cdot \text{HNO}_{3(aq)}$	$\Delta H_1 + \Delta H_2$	-59.6 ± 1.2
$2 \cdot \text{Th}(\text{NO}_3)_{4(s)} + 10 \cdot \text{H}_2\text{O}_{(l)} = 2 \cdot \text{Th}(\text{NO}_3)_4 \cdot 5\text{H}_2\text{O}_{(s)}$	$\Delta H_3$	-266.3 ± 3.2 <sup>[233]</sup>
$2\text{Th}_{(s)} + 4\text{N}_{2(g)} + 12\text{O}_{2(g)} = 2 \cdot \text{Th}(\text{NO}_3)_{4(s)}$	$\Delta H_4$	-2891.2 ± 3.0 <sup>[233]</sup>
$3/2 \cdot \text{N}_{2(g)} + 9\text{H}_{2(g)} + 3\text{P}_{(s)} + 6\text{O}_{2(g)} = 3 \cdot \text{NH}_4\text{H}_2\text{PO}_{4(s)}$	$\Delta H_5$	-4357.3 ± 1.2 <sup>[234]</sup>
$3 \cdot \text{NH}_4\text{NO}_{3(s)} = 3 \cdot \text{N}_{2(g)} + 6 \cdot \text{H}_2\text{O}_{(g)} + 9/2 \cdot \text{O}_{2(g)}$	$\Delta H_6$	1100.6 ± 0.5 <sup>[234]</sup>
$5 \cdot \text{HNO}_{3(g)} = 5/2 \cdot \text{N}_{2(g)} + 5/2 \cdot \text{H}_2\text{O}_{(g)} + 15/2 \cdot \text{O}_{2(g)}$	$\Delta H_7$	671.6 ± 0.4 <sup>[234]</sup>
$3 \cdot \text{NH}_4\text{NO}_{3(aq)} = 3 \cdot \text{NH}_4\text{NO}_{3(s)}$	$\Delta H_8$	-79.4 ± 0.7 <sup>[234]</sup>
$3 \cdot \text{NH}_4\text{H}_2\text{PO}_{4(s)} = 3 \cdot \text{NH}_4\text{H}_2\text{PO}_{4(aq)}$	$\Delta H_9$	48.8 ± 1.7 <sup>[234]</sup>
$5 \cdot \text{HNO}_{3(aq)} = 5 \cdot \text{HNO}_{3(g)}$	$\Delta H_{10}$	364.3 ± 0.6 <sup>[234]</sup>
$\text{H}_2\text{(g)} + 1/2 \cdot \text{O}_2\text{(g)} = \text{H}_2\text{O}_{(l)}$	$\Delta H_{11}$	-285.8 ± 0.1 <sup>[234]</sup>
$2 \cdot \text{Th}_{(s)} + 3 \cdot \text{P}_{(s)} + 13/2 \cdot \text{O}_{2(g)} + 3/2 \cdot \text{H}_{2(g)} = \text{Th}_2(\text{PO}_4)_2(\text{HPO}_4) \cdot \text{H}_2\text{O}_{(s)}$	$\Delta H_{f(\text{TPHPH})}^{\circ}$	-5754.2 ± 5.1

The thermo-chemical cycle for calculation of standard molar enthalpy of formation,  $\Delta H_f^{\circ}$  ( $\beta$ -TPD, s, 298.15 K) is given in **Table 6.8**. The formation of  $\beta$ -TPD from TPHPH precipitate involves irreversible reactions given in **Fig. 6.7**. In order to calculate the values of  $\Delta H_{13} - \Delta H_{15}$  in **Table 6.8**, one has to consider typical thermo-chemical cycle given in **Fig. 6.8**. The enthalpy changes of the following reaction:



can be calculated from the enthalpy of reaction at  $T$  and enthalpy of vaporization of  $\text{C}(l)$  as follows:

$$\begin{aligned} \Delta H_r^{\circ} = & \int_{298.15 \text{ K}}^T C_{p,m}^{\circ}(\text{A}, s, T) dT + \Delta H_r(T) + \int_T^{298.15 \text{ K}} C_{p,m}^{\circ}(\text{B}, s, T) dT \\ & + \int_T^{298.15 \text{ K}} C_{p,m}^{\circ}(\text{C}, g, T) dT - \Delta H_{\text{vap}}^{\circ}(l) \end{aligned} \quad (6.11)$$

Using the similar thermo-chemical cycle  $\Delta H_{13}-\Delta H_{15}$  (**Table 6.8**) can be calculated from the following equations:

$$\Delta H_r^\circ(13) = \int_{298.15 \text{ K}}^{450 \text{ K}} C_{p,m}^\circ(\text{TPHPH},s,T)dT + \Delta H_r(450 \text{ K}) + \int_{450 \text{ K}}^{298.15 \text{ K}} C_{p,m}^\circ(\text{TPHP},s,T)dT \\ + \int_{450 \text{ K}}^{298.15 \text{ K}} C_{p,m}^\circ(\text{H}_2\text{O},g,T)dT - \Delta H_{\text{vap}}^\circ(l) \quad (6.12)$$

$$\Delta H_r^\circ(14) = 2 \cdot \int_{298.15 \text{ K}}^{638 \text{ K}} C_{p,m}^\circ(\text{TPHP},s,T)dT + \Delta H_r(638 \text{ K}) + \int_{638 \text{ K}}^{298.15 \text{ K}} C_{p,m}^\circ(\alpha\text{-TPD},s,T)dT \\ + \int_{638 \text{ K}}^{298.15 \text{ K}} C_{p,m}^\circ(\text{H}_2\text{O},g,T)dT - \Delta H_{\text{vap}}^\circ(l) \quad (6.13)$$

$$\Delta H_r^\circ(15) = \int_{298.15 \text{ K}}^{1223 \text{ K}} C_{p,m}^\circ(\alpha\text{-TPD},s,T)dT + \Delta H_r(1223\text{K}) \\ + \int_{1223 \text{ K}}^{298.15 \text{ K}} C_{p,m}^\circ(\beta\text{-TPD},s,T)dT \quad (6.14)$$

The calculated enthalpy values of  $\beta$ -TPD are given in **Table 6.8**. The corresponding value is -10565.5  $\pm$  13.6 kJ $\cdot$ mol $^{-1}$ . Similarly, enthalpy of formation of TPHP and  $\alpha$ -TPD have been calculated from required thermo-chemical cycles given in **Table 6.9** and **Table 6.10**, respectively. The corresponding enthalpy of formation values of TPHPH, TPHP and  $\alpha$ -TPD are -5754.2  $\pm$  5.1, -5423.6  $\pm$  5.3 and -10409.4  $\pm$  13.3 kJ $\cdot$ mol $^{-1}$ , respectively.

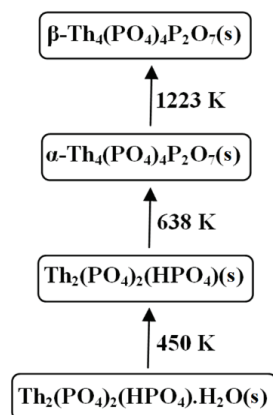


**Fig. 6.7:** Schematic diagram depicting stepwise thermal evolution of  $\beta$ -TPD.

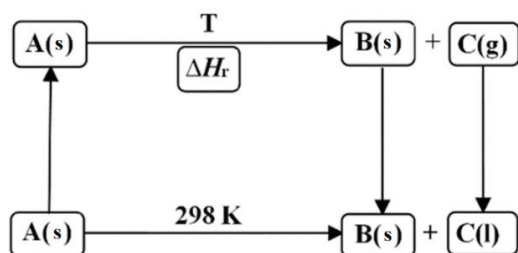


Fig. 6.8: Thermo-chemical cycle.

Table 6.8: Standard enthalpy of formation of  $\beta$ -TPD at 298 K.

$$(\Delta H_{\text{f}}^{\circ}(\beta\text{-TPD}) = 2 \cdot \Delta H_{12} + 2 \cdot \Delta H_{13} + \Delta H_{14} + \Delta H_{15} - 3 \cdot \Delta H_{16})$$

Reactions	$\Delta H_i$	$\Delta H_r / \text{kJ} \cdot \text{mol}^{-1}$
$2\text{Th}_{(s)} + 3\text{P}_{(s)} + 13/2 \cdot \text{O}_{2(g)} + 3/2 \cdot \text{H}_{2(g)} = \text{Th}_2(\text{PO}_4)_2(\text{HPO}_4) \cdot \text{H}_2\text{O}_{(s)}$	$\Delta H_{12}$	$-5754.2 \pm 5.1^a$
$\text{Th}_2(\text{PO}_4)_2(\text{HPO}_4) \cdot \text{H}_2\text{O}_{(s)} = \text{Th}_2(\text{PO}_4)_2(\text{HPO}_4)_{(s)} + \text{H}_2\text{O}_{(l)}$	$\Delta H_{13}$	$44.8 \pm 1.5^b$
$2 \cdot \text{Th}_2(\text{PO}_4)_2(\text{HPO}_4)_{(s)} = \alpha\text{-Th}_4(\text{PO}_4)_4\text{P}_2\text{O}_{7(s)} + \text{H}_2\text{O}_{(l)}$	$\Delta H_{14}$	$152.0 \pm 8.0^b$
$\alpha\text{-Th}_4(\text{PO}_4)_4\text{P}_2\text{O}_{7(s)} = \beta\text{-Th}_4(\text{PO}_4)_4\text{P}_2\text{O}_{7(s)}$	$\Delta H_{15}$	$-156.2 \pm 3.0^b$
$\text{H}_{2(g)} + 1/2 \cdot \text{O}_{2(g)} = \text{H}_2\text{O}_{(l)}$	$\Delta H_{16}$	$-285.8 \pm 0.1^{[234]}$
$4 \cdot \text{Th}_{(s)} + 6 \cdot \text{P}_{(s)} + 23/2 \cdot \text{O}_{2(g)} = \beta\text{-Th}_4(\text{PO}_4)_4\text{P}_2\text{O}_{7(s)}$	$\Delta H_{\text{f}}^{\circ}(\beta\text{-TPD})$	$-10565.5 \pm 13.6$

<sup>a</sup>Value taken from Table 6.6; <sup>b</sup>Using eqn. 6.12-6.14.

Table 6.9: Standard enthalpy of formation of TPHP at 298 K.

$$(\Delta H_{\text{f}}^{\circ}(\text{TPHP}) = \Delta H_{17} + \Delta H_{18} - \Delta H_{19})$$

Reactions	$\Delta H_i$	$\Delta H_r / \text{kJ} \cdot \text{mol}^{-1}$
$2 \cdot \text{Th}_{(s)} + 3 \cdot \text{P}_{(s)} + 13/2 \cdot \text{O}_{2(g)} + 3/2 \cdot \text{H}_{2(g)} = \text{Th}_2(\text{PO}_4)_2(\text{HPO}_4) \cdot \text{H}_2\text{O}_{(s)}$	$\Delta H_{17}$	$-5754.2 \pm 5.1^a$
$\text{Th}_2(\text{PO}_4)_2(\text{HPO}_4) \cdot \text{H}_2\text{O}_{(s)} = \text{Th}_2(\text{PO}_4)_2(\text{HPO}_4)_{(s)} + \text{H}_2\text{O}_{(l)}$	$\Delta H_{18}$	$44.8 \pm 1.5^b$
$\text{H}_{2(g)} + 1/2 \cdot \text{O}_{2(g)} = \text{H}_2\text{O}_{(l)}$	$\Delta H_{19}$	$-285.8 \pm 0.1^{[234]}$
$2 \cdot \text{Th}_{(s)} + 3 \cdot \text{P}_{(s)} + 6 \cdot \text{O}_{2(g)} + 1/2 \cdot \text{H}_{2(g)} = \text{Th}_2(\text{PO}_4)_2(\text{HPO}_4)_{(s)}$	$\Delta H_{\text{f}}^{\circ}(\text{TPHP})$	$-5423.6 \pm 5.3$

<sup>a</sup>Value taken from Table 6.6; <sup>b</sup>Using eqn. 6.12.

Table 6.10: Standard enthalpy of formation of  $\alpha$ -TPD at 298 K.

$$(\Delta H_{\text{f}}^{\circ}(\alpha\text{-TPD}) = 2 \cdot \Delta H_{20} + \Delta H_{21} - \Delta H_{22})$$

Reactions	$\Delta H_i$	$\Delta H_r / \text{kJ} \cdot \text{mol}^{-1}$
$2 \cdot \text{Th}_{(s)} + 3 \cdot \text{P}_{(s)} + 6 \cdot \text{O}_{2(g)} + 1/2 \cdot \text{H}_{2(g)} = \text{Th}_2(\text{PO}_4)_2(\text{HPO}_4)_{(s)}$	$\Delta H_{20}$	$-5423.6 \pm 5.3^a$
$2 \cdot \text{Th}_2(\text{PO}_4)_2(\text{HPO}_4)_{(s)} = \alpha\text{-Th}_4(\text{PO}_4)_4\text{P}_2\text{O}_{7(s)} + \text{H}_2\text{O}_{(l)}$	$\Delta H_{21}$	$152.0 \pm 8.0^b$
$\text{H}_{2(g)} + 1/2 \cdot \text{O}_{2(g)} = \text{H}_2\text{O}_{(l)}$	$\Delta H_{22}$	$-285.8 \pm 0.1^{[234]}$
$4 \cdot \text{Th}_{(s)} + 6 \cdot \text{P}_{(s)} + 23/2 \cdot \text{O}_{2(g)} = \alpha\text{-Th}_4(\text{PO}_4)_4\text{P}_2\text{O}_{7(s)}$	$\Delta H_{\text{f}}^{\circ}(\alpha\text{-TPD})$	$-10409.4 \pm 13.3$

<sup>a</sup>Value taken from Table 6.8; <sup>b</sup>Using eqn. 6.13.

### 6.3.7. Computational Studies

#### 6.3.7.1. Thermodynamic functions

The heat capacity,  $C_{p,m}^{\circ}$  and standard enthalpy of formation,  $\Delta H_{f,m}^{\circ}(298.15\text{ K})$  data of  $\beta$ -TPD were used to compute important thermodynamic functions viz. entropy,  $S_m^{\circ}(T)$ ; enthalpy,  $H_m^{\circ}(T)$ ; Gibbs energy function,  $\Phi_m^{\circ}(T)$   $\{\Phi_m^{\circ}(T) = -[G_m^{\circ}(T) - H_m^{\circ}(298.15\text{ K})]/T\}$ ; enthalpy of formation,  $\Delta H_{f,m}^{\circ}(T)$ ; Gibbs energy,  $G_m^{\circ}(T)$  and Gibbs energy of formation,  $\Delta G_{f,m}^{\circ}(T)$ . The thermodynamic relations used for computation of these functions are given in Section 2.5.2 of Chapter 2. The  $S_m^{\circ}(298.15\text{ K})$  of  $\beta$ -TPD has been calculated by assuming  $\Delta S_{\text{oxide}}^{\circ}(298.15\text{ K}) = 20\text{ J}\cdot\text{mol}^{-1}\cdot\text{K}^{-1}$ . The required thermodynamic data for computation were taken from Barin [235]. The calculated thermodynamic functions for  $\beta$ -TPD are given in **Table 6.11**.

**Table 6.11:** Thermodynamic functions for  $\beta$ -Th<sub>4</sub>(PO<sub>4</sub>)<sub>4</sub>P<sub>2</sub>O<sub>7</sub> (TPD).

$T$ (K)	$C_p^{\circ}$ (J·mol <sup>-1</sup> ·K <sup>-1</sup> )	$S_T^{\circ}$ (J·mol <sup>-1</sup> ·K <sup>-1</sup> )	$-H_T^{\circ}$ (kJ·mol <sup>-1</sup> )	$-G_T^{\circ}$ (kJ·mol <sup>-1</sup> )	$-(G_T^{\circ}-H_{298}^{\circ})/T$ (J·mol <sup>-1</sup> ·K <sup>-1</sup> )	$\Delta H_f^{\circ}$ (kJ·mol <sup>-1</sup> )	$\Delta G_f^{\circ}$ (kJ·mol <sup>-1</sup> )
298.15	581.7	624.1	-10565.5	-10751.6	624.1	-10565.5	-10038.4
300	583.5	627.7	-10564.4	-10752.7	624.0	-10565.5	-9907.0
400	645.0	805.2	-10502.6	-10824.7	648.0	-10580.3	-9686.5
500	674.1	952.6	-10436.5	-10912.8	694.6	-10590.1	-9466.4
600	690.5	1,077.1	-10368.2	-11014.5	748.3	-10587.2	-9247.0
700	700.8	1,184.4	-10298.6	-11127.7	803.1	-10598.8	-9028.3
800	707.8	1,278.4	-10228.1	-11250.8	856.7	-10504.6	-8809.9
900	713.0	1,362.1	-10157.1	-11383.0	908.3	-10512.5	-8592.1
1000	717.1	1,437.5	-10085.5	-11523.0	957.5	-10536.2	-8374.3
1100	720.4	1,506.0	-10013.7	-11670.3	1,004.4	-10549.5	-8156.9

#### 6.3.7.2. Phase diagram of Th-P-O system

It has been calculated by minimization of Gibbs energies of all phases present in Th-P-O system. The compounds in Th-O and P-O systems are well characterized as described in Section 2.5.3. of Chapter 2. Th-P system is characterized by four compounds: ThP, Th<sub>3</sub>P<sub>4</sub>, Th<sub>2</sub>P<sub>11</sub> and ThP<sub>7</sub>. Javorsky and Benz [236] reported phase diagram of Th-P up to 60 at. % of

P. ThP is the most stable thorium phosphide which melts congruently at 3263 K and Th<sub>3</sub>P<sub>4</sub> to decompose above 1373 K to ThP. Schnering et al. [237] found Th<sub>2</sub>P<sub>11</sub> to decompose at 740 K to Th<sub>3</sub>P<sub>4</sub> and Schnering and Vu [238] found ThP<sub>7</sub> to decompose to Th<sub>2</sub>P<sub>11</sub> at 650 K. The ternary compounds present in ThO<sub>2</sub>–P<sub>2</sub>O<sub>5</sub> system are controversial. Five ternary compounds: ThP<sub>2</sub>O<sub>7</sub>, ThP<sub>4</sub>O<sub>12</sub>, Th<sub>3</sub>P<sub>2</sub>O<sub>11</sub>, Th<sub>3</sub>P<sub>4</sub>O<sub>16</sub> and Th<sub>4</sub>P<sub>6</sub>O<sub>23</sub> have been reported in this system. Laud and Hummel [239], during the study of ThO<sub>2</sub>–P<sub>2</sub>O<sub>5</sub> system confirmed the existence of ThP<sub>2</sub>O<sub>7</sub>, Th<sub>3</sub>P<sub>2</sub>O<sub>11</sub> and Th<sub>3</sub>P<sub>4</sub>O<sub>16</sub>. Clavier et al. [240] reported that Cubic ThP<sub>2</sub>O<sub>7</sub> was stable up to 1373 K and above 1523 K, it decomposed to stable thorium phosphate-di-phosphate. Clavier et al. [240] and Benard et al. [241] completely re-examined the chemistry of thorium phosphates to resolve ambiguity in this system. Brandel et al. [242] doubted Th<sub>3</sub>P<sub>4</sub>O<sub>16</sub>, synthesized by Bamberger et al. [243]. Authors [239, 244] synthesized the most stable Th<sub>4</sub>(PO<sub>4</sub>)<sub>4</sub>P<sub>2</sub>O<sub>7</sub> by heating the precursors at 1523 K. Keskar et al. [245] could not synthesize Th<sub>3</sub>P<sub>2</sub>O<sub>11</sub> and Th<sub>3</sub>P<sub>4</sub>O<sub>16</sub> by solid state route by heating the reactants in required proportions at 1223 K, but identified both the reaction products as a mixture of β-Th<sub>4</sub>(PO<sub>4</sub>)<sub>4</sub>P<sub>2</sub>O<sub>7</sub> and ThO<sub>2</sub> and included only ThP<sub>2</sub>O<sub>7</sub>, ThP<sub>4</sub>O<sub>12</sub> and Th<sub>4</sub>P<sub>6</sub>O<sub>23</sub> for determination phase diagram of Sr-Th-P-O system. Present study also considers ThP<sub>2</sub>O<sub>7</sub>, ThP<sub>4</sub>O<sub>12</sub> and Th<sub>4</sub>P<sub>6</sub>O<sub>23</sub> as stable ternary compounds in Th-P-O system.

In order to compute the phase diagram of Th-P-O system, Gibbs energy of formation of unary, binary and ternary compounds present in this system are required. The data available for unary and binary compounds in the FactPS database of the FactSage software [221] were taken. However, these data for the ternary compounds are neither available in the FactSage database nor in the thermochemical data by Barin [235].

The thermodynamic functions for Th<sub>4</sub>P<sub>6</sub>O<sub>23</sub>(TPD) has been determined in this study (**Table 6.11**) have been taken for the computation. The Gibbs energy data for ThP<sub>2</sub>O<sub>7</sub>, ThP<sub>4</sub>O<sub>12</sub> along with two binary thorium phosphides: ThP<sub>7</sub> and Th<sub>2</sub>P<sub>11</sub> have been estimated in this study.

Thermodynamic functions of  $\text{Th}_3\text{P}_4$ ,  $\text{ThP}$  and  $\text{Th}$  reported in the FactPS database have been used for the estimation of  $S_m^\circ(298.15 \text{ K})$ ,  $\Delta H_{f,m}^\circ(298.15 \text{ K})$  and  $C_{p,m}^\circ(T)$  of  $\text{ThP}_7$  and  $\text{Th}_2\text{P}_{11}$ .

The heat capacities, enthalpy of formation and entropy at 298.15 K for these compounds have not been reported in the literature and estimated in this study. The entropy of formation of  $\text{AlPO}_4$ ,  $\text{Ca}_3(\text{PO}_4)_2$  and  $\text{Na}_3\text{PO}_4$  from their respective oxides have been calculated using the data reported in the literature [235] and found to be within  $10 \text{ J}\cdot\text{mol}^{-1}\cdot\text{K}^{-1}$ . Hence, for TPD it has been taken to be  $10 \text{ J}\cdot\text{mol}^{-1}\cdot\text{K}^{-1}$ . But while calculating the phase diagram by the minimization of Gibbs energy it has been found TPD is not stable at  $1000^\circ\text{C}$  and simply using  $\Delta S_{\text{oxides}}^\circ(\text{TPD},s,298.15 \text{ K}) = 20 \text{ J}\cdot\text{mol}^{-1}\cdot\text{K}^{-1}$ , TPD became stable with experimentally measured heat capacity and enthalpy of formation. Hence, entropy of formation from the oxide has been taken  $20 \text{ J}\cdot\text{mol}^{-1}\cdot\text{K}^{-1}$  for TPD. However,  $S_m^\circ(298.15 \text{ K})$  of  $\text{ThP}_2\text{O}_7$  and  $\text{ThP}_4\text{O}_{12}$  have been calculated as 189.6 and  $304.0 \text{ J}\cdot\text{mol}^{-1}\cdot\text{K}^{-1}$ , respectively, using  $S_m^\circ(298.15 \text{ K})$  of  $\text{ThO}_2$  and  $\text{P}_2\text{O}_5$  from Barin [235] and  $\Delta S_{\text{oxides}}^\circ(298.15 \text{ K}) = 10 \text{ J}\cdot\text{mol}^{-1}\cdot\text{K}^{-1}$ . The heat capacities for  $\text{ThP}_2\text{O}_7$  and  $\text{ThP}_4\text{O}_{12}$  have been estimated from the measured heat capacity of thermodynamically stable compounds TPD and  $\text{ThO}_2$  from the following reactions:

$$C_{p,m}^\circ(\text{ThP}_2\text{O}_7,s) = (1/3) \cdot [C_{p,m}^\circ(\text{TPD},s) - C_{p,m}^\circ(\text{ThO}_2,s)] \quad (6.15)$$

$$C_{p,m}^\circ(\text{ThP}_4\text{O}_{12},s) = C_{p,m}^\circ(\text{TPD},s) - [C_{p,m}^\circ(\text{ThP}_2\text{O}_7,s) + 2 \cdot C_{p,m}^\circ(\text{ThO}_2,s)] \quad (6.16)$$

The enthalpy of formation of  $\text{ThP}_2\text{O}_7$  has been calculated by adding enthalpy of formations of  $\text{Th}^{4+}$  and  $\text{P}_2\text{O}_7^{4-}$ . Then plotting enthalpy of formation of  $\text{ThP}_2\text{O}_7$  and TPD from oxide as a function of molecular weight of compounds with a constraint  $\Delta H_{\text{ox},m}^\circ(298.15 \text{ K}) = 0$  at  $M_{\text{wt.}} = 0$  and observed a straight line. From the slope and intercept of the line the enthalpy of formation of  $\text{ThP}_4\text{O}_{12}$  has been estimated. To make these compounds stable at room temperature its enthalpies were negligibly adjusted to  $-3080.9$  and  $-4660.5 \text{ kJ}\cdot\text{mol}^{-1}$ , respectively and these calculated enthalpy values have been taken for the phase diagram calculations.

The calculated enthalpy of formation of thorium phosphates are given in **Table 6.12**. The calculated Gibbs energy of formation,  $\Delta G_{f,m}^{\circ}$  values for  $\text{ThP}_2\text{O}_7$ ,  $\text{ThP}_4\text{O}_{12}$  and TPD are given below:

$$\Delta G_{f,m}^{\circ}(\text{ThP}_2\text{O}_7, s, T) \text{ kJ}\cdot\text{mol}^{-1} = -3069.2 + 0.6611\cdot(T/K) \quad (6.17)$$

$$\Delta G_{f,m}^{\circ}(\text{ThP}_4\text{O}_{12}, s, T) \text{ kJ}\cdot\text{mol}^{-1} = -4651.7 + 1.0937\cdot(T/K) \quad (6.18)$$

$$\Delta G_{f,m}^{\circ}(\text{TPD}, s, T) \text{ kJ}\cdot\text{mol}^{-1} = -10560.8 + 2.1871\cdot(T/K) \quad (6.19)$$

**Table 6.12:** Constants of the fitted equations for enthalpy increment and heat capacity data of compounds in binary Th-P system, ternary Th-P-O system and quaternary Th-P-O-H system. The enthalpy of formation and entropy at 298.15 K are also included.

Compounds	$\Delta H_{f,m}^{\circ}$ (298.15 K) /kJ·mol <sup>-1</sup>	$S_m^{\circ}$ (298.15 K) /J·mol <sup>-1</sup> ·K <sup>-1</sup>	$C_{p,m}^{\circ}(T) / \text{J}\cdot\text{mol}^{-1}\cdot\text{K}^{-1}$			$\Delta G_{f,m}^{\circ}(T) / \text{kJ}\cdot\text{mol}^{-1}$	
			$= a + b\cdot(T/K) + c\cdot(K/T)^2$	$= a + b\cdot(T/K) + c\cdot(K/T)^2$	$= a + b\cdot(T/K) + c\cdot(K/T)^2$	$= A + B\cdot(K/T)$	$= A + B\cdot(K/T)$
			a	b·10 <sup>3</sup>	- c·10 <sup>-6</sup>	A	B
$\beta$ -TPD(s) <sup>a</sup>	-10565.5	624.1	718.17	11.35	12.43	-10560.8	2.1871
$\alpha$ -TPD(s)	-10409.4	604.1	574.05	40.01	8.483	-10315.4	3.3160
$\text{Th}_2\text{P}_3\text{O}_{12}\text{H}(s)$	-5423.6	337.0	371.32	35.83	6.946	-5353.0	1.1046
$\text{Th}_2\text{P}_3\text{O}_{13}\text{H}_3(s)$	-5754.2	407.0	426.93	494.86	17.248	-5680.0	1.2578
$\text{ThP}_2\text{O}_7(s)$	-3070.9	189.6	216.29	6.70	3.84	-3069.2	0.6611
$\text{ThP}_4\text{O}_{12}(s)$	-4660.5	304.0	303.47	80.436	3.01	-4651.7	1.0937
$\text{Th}_2\text{P}_{11}(s)$	-1375.9	105.9	298.9	84.705	7.87	-1185.1	0.2568
$\text{ThP}_7(s)$	-720.6	91.9	198.6	1.162	4.96	-604.2	0.1376

<sup>a</sup>TPD =  $\text{Th}_4(\text{PO}_4)_4\text{P}_2\text{O}_7$ .

The Gibbs energy values of unary and binary compounds from FactPS database [221], ternary compounds from equations (6.17-6.19) were used for the computation of the phase diagram of Th-P-O system using FactSage software [221] at 600 K and 1 bar and is shown in **Fig. 6.9**.

It shows that TPD co-exists with  $\{\text{ThO}_2 + \text{O}_2(g)\}$  as well as with  $\{\text{ThO}_2 + \text{P}(l)\}$ . P-O system has two stable phases:  $(\text{P}_2\text{O}_3)_2(g)$  and  $(\text{P}_2\text{O}_5)_2$  at 600 K. Binary phase:  $\text{Th}_3\text{P}_4$  and  $\text{ThP}$  co-exist with  $\text{ThO}_2$  but not with TPD at 1 bar.  $\text{Th}_2\text{P}_{11}$  and  $\text{ThP}_7$  are not stable.

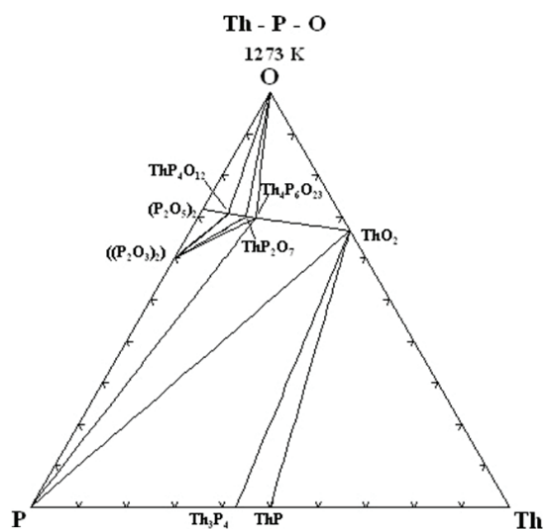


Fig. 6.9: Phase diagram of Th-P-O system.

### 6.3.7.3. Chemical potential diagram of Th-P-O system

The predominance area diagram is an important thermodynamic diagram since it gives the stability of the various phases as a function of chemical potentials of the components [246, 247]. The stability domain of each stoichiometric phase is defined by an area. Lines, between two single phases represent two-phase equilibria. Points denote three-phase equilibria.

Fig. 6.10 shows the predominance diagram of Th-P-O system at 1273 K.

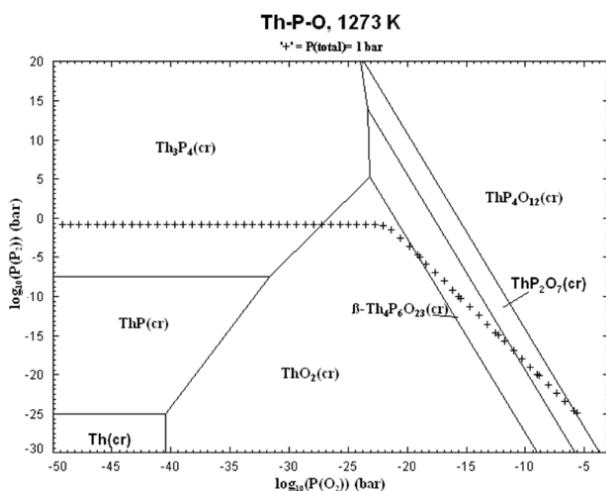
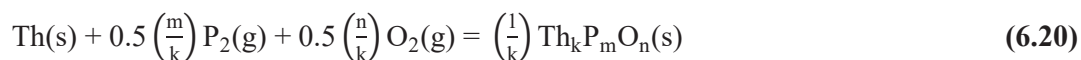


Fig. 6.10: The predominance diagram of Th-P-O system at 1273 K.

The various phases of this system have been plotted as a function of  $\log(p(\text{P}_2))$  along y-axis and  $\log(p(\text{O}_2))$  along x-axis. The basic computational procedure for the construction of a predominance diagram is based on the minimization of Gibbs energy method. It is assumed that ternary compounds are formed from the reaction of one mole of Th; hence it is not used as an axis variable. The formation of a typical ternary compound  $\text{Th}_k\text{P}_m\text{O}_n$  can be written as:



$$\Delta G(\text{Th}_k\text{P}_m\text{O}_n) = \Delta G^\circ(\text{Th}_k\text{P}_m\text{O}_n) + \left(\frac{RT}{k}\right) \ln \left\{ \frac{a(\text{Th}_k\text{P}_m\text{O}_n)}{a(\text{Th})^k p(\text{P}_2)^{0.5m} p(\text{O}_2)^{0.5n}} \right\} \quad (6.21)$$

where 'a' is the activity. Similarly, the Gibbs energy of each compound in Th-P-O system can be written using eqn. (6.21). The determination of a stable species for a given chemical potential is considerably tedious and complicated. FactSage software was used for these calculations. It generates an isothermal predominance area diagram that shows which possible compound phases are most stable over the specified ranges of the axes potentials. At any point on the diagram (**Fig. 6.10**) the chemical potential of elemental species  $\text{P}_2(\text{g})$  or  $\text{O}_2(\text{g})$  can be determined from the y- and x-coordinates. Required data for computation were taken from FactPS database of the programme and data given in **Table 6.12**. One of the advantage of FactSage software calculations is that one can produce diagrams for different combinations of axis (partial pressures of polymer species like  $\text{P}_4$ ,  $(\text{P}_2\text{O}_5)_2$ ,  $(\text{P}_2\text{O}_3)_2$ ..etc.), which can be related to the Gibbs phase diagram. The invariant point (three phase field) is independent of the choice of species ( $\text{P}_2/\text{O}_2$ ) for the axis. The '+' line on **Fig. 6.10** corresponds to reaction pathway at the  $P_{(\text{total})} = 1$  bar. Hence, along this line the sum of the partial pressures of all the gaseous species,  $p(\text{O}) + p(\text{O}_2) + p(\text{O}_3) + p(\text{P}) + p(\text{P}_2) + \dots p(\text{P}_4) + p((\text{P}_2\text{O}_3)_2) + p((\text{P}_2\text{O}_5)_2) + \dots$ , is 1 bar. In

**Fig. 6.10**,  $P_{(\text{total})} > 1$  bar above the '+' line, and  $P_{(\text{total})} < 1$  bar below the line. This figure shows that  $P_2(\text{g})$  is the predominant gaseous species over thorium phosphides, but its pressure decreases sharply over thorium phosphates. The partial pressure of oxygen containing species  $(P_2O_3)_2$  and  $(P_2O_5)_2$  are higher over thorium phosphates. The calculated invariant points of Th-P-O predominant diagram are given in **Table 6.13** along with the chemical potentials of  $P_2(\text{g})$  and  $O_2(\text{g})$ .

**Table 6.13:** The chemical potentials of phosphorus and oxygen at invariant points.

Phases at Invariant points	$\Delta\mu(P_2)^a$ /kJ·mol <sup>-1</sup>	$\Delta\mu(O_2)^a$ /kJ·mol <sup>-1</sup>
ThP <sub>4</sub> O <sub>12</sub> (s) + ThP <sub>2</sub> O <sub>7</sub> (s) + Th <sub>3</sub> P <sub>4</sub> (s)	507.6	-587.2
TPD(s) + ThP <sub>2</sub> O <sub>7</sub> (s) + Th <sub>3</sub> P <sub>4</sub> (s)	338.1	-571.1
TPD(s) + ThO <sub>2</sub> (s) + Th <sub>3</sub> P <sub>4</sub> (s)	128.5	-565.0
Th(s) + ThO <sub>2</sub> (s) + ThP(s)	-612.6	-987.5
ThO <sub>2</sub> (s) + ThP(s) + Th <sub>3</sub> P <sub>4</sub> (s)	-183.1	-772.7

<sup>a</sup>1273 K.

#### 6.3.7.4. E<sub>H</sub>-pH diagram for Th-P-H<sub>2</sub>O system

An E<sub>H</sub>-pH diagram depicts the dominant aqueous species and stable solid phases on a plane defined by the E<sub>H</sub> and pH axes. The vertical axis labeled with E<sub>H</sub> is the voltage potential of the species at room temperature calculated by the Nernst equation with respect to the standard hydrogen electrode (SHE). The thermodynamic data of the species can be related to standard electrode potential by relation:

$$E^\circ = \frac{\Delta G^\circ(298.15 \text{ K})}{nF} \quad (6.22)$$

where  $E^\circ$  is the standard electrode potential,  $\Delta G^\circ$  is the change in Gibbs energy when the half-cell reaction occurs under conditions in which the reaction of products is in their standard states,  $n$  is the number of moles of electron transferred in the half cell reaction.  $F$  is Faradays constant.

$E_H$ -pH diagram, maps out possible stable equilibrium phases of an aqueous electrochemical system. Hence, for Th-P-H<sub>2</sub>O,  $E_H$ -pH diagram of water should be taken along with that of Th-P-H-O system. Aqueous solutions exist only under conditions where water is not reduced to H<sub>2</sub>(g) or oxidized to O<sub>2</sub>(g). H<sub>2</sub>O can decompose into O<sub>2</sub>(g) and H<sub>2</sub>(g) according to following reactions:



The equilibrium potential of these reactions is calculated assuming the partial pressure of O<sub>2</sub>(g) and H<sub>2</sub>(g) to be 101.325 kPa using Nernst relation:

$$E/N (\text{H}^+/\text{H}_2) = 0.059 \cdot \text{pH} \quad (6.25)$$

$$E/N (\text{O}_2/\text{H}_2\text{O}) = 1.23 - 0.059 \cdot \text{pH} \quad (6.26)$$

Equations (6.25) and (6.26) set the theoretical stability region of water and species present inside this region are important. The strong oxidizing species are present at the top of the diagram and reducing species are found at the bottom of a diagram. Normally three types of reactions are considered in  $E_H$ -pH diagram: (i) electrochemical reactions of pure charge transfer (vertical line, independent of pH), (ii) electrochemical reactions involving electron and pH (sloping line), (iii) pure acid base reactions (horizontal line, reaction without electron transfer). The detailed method of construction of  $E_H$ -pH diagram is well explained in the literature [248-250].

The calculated  $E_H$ -pH diagram for Th-P-H<sub>2</sub>O system is given in **Fig. 6.11**. The phase equilibria involving different species in Th-P-O-H system have been calculated by the minimization of Gibbs energy method. The Gibbs energy of formation of Th<sub>2</sub>P<sub>3</sub>H<sub>3</sub>O<sub>13</sub>, Th<sub>2</sub>P<sub>3</sub>HO<sub>12</sub>, Th<sub>4</sub>P<sub>6</sub>H<sub>4</sub>O<sub>25</sub> have been calculated from solution calorimetric data using different thermo-chemical cycles. The Gibbs energy of these species, binary and pure phase from FactPS database and that for ternary thorium phosphates reported in **Table 6.12** have been used for computation. However, enthalpy of formation of quaternary compounds: Th(H<sub>2</sub>PO<sub>2</sub>)<sub>4</sub>, ThPO<sub>4</sub>·H<sub>2</sub>O, Th<sub>2</sub>H(PO<sub>4</sub>)<sub>3</sub>·H<sub>2</sub>O, Th(OH)·H<sub>2</sub>O, Th(HPO<sub>4</sub>)<sub>2</sub>·H<sub>2</sub>O, Th<sub>2</sub>(PO<sub>4</sub>)<sub>3</sub>·H<sub>2</sub>O, Th<sub>4</sub>(PO<sub>4</sub>)<sub>4</sub>(P<sub>2</sub>O<sub>7</sub>)·(H<sub>2</sub>O)<sub>2</sub> and H<sub>2</sub>Th(PO<sub>4</sub>)<sub>2</sub>·H<sub>2</sub>O of Th-P-H-O system have not been considered due to unavailability of thermodynamic data in the literature. The molar activity of dissolved species in the aqueous solution has been taken as 10<sup>-6</sup>.

The area under the continuous upper diagonal boundaries line(slope) from left to right and the continuous lower diagonal boundaries line from left to right on the **Fig. 6.11** is important to understand the release of actinides (Th<sup>4+</sup> and other radionuclides) from the repository to ground water. It shows that the Th<sup>4+</sup> is stable in high acidic condition and PO<sub>4</sub><sup>3-</sup> at high pH values.

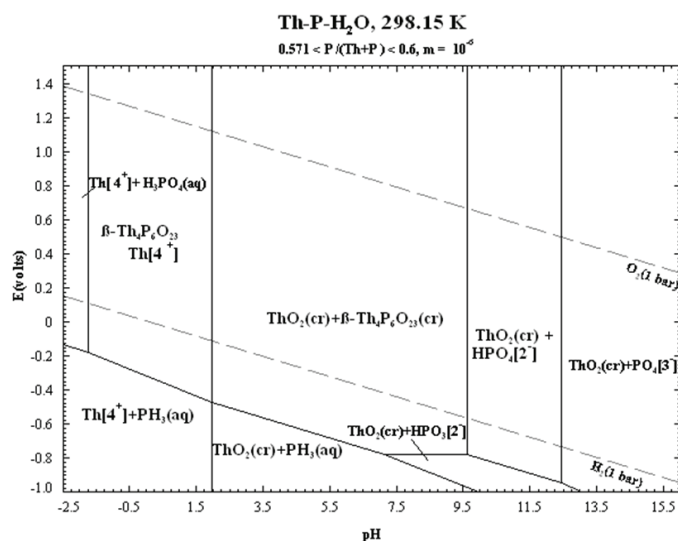


**Fig. 6.11:**  $E_H$ -pH diagram for Th-P-H<sub>2</sub>O system.

$\beta$ -TPD is stable in ground water in the pH range 2-9. It does not undergo any oxidation reduction reaction in this pH range. The thermodynamically most stable species are shown on the diagram and line represents co-existing phases.

## 6.4. CONCLUSIONS

The proposed  $\beta$ -Th<sub>4</sub>(PO<sub>4</sub>)<sub>4</sub>P<sub>2</sub>O<sub>7</sub> ( $\beta$ -TPD) as a candidate for waste immobilization matrix has been synthesized by solution chemistry method and characterized by TG-DTA, XRD and FT-IR spectroscopy. The heat capacity ( $C_p^0$ ) and enthalpy of formation ( $\Delta H_{f,m}^0$ ) of Th<sub>2</sub>(PO<sub>4</sub>)<sub>2</sub>(HPO<sub>4</sub>).H<sub>2</sub>O (TPHPH), Th<sub>2</sub>(PO<sub>4</sub>)<sub>2</sub>(HPO<sub>4</sub>) (TPHP) and  $\alpha$ -Th<sub>4</sub>(PO<sub>4</sub>)<sub>4</sub>P<sub>2</sub>O<sub>7</sub> ( $\alpha$ -TPD) have been measured to determine the enthalpy of formation of  $\beta$ -Th<sub>4</sub>(PO<sub>4</sub>)<sub>4</sub>P<sub>2</sub>O<sub>7</sub> ( $\beta$ -TPD) using solution calorimeter at 298 K. The molar heat capacity and enthalpy of formation of  $\beta$ -TPD were measured for the first time. Deviation in the heat capacity values of  $\beta$ -TPD from Neumann-Kopp rule is attributed to the difference in co-ordination number of the metal cations in the constituent oxides compared to that in  $\beta$ -TPD. The heat capacity ( $C_p^0$ ), enthalpy of formation ( $\Delta H_{f,m}^0$ ) at 298 K along with required literature data were used to determine Gibbs energy data of formation and thermodynamic functions of  $\beta$ -TPD. These data of  $\beta$ -TPD were used for the estimation of two binary and five ternary compounds of Th-P-O system, whose data were not reported in the literature.

The phase diagram and E<sub>H</sub>-pH diagrams have been calculated based on Gibbs energy data of all phases in Th-P-O system. The co-existence of different phases in the Th-P-O system can be calculated from Gibbs phase diagram. The oxygen and phosphorous potential required for stable  $\beta$ -Th<sub>4</sub>(PO<sub>4</sub>)<sub>4</sub>P<sub>2</sub>O<sub>7</sub> can be determined from the Th-P-O predominance diagram. The computed E<sub>H</sub>-pH diagram revealed that  $\beta$ -TPD to be stable in the ground water in the pH range 2-9. This diagram has also showed, ThO<sub>2</sub> to be stable at higher pH and Th<sup>4+</sup> ion to be at lower pH.

# ***CHAPTER-7***

---

## ***SUMMARY, CONCLUSIONS AND FUTURE DIRECTIONS***

This chapter presents a brief summary and conclusions of the work described in Chapters 3-6. The chapter also define some future extensions of the present studies. The thesis has aimed at the investigations of suitable alternate matrix for the immobilization of long-lived actinides present in HLW. The proposed matrix should have high radiation and chemical durability properties. Based on the literature survey, naturally occurring monazite minerals have displayed radiation resistance and chemical durability properties for billions of years. Thus, phosphate-based crystalline ceramic compounds have been proposed as a host matrix for disposal of long-lived actinides.

The present study is focused on the investigations of synthetic monazites  $REPO_4$  ( $RE = La, Nd, Sm$  and  $Gd$ ), monazite-cheralite solid solutions  $(La_{1-x}M_{x/2}Th_{x/2})PO_4$  ( $0 \leq x \leq 1$ ) ( $M = Ca, Sr$  and  $Ba$ ) and thorium phosphate-diphosphate ( $Th_4(PO_4)_4P_2O_7$ , TPD). As thermodynamic properties are one of the primary requirements for selection of any material. The present thesis deals with the synthesis, characterization, determination and interpretation of the thermodynamic properties of aforesaid phosphate-based ceramic matrices. Standard molar enthalpies of formation were measured to determine their thermodynamic stabilities. Based on the thermodynamic stability of monazite-cheralite solid solution, the most stable composition suitable for disposal of fission products ( $Sr^{2+}$ ) and long-lived minor actinides ( $Np^{4+}$ ,  $Am^{3+}$ ,  $Cm^{3+}$ ) was identified. To determine the behavior in the geological conditions, aqueous leaching studies were also carried out for monazite-cheralite solid solution.

The thesis work is broadly divided into four parts. The first part deals with the investigation of thermodynamic stabilities of synthetic monazite phases i.e.  $REPO_4$  ( $RE = La, Nd, Sm$  and  $Gd$ ). These phases were synthesized using solution route and characterized using thermogravimetric and X-ray diffraction techniques. An isoperibol solution calorimeter has been used to determine the enthalpy of formation of synthetic monazites phases i.e.  $LaPO_4$ ,  $NdPO_4$ ,  $SmPO_4$ ,  $GdPO_4$  and their hydrated rhabdophane phases i.e.  $LaPO_4 \cdot 0.8H_2O$ ,

NdPO<sub>4</sub>·0.75H<sub>2</sub>O, SmPO<sub>4</sub>·0.65H<sub>2</sub>O and GdPO<sub>4</sub>·0.55H<sub>2</sub>O. Their thermodynamic stabilities were considered to identify a suitable host matrix.

The second part of the thesis deals with the synthesis and characterization of charge coupled substituted monazite-cheralite solid solution viz. (La<sub>1-x</sub>M<sub>x/2</sub>Th<sub>x/2</sub>)PO<sub>4</sub> ( $0 \leq x \leq 1$ ) ( $M = \text{Ca, Sr and Ba}$ ). Samples are prepared using solid-state method and characterized using different techniques. The results suggested that a homogeneous solid solution is formed with (Ca<sup>2+</sup>, Th<sup>4+</sup>) and (Sr<sup>2+</sup>, Th<sup>4+</sup>) coupled substitution, whereas 15 % solid solubility is found for (Ba<sup>2+</sup>, Th<sup>4+</sup>) coupled substitution in LaPO<sub>4</sub>. The heat capacities of the samples were measured and the observed deviation from Neumann-Kopp rule could be attributed to the dissimilarity in co-ordination number of the metal cations. Standard molar enthalpy of formation of solid-solutions are measured and important thermodynamic functions have been generated. The calculated Gibbs energy data indicates that the stability of substituted LaPO<sub>4</sub> is mainly enthalpy driven. The excess enthalpy of mixing data is calculated and the corresponding enthalpy minima provided the information about the most stable thermodynamic composition for immobilization of different ions.

In the third part, leaching studies of the selected compositions of charge couple substituted monazite-cheralite solid-solutions, (La<sub>1-x</sub>M<sub>x/2</sub>Th<sub>x/2</sub>)PO<sub>4</sub> ( $0 \leq x \leq 1$ ) ( $M = \text{Ca, Sr and Ba}$ ) are carried out using standard Product Consistency Test (PCT), approved by the American Society of Testing Materials (ASTM). All the samples were kept inside Teflon lined stainless-steel vessels with 10 ml of demineralized water as leachant at 363 K for a period of 7 days. The elemental analysis of the leachant solution was carried out using ICP-AES technique and normalized leach rate for the leached ions was determined.

The fourth part deals with the investigation of thermodynamic properties of β-Th<sub>4</sub>(PO<sub>4</sub>)<sub>4</sub>P<sub>2</sub>O<sub>7</sub> (β-TPD) as well as phase investigations in Th-P-O and Th-P-H<sub>2</sub>O system. The compound was prepared with solution route and characterized using different techniques.

The heat capacity and the standard enthalpy of formation of  $\beta$ -TPD and other relevant phases viz.  $\text{Th}_2(\text{PO}_4)_2(\text{HPO}_4)\cdot\text{H}_2\text{O}$  (TPHPH),  $\text{Th}_2(\text{PO}_4)_2(\text{HPO}_4)$  (TPHP) and  $\alpha\text{-Th}_4(\text{PO}_4)_4\text{P}_2\text{O}_7$  ( $\alpha$ -TPD) have been measured. The thermodynamic functions for  $\beta$ -TPD have been computed using  $\Delta H_f^\circ(298.15\text{ K})$ ,  $C_{p,m}^\circ(T)$  and other auxiliary data from the literature. The Gibbs phase diagram and predominant area diagram for Th-P-O system have been computed. The level of oxygen and phosphorous potential required to stabilize  $\beta$ -TPD have been determined from the predominance diagram.  $E_{\text{H}}\text{-pH}$  diagram of Th-P-H<sub>2</sub>O system was computed to determine the stability of  $\beta$ -TPD and other aqueous phases in groundwater.

The experimental and computational results of the thesis is immensely helpful in selection of suitable phosphate-based matrices for disposal of long-lived radionuclides and contribute to the thermodynamic database for phosphate-based materials. The thesis concludes:

- *The enthalpy of formation of rare earth orthophosphate,  $\text{REPO}_4$  ( $\text{RE} = \text{La, Nd, Sm and Gd}$ ) have been measured and based on the thermodynamic stability data, the most stable host matrix has been identified. The standard molar enthalpy of formation ( $\Delta H_{f,ox}^\circ$ ) of ( $\text{LaPO}_4$ ,  $s$ ,  $298\text{ K}$ ) is found to be most negative and thermodynamically most stable amongst the orthophosphate and could be considered as a host matrix for immobilization of long-lived radionuclides.*
- *The standard molar enthalpy of formation of monazite-cheralite solid solutions,  $(\text{La}_{1-x}\text{M}_{x/2}\text{Th}_{x/2})\text{PO}_4$  ( $0 \leq x \leq 1$ ) ( $\text{M} = \text{Ca, Sr and Ba}$ ) and thorium phosphate diphosphate ( $\text{Th}_4(\text{PO}_4)_4\text{P}_2\text{O}_7$ , TPD) have been determined for the first time.*
- *Monazite-cheralite solid solutions are found to be thermodynamically more stable than their corresponding end-members viz.  $\text{LaPO}_4$  and  $(\text{M}_{0.5}\text{Th}_{0.5})\text{PO}_4$  ( $\text{M} = \text{Ca, Sr and Ba}$ ). The highest thermodynamically stable composition for the solid solutions are found to be at  $x = 0.25$  for  $(\text{La}_{1-x}\text{Ca}_{x/2}\text{Th}_{x/2})\text{PO}_4$ ,  $x = 0.3$  for  $(\text{La}_{1-x}\text{Sr}_{x/2}\text{Th}_{x/2})\text{PO}_4$  and  $x = 0.2$  for  $(\text{La}_{1-x}\text{Ba}_{x/2}\text{Th}_{x/2})\text{PO}_4$ .*

- *The heat capacities of  $(La_{1-x}M_{x/2}Th_{x/2})PO_4$  ( $0 \leq x \leq 1$ ) ( $M = Ca, Sr$  and  $Ba$ ) solid solutions and  $\alpha-Th_4(PO_4)_4P_2O_7$  were determined for the first time. The experimental data for the intermediate compositions of these solid solutions suggest that the heat capacity is not compositionally weighted heat capacities of the constituent oxides.*
- *The leaching studies were carried out to demonstrate the chemical durability of  $(La_{1-x}M_{x/2}Th_{x/2})PO_4$  ( $0 \leq x \leq 1$ ) ( $M = Ca, Sr$  and  $Ba$ ) solid solutions under geological conditions. The normalized leach rate value for substituted elements in the solid solutions is below  $10^{-10} \text{ g.cm}^{-2}.\text{d}^{-1}$ , which is lower compared to the leaching rate in borosilicate glass. The leaching studies results corroborate the results of thermodynamic stability of substituted solid solutions.*
- *The study purposes  $(La_{0.7}Sr_{0.15}Th_{0.15})PO_4$  as the most suitable composition for immobilization of divalent fission product ( $Sr^{2+}$ ), trivalent actinides ( $Am^{3+}, Cm^{3+}$ ) and tetravalent actinides ( $Pu^{4+}, Np^{4+}$ ). Moreover, trivalent lanthanides ( $Gd^{3+}$ ) can be incorporated at La-site as neutron poisons to reduce criticality risks at higher waste loadings.*
- *The thermodynamic investigations of thorium phosphate-diphosphate (TPD) and other related precursor phases used to determine Gibbs phase diagram, chemical potential diagram for Th-P-O system and  $E_H$ -pH diagram for Th-P- $H_2O$  system.*

The results of the present thesis substantiates the potential of using phosphate-based crystalline ceramic matrices viz. synthetic monazite  $REPO_4$  ( $RE = La, Nd, Sm$  and  $Gd$ ), monazite-cheralite solid solutions  $(La_{1-x}M_{x/2}Th_{x/2})PO_4$  ( $0 \leq x \leq 1$ ) ( $M = Ca, Sr$  and  $Ba$ ) and thorium phosphate diphosphate ( $Th_4(PO_4)_4P_2O_7$ , TPD), as nuclear waste forms for the immobilization of long-lived trivalent and tetravalent actinides and fission product present in the HLW.

## Future scope

The present investigation indicates that the charge couple involving  $(\text{Ca}^{2+}, \text{Th}^{4+})$ ,  $(\text{Sr}^{2+}, \text{Th}^{4+})$  and  $(\text{Ba}^{2+}, \text{Th}^{4+})$  could be substituted in synthetic monazite and leads to the formation of thermodynamically stable products having good chemical durability. Thermodynamic measurements similar to the present work yield useful database of waste matrices for immobilization of radionuclides. The future extension of the work can be briefly described as:

- *Thermodynamic investigations of  $\text{La}_2\text{O}_3\text{-SrO-NpO}_2\text{-P}_2\text{O}_5$ ,  $\text{La}_2\text{O}_3\text{-SrO-AmO}_2\text{-P}_2\text{O}_5$  and  $\text{Cm}_2\text{O}_3\text{-SrO-NpO}_2\text{-P}_2\text{O}_5$  systems can be carried out by studying compounds involving their surrogate elements.*
- *Chemical durability studies of aforementioned systems as a function of time and temperature with varying pH of the system.*
- *Irradiation studies on monazite-cheralite solid solutions  $(\text{La}_{1-x}\text{Sr}_{x/2}\text{Th}_{x/2})\text{PO}_4$  ( $0 \leq x \leq 1$ ).*

The consolidated results will provide a possible solution for disposal of long-lived radioactive waste in a stable matrix like monazite-cheralite solid solution.

**REFERENCES:**

- [1] R.L. Orbach, *The Achilles Heel of Nuclear Energy, Disposal of Spent Fuel*, The Energy Institute, The University of Texas at Austin, November 23, 2009.
- [2] *The Principles of radioactive waste management, safety Fundamentals*, Safety Series No. 111-F, IAEA, Vienna 1995.
- [3] <https://www.iaea.org/geco/> Global Energy and CO<sub>2</sub> Status Report – March 2019.
- [4] <http://www.world-nuclear.org>
- [5] IAEA *Climate Change and Nuclear Power*, 2018.
- [6] M.I. Ojovan, W.E. Lee, “*An Introduction to Nuclear Waste Immobilisation*” (Second Edition), Elsevier (2014) ISBN-9780080993928.
- [7] <http://www.world-nuclear.org/information-library/facts-and-figures/reactor-database.aspx>
- [8] <http://www.barc.gov.in>
- [9] K.R. Rao, *Curr. Sci.*, **81** (2001) 1534.
- [10] I. Johnson, *J. Nucl. Mater.*, **154** (1988) 169.
- [11] D. Caurant, P. Loiseau, O. Majerus, V. Aubin-Chevaldonnet, I. Bardez and A. Quintas, “*Glasses, Glass-ceramics and ceramics for immobilization of highly radioactive nuclear wastes*”, Nova Science Publishers, Inc., New York, 2009.
- [12] P.K. Wattal, *Progress in Nuclear Energy*, **101** (2017) 133-145.
- [13] B.L. Cohen, *Rev. Mod. Phys.*, **49** (1977) 1-20.
- [14] B.E. Burakov, M.I. Ojovan, W.E. Lee, “*Crystalline Materials for Actinide Immobilisation*”, **Vol. 1**. (2010) <https://doi.org/10.1142/p652>.
- [15] P. Sengupta, C.P. Kaushik, G.K. Dey, “*Immobilization of High Level Nuclear Wastes: The Indian Scenario*”. Ramkumar M. (Ed.), Springer Earth System Sciences (2013) ISBN: 978-3-642-32917-3.
- [16] D.E. Day, Z. Wu, C.S. Ray, and P. Hrma, *J. Non-Cryst. Solids*, **241** (1998) 1-2.

- [17] A.E. Ringwood and P.M. Kelly, *Philos. Trans. R. Soc. London*, **319** (1986) 63-82.
- [18] A. Breithaupt, “*Neue krystallographische Bestimmung und mineralogische Charakteristik verschiedener Mineralspecien*”, *Journal für Chemie und Physik*, D. F. W. Schweigger-Seidel (Ed.) (1829) 296-306.
- [19] L.A. Boatner and B.C. Sales, “*Monazite, in Radioactive waste forms for the future*”, (Eds.) W. Lutze and R.C. Ewing, Elsevier Science Publishers (1988) 495-564.
- [20] L.A. Marinova and V.N. Yaglov, *Russ. J. Phys. Chem*, **50** (1976) 477-478.
- [21] Z.S. Cetiner, S.A. Wood and C.H. Gammons, *Chem. Geol*, **217** (2005) 147–169.
- [22] C.M. Gramaccioli, T.V. Segalstad, *Am Mineral*, **63** (1978) 757–761.
- [23] W.C. Overstreet. The geological occurrence of monazite, *US Geol Surv Professional Paper 539*, pp. 327.
- [24] J.M. Pyle, F.S. Spear, R.L. Rudnick, W.F. McDonough. *J Petrol*, **42**(11) (2001) 2083–2107.
- [25] G. Balachandran, *Treatise Process Metall.*, 3 (2014) 1291-1340.
- [26] E.H. Oelkers, J.M. Montel, *Elements*, **4**(2) (2008) 113-116.
- [27] O.H. Leonardos Jr., *Econ. Geol*, **69** (1974) 1126-1128.
- [28] L.A. Boatner, G.W. Beall, M.M. Abraham, C.B. Finch. P.G. Huray and M. Rappaz, “*Monazite and other lanthanide orthophosphates as alternate waste forms*”, in *Scientific basis for nuclear waste management*, **Vol. 2**, (Eds.) C.J.M. Northrup Jr, Plenum Press, Boston (1979) 289-96.
- [29] G.J. McCarthy, W.B. White and D.E. Pfoertsch, *Mater. Res. Bull*, **13** (1978) 1239-1245.
- [30] Y. Ni, J.M. Hugues, A.N. Mariano, *Am Mineral*, **80** (1995) 21-26.
- [31] G.W. Beall, L.A. Boatner, D.F. Mullica, W.O. Milligan, *J Inorg Nucl Chem*, **43** (1981) 101–105.
- [32] D.F. Mullica, W.O. Milligan, D.A. Grossie, G.W. Beall, L.A. Boatner, *Inorg Chim Acta*,

- 95 (1984) 231-236.
- [33] D.F. Mullica, D.A. Grossie, L.A. Boatner, *Inorg Chim Acta*, **109** (1985) 105-110.
- [34] L.A. Boater, G.W. Beall, M.M. Abraham, C.B. Finch, P.G. Huray, M. Rappaz, *Scientific basis for nuclear waste Management*, **2** (1980) 289-296.
- [35] K. Byrappa, *Prog. Cryst. Growth*, **13** (1986) 163-196.
- [36] D. Bregiroux, F. Audubert, T. Charpentier, D. Sakellariou, D. Bernache-Assollant, *Solid State Sci.*, **9** (2007) 432-439.
- [37] O. Terra, N. Clavier, N. Dacheux, R. Podor, *New J. Chem.*, **27** (2003) 957-967.
- [38] E.E. Boakye, P. Mogilevsky, *J. Am. Ceram. Soc.*, **88** (2005) 2740-2746.
- [39] S. Lucas, E. Champion, D. Bregiroux, D. Bernache-Assollant, F. Audubert, *J. Solid State Chem.*, **177** (2004) 1302-1311.
- [40] H. Meyssamy, K. Riwozki, A. Kornovski, S. Naused, M. Hause, *Adv. Mater.*, **11** (1999) 840-844.
- [41] D.F. Mullica, David A. Grossie, L.A. Boatner, *J. Solid State Chem.*, **58**(1) (1985) 71-77.
- [42] C. Thiriet, R.J.M. Konings, P. Javorský, N. Magnani, F. Wastin, *J. Chem. Thermodyn.*, **37** (2) (2005) 131-139.
- [43] K. Horchani-Naifer, M. Férid, *Inorganica Chim, Acta*, **362** (6) (2009) 1793-1796.
- [44] R. Jardin, C.C. Pavel, P.E. Raison, D. Bouëxière, H. Santa-Cruz, R.J.M. Konings, K. Popa, *J Nucl. Mater.*, **378** (2008) 167-171.
- [45] K. Popa, R.J.M. Konings, *Thermochim. Acta*, **445** (2006) 49-52.
- [46] S. Ushakov, K. Helean, A. Navrotsky, L.J. Boatner, *Mater. Res.*, **16** (2001) 2623-2633.
- [47] K. Popa, D. Sedmidubský, O. Beneš, C. Thiriet, R.J.M. Konings, *J. Chem. Thermodyn.*, **38** (2006) 825-829.
- [48] K. Popa, F. Jutier, F. Wastin, R.J.M. Konings, *J. Chem. Thermodyn.*, **38** (2006) 1306-1311.

- [49] K.S. Gavrichev, V.M. Gurevich, M.A. Ryumin, A.V. Tyrin, L.N. Komissarova, *Geochem. Int.*, **54** (2016) 362-368.
- [50] A. Blanca-Romero, P.M. Kowalski, G. Beridze, H. Schlenz, D. Bosbach, *J. Comput. Chem.*, **35** (2014) 1339-1346.
- [51] J.R. Rustad, *Am. Mineral.*, **97** (2012) 791-799.
- [52] K. Popa, R.J.M. Konings, T. Geisler, *J. Chem. Thermodyn.*, **39** (2007) 236–239.
- [53] R.J.M. Konings, M. Walter, K. Popa, *J. Chem. Thermodyn.*, **40** (2008) 1305-1308.
- [54] S. Neumeier, P. Kegler, Y. Arinicheva et al., *J. Chem. Thermodyn.*, **105** (2017) 396–403.
- [55] A. Thust, A. Hirsch, E. Haussühl et al. *Phys. Chem. Miner.*, **45** (4) (2018) 323-332.
- [56] L. Nasdala, R. Grotzschel, S. Probst, B. Bleisteiner, *Can. Mineral.*, **48** (2010) 351-359.
- [57] V. Picot, X. Deschanel, S. Peugot, B. Glorieux, A.M. Seydoux-Guillaume, R.J. Wirth, *Nucl. Mater.*, **381** (2008) 290-296.
- [58] B.E. Burakov, M.A. Yagovkina, V.M. Garbuzov, A.A. Kitsay, V.A. Zirlin, *Mater. Res. Soc. Symp. Proc.*, **824** (2004) 219-224.
- [59] D. Bregiroux, R. Belin, P. Valenza, F. Audubert, D.J. Bernache-Assollant, *Nucl. Mater.*, **366** (2007) 52-57.
- [60] M. Petek, M.M. Abraham and L.A. Boatner, ORNL Report No. CONF-811122-45 (1981) 1-7.
- [61] Y. He, Y. Lü and Q. Zhang, *J. Nucl. Mater.*, **376** (2008) 201-206.
- [62] E. du Fou de Kerdaniel, Thèse de l'Université Paris Sud-Paris XI, Paris (2007).
- [63] E.H. Oelkers, F. Poitrasson, *Chem. Geol.*, **191** (2002) 73-87.
- [64] M. Ishida, K. Kikuchi, T. Yanagi, R. Terai, *Nucl. Chem. Waste Manage.*, **6** (1986) 127-131.
- [65] B. Sales, C. White, L. Boatner, *Nucl. Chem. Waste Manage.*, **4** (1983) 281-289.
- [66] J. Ma, Y. Teng, Y. Huang, L. Wu, K. Zhang, X. Zhao, *J. Nucl. Mater.*, **465** (2015) 550-

555.

[67] J. Ma, Y. Teng, L. Wu, K. Zhang, Y. Huang, X. Zhao, G. Wang, *Ceram. Int.*, **41** (2015) 14597-14603.

[68] F. Brandt, S. Neumeier, T. Schuppik, Y. Arinicheva, A. Bukaemskiy, G. Modolo, D. Bosbach, *Prog. Nucl. Energy.*, **72** (2014) 140-143.

[69] J.M. Hugues, E.E. Foard, M.A. Hubbard, Y. Ni, *NeuesJb Miner Mon*, **8** (1995) 344-350.

[70] P.E. Raison, R. Jardin, D. Bouëxière, R.J.M. Konings, T. Geisler, C.C. Pavel, J. Rebizant, K. Popa, *Phys. Chem. Minerals*, **35** (2008) 603-609.

[71] K. Popa, T. Shvareva, L. Mazeina, E. Colineau, F. Wastin, R.J.M. Konings, A. Navrotsky, *Am. Mineral*, **93** (2008) 1356-1362.

[72] R. Podor, M. Cuney, *Am. Mineral*, **82** (1997) 765-771.

[73] Y. Dusausoy, N.E. Ghermani, R. Podor, M. Cuney, *Eur. J. Mineral*, **8** (1996) 667-673.

[74] R. Podor, M. Cuney, C.N. Trung, *Am. Mineral*, **80** (1995) 1261-1268.

[75] M. Keskar, R. Phatak, S.M. Sali, K. Krishnan, N.D. Dahale, N.K. Kulkarni, S. Kannan, *J. Nucl. Mater.*, **409** (1) (2011) 9-17.

[76] M. Keskar, B.G. Vats, R. Phatak, K. Krishnan, S.K. Sali, S. Kannan, *J. Alloy Compd*, **725** (2017) 1199-1209.

[77] K. Popa, G. Wallez, P.E. Raison, D. Bregiroux, C. Apostolidis, P. Lindqvist-Reis, R.J.M. Konings, *Inorg. Chem*, **49** (2010) 6904-6908.

[78] G. Wallez, D. Bregiroux, K. Popa, P.E. Raison, C. Apostolidis, P. Lindqvist-Reis, R.J.M. Konings, A.F. Popa, *Eur. J. Inorg. Chem*, 2011 (2011) 110-115.

[79] J.M. Montel, J.L. Devidal, D. Avignat, *Chem. Geol*, **191**(1-3) (2002) 89-104.

[80] O. Terra, N. Dacheux, N. Clavier, R. Podor, F. Audubert, *J. Am. Ceram. Soc.*, **91** (2008) 3673-3682.

[81] A. Tabuteau, M. Pagès, J. Livet, C. Musikas, *J. Mater. Sci. Lett.*, **7** (1988) 1315-1317.

- [82] D. Qin, A. Mesbah, C. Gausse, S. Szenknect, N. Dacheux, N. Clavier, *J. Nucl. Mater.*, **492** (2017) 88-96.
- [83] A. Thust, Y. Arinicheva, E. Hausstätter, J. Ruiz-Fuertes, L. Bayarjargal, S.C. Vogel, S. Neumeier, B. Winkler, *J. Am. Ceram. Soc.*, **98** (12) (2015) 4016-4021.
- [84] N. Huittinen, Y. Arinicheva, P.M. Kowalski, V.L. Vinograd, S. Neumeier, D. Bosbach, *J. Nucl. Mater.*, **486** (2017) 148-57.
- [85] P. M. Kowalski, Y. Ji, Y. Li, Y. Arinicheva, G. Beridze, S. Neumeier, A. Bukaemskiy, D. Bosbach, *Nucl. Instr. Meth. Phys. Res. B*, **393** (2017) 68-72.
- [86] Y. Li, P.M. Kowalski, A. Blanca-Romero, V. Vinograd, D. Bosbach, *J. Solid State Chem.*, **220** (2014) 137-141.
- [87] P. M. Kowalski, Y. Li, *J. Eur. Ceram. Soc.*, **36** (2016) 2093-2096.
- [88] A. Navrotsky, W. Lee, A. Mielewczyk-Gryn, S.V. Ushakov, A. Anderko, H. Wu, R.E. Riman, *J. Chem. Thermodyn.*, **88** (2015) 126-141.
- [89] A. Hirsch, P. Kegler, I. Alencar, J. Ruiz-Fuertes, A. Shelyug, L. Peters, C. Schreinemachers, A. Neumann, S. Neumeier, H.-P. Liermann, A. Navrotsky, G. Roth, *J. Solid State Chem.*, **245** (2017) 82-88.
- [90] S.V. Ushakov, A. Navrotsky, J.M. Farmer, L.A. Boatner, *J. Mater. Res.*, **19** (2004) 2165-2175.
- [91] D. Qin, A. Mesbah, J. Lautru, S. Szenknect, N. Dacheux, N. Clavier, *J. Eur. Ceram. Soc.*, in press, <https://doi.org/10.1016/j.jeurceramsoc.2019.10.050>.
- [92] B.C. Sales, C.W. White and L.A. Boatner, *Nucl. Chem. Waste Mgmt.*, **4** (1983) 281-289.
- [93] E. Veilly, E. du Fou de Kerdaniel, J. Roques, N. Dacheux and N. Clavier, *Inorg. Chem.*, **47** (2008) 10971-10979.
- [94] E. du Fou de Kerdaniel, N. Clavier, N. Dacheux, O. Terra, R. Podor, *J. Nucl. Mater.*, **362** (2007) 451-458.

- [95] N. Dacheux, R. Podor, V. Brandel, M. Genet, *J. Nucl. Mater.*, **252** (1998) 179-186.
- [96] N. Dacheux, A.C. Thomas, V. Brandel, M. Genet, *J. Nucl. Mater.*, **257** (1998) 108-117.
- [97] N. Dacheux, A. C. Thomas, V. Brandel, M. Genet, *AIP Conf. Proc.*, **532** (2000) 216-16.
- [98] V. Brandel, N. Dacheux, M. Genet, R. Podor, *J. Solid State Chem.*, **159** (1) (2001) 139-148.
- [99] V. Brandel, N. Dacheux, E. Pichot, M. Genet, J. Emery, J.Y. Buzaré, R. Podor, *Chem. Mater.*, **10** (1998) 345-350.
- [100] V. Brandel, N. Dacheux, M. Genet, R. Podor, *J. Solid State Chem.*, **159** (2001) 139-148.
- [101] D. Qin, C. Gausse, S. Szenknect, A. Mesbah, N. Clavier, N. Dacheux, *J. Chem. Thermodyn.*, **114** (2017) 151-164.
- [102] P. Bénard, V. Brandel, N. Dacheux, S. Jaulmes, S. Launay, C. Lindecker, M. Genet, D. Louër, M. Quarton, *Chem. Mater.*, **8** (1996) 181-188.
- [103] N. Clavier, N. Dacheux, R. Podor, *Inorg. Chem.*, **45** (2006) 220-229.
- [104] N. Dacheux, B. Chassigneux, V. Brandel, P. Le Coustumer, M. Genet and G. Cizeron, *Chem. Mater.*, **14** (2002) 2953-2961.
- [105] S. Launay, G. Wallez, M. Quarton, *Chem. Mater.*, **13** (2001) 2833-2837.
- [106] C. Tamain, A. Özgümüs, N. Dacheux, F. Garrido, L.J. Thomé, *J. Nucl. Mater.*, **352** (2006) 217-223.
- [107] C. Tamain, N. Dacheux, F. Garrido, A. Habert, N. Barré, A. Özgümüs, L.J. Thomé, *J. Nucl. Mater.*, **358** (2006) 190.
- [108] C. Tamain, N. Dacheux, F. Garrido, L.J. Thomé, *J. Nucl. Mater.*, **362** (2007) 459-465.
- [109] A.C. Thomas, N. Dacheux, P. Le Coustumer, V. Brandel, M. Genet. *J. Nucl. Mater.*, **281** (2000) 91-105.
- [110] A.C. Thomas, N. Dacheux, P. Le Coustumer, V. Brandel, M. Genet, *J. Nucl. Mater.*, **295** (2001) 249-264.

- [111] A.C. Robisson, N. Dacheux, J.J. Aupiais, *J. Nucl. Mater.*, **306** (2002) 134-146.
- [112] A. R West, “*Solid State Chemistry and its Applications*”, John Wiley & Sons, Singapore (2008).
- [113] B. C. Smith, “*Fundamentals of Fourier Transform Infrared Spectroscopy*”, CRC Press: Boca Raton (2011), ISBN 9781420069297.
- [114] G.I. Goldstein, D.E. Newbury, P. Echlin, D.C. Joy, C. Fiori, E. Lifshin, *Scanning electron microscopy and x-ray microanalysis*. New York: Plenum Press. (1981).
- [115] P. W. Atkins, “*Physical Chemistry*”, 5<sup>th</sup> ed. W. H. Freeman, New York (1994).
- [116] G. Höhne, W. Hemminger, H.J. Flammersheim, “*Differential Scanning Calorimetry- An Introduction for Practitioners*”, Springer-Verlag, Berlin (1996), ISBN 978-3-662-03302-9.
- [117] M. Sorai, “*Comprehensive Handbook of Calorimetry and Thermal Analysis*”, Wiley, (2004), ISBN 0-470-85152-X.
- [118] M. E. Brown, *Handbook of Thermal Analysis and Calorimetry*, Vol. I, Principles and Practice, Elsevier Science (1998), ISBN: 9780080539591.
- [119] R. F. Speyer, Marcel Dekker, “*Thermal Analysis of Materials*”, New York, (1993), ISBN 9780824789633.
- [120] B. Wunderlich, “*Thermal Analysis*”, New York: Academic Press. (1990), ISBN: 9780323139670.
- [121] E. Gmelin, S.M. Sarge, *Pure & Appl. Chem.*, **67** (11) (1995) 1789-1800.
- [122] J.E. Callanan, S.A. Sullivan, *Rev, Sci. Instu.*, **57** (1986) 2284-2289.
- [123] G.H.W. Hohne, E. Glogler, *Thermochim. Acta.*, **151** (1989) 295-304.
- [124] S.C. Mraw, C.Y. Ho (Ed.), *Specific heat of solids*, New York, NY: Hemisphere Publishing Corp., Taylor and Francis Group (1988) 395-435.
- [125] R. Hultgren, P.D. Desai, D.T. Hawkins, M. Gleigev, K.K. Kelley, *Selected values of the thermodynamic properties of the elements*. Metal Park, Ohio (1973).

- [126] B.R. Capelli, R. Ferro, A. Borsese, *ThermochimActa*, **10** (1974) 13-21.
- [127] R. Stevens, J. Boerio-Goates, *J. Chem. Thermodynamic.*, **36** (2004) 857–863.
- [128] Calvet E, Pratt H, *Traite de Microcalorimetric*, Paris (1956).
- [129] N.B.S. Certified Standard Reference Material 720, Synthetic Sapphire ( $\text{Al}_2\text{O}_3$ ); August 26, 1970. N.B.S.
- [130] R.A. Young, *The Rietveld Method*, (Oxford University Press, 1995).
- [131] J. Rodriguez-Carvajal, Fullprof 2000 Version 1. 6, Laboratoire Leon Brillouin, Gifsur Yvette, France, 2000.
- [132] J.J. Van Laar, *Physikalische Chemie*, **6364**: 216–253 (1908) 257–297.
- [133] L. Kaufman, H. Bernstein, Computer calculation of phase diagrams with special reference to refractory metals. Academic Press; New York: 1970.
- [134] N. Saunders, A. P. Miodownik, CALPHAD (Calculation of phase diagrams): A comprehensive guide. Pergamon; Oxford: 1998
- [135] P. J. Spencer, *Calphad* **32** (2008) 1–8.
- [136] T. Dinsdale, *Calphad* **15** (1991) 317–425.
- [137] G. Eriksson, *Chemica. Scripta.*, **8** (1975) 100–103.
- [138] H.L. Lukas, E-Th Henig, B. Zimmermann, *Calphad* **1** (1977) 225–236.
- [139] E. Kozeschnik, B. Buchmayr, MatCalc – A simulation tool for multicomponent thermodynamics, diffusion and phase transformation kinetics. *Mathematical Modelling of Weld Phenomena*, 2001; 5 (2001) 349–361.
- [140] R.H. Davies, A.T. Dinsdale, J.A. Gisby, J.A.J. Robinson, S.M. Martin, *Calphad*, **26** (2002) 229–271.
- [141] W. Cao, S-L Chen, F. Zhang, K. Wu, Y. Yang, Y.A. Chang, R. Schmid-Fetzer, W.A. Oates, *Calphad*, **33** (2009) 328–342.
- [142] N. Saunders, Z. Guo, X. Li, A.P. Miodownik, J-Ph. Schillé. *JOM* **55** (2003) 60–65.

- [143] P. Shi, A. Engström, B. Sundman, J. Ågren, *Materials Science Forum*, **675-677** (2011) 961–974.
- [144] C.W. Bale, E. Bélisle, P. Chartrand, S.A. Decterov, G. Eriksson, K. Hack, I-H. Jung, Y.B. Kang, J. Melançon, A.D. Pelton, C. Robelin, S. Petersen, *Calphad* **33** (2009) 295–311.
- [145] ASTM Standard Test Methods for Determining Chemical Durability of Nuclear, Hazardous, and Mixed Waste Glasses and Multiphase Glass Ceramics: The Product Consistency Test (PCT). ASTM International (2008).
- [146] R.C. Ewing, Nuclear waste forms for actinides. *Proc. Natl. Acad. Sci. U. S. A.*, **96** (1999) 3432–3439.
- [147] A. Shelyug, A. Mesbah, S. Szenknect, N. Clavier, N. Dacheux and A. Navrotsky, *Front. Chem.*, **6** (2018) 604.
- [148] S. Neumeier, P. Kegler, Y. Arinicheva et al., *J. Chem. Thermodyn.*, **105** (2017) 396–403.
- [149] V.S. Yungman, *Thermal Constants of Substances*, Begell House, 1999.
- [150] S.V. Ushakov, K.B. Helean, A. Navrotsky, *J. Mater. Res.*, **16** (2001) 2623–2633.
- [151] K.B. Helean, A. Navrotsky, *J. Therm. Anal. Calorim.*, **69** (2002) 751–771.
- [152] K. Popa, D. Sedmidubsky, C. Thiriet, R.J.M. Konings, *J. Chem. Thermodyn.*, **38** (2006) 825-829.
- [153] F. Poitrasson, E. Oelkers, J. Schott, J.L. Montel, *Geochim. Cosmochim. Acta.*, **68** (2004) 2207–2221.
- [154] S.A. Wood, A.E. Williams-Jones, *Chem. Geol.*, **115** (1994) 47–60.
- [155] M.A. Williamson, J.C. Huang, R.L. Putman, *Fundamental thermodynamics of actinide-bearing mineral waste forms*. US: Department of Energy; 2000. pp. 14.
- [156] Z.S. Cetiner, A. Scott, T. Wooda, H. Christopher, H. Gammons, *Chem. Geol.*, **217** (2005) 147–169.
- [157] L.A. Marinova, V.N. Yaglov. *Rus. J. Phys. Chem.*, **50** (1976) 477-478.

- [158] L.A. Marinova, V.P. Glibin, A.I. Volkov, *Rassh Tezisi Dokl Tbilissi Meznieba.*, **71** (1973).
- [159] I. Ousoubalyev, M. Batkybekova, V. Yousoupov, M. Kydynov, *4e Confe'rence internationale de Thermodynamique Chimique* (1975) 217–223.
- [160] J. Rodriguez–Carvajal, Fullprof 2000 Version 1.6, Laboratoire Leon Brillouin, Gif sur Yvette, France (2000).
- [161] A. Mesbah, N. Clavier, E. Elkaim, C. Gausse, I. Kacem and S.S. Ben et al. *Cryst. Growth Des.*, **14** (2014) 5090–5098.
- [162] PCPDFWIN version 2.2, JCPDS-ICDD, 2001.
- [163] D.D. Wagman et al. NBS Tech. Note 270-7. Selected values of chemical thermodynamic properties, 1973.
- [164] J.B. Pedley, A. Kirk, S. Seilman, L.G. Heath, Computer analysis of thermo chemical data, CATCH tables. Brighton: University of Sussex; 1972.
- [165] R.D. Shannon, *Acta. Cryst.*, **A32** (1976) 751-767.
- [166] C. Gausse, S. Szenknect, D.W. Qin, A. Mesbah, N. Clavier, S. Neumeier et al., *Eur. J. Inorg. Chem.*, **28** (2016) 4615–4630.
- [167] K. Popa, R.J.M. Konings, T. Geisler, *J. Chem. Thermodyn.*, **39** (2007) 236–239.
- [168] S. Neumeier, P. Kegler, Y. Arinicheva et al., *J. Chem. Thermodyn.*, **105** (2017) 396–403.
- [169] A. Thust, A. Hirsch, E. Haussühl et al, *PhysChem Minerals* **45** (2018) 323-332.
- [170] A. Thust, Y. Arinicheva, E. Haussühl, J. Ruiz-Fuertes, L. Bayarjargal, S.C. Vogel, S. Neumeier, B. Winkler, *J. Am. Ceram. Soc.*, **98** (12) (2015) 4016-4021.
- [171] R.J.M. Konings, M. Walter, K. Popa, *J. Chem. Thermodyn.*, **40** (2008) 1305–1308.
- [172] D. Qin, A. Mesbah, C. Gausse, S. Szenknect, N. Dacheux, N. Clavier, *J. Nucl. Mater.*, **492** (2017) 88-96.
- [173] J. Rodriguez-Carvajal, Fullprof 2000 Version 1. 6, Laboratoire Leon Brillouin, Gifsur

Yvette, France, 2000.

[174] R.D. Shannon, *Acta. Cryst.*, A **32** (1976) 751-767.

[175] K.S. Gavrichev, M.A. Ryumin, A.V. Tyurin, V.M. Gurevich, L.N. Komissarova, *Thermochim. Acta*, **474** (2008) 47–51.

[176] D.F. Mullica, W.O. Milligan, D.A. Grossie, G.W. Beall and L.A. Boatner. *Inorganica Chimica Acta*, **95** (1984) 231-236.

[177] S.V. Ushakov, K.B. Helean, A. Navrotsky, L.A. Boatner, *J. Mater. Res.*, **16** (2001) 2623–2632.

[178] P.E. Raison, R. Jardin, D. Bregiroux, R.J.M. Konings, T. Geisler, C.C. Pavel, J. Rebizant K. Popa, *Phys. Chem. Miner.*, **35** (2008) 603-609.

[179] K. Popa, T. Shvareva, L. Mazeina, E. Colineau, F. Wastin, R.J.M. Konings, A. Navrotsky, *Am. Miner.*, **93** (2008) 1356–1362.

[180] Y. Hikichi, K. Hukuo, and J. Shiokawa, *Nippon Kagaku Kaishi*, **12** (1978) 1635–1640.

[181] D. Rose, *Neues Jahrb. Mineral. Mh.*, **6** (1980) 247-257.

[182] R. Podor, M. Cuney, *Am. Mineral.*, **82** (1997) 765-771.

[183] J.M. Montel, J.L. Devidal, D. Avignat, *Chem Geol.*, **191** (2002) 89–104.

[184] M. Keskar, R. Phatak, S.M. Sali, K. Krishnan, N.D. Dahale, N.K. Kulkarni, S. Kannan, *J. Nucl. Mater.*, **409** (2011) 9-17.

[185] G. Wallez, D. Bregiroux, K. Popa, P.E. Raison, C. Apostolidis, P. Lindqvist-Reis, R.J.M. Konings, A.F. Popa, *Eur. J. Inorg. Chem.*, **2011** (2011) 110-115.

[186] K. Momma, F. Izumi, VESTA 3 for three-dimensional visualization of crystal, volumetric and morphology data, *J. Appl. Crystallogr.*, **44** (2011) 1272-1276.

[187] I. Barin, Thermochemical Data of Pure Substance, third ed., VCH, Weinheim, Federal Republic of Germany., 1995.

[188] C. Thiriet, R.J.M. Konings, P. Javorsky, N. Magnani, F. Wastin. *J. Chem. Thermodyn.*,

- 37 (2005) 131-139.
- [189] K. Popa, D. Sedmidubsky, C. Thiriet, R.J.M. Konings, *J. Chem. Thermodyn.*, **38** (2006) 825-829.
- [190] F.E. Neumann, *Ann. Phys.*, **99** (183 1) 9.
- [191] H. Kopp, *Ann. Chem. Pharm. Suppl.*, **3** (1864), 289-342.
- [192] H.Y. Xiao, Y. Zhang, W.J. Weber, *Acta Materialia*, **61** (2013) 467-476.
- [193] R.A. Robie, B.S. Hemingway, *Thermodynamic properties of minerals and related substances at 298.15 K and 1 bar pressure and at higher temperatures*. U.S. Geological Survey Bulletin 2131; U.S. Geological Survey: Reston, VA, 1995.
- [194] J. Dicarolo, A. Mehta, D. Banschick, and A. Navrotsky. *J. Solid State Chem.*, **103** (1993) 86-92.
- [195] Z. Zhou and A. Navrotsky. *J. Mater. Res.*, **7** (11) (1992).
- [196] Y.-Q. Zhang, A. V. Radha, and A. Navrotsky. *Geochim. Cosmochim. Acta*, **115**, (2013) 92-99.
- [197] C. Drouet and A. Navrotsky. *Geochim. Cosmochim. Acta*, **67**, (2003) 2063-2076.
- [198] L. Mazeina, S. V. Ushakov, A. Navrotsky, and L. A. Boatner. *Geochim. Cosmochim. Acta*, **69** (2005) 4675–83.
- [199] J. Cheng, A. Navrotsky, *J. Solid State Chem.*, **178** (2005) 234–244.
- [200] M. René, *Descr. Inorg. Chem. Res. Met. Compd*, InTech (2017), DOI:10.5772/intechopen.68304
- [201] L.A. Marinova, V.P. Glibin, A.I. Volkov. *Rassh Tezisi Dokl Tbilissi Mezniebna*, (1973) 71.
- [202] L.A. Marinova, V.N. Yaglov. *Rus J Phys Chem.*, **50** (1976) 477.
- [203] G. Zhang, H. Hattori, K. Tanabe, *Appl. Catal.*, **36** (1988) 189-197.

- [204] A. D. Nelson, T. H. Bray, F. A. Stanley, T. E. Albrecht-Schmitt, *Inorg. Chem.*, **48** (10) (2009) 4530-4535.
- [205] M. Bertolus and M. Defranceschi, *J. Phys. Chem.* **B 110** (39) (2006) 19226-19232.
- [206] W. G. Ramsey, N.E. Bibler, T. E. Meaker, *Waste Management Symposia*, (1995) 23828-23907.
- [207] C. Guy, F. Audubert, J.-E. Lartigue, C. Latrille, T. Advocat, C. Fillet, *C.R. Phys.*, **3** (2002) 827-837.
- [208] C. Lopez, X. Deschanel, J. M. Bart, J. M. Boubals, C. Den Auwer, E. Simoni, *J. Nucl. Mater.*, **312** (1) (2003) 76-80.
- [209] B. C. Sales, White, C.W., and Boatner, L.A. (1983), *Nucl. Chem. Waste Man.*, **4** (1983) 281–289.
- [210] E.H. Oelkers, F. Poitrasson, *Chem. Geol.*, **191** (2002)73–87.
- [211] O. Terra, N. Clavier, N. Dacheux, and R. Podor, *New J Chem*, **27** (2003) 957–967.
- [212] E. du Fou de Kerdaniel, N. Clavier, N. Dacheux, O. Terra and R. Podor, *J. Nucl. Mater*, **362** (2007) 451-458.
- [213] E. Veilly, E. du Fou de Kerdaniel, J. Roques, N. Dacheux and N. Clavier, *Inorg. Chem.*, **47** (2008) 10971-10979.
- [214] N. Dacheux, N. Clavier and R. Podor, *American Mineralogist*, **98** (2013) 833–847.
- [215] ASTM C1285-02, ASTM, Conshohocken, USA, **15** (2002) 1-26.
- [216] D.C. Stewart, “*Data for Radioactive Waste Management and Nuclear Applications*”, A Wiley- Interscience Publication, Arogonne National Lab, California, USA (1985) 170.
- [217] S.V. Yudintsev, E.V. Aleksandrova, T.S. Livshits, V.I. Mal’kovskii, Y.V. Bychkova, B.R. Tagirov, *Dokl. Earth Sci.*, **458** (2) (2014) 1281-1284.

- [218] R.L. Russell, M.J. Schweiger, Jr. J.H. Westsik, P. Hrma, D.E. Smith, A.B. Gallegos, M.R. Telander, S.G. Pitman, Low Temperature Waste Immobilization Testing, PNNL-16052 Rev. 1, Pacific Northwest National Laboratory (2006).
- [219] B.C. Sales, L.A. Boatner, H. Naramoto and C.W. White, *J. Non-Cryst. Solids*, **53** (1982) 201-226.
- [220] B.D. Begg, N.J. Hess, W.J. Weber, R. Devanathan, J.P. Icenhower, S. Thevuthasan, B.P. McGrail, *J. Nucl. Mater.*, **288** (2001) 208–216.
- [221] FactSage, Version 6.3, The Integrated Thermodynamic Data Bank System, GTT-Technologies, GmbH, Germany, 1976-2006.
- [222] V.K. Wadhawan, LATPAR, Neutron Physics Division, BARC, Private Communication.
- [223] N. Dacheux, B. Chassigneux, V. Brandel, P. Le Coustumer, M. Genet, G. Cizeron, *Chem. Mater.* **14** (7) (2002) 2953–2961.
- [224] PCPDFWIN version 2.2, Joint Committee on Powder Diffraction Standards, JCPDS-ICDD (2001).
- [225] A.C. Chapman, L.E. Thirlwell, *Spectrochim. Acta*, **20** (1964) 937–947.
- [226] S. Bruque, M.A.G. Aranda, E.R. Losilla, P. Oliveira-Pastor, P. Maireles-Tores, *Inorg. Chem.*, **34** (1995) 893–899.
- [227] D.E.C. Corbridge, *J. Appl. Chem.* **6** (1956) 456–465.
- [228] K. Nakamoto, “*Infrared and Raman Spectra of Inorganic and Coordination Compounds*”, Wiley, New York (1986) pp. 106, 115, 383.
- [229] V. Brandel et al. *J Solid State Chem.*, **159** (2001) 139-148.
- [230] Materials Research Bulletin **40** (2005) 2225–2242.
- [231] P. Bénard et. al, *Chem. Mater.* **8** (1996) 181-188.
- [232] N. Dacheux, N. Clavier, G. Wallez, V. Brandel, J. Emery, M. Quarton, M. Genet, *Mater. Res. Bullet.*, **40** (2005) 2225–2242.

- [233] E.H.P. Cordfunke, P.A.G. O'Hare, The Chemical Thermodynamics of Actinide elements and compounds, Part 3, V. Medvedev (Eds.), M.H. Rand, E.F. Westrum, F.L. Oetting, IAEA, Vienna 1978.
- [234] J.B. Pedley, A. Kirk, S. Seilman, L.G. Heath, Computer Analysis of Thermo Chemical data, CATCH tables, 1972.
- [235] I. Barin, Thermochemical Data of Pure Substance, third ed., VCH, Weinheim, Federal Republic of Germany, 1995.
- [236] C.A. Javorsky, R. Benz, *J. Nucl. Mater.*, **23** (1967) 192–198.
- [237] H.G. Schnering, M. Wittmann, R. Nesper, *J. Less Comm. Met.*, **76** (1980) 213–226.
- [238] H.G. Schnering, D. Vu, *J. Less Comm. Met.*, **116** (1986) 259–270.
- [239] K.R. Laud, F.A. Hummel, *J. Am. Ceram. Soc.*, **54** (1971) 296–298.
- [240] N. Clavier, G. Wallez, N. Dacheux, D. Bregiroux, M. Quarton, P. Beaunier, *J. Solid State Chem.*, **181** (2008) 3352–3356.
- [241] P. Bénard, V. Brandel, N. Dacheux, S. Jaulmes, S. Launay, C. Lindecker, M. Genet, D. Louer, M. Quarton, *Chem. Mater.*, **8** (1996) 181–218.
- [242] V. Brandel, N. Dacheux, M. Genet, *Radiochemistry*, **43** (2001) 16–22.
- [243] C.E. Bamberger, R.G. Haire, G.M. Begun, H.E. Hellwege, *J. Less Com. Met.*, **102** (1984) 179–186.
- [244] N. Clavier, N. Dacheux, R. Podor, *Inorg. Chem.*, **45** (2006) 220–229.
- [245] M. Keskar, R. Phatak, S.K. Sali, K. Krishnan, N.D. Dahale, N.K. Kulkarni, S. Kannan, *J. Nucl. Mater.*, **409** (2011) 9–17.
- [246] H. Yokokawa, T. Kawada, M. Dokiya, *J. Am. Ceram. Soc.*, **72** (1989) 2104–2110.
- [247] H. Yokokawa, *J. Phase Equilibria*, **20** (1999) 258–287.
- [248] D.G. Brookins, *E<sub>H</sub>-pH Diagrams for Geochemistry*, Springer-Verlag, New York (1988) pp. 176.

[249] M. Pourbaix, *Atlas of Electrochemical Equilibria in Aqueous Solutions*, Pergamon Press, Oxford (1966) pp. 644.

[250] R.M. Garrels, C.L. Christ, *Solution, Minerals and Equilibria*, Freeman, Cooper & Company, San Francisco, 1965, pp. 450.